The Astbury Centre for
Structural Molecular Biology

UNIVERSITY OF LEEDS

ANNUAL REPORT 2019

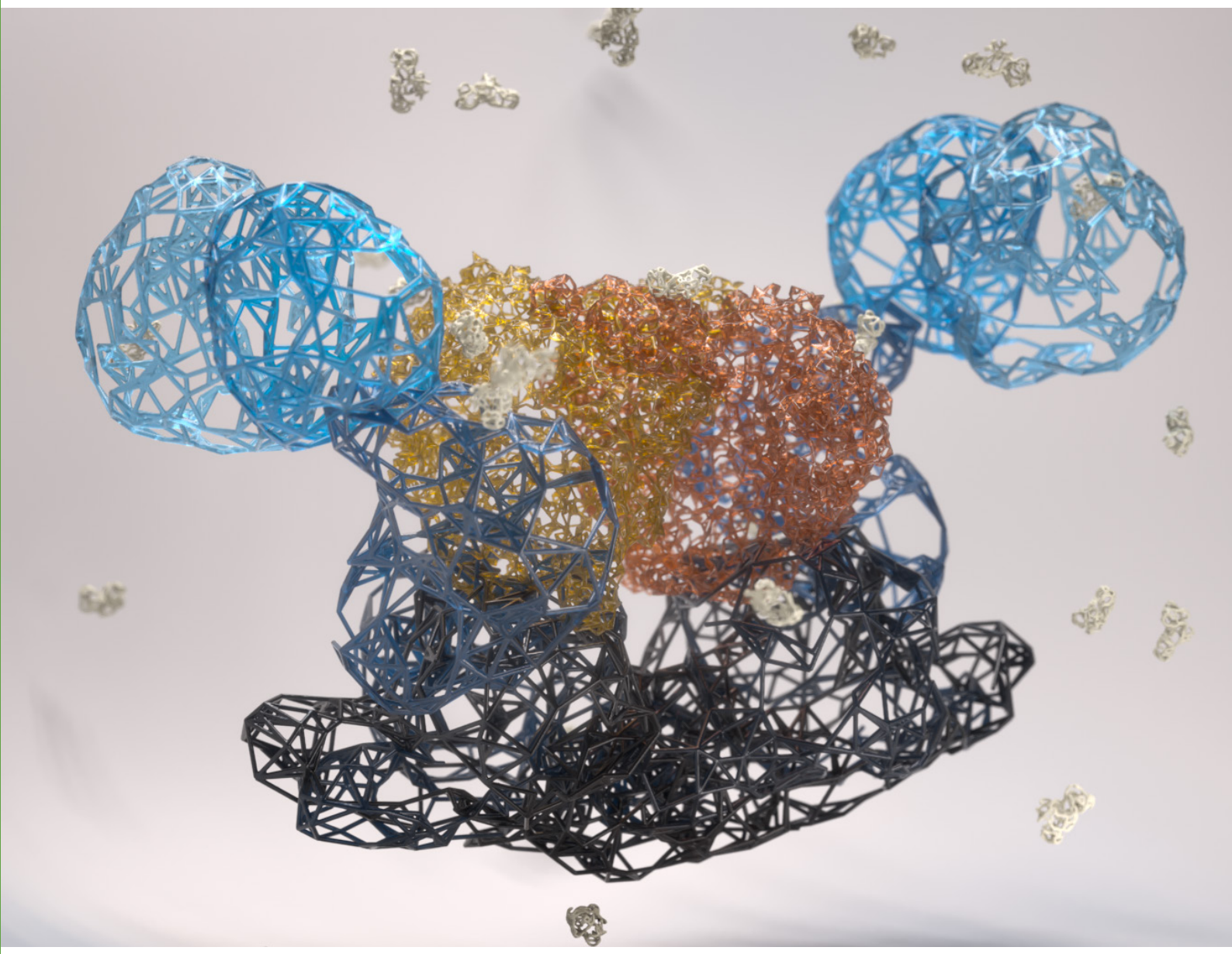

Front cover illustration

Stylised depiction of the structure of the human BRISC deubiquitylase:SHMT2 complex solved at 3.8Å using cryo-electron microscopy. The research, which was led by the Astbury Centre's Elton Zeqiraj, was published in Nature and is described pages 105-106

Mission Statement

The Astbury Centre for Structural Molecular Biology will promote interdisciplinary research of the highest standard on the structure and function of biological molecules, biomolecular assemblies and complexes using physico-chemical, molecular biological and computational approaches.

Introduction

Welcome to the Annual Report of the Astbury Centre for Structural Molecular Biology for 2019. The year has been very busy, as you will see below, and it doesn't seem long at all since I was writing the Director's report for 2018! In the following pages you will find some new and exciting research from members of the Centre, which spans beautiful new structures, fascinating biophysical mapping of proteins and macromolecules in dynamic action, new chemical probes and methodologies that are enabling new insights into life *in vitro* and in cells, alongside the exploitation of the results obtained for application in biotechnology, bioengineering and medicine. Each portrays the insights made possible by the interdisciplinary research enjoyed within the Centre. I would like to thank every member of the Centre for their hard work over the year: our Support staff, Technicians, Facility Managers, Staff Scientists Students, Post-docs, Fellows and Academic staff. And, of course, Lucy Gray for her excellent organisation and administrative support without which we could not function. Thank you all.

2019 was a special year for the Centre as we marked the 20th anniversary of our inauguration as The Astbury Centre for Structural Molecular Biology. This fantastic milestone was celebrated on Friday 12th April 2019 with a wonderful day of science, networking, reminiscing and looking forward. Current, past and our visiting Astbury members gave talks and we were excited to welcome Tony North and Simon Phillips back to Leeds, past Astbury Chairs of Biophysics and Simon was the first Astbury Director responsible for setting it up all those years ago. 200 current and past Astbury members were there to mark the occasion!

During 2019 we continued to enjoy an excellent seminar series (organised by Joe Cockburn), hosting 9 lectures during the year with speakers from the UK and Europe. On 12th and 13th September, 164 members attended the Centre's Biennial Research Retreat held at The Palace Hotel in Buxton for the first time. The retreat was a great success and students, post-docs and PIs shared their recent exciting scientific discoveries, through talks, posters and flash poster presentations. Poster prizes were awarded to David Nicholson, Devon Legge and Claudia Stohrer. Well done all! We look forward now to events during 2020 including the Astbury Conversation 2020 and the Astbury Research Away Day - watch out for an update on these events in the coming months and in next year's report.

The 2019 VC Jordan/PR Radford Prize for the best PhD thesis in the Astbury Centre was awarded to Dan Hurdiss. This annual prize was established in 2017 by a generous donation from Leeds University alumnus Professor Craig Jordan and we were delighted to welcome Craig back to Leeds to present the award to Dan at the Astbury 20th anniversary celebration day. More information and instructions on how to nominate students can be found here http://www.astbury.leeds.ac.uk/prize/.

The Centre welcomed two new PI members in 2019: Morgan Herod (University Academic Fellow and MRC CDA Fellow, School of Molecular and Cellular Biology) and Yoselin Alfonso-Benitez (University Lecturer in the School of Biology). We look forward to their involvement in Astbury Centre activities. We were also delighted to welcome our new PhD students and postdocs to the Centre this year, bringing our total number of researchers to >400, including 72 academic staff, 186 PhD students, >100 postdoctoral researchers and 14 Research Fellows.

Astbury Centre members published their research in a wide range of journals in 2019 including Journal of the American Chemical Society, Nature Communications and Nucleic Acids Research. A full list can be found at the end of this report. In terms of grant income, Astbury members also enjoyed many successes in 2019. £13M of new project and programme grants brings the Astbury grant portfolio to a highly impressive £68M share of £107M of grants: a testament to the hard work and successes of our members. We are much indebted to the funding agencies who support our science, including BBSRC, EPSRC, MRC, the Wellcome Trust, CRUK, other charities, ERC, EU and Industry. We also

acknowledge, with thanks, the support of the University of Leeds; the Faculties of Biological Sciences, Engineering and Physical Sciences and Medicine and Health, and the Schools of Chemistry, Molecular and Cellular Biology, Biomedical Sciences, Biology and Physics and Astronomy for their support of the Centre and our research.

Several Astbury members achieved success in terms of peer recognition. Alison Ashcroft received the BMSS Medal for sustained contributions to the development of mass spectrometry. Patricija van Oosten Hawle was awarded The Ferruccio Ritossa Early Career Award, Qian Wu was awarded the Biochemical Society early career research award 2019 and Megan Wright was awarded a Young Investigator Award by the American Chemical Society. It will not escape your notice that all four are females at every career stage – well done all. Congratulations also go to Lorna Dougan who was promoted to Professor and Darren Tomlinson for his promotion to Associate Professor. Well done all on your much-deserved achievements.

The Astbury Centre continued to contribute to public engagement events in 2019 with a significant presence at the 'Be Curious' event in March and The Astbury Biostructure Laboratory hosted a stand at Leeds City Museum science Fair in March 2019, showcasing structural biology at Leeds. We are currently looking forward to the third Astbury Conversation that will be held at the University of Leeds on 23rd & 24th March 2020 on the topic 'Seeing into Cells' (see https://astburyconversation.leeds.ac.uk). We are busy planning and looking forward to a fantastic two days of cutting edge science, with the Plenary Public Lecture to be given by Nobel laureate Richard Henderson.

The Astbury Society, led by the presidents Eleanor Todd and Frank Charlton, organised a fantastic array of Astbury activities in 2019. These included the famous Christmas quiz night, coffee mornings and bake sales and the seventh Astbury May Ball. Fundraising at all these events resulted in the Society has raised an impressive £6,601.65 to date for the Leeds Children's Charity. See http://www.astbury.leeds.ac.uk/about/society.php for photos of these events.

I hope that you enjoy reading this Annual Report. Thank you to David Brockwell and Lucy Gray for editing this report, Ralf Richter, Robin Bon and Peter Adams for proofreading it, everyone who contributed reports, and all who participated in the Astbury Centre's activities in 2019. We are set for an exciting year ahead. I look forward to reporting on our successes in next years report!

Sheena E. Radford, FMedSci, FRS

Director, Astbury Centre for Structural Molecular Biology,
Leeds, February 2020

Please note that this report (as well as those from previous years) is also available as a PDF document which can be downloaded from our website (www.astbury.leeds.ac.uk).

CONTENTS

Contributions indexed by Astbury Centre Principal Investigator

A nanotechnology approach to photosynthesis: proteoliposomes as a controllable platform to combine synthetic chromophores with light-harvesting proteins

Ashley Hancock, Sophie Meredith and Peter Adams

Introduction

Light-Harvesting Complex II (LHCII) is a chlorophyll-protein antenna complex that efficiently absorbs solar energy and transfers electronic excited states to photosystems I and II. We considered whether LHCII could be "enhanced" by interfacing it with synthetic nanomaterials. Bio-hybrid nanomaterials have great potential for combining the most desirable aspects of biomolecules and the contemporary concepts of nanotechnology to create highly efficient light-harvesting materials. Light harvesting proteins are optimized to absorb and transfer solar energy with remarkable efficiency but have a spectral range that is limited by their natural pigment complement.

Results and Discussion

We present the development of model membranes ("proteoliposomes") in which the absorption range of the membrane protein Light-Harvesting Complex II (LHCII) is effectively enhanced by the addition of lipid-tethered Texas Red (TR) chromophores. Energy transfer from TR to LHCII is observed with up to 94% efficiency and increased LHCII fluorescence of up to three-fold when excited in the region of lowest natural absorption. The new self-assembly procedure offers the modularity to control the concentrations incorporated of TR and LHCII, allowing energy transfer and fluorescence to be tuned. Fluorescence Lifetime Imaging Microscopy provides single-proteoliposome-level quantification of energy transfer efficiency and confirms that functionality is retained on surfaces. Designer proteoliposomes could act as a controllable light harvesting nanomaterial and are a promising step in the development of bio-hybrid light harvesting systems. Other work in progress is indicating that the above methodology can be extended to a range of different dye molecules which would cover a broad palette of colours. Furthermore, we expect that excitation energy can be transferred from such synthetic dyes to a broad range of photosynthetic proteins (unpublished data).

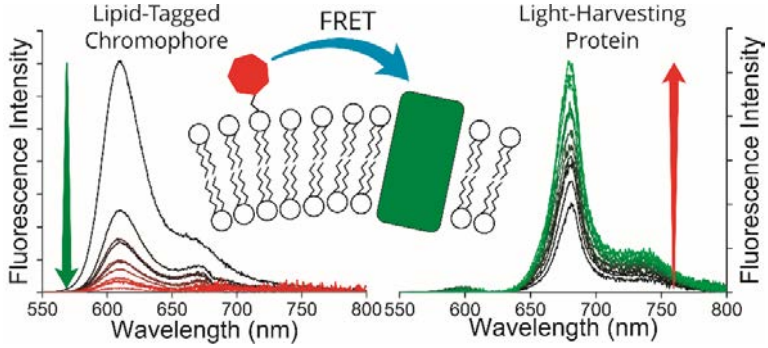

Figure 1: *Centre:* Cartoon showing the concept for the model membranes. Lipids are shown in *black*, the Texas Red (TR) chromophore in *red* and the LHCII membrane protein in *green*. Forster Resonance Energy Transfer (FRET) occurs from TR to LHCII. *Left:* Graph of fluorescence emission from the TR chromophore, showing quenching due to FRET. *Right:* Graph of fluorescence emission from the LHCII protein, showing enhanced fluorescence due to FRET.

In other research, we are developing "hybrid model membranes" which combine natural membranes extracted from chloroplasts which we have combined with synthetic lipid vesicles. Our preliminary analysis by fluorescence spectroscopy and microscopy gives a promising indication that the photosynthetic proteins are still optically intact and active. Atomic force microscopy shows single layer structures with hints that we may be able to identify single proteins (unpublished data).

Publications

Hancock, A.M., Meredith, S.A., Connell, S.D., Jeuken, L.J.C., Adams, P.G. (2019) Proteoliposomes as energy transferring nanomaterials: enhancing the spectral range of light-harvesting proteins using lipid-linked chromophores. *Nanoscale*. **11**: 16284-16292.

Funding

This work was funded by a BBSRC fellowship grant, studentships from EPSRC and BBSRC and BBSRC equipment grants.

Collaborators

University of Leeds: Simon Connell, Lars Jeuken, Stephen Evans
External: C. Neil Hunter (University of Sheffield), Kenichi Morigaki (University of Kobe, Japan)

Structural and functional studies of a peroxisome ABC transporter

David Carrier, Jack Wright and Alison Baker

Introduction

ABC transporters couple ATP hydrolysis to movement of molecules across membranes. They are found in pro- and eukaryotic cells and can function as importers or exporters. Importers are mainly found in prokaryotes and capture nutrients from the periplasm and transport them into the cell. Exporters are found in both pro- and eukaryotes and move molecules from the cytosol to the cell exterior. Many exporters display substrate polyspecificity leading to them being significant in drug resistance. The functional unit of an ABC transporter consists of two groups of transmembrane domains (TMDs) and two nucleotide binding domains (NBDs). These can be the products of four different gene products, commonly seen in prokaryotes, or fused in different combinations e.g $(TMD\text{-}NBD)_2$ (often termed half transporters) or NBD_2 plus TMD_2. As well as plasma membrane localised ABC transporters, eukaryotic cells possess ABC transporters in the membranes of their organelles. One such group are the peroxisome ABC transporters which belong to the ABC subfamily D. Humans have 3 peroxisome ABC transporters, ABCD1, ABCD2 and ABCD3, which are homodimers of a TMD-NBD fused half transporter. They have distinct but overlapping substrate specificity for acyl CoAs which are substrates for peroxisomal β-oxidation. *Saccharomyces cerevisiae* has a single heterodimeric peroxisome ABC transporter that transports long and very long chain fatty acyl CoA. In contrast plants have a single peroxisome transporter which is a fused heterodimer and which is required for metabolism of a very diverse group of fatty acid and aromatic molecules. Genetics shows that activation of substrates for β-oxidation takes place in the peroxisome yet the substrates of the transporter are CoA esterified. In earlier work we showed that the Arabidopsis peroxisomal ABCD1 transporter (also known as COMATOSE) possesses acyl CoA thioesterase (ACOT) activity. In this work we used mutagenesis to dissect the ATPase and ACOT activities.

Results

Using modelling and residue conservation we identified candidates for ACOT catalytic residues. We created mutants and expressed them in *S. cerevisiae* cells lacking the native peroxisomal ABC transporter. Wild type COMATOSE can rescue the β-oxidation defect of these yeast cells but the mutants could not despite being expressed at similar levels to wild type and correctly targeted to peroxisomes. Similarly, a mutant defective in ATPase could not rescue β-oxidation. Expression of a representative ACOT mutant in insect cells showed that the mutant retained substrate stimulated ATPase – demonstrating that it is correctly folded – but strongly reduced ACOT activity. Conversely the ATPase mutant had strongly reduced ATPase activity and ATP stimulated ACOT activity. Thus ACOT activity depends on ATPase but not vice versa and the two activities can be separated by mutagenesis. Further functional studies combined with structural information are now required to understand the relationship between substrate binding, ACOT and ATPase activity and transport.

Publications

Carrier, D., van Roermund, C., Schaedler, T., Rong, H., Ijlst, L., Wanders, R., Baldwin, S. Waterham, H., Theodoulou, F. and Baker, A. (2019) Mutagenesis separates ATPase and thioesterase activities of the peroxisomal ABC transporter COMATOSE. *Sci Rep*. **9**:10502

Funding

This work was funded by the BBSRC

Collaborators

University of Leeds: Adrian Goldman, Stephen Muench
External: Amsterdam Medical Centre

Rescue of infectious recombinant Hazara nairovirus from cDNA reveals the nucleocapsid protein DQVD caspase cleavage motif is required for a role other than cleavage

J. Fuller, R. A. Surtees, G.S. Slack, J. Mankouri, R. Hewson and J. N. Barr

Introduction

The *Nairoviridae* family of the *Bunyavirales* order comprises tick-borne tri-segmented negative strand RNA viruses, with several members associated with serious or fatal disease in humans and animals. A notable member is Crimean-Congo hemorrhagic fever virus (CCHFV), which is the most widely distributed tick-borne pathogen, and associated with devastating human disease with case/fatality rates averaging 30%. Hazara virus (HAZV) is closely related to CCHFV, sharing the same serogroup and many structural, biochemical and cellular properties. To improve understanding of HAZV and nairovirus multiplication cycles, we report for the first time a rescue system permitting efficient recovery of infectious HAZV from cDNA. This system now allows reverse genetics analysis of nairoviruses without the need for high biosafety containment, as is required for CCHFV.

Results

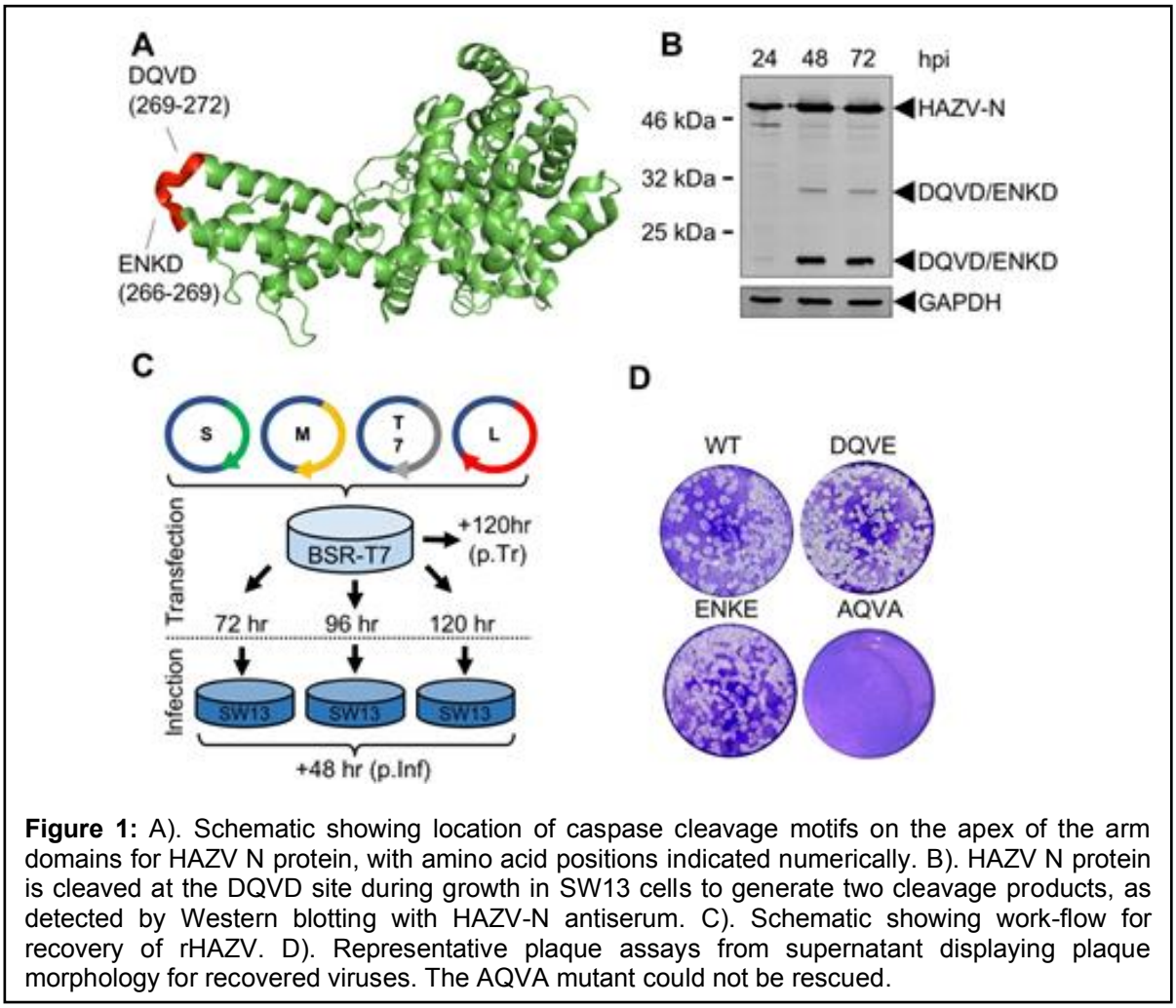

Figure 1: A). Schematic showing location of caspase cleavage motifs on the apex of the arm domains for HAZV N protein, with amino acid positions indicated numerically. B). HAZV N protein is cleaved at the DQVD site during growth in SW13 cells to generate two cleavage products, as detected by Western blotting with HAZV-N antiserum. C). Schematic showing work-flow for recovery of rHAZV. D). Representative plaque assays from supernatant displaying plaque morphology for recovered viruses. The AQVA mutant could not be rescued.

We used this rescue system to test the importance of a conserved DQVD caspase cleavage site exposed on the apex of the HAZV nucleocapsid protein arm domain that is cleaved during HAZV infection, and for which the equivalent DEVD sequence was recently shown to be important for CCHFV growth. Infectious HAZV bearing an un-cleavable DQVE sequence was rescued and exhibited equivalent growth parameters to wild-type in both mammalian

and tick cells, showing this site, and also N protein cleavage, was dispensable for virus multiplication. In contrast, substitution of the DQVD motif with the similarly un-cleavable AQVA sequence could not be rescued despite repeated efforts. Together, this work highlights the importance of this caspase cleavage site in the HAZV lifecycle, and reveals the DQVD sequence performs a critical role aside from caspase cleavage.

Publications

Fuller, J., Surtees, R.A., Slack, G.S., Mankouri, J., Hewson R., Barr, J.N. (2019) Rescue of Infectious Recombinant Hazara Nairovirus from cDNA Reveals the Nucleocapsid Protein DQVD Caspase Cleavage Motif Performs an Essential Role other than Cleavage *J Virol*. DOI: 10.1128/JVI.00616-19

Funding

This work was supported by a PhD studentship from Public Health England, awarded to JNB.

Collaborators

This work was a multi-site collaboration between JNB and Dr Roger Hewson, National Infection Service, Public Health England, Porton Down, Salisbury SP4 0JG, United Kingdom

Covalent Aurora-A inhibition by coenzyme A

Selena Burgess and Richard Bayliss

Introduction

Aurora-A is a Ser/Thr protein kinase that coordinates cell cycle events, such as mitotic entry, with the reorganization of the microtubule network in mitotic spindle assembly and ciliary resorption. Crystal structures of Aurora-A have driven the development of ATP-competitive Aurora-A inhibitors that are under investigation in the clinic. The recent discovery of Aurora-A functions in key cancer pathways, such as Rb (retinoblastoma) mutation and overexpression of N-myc has reinvigorated interest in finding new ways to target Aurora-A. Here we describe a naturally-occurring molecule, coenzyme A, as a covalent Aurora-A inhibitor.

Results

Coenzyme A (CoA) is a ubiquitous small molecule that has many functions in cellular metabolism, including in the citric acid cycle. Proteins such as Aurora-A can be modified on cysteine residues with a CoA group (CoAlation), and this may contribute to the cellular response to oxidative and metabolic stress. Selena Burgess determined the crystal structure of the Aurora-A/CoA complex to a resolution of 2.5 Å using X-ray crystallography (Fig. 1). Coenzyme A occupies the ATP binding site of Aurora-A in a binding mode similar to that of ADP. The extended CoA pantetheine moiety forms a disulfide bond with the side chain of Cys 290 on the kinase activation loop. The 3' phosphate group of CoA, which is not present on ATP or ADP, forms a H-bond with the side chain of Thr 217. CoA is thus a selective and covalent inhibitor of Aurora-A.

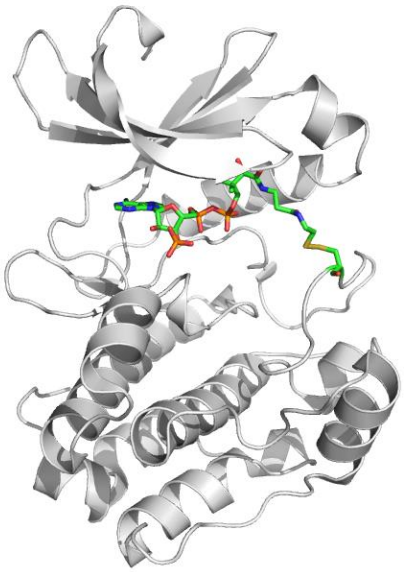

Figure 1: Crystal structure of Aurora-A bound to coenzyme A.

Aurora-A kinase is shown in cartoon representation and coloured grey. Coenzyme A and Cys290 of Aurora-A are shown in stick representation, with the colour scheme: carbon – green; nitrogen – blue ; oxygen – red; phosphorus – orange; sulfur – yellow

Funding

This work was funded by Cancer Research UK.

Collaborators

External: P. Eyers and C.Eyers (University of Liverpool), I.Gout (University College London)

Membrane mechanics regulate ESCRT activity

Andrew Booth and Paul Beales

Introduction

The Endosomal Sorting Complex Required for Transport (ESCRT) is involved in wide-ranging membrane repair and remodelling functions in the cell. These cytosolic proteins have a unique topology of action on biomembranes by instigating membrane bending and budding away from the cytoplasm and can activate membrane scission at the bud neck. ESCRTs play important roles in diverse membrane-associated processes including multivesicular body formation, viral budding, membrane repair and membrane scission during cytokinesis. The best current models for ESCRT structure and function implicate the assembly of spiral complexes within the necks of membrane buds. However many questions still remain about the precise mechanisms of functions and the roles of the different protein components within these complexes. Our interests in ESCRTs has been to repurpose them *in vitro* as membrane remodelling machinery for assembly of multicompartment (eukaryote-like) artificial cells for synthetic biology applications. An important challenge in this application is to understand how the activity of ESCRTs can be controlled and regulated. Understanding *in vitro* ESCRT regulation also has important implications for ESCRT biology.

Results

We investigated the activity of reconstituted ESCRT complexes on giant unilamellar vesicle (GUV) model membranes by confocal microscopy. ESCRT activity can be quantified by monitoring the formation of intraluminal vesicles (ILVs) that form inside the GUVs following the addition of ESCRT. ILVs are distinguished from multilamellar vesicles that form naturally during the electroformation of GUVs by the uptake of a fluorescent cargo that is added to extravesicular medium. Our goal was to be able to control the number of ILVs per GUV and ILV size created by ESCRTs. Early experiments quickly revealed that variation of the protein stoichiometry (by changing the concentration of one protein at a time compared to other proteins in the complex) gave only very weak control of ESCRT activity. Furthermore, the variability of GUV architecture we aspired to control was evident within individual experiments for GUVs under identical conditions. For example, GUVs with no ILVs, with many small ILVs and with a few large ILVs coexisted (Figure 1). However, notably, it was very rare for small and large ILVs to coexist in the same GUV, suggestive that ILV morphologies were a property of individual GUVs controlled by a property that could be variable within a single sample.

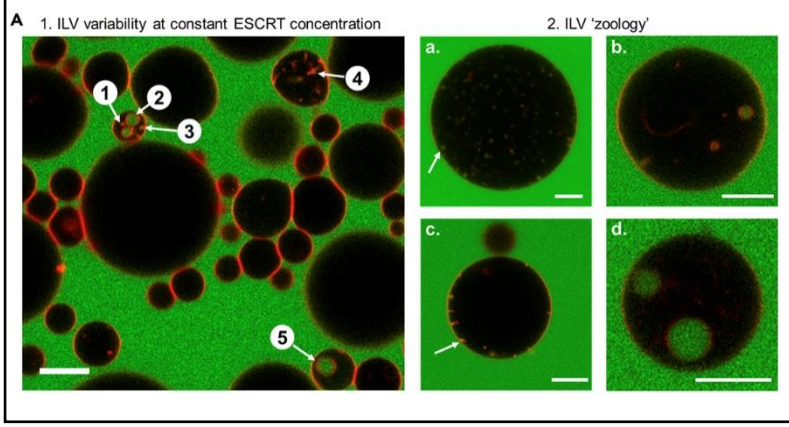

Figure 1: A.1: A cross section (3.1 μm depth) through GUVs incubated with ESCRT-II, Vps20, Vps24, Vps2 (10 nM), and Snf7 (50 nM). A number of different ILV sizes are (1–5). A.2: ILV morphology, a range of commonly observed ILV states. (a) Many similarly sized ILVs plus buds, (b) few ILVs of varying dimensions, (c) "stalled" ILV buds with few or no coincident free-floating ILVs, (d) unusually large ILVs ~5 μm in diameter. Red, Rhodamine-PE; green, Alexa Fluor 488-labeled dextran. All scale bars, 10 μm.

One property that is known to vary within individual GUV populations is the tension within their membranes. As the activity of ESCRTs requires mechanical deformation of the membrane, this became an attractive hypothesis and the focus of further study. The membrane tension distribution within a GUV population can be controlled by changing the osmotic pressure difference of the aqueous media inside and outside of the GUVs. Osmotic relaxation of membrane tension significantly increased the activity of ESCRTs upon GUV

membranes, supporting our hypothesis. This could be further investigated by quantification of membrane tension in GUVs. We used a technique called flicker spectroscopy where a movie is taken of the temporal thermal fluctuations of GUV membranes. Image analysis reveals the power spectrum of the mean squared amplitude of membrane undulations as a function of their wave number around the circumference of the GUV. Fitting the power spectrum using prediction of the Helfrich ansatz for the mechanical properties of GUV membranes modelled as fluid elastic sheets reveals the bending rigidity and tension of the membrane.

We show that our osmotic relaxation protocol decreases membrane tension by approximately an order of magnitude. Furthermore, upon addition of ESCRTs, membrane tension increases (Figure 2). This can be understood by the formation of ILVs removing excess membrane from relaxed GUVs, inherently increasing their tension. As high tension GUVs show much reduced GUV activity, this implies that membrane tension acts as a negative feedback regulator of ESCRT activity. At low tension, the membrane has ample excess area for ESCRTs to easily generate ILVs with minimal resistance from tension in the membrane. However the removal of excess area during ILV generation increases tension and therefore suppresses downstream ESCRT activity.

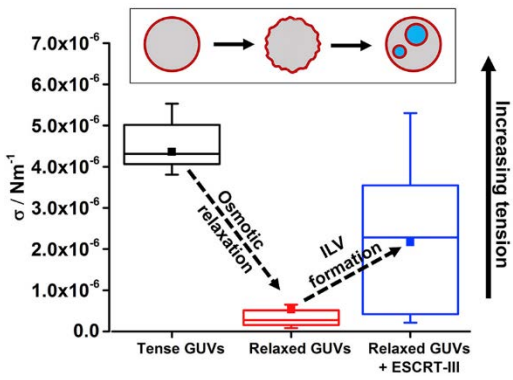

Figure 2: The distribution of membrane tension σ in GUV samples. "Tense" GUVs were those that were not exposed to an osmotic gradient. The membrane tension of osmotically "relaxed" GUVs was measured before (pre-protein) and after (post-protein) the addition of the ESCRT proteins to assess the effect of ILV formation on membrane tension. Box descriptions: ■, mean values; line termini correspond to the minimum and maximum observed values; the upper and lower bounds of the boxes correspond to the 75th and 25th percentile values, respectively; and the inner line corresponds to the 50th percentile. *n* = 10.

In summary, we find that membrane mechanical properties, namely tension, regulates ESCRT activity. As *in vitro* membrane tension can be dynamically controlled by osmotic pressure changes, this presents an attractive mechanism by which ESCRT activity can be dynamically controlled during the formation of multicompartment artificial cells. Furthermore, the biological implications are appealing: changes in *in vivo* membrane tension could plausibly act as a physiological switch to activate and deactivate ESCRTs. For example, membrane damage would trigger an instantaneous drop in tension, and fusion of early endosomes to form a late endosome will create significant excess membrane area for ESCRTs to be able to efficiently act upon. Future work will also further explore the role of membrane bending rigidity and lateral heterogeneities in membrane mechanics as a result of lipid phase separation and the formation of lipid rafts: islands of membrane with different local lipid compositions and hence modulated mechanical properties.

Publications

Booth, A., Marklew, C.J., Ciani, B. and Beales, P.A.; *In vitro* membrane remodelling by ESCRT is regulated by negative feedback from membrane tension. *iScience* **15**, 173-184 (2019).

Funding

This work was funded by the EPSRC.

Collaborators

External: B. Ciani and C. Marklew (University of Sheffield).

Linking plasmodesma structural changes to the control of intercellular signalling and root response to abiotic stress conditions

Philip Kirk, Sam Amsbury, Candelas Paniaguas and Yoselin Benitez-Alfonso

Introduction

Intercellular signalling is essential for coordinated plant growth and for adaptation and responses to a changing environment. Some signals move in the intercellular spaces (apoplast) but larger molecules (such as transcription factors and signalling RNA molecules) require channels (named plasmodesmata, PD) traversing cell walls to provide symplasmic (cytoplasm-to-cytoplasm) connectivity between neighbouring cells. PD structure and transport capacity are regulated by the surrounding cell walls and, specifically, by the accumulation of the β-(1,3) glucan callose. Extracellular and intracellular signals are perceived by membrane-localized receptors which in turn modulate intercellular symplasmic permeability via callose synthesis/degradation. Changes in symplasmic permeability affect the expression of non-cell autonomous signals and regulators modifying organ growth and development. Understanding how receptor signalling influences callose dynamics and PD structure and the transport of developmental factors could open doors to new strategies for improving plant adaptation to climate change. Recently, we made significant advances in dissecting components of this mechanism and its significance in the response to osmotic stress conditions. Mannitol treatment reduces water potential and induces oxidative stress triggering changes in root growth and architecture. Root phenotypic modifications were associated with increased callose and reduction in symplasmic permeability (reported by measuring changes in the diffusion of the protein GFP). Plasma membrane-located leucine-rich repeat receptor like kinases (LRR-RLKs), such as KIN7 (Kinase7) conditionally and dynamically associate with PD upon mannitol treatment and are required to regulate callose accumulation. Affecting callose metabolism alters root responses to mannitol indicating the importance of this mechanism. In parallel, we developed a mathematical model to demonstrate that changes in symplasmic permeability in response to abiotic stresses could be explained by a reduction in PD aperture imposed by callose accumulation at the PD neck region. The identification of KIN7, its relationship to callose, PD ultrastructure and symplasmic permeability shed some light on the mechanisms that mediate root response to abiotic stress conditions.

Results

Seeds of *Arabidopsis thaliana* were grown on agar plates 8 g/L containing MS salts including vitamins 2.2 g/L, sucrose 10 g/L and MES 0.5 g/L at pH 5.8 in a culture room at 22°C in long day light conditions (150 µE/m²/s) for 6 days and then transferred to the same media (control) or to media supplemented with mannitol 0.4 M. After 3 days of exposure to mannitol, root length and lateral root (LR) number were calculated and found reduced in comparison to seedlings in control media (Fig. 1A). Mannitol treatment also modified callose and symplasmic permeability as demonstrated by a reduction of GFP diffusion to outer

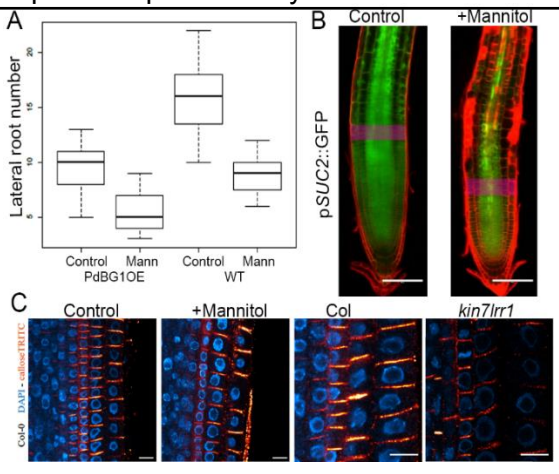

Figure 1: Callose regulates root response to mannitol. A: LR number in wild type (WT) and in roots over-expressing PdBG1 (PdBG1OE) in control and mannitol (Mann) conditions. WT showed a decrease in LR number but the effect is reduced in PdBG1OE. B: Arabidopsis roots expressing GFP under the phloem promoter pSUC2 in control and mannitol treatment showed a reduction in GFP diffusion in mannitol treatment. Red: PI counterstain. C: Callose immuno-fluorescence shows increased levels in epidermal cells after mannitol treatment and reduced levels in the *kin7lrr1* mutant in comparison to WT (Col). Blue: DAPI. Scale (B) = 50 µm, (C) = 10 µm.

tissues when expressed under the phloem specific promoter SUC2 (Fig. 1B-C). To test the role of callose, we studied a transgenic line over-expressing the PD associated β-(1,3) glucanase PdBG1 (which degrades callose) using the CaMV 35S promoter (PdBG1OE). In control conditions, primary root length was not significantly affected by over-expression of PdBG1 however LR number was reduced (Fig. 1A). Following mannitol treatment, LR number was reduced in PdBG1OE but the effect was attenuated compared to wild type (Fig. 1). We tested if KIN7 (which rapidly relocated to PD upon mannitol treatment) was behind callose regulation. Loss of function *kin7.lrr1* shows a reduction in LR number and impaired response to mannitol. Immuno-localisation revealed that callose levels are reduced in the *kin7.lrr1* mutant supporting a role for KIN7 in regulating callose metabolism. To mechanistically link the increase in callose and the reduction in symplasmic permeability, we built a computational model to calculate permeability from a geometrical description of individual PDs, considering the flow towards them and including the impact of PD clustering (Fig. 2). Our open source interactive multi-level model (named PDinsight) allows us to test *in*

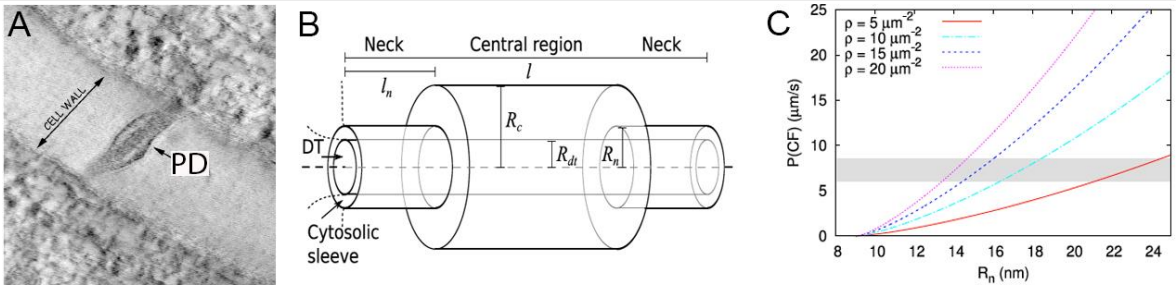

Figure 2: Modelling PD geometry and permeability. A: Picture shows a single PD within Arabidopsis cell walls. B: Individual PDs were modelled using multiple cylinders with a total length l, neck radius R_n and neck length l_n, central region radius R_c and desmotubule radius R_{dt}. C: CF effective permeability (P(CF)) is calculated for different densities ρ (different colour curves). The horizontal gray band indicates values in control samples. Default parameters: α (CF) = 0.5 nm, Diffusion constant D = 162 µm^2/s, l_n = 25 nm, l = 100 nm, R_{dt} = 8 nm.

silico how changes in typical PD features are linked to measured permeabilities. Past research indicates that callose is deposited in the PD neck region reducing PD cytoplasmic aperture. Carboxy-Fluorescein (CF), a molecule with Stokes radius α (CF) = 0.5 nm, show a permeability (P(CF)) of 6 - 8.5 µm/s in roots grown in control media but reduced to 1 µm/s in roots exposed to high oxidative conditions. Applying our model for diffusion using as default parameters determined by EM indicates that reduction in P values are reasonably achieved by a reduction of PD neck radius (R_n) from 16.3 nm to 11 nm (Fig. 2C). Without change in R_n, a more drastic reduction in PD density (more than double) would be required to reproduce P(CF) change supporting callose-driven constriction as the most plausible mechanism.

In summary, we found that the regulation of LR development in response to mannitol occurs via a mechanism involving the receptor KIN7 and the synthesis and/or degradation of PD-associated callose. Callose accumulation restricts symplasmic permeability likely through reduction of PD aperture as predicted using mathematical modelling. Current work is now focussed on dissecting new components of this mechanism. Correlative Fluorescent EM (CFEM) will be applied to allow simultaneous visualization of PD-callose and receptor protein accumulation and measurements of PD geometrical parameters. By building knowledge on PD ultrastructural features that influence intercellular signalling, the goal is to identify new strategies to improve plant development and resilience to challenging growth conditions.

Publications

Deinum, E.E., Mulder, B.M., Benitez-Alfonso, Y. (2019) From plasmodesma geometry to effective symplasmic permeability through biophysical modelling. *Elife*. **8**. pii: e49000.

Grison, M.S., Kirk, P., Brault, M.L., Wu, X.N., Schulze, W.X., Benitez-Alfonso, Y., Immel, F., Bayer, E.M. (2019) Plasma Membrane-Associated Receptor-like Kinases Relocalize to Plasmodesmata in Response to Osmotic Stress. *Plant Physiol.* **181(1):**142-160.

Funding
This work was funded by The Leverhulme Trust, BBSRC DTP and the University of Leeds.

Collaborators
University of Leeds: Simon Connell, John Paul Knox.
External: Eva Deinum, Bela Mulder, Emmanuelle Bayer.

Engineering novel natural products and binding motifs

Ieva Drulyte, Daniel Van, Emily Turri, Adam Nelson and Alan Berry

Introduction

Natural products belong to an extensive family of diverse organic molecules: in excess of 200,000 discovered and extracted from various sources. Of particular interest are the polyketide, non-ribosomal peptide and isoprenoid classes, contributing to the pharmaceutical, cosmetic and biofuel industries. These classes of natural products are synthesised by polyketide synthases, non-ribosomal peptide synthases and terpene synthases, respectively; and our interest lies in understanding the structure-function relationship of these enzymes; facilitating our engineering efforts to synthesise existing and novel natural products.

Structural studies in indanomycin biosynthesis

Indanomycin, an antibiotic active against Gram-positive bacteria, is produced by a hybrid nonribosomal peptide synthetase-polyketide synthase (NRPS/PKS) from *Streptomyces antibioticus* NRRL 81673. We are interested in the chemistry involved in the generation of mature polyketide. IdmH, a putative post-PKS cyclase enzyme, was thought to catalyze the indane ring formation via a Diels-Alder [4+2] cycloaddition reaction. The Diels-Alder reaction, despite being widely used in synthetic organic chemistry, is an extremely rare reaction in nature, which makes IdmH a particularly exciting enzyme to study. IdmH was cloned, heterologously expressed and purified. To aid crystallization, we made a mutant of IdmH lacking a flexible loop and solved its crystal structure to 2 Å resolution (Figure 1). To investigate the reaction catalysed by IdmH, we assigned 88% of the backbone NMR resonances and demonstrated using chemical shift perturbation of the [^{15}N]-labelled IdmH, that indanomycin binds in the active site pocket. Finally, combined quantum mechanical / molecular mechanical (QM/MM) modelling of the IdmH reaction shows that the active site of the enzyme provides an appropriate environment to promote indane ring formation, supporting the assignment of IdmH as the key Diels-Alderase catalysing the final step in the biosynthesis of indanomycin through a similar mechanism as other recently characterised Diels-Alderases involved in polyketide tailoring reactions.

Figure 1: Atomic model of IdmH, a polyketide cyclase from indanomycin NRPS/PKS.

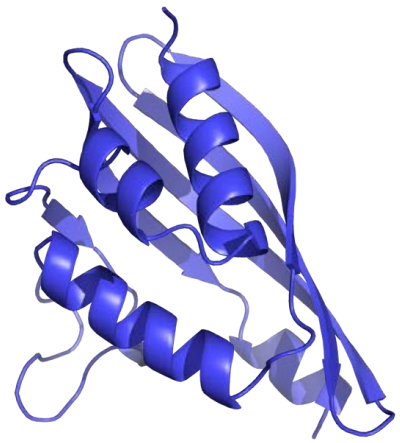

Structural studies of NRPS/PKS megasynthases

We are interested in elucidating structures of enzymes within biosynthetic gene clusters (BGC). BGC consist of multiple types of proteins involved in the synthesis and release of natural products. NRPSs and PKSs are large proteins that consist of modular domains that come together and form modules. Understanding the structure-function relationship of NRPS/PKS megasynthases is key to understanding why reengineering attempts have been relatively unsuccessful. There are a handful of module structures published, but very little information on di-modules and full megasynthases is available. The information provided by these larger structures will be crucial in understanding inter-module interactions. These large enzymes are a potential source of novel antibiotics: if we can understand their structure-function relationship, we can synthesise novel compounds by taking advantage of their modular nature. We are purifying proteins from the endogenous organisms as well as carrying out recombinant expression in *E. coli* to study them by cryo-electron microscopy and X-ray crystallography. We aim to use the structural data to further our understanding and explain the dynamics of the module to aid in rational protein redesign.

Engineering selina-4(15),7(11)-diene synthase for novel activities

Selina-4(15),7(11)-diene synthase produces selina-4(15),7(11) diene and germacrene B from farnesyl pyrophosphate. Initial work has been focused on redesigning the enzyme active site to produce novel activities and novel terpenes. Previously 28 enzyme variants have been designed and produced using site-directed mutagenesis and screened for altered product profiles to determine the impact on the catalytic reaction. Screening is carried out using gas chromatography, mass spectrometry and any novel terpenes will be characterized using 2D NMR. Kinetic analysis of the variants is underway using a malachite green assay. In this assay, the inorganic pyrophosphate generated in the first step of the terpene synthase reaction is converted into two inorganic phosphate ions using inorganic pyrophosphatase and the phosphate is quantified as a malachite green complex. We are then utilizing the product profiles and kinetics to identify 'hot-spots' in the active site which produce novel active enzymes.

Funding

Our work is funded by BBSRC and The Wellcome Trust.

Publications

Drulyte, I., Obajdin, J., Trinh, C. H., Kalverda, A. P., van der Kamp, M. W., Hemsworth G., Berry, A. (2019) Crystal structure of the putative cyclase IdmH from the indanomycin nonribosomal peptide synthetase/polyketide synthase. *IUCrJ,* **6**: 1120-1133.

Collaborators

University of Leeds: Glyn R. Hemsworth, Chi H. Trinh, Arnout P. Kalverda
External: University of Bristol, Mark W. van der Kamp

Photocatalytic proximity labelling of MCL-1 by a BH3 ligand

Hester Beard, Jacob Hauser, Martin Walko, Rachel George, Andrew Wilson and Robin Bon

Introduction

Most cellular proteins function as dynamic complexes with other proteins and, conversely, protein–protein interactions (PPIs) play key roles in the regulation of most biological processes. While stable PPIs are usually associated with multi-subunit protein complexes and quaternary structure, transient PPIs regulate multiple cellular processes, and are implicated in a variety of disease states. Ongoing efforts to study transient PPIs may lead to better understanding of the processes of life and the development of novel diagnostics and therapeutics. As part of such efforts, the ability to selectively introduce chemical labels onto proteins involved in specific PPIs would provide new tools to study such PPIs, including the construction of protein-based biosensors or affinity enrichment reagents for dynamic interactome analysis. Ligand-directed protein labelling (LDL) allows the introduction of diverse chemical functionalities onto proteins without the need for genetically encoded tags. Here we report a method for the rapid labelling of a protein using a peptide probe designed to mimic an interacting BH3 ligand within a BCL-2 family protein-protein interactions (Figure 1).

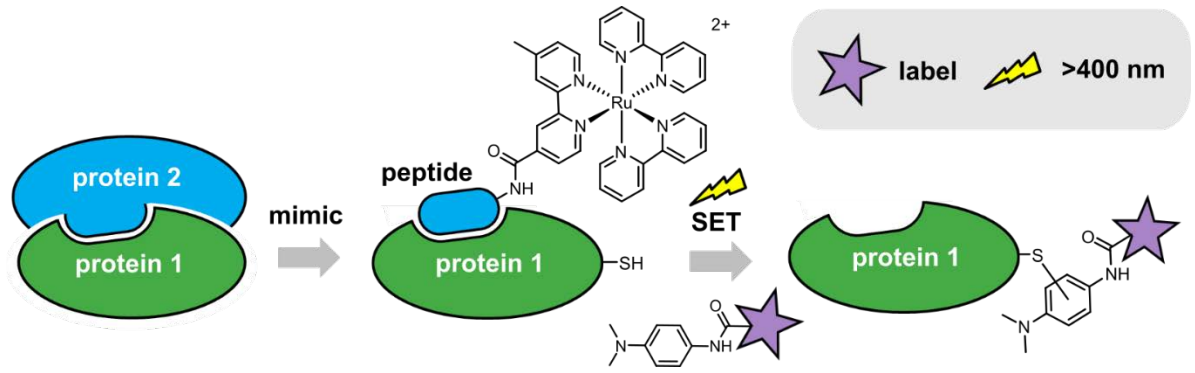

Figure 1: Use of a peptide-based probe, which mimics protein 2 within a protein-protein interaction (NOXA-B), for selective, photocatalytic single electron transfer labelling of protein 1 (the anti-apoptotic protein MCL-1).

Results

We developed the peptide-based protein mimic Ru(II)(bpy)3-NOXA-B as an LDL reagent for the selective photocatalytic, ligand-directed labelling of the anti-apoptotic BCL-2 protein, MCL-1. Single electron transfer (SET) photolabelling of recombinant MCL-1 with three different dimethylaniline derivatives was achieved, with irradiation times of 1 min, and in-gel fluorescence measurements and ESI-MS analysis allowed relative quantification of labelling. Tandem MS experiments revealed that the predominant labelling site of MCL-1 was a single cysteine residue (Cys286), an amino acid not previously reported to react via this type of LDL chemistry. Experiments using targeted vs. non-targeted SET reagents, competition experiments, and labelling experiments in mixtures of proteins support a ligand-directed nature of SET photolabelling with Ru(II)(bpy)3-NOXA-B.

Publications

Beard, H.A., Hauser, J.R., Walko, M., Rachel, R.M., Wilson, A.J. & Bon, R.S. (2019) Photocatalytic proximity labelling of MCL-1 by a BH3 ligand. *Communications Chemistry* ***2***: 133.

Funding

This work was funded by EPSRC, BBSRC and the Wellcome Trust.

A novel molecular architecture for trans-splicing of mRNAs in trypanosomatids

Arnout Kalverda, Andrew Wilson and Alex Breeze

Introduction

The eukaryotic translation machinery is highly complex, and recent work has highlighted particularly distinctive features in trypanosomatids. These differences are of special interest because trypanosomatids are a worldwide threat to human health and analysis of distinctive molecular features may help identify potential drug targets. One remarkable feature is the involvement of a large number of isomers of eIF4E, which bind to a highly modified cap4 structure added to the 5' end of the monocistronic mRNAs during processing. Furthermore, two of the eIF4E isomers (3 and 4) are cytoplasmic proteins with long N-terminal extensions absent from other eukaryotic counterparts, and prior data have suggested a direct interaction between the N-terminal extension of *Leishmania* eIF4E4 and poly-A binding protein (PABP1). We set out to determine whether an alternative protein-mediated 5'-3' mRNA interaction chain forms in *Leishmania*, and to characterize key structural features underpinning its assembly, using an array of structural and biophysical methods.

Results

Our first objective was to characterize the interactions of eIF4E4 and PABP1 from *Leishmania* and to define the protein domains that mediate these interactions. We prepared *E.coli* expression constructs that covered all potential interaction sites (Fig. 1A,B). Using microscale thermophoresis (MST), we identified a strong interaction (K_D = 22 nM) between the PABC domain of PABP1 ('segment J') and an approximately 5 kDa region ('segment iv') of the extended N-terminal domain of eIF4E4. Sequence analysis of eIF4E4(iv) revealed the presence of a candidate PAM2 motif, a consensus recognition site found in other proteins that bind to poly(A)-binding proteins. We then used NMR to identify the amino acids comprising the respective binding motifs. The ^{1}H-^{15}N HSQC NMR spectra (Fig. 1C,D) showed PABP1(J) to be folded, while eIF4E4(iv) displayed amide resonance chemical shift dispersion characteristic of an intrinsically disordered domain. Addition of either unlabeled domain to the other in uniformly ^{15}N-^{13}C-labeled form induced selective chemical shift perturbations (CSPs) indicative of specific binding. Binding of unlabeled eIF4E4(iv) to ^{15}N-^{13}C- labeled PABP1(J) enabled us to identify interactions involving residues in PABP1 that manifest homology to the 70-residue MLLE (here M**F**LE) domain, previously demonstrated to mediate interactions with PABP binding partners. In the reciprocal experiment, addition of PABP1(J) to ^{15}N-^{13}C-eIF4E4(iv) caused major CSPs that map to the region N141-G150 of eIF4E4, which matches the putative PAM2 motif that we identified via our initial binding studies. In further work, we were able to solve the crystal structures of PABP1(J) and of PABP1(J) co-crystallized with a synthetic eIF4E4 PAM2 peptide (Fig. 2A), both to a resolution of ~2 Å. Obtaining these structures enabled us to locate the binding motif for eIF4E4 in relation to the three-dimensional structure of *Leishmania* PABP1. The structure of the complex reveals how the eIF4E4 peptide binds across the three α-helical segments of the 70-residue PABC domain of PABP1 in a similar fashion to other PABC-interacting proteins. The structural data

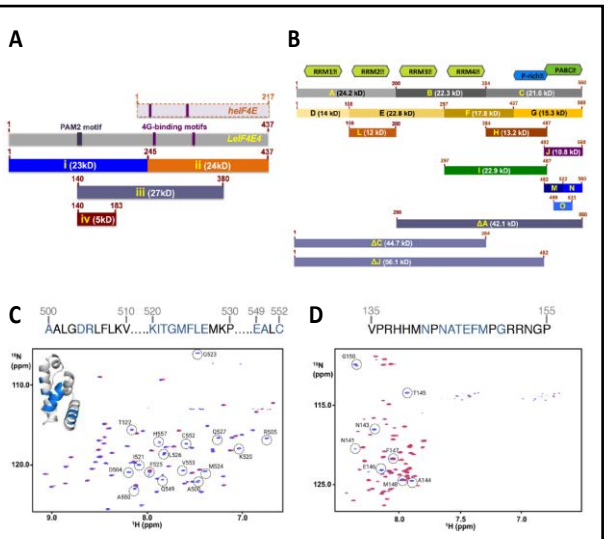

Figure 1: Identification of domains involved in the *Leishmania* translation machinery. Expression constructs from eIF4E4 **A** and PABP1 **B**. HSQC NMR spectra of ^{15}N,^{13}C-PABP1(J) without (blue) / with (red) eIF4E4(iv) **C** and ^{15}N,^{13}C-eIF4E4(iv) without (blue) / with (red) PABP1(J) **D**. Affected residues shown in blue on peptide sequences. Panel at top left of **C** shows PABP1(J) crystal structure coloured blue to indicate CSPs on binding of eIF4E4(iv).

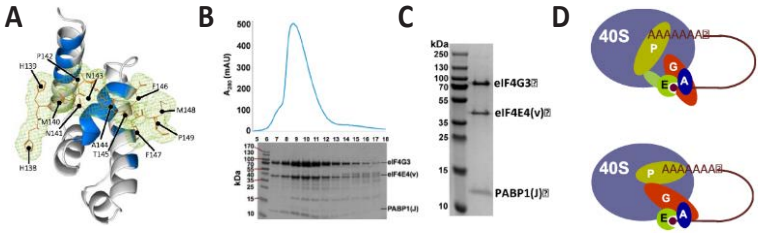

Figure 2: A X-ray crystal structure of *Leishmania* PAPB1(J) (ribbons) with eIF4E4(iv) PAM2 peptide (green density) bound. **B** Co-elution on SEC of heterotrimeric complex of eIF4E4(v):PABP1(J):eIF4G3. **C** fractions 7-8 from SEC illustrating highly pure complex. **D** schematic representation of cap-binding complex in *Leishmania* (top) compared with the canonical eukaryotic counterpart (bottom), illustrating the role of the disordered N-terminal extension in *Leishmania* eIF4E4 (green protuberance) in mediating the bridging interaction.

prompted us to use mutational analysis coupled with MST to explore further the role of conserved residues in the eIF4E4 PAM2 motif in binding. Our results on a series of FITC-labelled synthetic 14mer peptides indicated E146 and F147 contribute the most energetically important interactions, while the methionines at positions 140 and 148 do not make substantial individual contributions. We also tested the importance of PABP1 F525 in the interaction with eIF4E4. Mutation of this Phe to an Ala resulted in a 25-fold loss in binding affinity as measured using MST, confirming its importance to the interaction. Armed with these novel data from short polypetide fragments, we wanted to establish a quantitative understanding of the relative significance of interactions between eIF4E4, eIF4G3 and PABP1 using longer or full-length protein constructs. Fluorescence anisotropy experiments revealed that a high-affinity interaction (average of calculated K_D values = 0.34 μM) occurs between Alexa-647-labelled eIF4G3 and the complex eIF4E4(v):PABP1. In contrast, MST detected no binding between eIF4G3 and PABP1, and this negative outcome was also reflected in pull-down results obtained with lysates from *E.coli* strains that co-produce these two proteins. We then attempted formation of a heterotrimeric complex that would throw more light onto the eIF4E4-mediated interactions that bridge the 5' and 3' ends of mRNAs in *Leishmania*. Since a longer eIF4E4 construct (eIF4E4v) included the putative binding motifs for both PABP1 and eIF4G3, we tested the hypothesis that eIF4E4(v) would be able to form a scaffold upon which the two other protein domains could be assembled. Cobalt-column affinity chromatography followed by SEC led us to identify complexes formed upon mixing eIF4E4(v), PABP1(J) and full-length eIF4G3 (Fig. 2C). By this means, we were able to isolate a soluble heterotrimeric eIF4E4(v):PABP1(J):eIF4G3 complex (Fig. 2D).

In conclusion, we have demonstrated that the N-terminal extension found in *Leishmania* eIF4E4 acts as a focal structural element in formation of a unique type of eukaryotic cap-binding complex architecture. Because the N-terminal extension adds a PABP1 binding site to the cap- and eIF4G- binding sites generally present in other eukaryotic eIF4Es, the *Leishmania* eIF4E4 factor replaces eIF4G as the core 'scaffolding' protein in the cap-binding complex. We conclude that this N-terminally extended eIF4E anchors eIF4G and PABP1 directly to 5'-end-cap4-modified mRNAs. We note that future work could reveal further interaction interfaces that may be worthy of consideration as potential drug targets.

Publications

Dos Santos Rodriguez, F., Firczuk, H., Breeze, A.L., Cameron, A.D., Walko, M., Wilson, A.J., Zanchin, N.I.T. & McCarthy, J.E.G. (2019) The *Leishmania* PABP1–eIF4E4 interface: A novel 5′–3′ interaction architecture for trans-spliced mRNA. *Nucleic Acids Res*. **47**, 1493-1504.

Funding

This work was funded by the MRC (to Warwick and Leeds) and Fundação Araucária (to Instituto Carlos Chagas FIOCRUZ-Paraná).

Collaborators

External: John McCarthy, Alex Cameron (Warwick), Nilson Zanchin (FIOCRUZ Institute, Curitiba, Brazil)

Flow-induced aggregation: from fundamental mechanisms to industrial applications

Leon Willis, Ioanna Panagi, Samantha Lawrence, Alex Page, Frank Sobott, Sheena Radford, Nikil Kapur and David Brockwell

Introduction: Despite over 80 monoclonal antibody (mAb) therapies being marketed to date, the successful development of these protein-based medicines can be hindered by the tendency of proteins to unfold, misfold and aggregate. Aggregates can illicit immunologic reactions in patients and delay large-scale manufacturing. Understanding why mAbs aggregate and predicting which molecules are the least aggregation-prone, is of great interest to industry and academia. We have previously developed an extensional and shear flow device (EFD), which subjects proteins to hydrodynamic forces similar to those found in bioprocessing. We have used the EFD to investigate how different flow regimes induce the aggregation of bovine serum albumin, as well as modulate the aggregation landscapes of three model mAbs (WFL, mAb1 and STT). Here, we build on this work to understand the effect of surface chemistry on flow-induced aggregation of different mAbs. Finally, we assess the utility of the EFD as a tool to predict mAb aggregation, screening a panel of 33 clinically relevant mAbs and comparing the EFD data to those from twelve alternative biophysical tests.

The role of surfaces in flow-induced aggregation: The EFD consists of two Hamilton syringes connected together *via* a borosilicate capillary (Figure 1a). The design of the device generates defined extensional and shear flow fields, validated using computational fluid dynamics (CFD). The wettability of the glass surfaces in the EFD, characterised by the water contact angle (CA), was modified by treatment with monoacrylated polyethylene glycol (more hydrophilic than glass, CA < 47°) or an array of silanes (more hydrophobic than glass, CA > 47°). The aggregation-prone mAb, WFL (AstraZeneca), was stressed in the EFD for 0 or 100 passes and the resulting aggregation quantified using a pelleting assay.

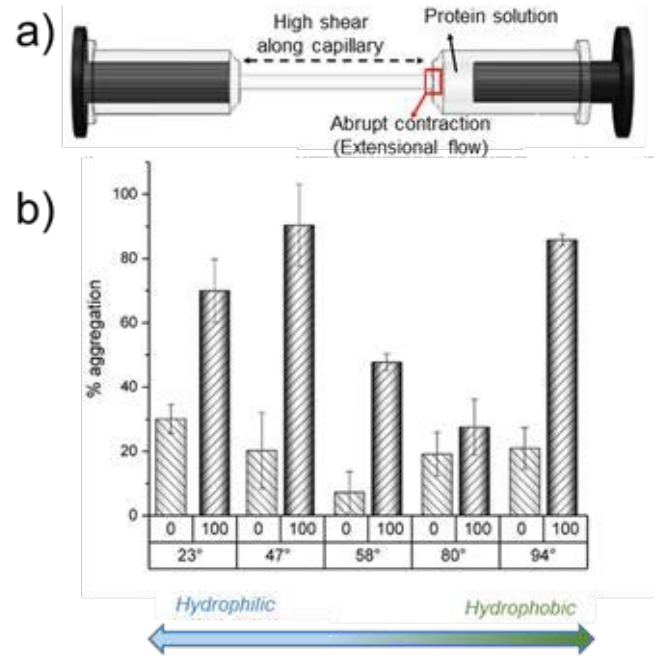

Figure 1: (a) Overview of the EFD. 0.5 mL of mAb solution is loaded into the EFD. Once assembled, the solution is repeatedly shuttled from one syringe to the other (defined as one pass). The plungers are driven at a defined velocity by a stepper motor (typically 8 mm/s). The 15:1 diameter ratio between the syringe and the capillary generates an abrupt contraction, subjecting proteins to a harsh extensional flow (strain rate = 11,750/s) for ~20 µs at every pass. This is followed by a strong shear flow for ~ 40 ms (shear rate = 52,000/s) along the capillary. **(b) Effect of surface chemistry on the flow-induced aggregation of WFL.** The surfaces of the EFD (syringes and capillary) were modified to have different wettabilities, as characterised by the contact angle. For reference, the bare glass = 47°. The protein (in 150 mM ammonium acetate, pH 6) was stressed for 0 or 100 passes in the EFD, followed by quantification of protein in the pellet and supernatant fraction following

The data show that for two silanes of intermediate hydrophobicity (contact angles = 58° and 80° for silanes B and C, respectively), the extent of aggregation under flow for WFL is greatly reduced, especially compared to the original glass surface (47°) (Figure 1b). In particular, silane B (n-Hexyltrimethoxysilane) was found to have the most protective effect

against mAb aggregation under flow, corroborated in similar experiments with the generic antibody, mAb1. By performing EFD aggregation experiments using hybrid EFDs, where the contact angle of the syringe/capillary surfaces were systematically modified or kept constant, we were able to determine that the syringe surfaces are the most protective. Quartz crystal microbalance (QCM) experiments show that a monolayer of protein forms on each surface, regardless of its contact angle. Excipients such as arginine and polysorbate 20 have the ability to suppress aggregation under flow through bulk or surface effects, respectively. Together, our data show that the surface and flow have a synergistic effect on the extent of mAb aggregation. Silanisation of surfaces found in biopharmaceutical processing may be an alternative formulation strategy to using excipients. The molecular details of how the mAb aggregation mechanism under flow is affected by such surfaces, is a current focus of the group.

Screening clinically relevant mAbs with the EFD

'Developability' can be defined as the physicochemical attributes of a molecule which allow it to successfully transition from the lab to a manufacturable drug. Many biophysical assays, including *in silico* algorithms, are employed by industry to predict which mAbs are likely to fail during development, including being aggregation prone. Collaborators at Adimab subjected 137 mAbs, whose variable regions were derived from clinical proteins, to 12 different biophysical assays. Analysis of the data revealed similar behaviour amongst mAbs in certain assays. How aggregation-prone are clinically relevant mAbs under flow? How does the EFD compare to other developability assays? To address these questions, we subjected a subset of 33 of the 137 mAbs to stress in the EFD under identical flow and buffer conditions. The samples, including 0 passes controls, were analysed using the afore-mentioned insoluble protein pelleting assay. The data showed that the mAbs in the subset aggregated under flow over a wide range, with ~1/3 of molecules showing low levels of aggregation (<20% protein in pellet) (Figure 2a).

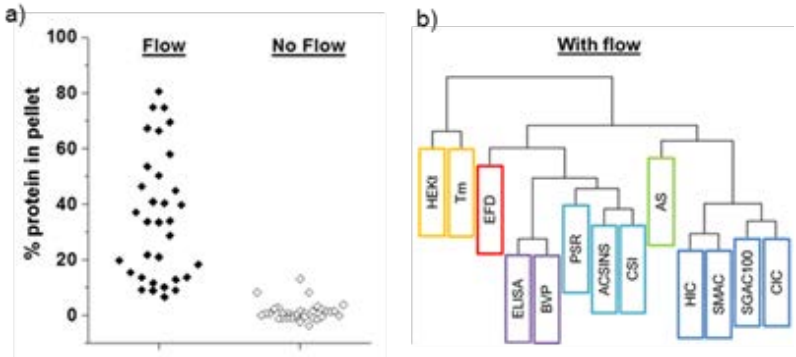

Figure 2: (a) Spread of aggregation by the 33 clinically relevant mAbs under flow. The mAbs (0.5 mg/mL in HEPES-buffered saline, pH 7.3) were stressed for 0 or 200 passes in the EFD (plunger velocity = 8 mm/s). **(b) Hierarchical clustering of the EFD data with those from 12 other assays.** The coloured boxes indicate assays which probe similar biophysical properties.

Hierarchical clustering (Figure 2b), comparing the behaviour of each mAb in the EFD, to their corresponding behaviour in 12 different biophysical assays, show that the EFD occupies a unique branch on the 'family tree' of assays, i.e. behaviour under flow cannot be predicted by the other biophysical tests. As such, the EFD is a novel developability tool.

Funding

This work was funded by the EPSRC, BBSRC and AstraZeneca Plc.

Collaborators

External: Drs David Lowe, Richard Turner, Nick Bond and Paul Varley (AstraZeneca), Drs Tushar Jain and Max Vásquez (Adimab)

Structural studies on the ciliary transition zone

Alice Webb, Alice Walter, Katie Jameson, Simon Connell, Ralf Richter, Michelle Peckham and Joseph Cockburn

Introduction

Cilia are microtubule-based organelles located on most mammalian cells. Perhaps the best-known examples of cilia are the motile cilia of airway epithelial cells, or the sperm cell flagellum. However, most cells in the body also possess a non-motile, primary cilium, which functions as a "cellular antenna", allowing cells to sense their environment. For example, the rod and cone cells in the retina use their primary cilia to detect light, allowing us to see. Similarly, the primary cilia of cells lining the kidney tubules detect the flow of urine. Primary cilia require a specific composition distinct from the rest of the cell. This is maintained by the transition zone, a structure that "plugs" the ciliary base and regulates exchange of material with the rest of the cell (Figure 1). Mutations in transition zone proteins cause a spectrum of inherited, recessive developmental conditions ("ciliopathies"). Patients (typically children and young adults) usually have kidney cysts, along with various other defects of the central nervous system, eye and skeleton. The relationships between mutations and the conditions they cause are very complicated: a given condition can result from a mutation in one of several genes, and different mutations in a particular gene can give rise to different disorders. Understanding these relationships will be essential to the development of preventative treatments or therapies that retard/reverse disease progression.

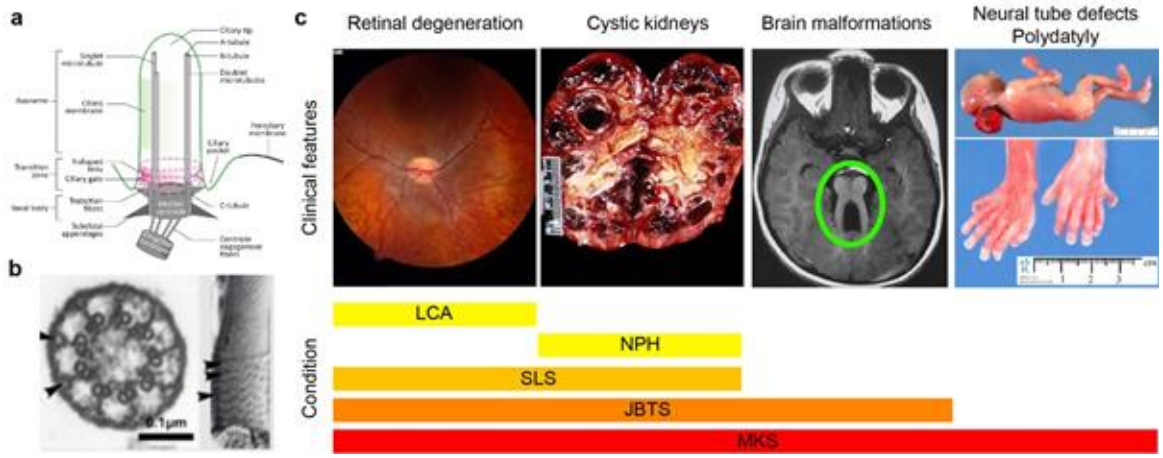

Figure 1: The primary cilium and ciliopathies**. a** overview of the primary cilium architecture. **b** key features of transition zone ultrastructure revealed by electron microscopy. The image on the left shows a negatively stained cross section through the transition zone revealing the Y-links. Freeze-fracture EM reveals the ciliary necklace on the surface of the transition zone membrane. **c** the ciliopathy disease spectrum associated with mutations in transition zone proteins. The upper panel shows major clinical features whilst examples of associated conditions are shown below colour coded by severity. Abbreviations: LCA – Leber's congenital amaurosis; NPH – nephronophthisis; SLS – Senior-Løken syndrome; JBTS – Joubert syndrome; MKS – Meckel syndrome.

Understanding the molecular architecture of the transition zone will allow us to unravel the complexity in genotype-phenotype associations for these ciliopathy disorders. To meet this challenge, we have established an interdisciplinary collaboration across Astbury Centre and the Faculty of Medicine and Health at the University of Leeds which will allow us to obtain high-resolution structures of transition zone proteins and their complexes by X-ray crystallography and/or cryo-electron microscopy, identify how they are organised at the ciliary base inside healthy and patient-derived cells using super-resolution microscopy, and then use these models to formulate and test hypotheses about how mutations disrupt primary cilium function in patient cells and retinal organoids.

Funding
This work was funded by the BBSRC and the Wellcome Trust

Collaborators
University of Leeds: Prof. Colin Johnson (Faculty of Medicine and Health)

The hierarchical emergence of worm-like chain behaviour from globular domain polymer chains

Benjamin Hanson, David Head and Lorna Dougan

Introduction

Biological organisms contain many hierarchically organised structures in order to modulate mechanical behaviour and organisation across multiple length scales, such that a macroscopic effect can be generated from microscopic objects. The physical properties of these microscopic structures, then, are not only a function of the intrinsic properties of the structural subunits themselves, but a function of the organisation of these subunits in three-dimensional space. An example of this type of system is the polyprotein titin. Titin forms from the expression and assembly of a variety of globular protein subunits which assemble into long filaments. These filaments then provide the mechanical properties necessary for muscles to function at the macroscale. The I27 domain of titin is relatively rigid when folded, whereas the PEVK domain is significantly less stable; so much so that under slight tensile force it will unfold into the constituent amino acid chain. This means that within titin, the arrangement of subdomains along the contour of the polymer will affect local interactions between the domains, and thus the hierarchical mechanical properties of the polyprotein.
Many other such hierarchical polyproteins exist within biological organisms, and the rational design of similar systems is of current interest. In addition, though, colloidal polymers have been designed where the colloidal subdomains are connected together not by amino-acid chains, but by dispersive interactions such as Van der Waals forces, or by electrostatic interactions between functionalised 'sticky patches'. These types of system can therefore be generalised as 'globular domain polymers', defined as polymers with an inhomogeneous aspect ratio along the polymer contour.

Using coarse-grained, dynamic computer simulations, we modelled these polymeric objects as spherical beads (globular domains) connected explicitly at the surface (N and C termini) by Hookean springs (amino acid chains). Using the persistence length, L_p, and contour length, L_c, as representative hierarchically emergent parameters, we measured how these 'intrinsic' polymeric values are affected by differences in the sphere radius, spring equilibrium length, and the effective stiffnesses of both types of subdomain. To connect with experimental results, we also performed simulations under single molecule force

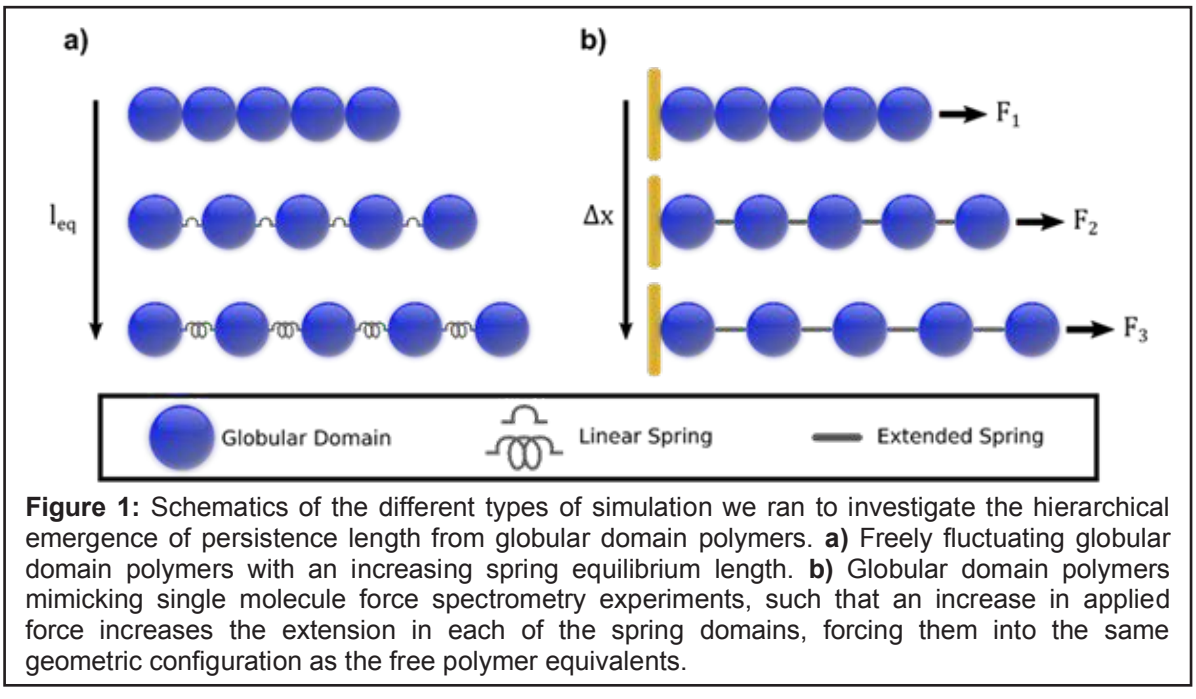

Figure 1: Schematics of the different types of simulation we ran to investigate the hierarchical emergence of persistence length from globular domain polymers. **a)** Freely fluctuating globular domain polymers with an increasing spring equilibrium length. **b)** Globular domain polymers mimicking single molecule force spectrometry experiments, such that an increase in applied force increases the extension in each of the spring domains, forcing them into the same geometric configuration as the free polymer equivalents.

spectroscopy (SMFS) conditions, to observe whether the persistence length measured in the

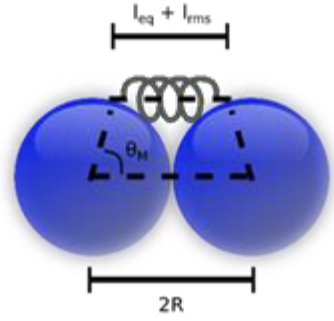

Figure 2: The local emergence of bending resistance as a function of geometric arrangement of globular domains. The angle θ_M is the maximum angle before the spheres begin to sterically interact, and is a function of the ratio between the length (and fluctuations) of the linker domain and the radius of the sphere.

free polymer is equivalent to that measured for globular domain polymers under continuously increasing force.

Theoretical Development

Spheres, representing globular domains, are geometrically rigid objects with radius R. On each sphere we define explicit N and C termini to which the springs connect. The Hookean springs have equilibrium length l_{eq} and root-mean square fluctuations l_{rms}. To model variability in the stiffness of the protein domains, we introduce a steric interaction potential based on the volumetric overlap of two spheres, which itself has an associated stiffness constant k_{st}. The geometric arrangement and intrinsic properties combine, causing the hierarchical emergence of polymeric properties.

Results

We observed that for free polymers, increasing the protein stiffness increases the persistence length, but the effect is significantly greater if the domain length scale ratio, $\hat{l}_{\mathrm{eq}} = l_{\mathrm{eq}}/2R$, is small (Figure 3a). This indicates that it is the combination of intrinsic properties and geometric arrangement combine non-trivially to generate hierarchical mechanical properties such as the persistence length. Due to that geometric effect, the application of SMFS conditions to a polymer continuously alters the effective persistence length as a function of applied force. We find that the worm-like chain model can be fit to our simulations (Figure 3b), but the measured persistence lengths are not equivalent to the free polymers'. Rather, we postulate that the measured persistence length of a polyprotein under SMFS conditions is an effective amalgamation of the persistence length at each different level of applied extension.

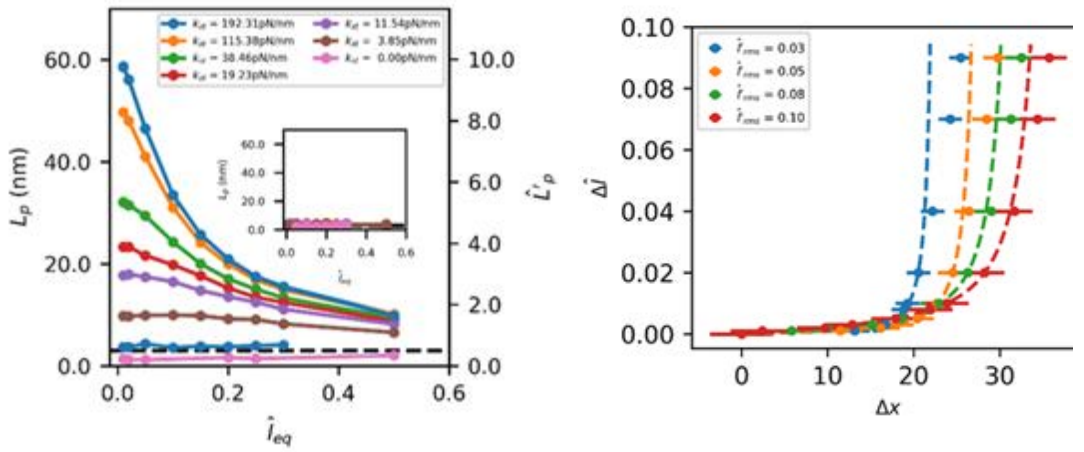

Figure 3: The behaviour of globular domain polymers when freely fluctuating and under the application of SMFS conditions. **a)** Persistence length as a function of length scale ratio and protein stiffness in free polymer simulations. **b)** Extension and a function of normalised applied force (dependent variable on *x*-axis for experimental comparison).

Publications

Hanson, B.S., Head, D. and Dougan, L. (2019) The hierarchical emergence of worm-like chain behaviour from globular domain polymer chains. *Soft Matter,* **15**(43), 8778-8789

Funding

This project was supported by a grant from the Engineering and Physical Sciences Research Council (EPSRC) EP/P02288X/1.

Biomolecular self-assembly under extreme Martian mimetic conditions

Harrison Laurent and Lorna Dougan

Introduction

Water is renowned as “the solvent of life”, driving protein folding and mediating biochemical reactions. The recent discovery of a subsurface lake on Mars has provided a new extra-terrestrial environment that is potentially similar to the life-harbouring subsurface lakes on Earth. The Martian regolith analysis performed by the Phoenix lander at its landing site in the Vastitas Borealis plains showed that the ionic makeup is dominated by magnesium perchlorate ($Mg(ClO_4)_2$). While $Mg(ClO_4)_2$ becomes highly bactericidal when combined with UV flux levels consistent with what would be expected at the Martian surface, or when desiccated, its presence at the surface suggests that it is also likely present in the subsurface water. This therefore provides a new environment sheltered from the damaging combined effects of $Mg(ClO_4)_2$ and UV radiation, and is potentially suitable for life. This highly chaotropic salt has also been shown to have a drastic effect on the hydrogen bonding network of water, resulting in a pressurising effect equivalent to ~3 GPa and a reduction of melting temperature to 206 K at a concentration of 44 wt%. This phenomena leads us to ask the question: how does the presence of $Mg(ClO_4)_2$ affect the hydration and self-association of biological molecules in water. This was studied using glycine as a model biological molecule due to its high solubility, molecular simplicity, and previously recorded presence in astronomical environments.

Results

To study the hydration and self-association of glycine, neutron diffraction experiments were performed on the NIMROD instrument at the ISIS Facility, Rutherford Appleton Laboratories. This was done at 25 °C for glycine in water, and at 25 °C and -20 °C for glycine + water + 40 wt% $Mg(ClO_4)_2$. Hydrogen/deuterium isotopic substitution was used to exploit the large difference in the coherent neutron scattering length between hydrogen and deuterium. This yields several scattering curves of identically structured samples. The raw scattering data are then corrected for multiple scattering, inelasticity effects, etc. using Gudrun, and then used to produce simulated boxes of molecules whose scattering patterns are consistent with the corrected data through empirical potential structure refinement (EPSR). The resulting

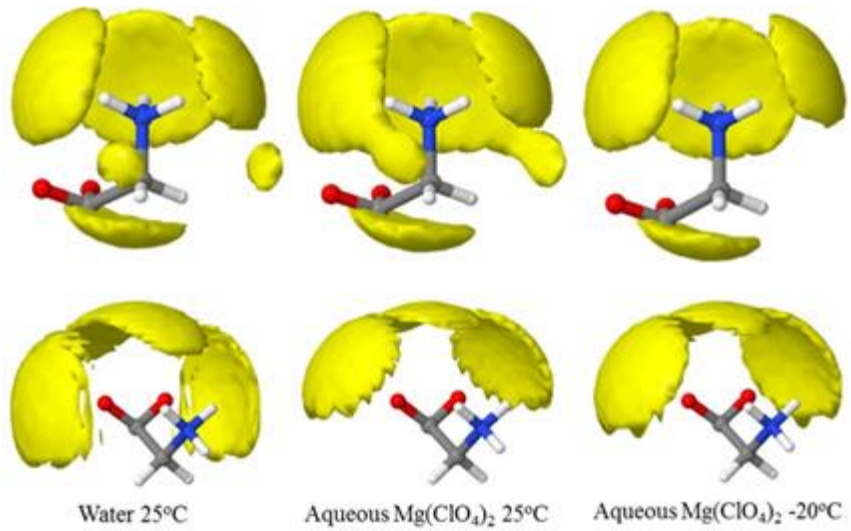

Figure 1: Areas of preferential hydration (yellow) around a central amine group (top) or central carbonyl group (bottom) of glycine under the three conditions studied in this work. Areas in yellow are surface contours containing the highest 15 % probability areas of finding a water molecule within a distance of 5 Å from the central atom.

hydration of glycine can be visualised using the spatial density functions shown in Figure 1. As shown here, the presence of $Mg(ClO_4)_2$ at 25 °C causes the hydration areas to become less well defined around the amine group when compared with pure aqueous glycine at 25 °C, however this effect is reduced at the lower temperature of -20 °C. Around the carbonyl group the presence of $Mg(ClO_4)_2$ causes the areas of preferential hydration to become more localized directly above the CO bond, and the central area of preferential hydration shared between both carbonyl oxygens to shrink. Again this affect is reduced at the lower temperature. This is consistent with a reduction in hydrogen bonding between the amine and carbonyl groups and the surrounding water molecules as a result of $Mg(ClO_4)_2$. The hydrogen bonding is then subsequently increased as a result of lowering the temperature, consistent with previous neutron scattering experiments on aqueous organic molecules, causing the hydration structure of glycine in aqueous $Mg(ClO_4)_2$ at -20 °C to be more reminiscent of the pure aqueous glycine at 25 °C.

EPSR analysis also allows us to examine the clustering of glycine. Two glycine molecules are considered clustered if a carbonyl oxygen from one molecule is within a threshold distance of an amine hydrogen on the second molecule. This threshold distance corresponds to the first minima in the amine hydrogen – carbonyl oxygen intermolecular radial distribution function. The resulting cluster size distributions are shown in Figure 2. As this clustering is based on the interactions between the hydrophilic areas of the glycine molecules, both of which are capable of forming hydrogen bonds, it is likely that cluster formation is a result of intermolecular hydrogen bonding. As shown in Figure 2, this clustering is reduced in the presence of $Mg(ClO_4)_2$, but partially recovers at lower temperature. This is therefore consistent with the glycine hydration results, which showed a recovery of hydrogen bonding at lower temperature. These results show that while $Mg(ClO_4)_2$ acts to reduce hydrogen bonding in the system, likely due to the screening of electrostatic interactions, it is not capable of destroying it completely, and it is temperature dependent.

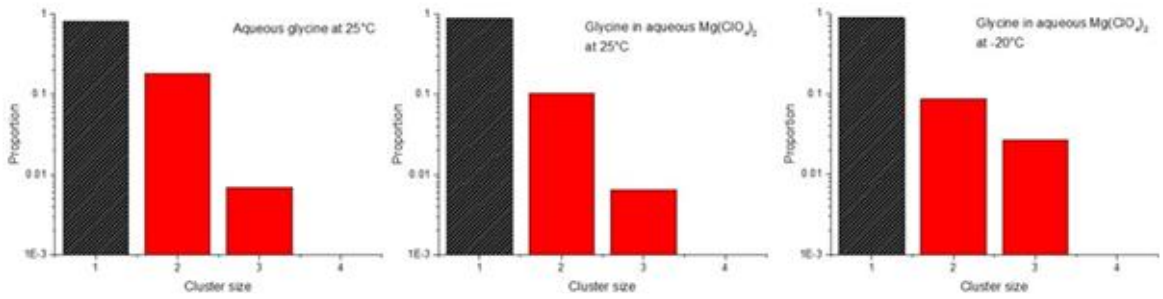

Figure 2: Glycine cluster size distributions for aqueous glycine at 25 °C (left), glycine in aqueous $Mg(ClO_4)_2$ at 25 °C (middle), and glycine in aqueous $Mg(ClO_4)_2$ at -20 °C (right). Total fraction of glycine molecules in clusters of 2 or more calculated to be 0.320, 0.203 and 0.221 respectively. Fraction of monomers shown in black and white.

Publications

Laurent, H., Soper, A., and Dougan, D., Biomolecular self-assembly under extreme Martian mimetic conditions (2019) *Molecular Physics*, **117**(22), 3398-3407

Funding

This project was supported by a grant from the Engineering and Physical Sciences Research Council (EPSRC) EP/P02288X/1. Harrison Laurent is jointly supported by an EPSRC DTA studentship and an ISIS Facility Development Studentship.

Collaborators

External: Alan Soper (ISIS Facility, Rutherford Appleton Laboratories)

Respiratory Syncytial Virus M2-1 protein could remain bound to viral mRNAs during their entire life time

Muniyandi Selvaraj, Georgia Pangratiou, Jamel Mankouri, John Barr and Thomas Edwards

Introduction

The negative-stranded RNA virus human respiratory syncytial virus (HRSV) is a leading cause of respiratory illness, particularly in the young, elderly, and immunocompromised, and has been linked to the development of asthma. HRSV replication depends on the phosphoprotein (P) and polymerase (L), whilst transcription also requires M2-1. M2-1 interacts with HRSV-P and RNA at overlapping binding sites. Whilst these interactions are necessary for transcriptional activity, the mechanism of M2-1 activity is unclear.

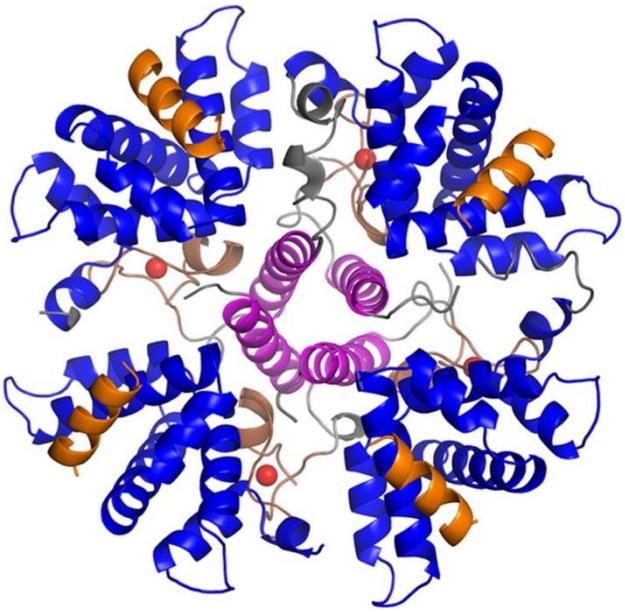

Figure 1: Crystal structure of the M2-1/P complex. The M2-1/P complex with M2-1 in its tetramer state, The N-terminal zinc-binding domain is shown with a coordinated zinc ion (red sphere), the oligomerization helix is shown in pink, the core domain is shown in blue, and the P90–110 peptide is shown in orange.

Results

We recently solved the crystal structure of M2-1 in complex with the minimal P interaction domain (Selvaraj et al *mBio* 2018), revealing molecular details of the M2-1/P interface and defining the orientation of M2-1 within the tripartite complex (Figure 1). The M2-1/P interaction is relatively weak, suggesting high-affinity RNAs may displace M2-1 from the complex. These results constitute an important step toward the understanding of RSV transcription process and, on a broader level, of RSV RNA-dependent RNA polymerase regulation and functioning. Interestingly, these results suggest that M2-1 could play a posttranscriptional role in viral mRNA metabolism which is consistent with previous descriptions of concentration of newly synthetized viral mRNAs together with M2-1 in inclusion body-associated granules (IBAGs).

In this model, M2-1 would remain bound with viral mRNAs in the cytosol to regulate mRNA translation and/or stability. However, a critical incongruity of this model is the potentially very small amount of M2-1 protein. Marie-Anne Rameix-Welti (Université Versailles Saint Quentin en Yvelines, Montigny-le-Bretonneux, France) has provided calculations to suggest that at 24 hours post-infection, there would be more than enough M2-1 tetramers in the cell to bind with all viral mRNAs. We appreciate these efforts to quantify the components of the proposed model which, although hypothetical, do lend support to its feasibility. Of course, we look forward to the time when such quantities can be experimentally determined.

Unfortunately, this does leave an additional problematic scenario. During primary transcription, when the only available transcriptase and source of M2-1 is the RdRp bound to the infecting vRNA, our model posits that one tetramer of M2-1 is required for the generation

of each RSV mRNA. As the M2 gene is the ninth transcriptional unit to be encountered by a transcribing mRNA, provision of newly synthesized M2 mRNAs to provide a pool of M2-1 protein would require a total of nine M2-1 tetramers to be brought into the infected cell. A critical gap in the current model is in the identification of the source of these additional M2-1 molecules. Options include the repurposing of the M2-1 that is thought to be associated with the matrix in the virion or alternatively, the presence of multiple RdRps per genome. No experimental evidence for either of these possibilities currently exists. The model we proposed has some notable gaps, but we view it as a starting point and hope the gaps may soon be closed following careful experimentation.

Publications

Edwards, T.A. and Barr, J.N. (2019). Reply to Rameix-Welti, “No incongruity in respiratory syncytial virus M2-1 protein remaining bound to viral mRNAs during their entire life time.” *mBio* **10**:e00629-19.

Funding

This work was funded by the Wellcome Trust, BBSRC, the University of Leeds and the MRC.

Collaborators

External: Charles-Adrien Richard and Jean-François (Éléouët. Unité de Virologie et Immunologie Moléculaires (UR892), INRA, Université Paris-Saclay, Jouy-en-Josas, France)
Julian Hiscox (University of Liverpool)

Cell under stress: high-throughput analysis of single cells and disease progression

Fern Armistead, Julia Gala De Pablo, Sally Peyman and Stephen Evans

Introduction

The deformability of a cell is the direct result of a complex interplay between the different constituent elements at the subcellular level, coupling a wide range of mechanical responses at different length scales. Changes to the structure of these components can also alter cell phenotype, which points to the critical importance of cell mechanoresponse for diagnostic applications. The response to mechanical stress depends strongly on the forces experienced by the cell. We use cell deformability in both shear-dominant and inertia-dominant microfluidic flow regimes to probe different aspects of the cell structure. We investigate the deformability of three colorectal cancer (CRC) cell lines using a range of flow conditions. These cell lines offer a model for CRC metastatic progression; SW480 derived from primary adenocarcinoma (Dukes stage B), HT29 from the primary tumor (Dukes stage C) and SW620 from lymph-node metastasis (Duke stage C). HL60 (leukemia cells) were also studied as a model circulatory cell, offering a non-epithelial comparison. We demonstrate that microfluidic induced flow deformation can be used to robustly detect mechanical changes associated with colorectal cancer (CRC) progression. We also show that single-cell multivariate analysis, utilising deformation and relaxation dynamics, offers a more accurate method to distinguish the complex mechanical response of these different cell types. These results emphasise the benefit of high-throughput and multiple parameter determination for improving detection and accuracy of disease stage diagnosis.

Results

In the inertial regime, we follow cellular response from (visco-)elastic through plastic deformation to cell structural failure and show a significant drop in cell viability for shear stresses >11.8 kPa. Comparatively, a shear-dominant regime requires lower applied stresses to achieve higher cell strains. From this regime, deformation traces as a function of time contain a rich source of information including maximal strain, elastic modulus, and cell relaxation times and thus provide a number of markers for distinguishing cell types and potential disease progression. These results emphasize the benefit of multiple parameter determination for improving detection and will ultimately lead to improved accuracy for diagnosis. We present results for leukemia cells (HL60) as a model circulatory cell as well as for a colorectal cancer cell line, SW480, derived from primary adenocarcinoma (Dukes stage B). SW480 were also treated with the actin-disrupting drug latrunculin A to test the sensitivity of flow regimes to the cytoskeleton. We show that the shear regime is more sensitive to cytoskeletal changes and that large strains in the inertial regime cannot resolve changes to the actin cytoskeleton.

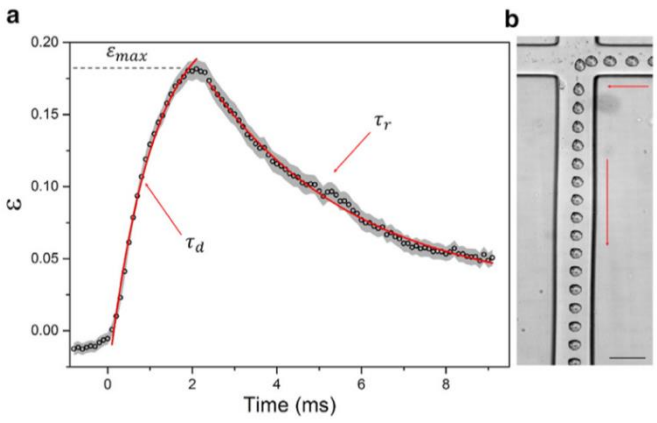

Figure 1: (a) Strain, ε, as a function of time, averaged over 50 cells, with the standard error shown in gray. Flow rate was fixed at 5 mL/min, and the suspension medium viscosity was 33 cP. The exponential fits shown in red were used to quantify the deformation and relaxation of the cells and determine the elastic modulus of cells. (b) A superimposition of brightfield images of a cell as it deforms and relaxes at 5 mL/min is shown. Scale bar, 30 μm. The arrows indicate the direction of cell motion.

Three colorectal cancer cell lines, representing different states of disease progression, were studied in the shear and inertia-dominant flow regimes. The cell types could only be

differentiated under certain flow conditions, indicating that in the inertial regime low-strain regimes are sensitive to cytoskeletal changes whereas high-strain regimes are not. Additionally, at a critical flow rate in the inertia-dominant regime we saw an increase in gradient of *DI* as a function of flow rate, this occurs due to the breakdown of the cells internal structure, and as such the mechanical properties probed beyond this point would depend only on the viscous properties of the cytoplasm. This corroborated previous works that show that changes to actin structure associated with metastatic progression result in the cells becoming softer. In the shear dominant regime, we measured deformation traces and determined multiple characteristic parameters, including maximum strain ε_{max}, elastic modulus *E* and relaxation time τ_r. Interestingly, the elastic modulus values of each cell line were of the same order of magnitude as previous AFM measurements, in spite of the different modes and timescales of operation.

Our results are the first example of using microfluidic deformation to distinguish between non-metastatic and metastatic CRCs and support the expectation that metastatic cells are more deformable than non-metastatic cells due to cytoskeletal changes. Further, we found that multiple parameters were needed to be able to distinguish the four cell types from each other. We observed that SW620 and HT29 are more deformable and softer than SW480, and also do not recover their original strain suggesting that they undergo an additional slower relaxation process, occurring over a time period too long to be captured in our experiments. Single cell and multiple parameter analysis showed changes in the mechanical properties of CRC cells that could be partially attributed to specific sub-structural changes, and that these can also be used to classify different cell types. Results show that a single-cell high-throughput technique must be combined with multiparameter analysis in order to advance our understanding of cancer progression, and to accurately classify heterogeneous samples of diseases states.

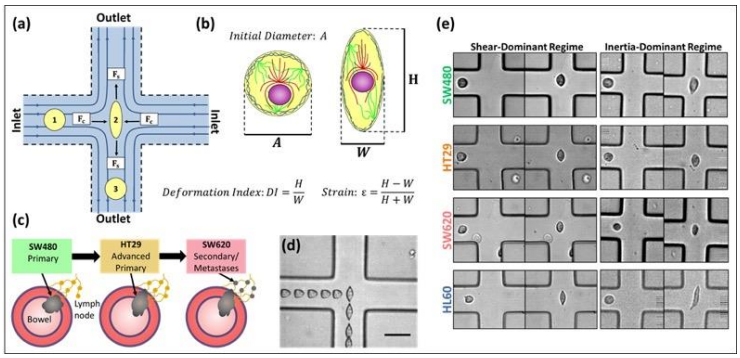

Figure 2: (a) Schematic of cross-flow region. (b) Schematic of a cell including the nucleus and cytoskeletal filaments (actin, microtubules and intermediate filaments) which are the main contributors of cell stiffness. Also included are parameters extracted from high speed videos of cell deformation: A is the initial diameter of the cell before it deforms, H is the height of the cell and *W* is the width of the cell. (c) Schematic describing the model for colorectal cancer progression using the three cell lines: SW480, HT29 and SW620. (d) Superimposed bright field images showing a single cell entering (from left) the stagnation point (SP) of an extensional flow device and exiting to the bottom of the chamber. (e) Example images of deformation events of SW480, HT29, SW620 and HL60 cell lines. Including an image before the cell is deformed and an image of the deformation at the SP, for a shear-dominant and inertia-dominant-flow regime. Images from the shear-dominant regime were at a flow rate of *Q* = 50 µl/min with suspension buffer viscosity of µ = 33 cP, and in the inertia dominant regime *Q* = 600 µl/min and µ ≈ 1 cP.

Publications

Armistead, F.J., Gala De Pablo, J., Gadelha, H., Peyman, S.A., Evans, S.D., (2019) Cells Under Stress: An Inertial-Shear Microfluidic Determination of Cell Behavior. *Biophys J.* **116**(6):1127-36.

Funding

This work was funded by the University of Leeds.

Collaborators

External: Hermes Gadelha (University of Bristol)

Structure-based design approaches to tackle antimicrobial resistance

Colin Fishwick

Introduction

The 2016 O'Neill Review on Antimicrobial Resistance (AMR) suggested that by 2050 there would be ~10 million deaths globally due to AMR, with a concomitant loss of ~100 trillion USD in output. AMR is widespread and global, and even today deaths due to AMR approach 1 million per annum. One of O'Neill's key recommendations was for the development of new antibiotics, recognising that no truly new classes have been produced for decades. Our group specialises in structure-based design to identify novel bioactive molecules for portfolio of anti-infective targets. The research is highly interdisciplinary, with the aim of producing a holistic approach to tackle AMR.

Inhibitors of DNA gyrase

DNA topoisomerases are enzymes that catalyse topological changes in DNA; they are present in all cell types and are essential for survival. Our lab has worked on compounds that bind the aminocoumarin pocket, which overlaps with the ATP-binding site in the gyrase B protein. Using the *de novo* molecular-design program SPROUT, we have developed a series of compounds possessing promising antibacterial activity based on a pyridine-3-carboxamide core. Detailed structural characterisation of the binding mode of these inhibitors within GyrB has been established (Fig. 1) confirming the original *in silico* binding mode. A key feature of these compounds is the ability to form a network of hydrogen bonds involving all three nitrogen atoms shared between the urea and pyridine units, with a bound water and serine and aspartate residues from the protein. Development of the physicochemical properties of these compound class is continuing to optimise entry into Gram-negative bacteria.

Studies on the inhibition of beta-lactamases by cyclic boronates

The beta-lactam antibiotics represent the most successful drug class for treatment of bacterial infections. Resistance to them, importantly via production of beta-lactamases, which collectively are able to hydrolyse all classes of beta-lactams, threatens their continued widespread use. We designed and synthesised a number of bicyclic boronates which show potential as broad spectrum inhibitors of the mechanistically distinct serine- (SBL) and metallo- (MBL) beta-lactamase families. Using biophysical methods we have investigated the binding mode of these bicyclic boronates in complex with AmpC from *Pseudomonas aeruginosa* which revealed that it binds to form a tetrahedral boronate species (Fig. 1). Microbiological studies on the clinical coverage (in combination with meropenem) and induction of beta-lactamases by bicyclic boronates further support the promise of such compounds as broad spectrum beta-lactamase inhibitors. Further structure-activity

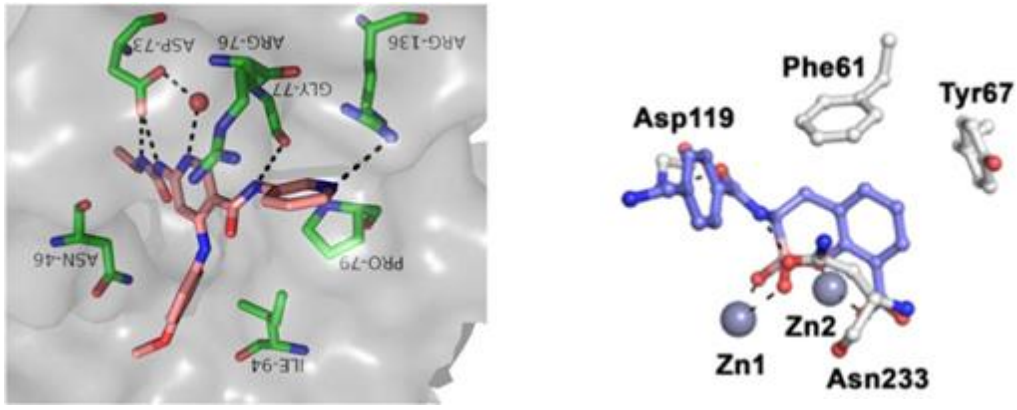

Figure 2: Left: Co-cystal structure of *de novo* designed inhibitor with *E.coli* GyrB. Right: Cyclic boronate inhibitor in complex with VIM-2 metallo-β-lactamase.

relationship work on this series is ongoing.

Publications

Cahill, S.T., Tyrrell, J.M., Calvopina, K., Robinson, S.W., Lohans, C.T., McDonough, M.A., Cain, R., Fishwick, C.W.G., Avison, M.B., Walsh, T.R., Schofield, C.J., Brem, J. (2019) Studies on the inhibition of AmpC and other beta-lactamases by cyclic boronates. *BBA - General Subjects*, **1863**: 742-748.

Narramore, S., Stevenson, C.E.M., Maxwell, A., Lawson, D.M., Fishwick, C.W.G. (2019) New insights into the binding mode of pyridine-3-carboxamide inhibitors of E. coli DNA gyrase. *Bio Med Chem*, **27**: 3546-3550.

Funding

This work was funded by Medical Research Council.

Collaborators

External: Chris Schofield (University of Oxford), Timothy Walsh (Cardiff University), Tony Maxwell (John Innes Centre)

Structure of specialized ribosomes

Tayah Hopes, Michaela Agapiou, Karl Norris, Julie Aspden and Juan Fontana

Introduction

The tight control of protein synthesis is essential for all life. Traditionally, it has been considered that ribosomes are homogenous macromolecular machines lacking any capacity to regulate translation. However, it is now becoming clear that ribosomes can also preferentially translate specific mRNA transcripts through variations in their protein and RNA composition, generating different types of ribosomes, termed “specialised ribosomes”. One mechanism for this specialisation is through the incorporation of ribosomal protein paralogs, which are known to exhibit tissue specific expression (e.g. RpL22-like in *Drosophila melanogaster* testis). The functions of these specialised ribosomes are beginning to be elucidated. For instance, mutations in specific ribosomal proteins exhibit precise phenotypes e.g. impaired fertility.

This project aims to characterise the structure and composition of specialised ribosomes with a switched paralog.

Results

Tandem Mass Tag (TMT) quantitative mass spectrometry of ribosomes from different *D. melanogaster* tissues, suggested specialised ribosome populations exist in *D. melanogaster* gonads. To understand the consequences of ribosome specialisation we performed cryo-electron microscopy (cryo-EM) of 80S ribosomes from testis and ovary .We obtained averages at 3.5 Å (for testis 80S ribosomes) and 3.0 Å (for ovary 80S ribosomes) (Figs. 1A & B). The main difference between the two is the presence of an additional density in the testis ribosome.

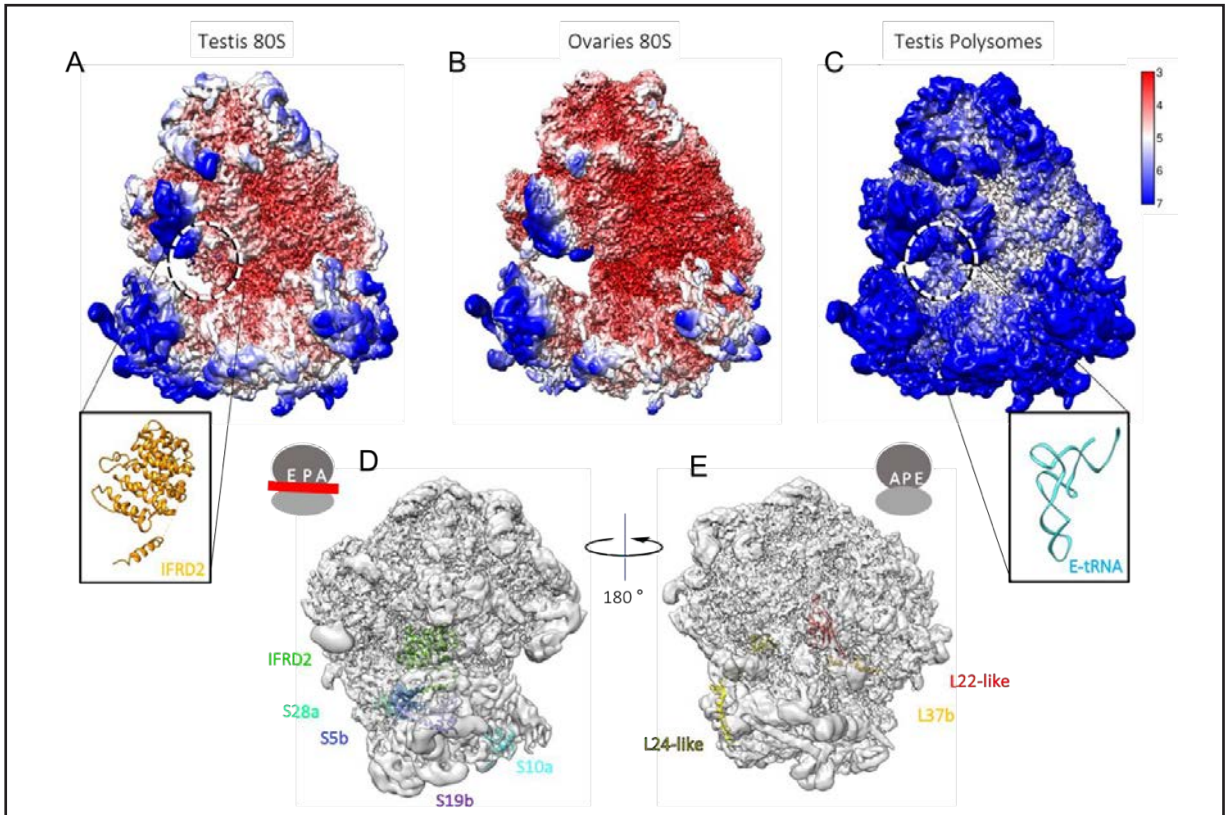

Figure 1: Cryo-EM of specialised ribosomes from *D. melanogaster*. A to C, cryo-EM averages of testis 80S, ovary 80S and testis polysomes colour-coded according to resolution (resolution scale bar at the right). Testis 80S have a density at the mRNA site that corresponds to an IFRD2 ortholog, which inactivates ribosomes. Ovary 80S ribosomes lack this density. Testis polysomes contain mRNA and a tRNA in that same region. D & E, localisation of paralog switching events in the ribosome. Small subunit paralog switching events map to the mRNA channel, while large subunit paralog switching events locate at the back of the ribosome.

By combining the EM density map of this region with TMT data, we identified this density to be CG31694-PA, an ortholog of IFRD2, which has been previously found to inactivate ribosomes from rabbit reticulocytes. These results suggest that 80S ribosomes from *D. melanogaster* are not actively translating mRNA, as they lack densities for tRNA and mRNA, and that testis ribosomes are further inactivated by CG31694-PA. To verify that the presence of CG31694-PA does not affect the testis paralog switching events, we solved the structure of polysomes purified from testis (Fig. 1C; resolution 4.9 Å). In this average, there is no density for CG31694-PA; rather, there is density for E-tRNA, suggesting these are actively translating ribosomes. We then mapped the different paralog switching events in the testis 80S ribosome (Figs. 1D & E). By doing this, we identified three clusters of paralogs undergoing switching: 1) Paralogs from the small subunit then to cluster at the mRNA channel, potentially providing the ribosome the capability of interacting with specific mRNAs. 2) Two paralogs locate at the ribosome stalks, possibly providing additional interactions with the mRNA during translation. 3) Paralogs within the large subunit tend to be exposed to the outside and cluster at the back of the ribosome, providing possible binding regions for factors that might regulate translation by the ribosome.

Altogether our data reveal ribosome heterogeneity occurs in a tissue specific manner. In *D. melanogaster*, paralog switching events are most abundant in the gonads and our structural analysis has provided insights into how this switch might regulate translation mechanistically. Additionally, we performed an evolutionary analysis of a paralog pair (RpL22 and RpL22-like) that suggests specialisation may represent a conserved mechanism of translation regulation across eukaryotes.

Funding
This work was funded by BBSRC, MRC, Wellcome Trust, Royal Society and White Rose University Consortium Collaboration Fund.

Collaborators
External: Charley G.P. McCarthy and Mary J O'Connell (University of Nottingham)

In vivo detection of protein turnover changes in mouse models of neurodegenerative disease by stable isotope labelling and mass spectrometry

René Frank

Introduction

In the mammalian brain, the rate of protein turnover ranges from minutes to several days. This extraordinary flux poses a particular challenge for the brain because information must outlive the molecular substrates in which they are stored. In postmitotic cells, including neurons, the rate of proteome turnover is regulated by mechanisms including, the rate of synthesis, ubiquitin-proteasome and autophagy-mediated degradation. Protein turnover perturbations cause severe neurological dysfunction. Indeed, the most common neurodegenerative diseases, including Alzheimer's disease (AD) are characterized by imbalances in the turnover of a few proteins, including Abeta and MAPtau, resulting in their accumulation into mis-folded protein aggregates. These inclusions appear to be resistant to cellular mechanisms of repair. However, it is not known if neurodegenerative diseases have an impact on global proteome turnover in the mammalian brain itself.

In vivo metabolic labelling and global proteomic profiling has the capacity to measure the dynamics of individual proteins throughout the proteome. Here, we established a method using ^{13}C heavy lysine (K6) labelling to detect global proteome turnover change in mice. Next, we developed the assay to simultaneously measure changes in protein turnover and expression level *in vivo*. This multiplex screen of proteome dynamics is potentially applicable to any protein in any tissue and distinguishes between changes driven by synthesis or degradation of a protein. We applied this screen to quantify ~1000 proteins in three mouse models of neurodegenerative disease at pre-symptomatic and symptomatic ages. In all models that we tested (*TgCRND8, App$^{NL\text{-}F/NL\text{-}F}$*, *TgSOD1-G93A*), increased neuropathology was associated with increased protein turnover and changes in the amount of some specific proteins, caused by measurable alterations in their synthesis or degradation. This resource reveals novel signatures of pathology, facilitates comparisons between different mouse models of disease and contrasts neurodegeneration with the mechanisms of ageing in healthy wildtype mice.

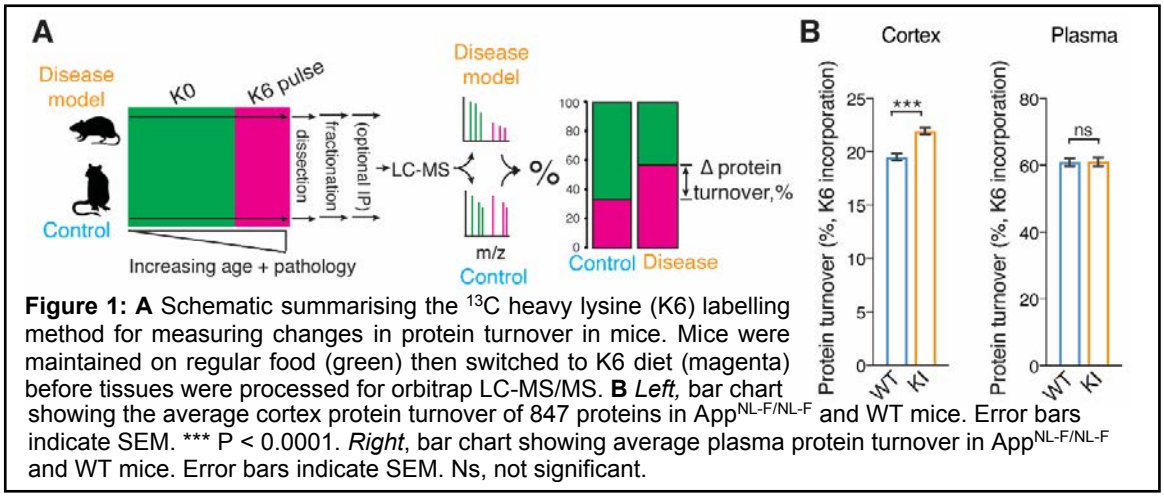

Figure 1: A Schematic summarising the ^{13}C heavy lysine (K6) labelling method for measuring changes in protein turnover in mice. Mice were maintained on regular food (green) then switched to K6 diet (magenta) before tissues were processed for orbitrap LC-MS/MS. **B** *Left,* bar chart showing the average cortex protein turnover of 847 proteins in App$^{NL\text{-}F/NL\text{-}F}$ and WT mice. Error bars indicate SEM. *** P < 0.0001. *Right*, bar chart showing average plasma protein turnover in App$^{NL\text{-}F/NL\text{-}F}$ and WT mice. Error bars indicate SEM. Ns, not significant.

Results

To quantify changes in protein turnover, mice were fed a diet in which the essential amino acid, lysine (K0), was replaced with a ^{13}C stable isotope derivative (K6) for 6-8 days (Fig. 1A). The rate of K6 incorporation was directly quantified by the ratio of K6 to K0 in each mouse. At the end of this labelling period the brain cortex from these mice were collected for LC-MS (Fig. 1A). Measuring the change in K6 incorporation between disease and control tissues gave a snapshot of proteome turnover associated with the disease (Fig. 1B).

In each tissue sample from each mouse we identified an average of 72,261 peptides (± 4,231 sd). In *App*$^{NL\text{-}F/NL\text{-}F}$ mice with advanced β-amyloidosis, forebrain GAPT increased by 15.7% ($P < 0.0001$, $n = 721$), with 53 proteins being made or degraded faster (Fig. 1B, *left*). In contrast, serum protein turnover ($P = 0.961$, $n = 95$) did not change significantly (Fig. 1B, *right*), indicating that the decrease in protein turnover is specific to the pathologically affected forebrain tissue.

The kinetics of protein turnover determines the expression level of all proteins. Therefore, the simultaneous measurement of turnover and expression level of each protein can give a comprehensive description of proteome dynamics and mechanistic insight. To this end, we next combined turnover measurements with expression level measurements by exploiting recent improvements of label-free quantification (using MaxLFQ). In each mouse model of disease dataset, an average of 4,357 proteins (± 654 sd) were quantified by label-free quantification.

We plotted the change in flux versus the expression level of each protein as depicted in Figure 2 to determine the effect of changing turnover on expression levels. Comparing pre-symptomatic and symptomatic *App*$^{NL\text{-}F/NL\text{-}F}$ showed a 5-fold increase in the number of significantly changed proteins (Fig. 2B). Thus, increased pathology correlated with increased imbalances in the proteome. Different proteins were differentially affected, suggesting specific pathways are impacted at early versus late stages of pathology. Analysis of the symptomatic *App*$^{NL\text{-}F/NL\text{-}F}$ dataset using the KEGG showed that significantly changed proteins converged on several pathways that appear to be prevalent in presynaptic functions, including synaptic vesicle recycling and mitochondria. Thus, multidimensional proteome dynamics have identified specific proteins and pathways dysregulated as a consequence of disease.

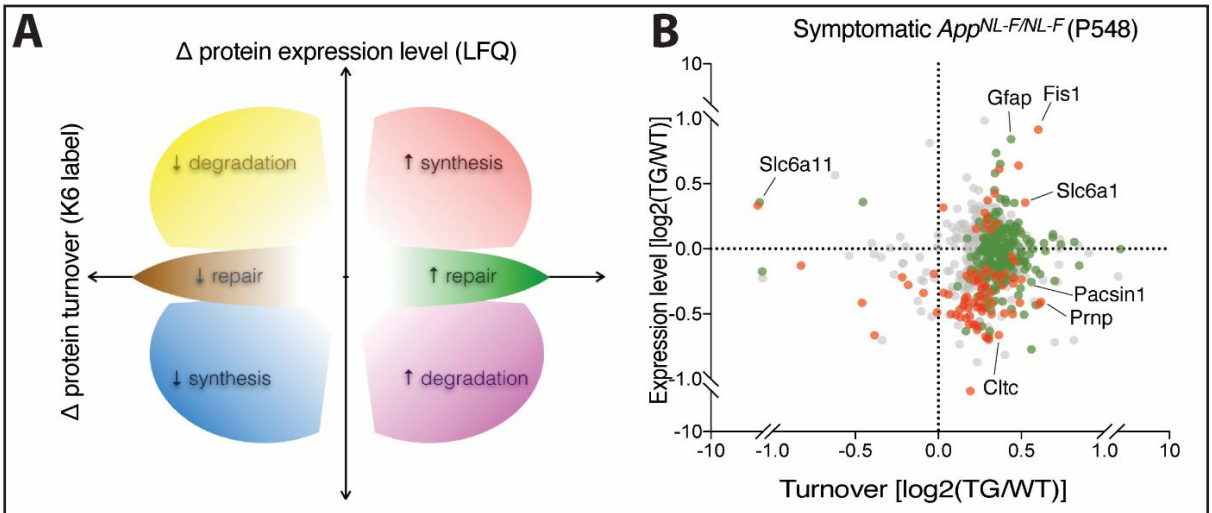

Figure 2: A 'Dynablot' schematic showing the change in protein turnover (*x*-axis, K6 label) plotted against the change in steady state expression level (*y*-axis, LFQ). **B** Dynaplot of cortex proteins in symptomatic (P548) *App*$^{NL\text{-}F/NL\text{-}F}$ mice, as compared to healthy, age-matched control mice. *X*-axis, change in protein turnover in *App*$^{NL\text{-}F/NL\text{-}F}$ (Tg) versus WT expressed as log ratio of K6 incorporation. *Y*-axis, change in protein expression level in *App*$^{NL\text{-}F/NL\text{-}F}$ versus WT measured by label free-quantification using MaxLFQ. Green, red, and grey datapoints correspond to proteins with significant changes ($P < 0.05$) in protein turnover, expression level and non-significant, respectively.

Funding

This work was funded by the Medical Research Council.

Collaborators

External: Byron Andrews, Mark Skehel, Sarah Maslen, and Leonardo Almeida-Souza (MRC Laboratory of Molecular Biology).

Integral membrane proteins as drug targets

Alexandra Holmes, Steven Harborne, Aaron Wilkinson, Jannik Strauss, Roman Tuma, Antreas Kalli, Christos Pliotas and Adrian Goldman

Introduction

Membrane pyrophosphatases (M-PPases) occur in plants, protozoan parasites and prokaryotes. They are associated with low-energy stress: overcoming saline or drought conditions in plants or rapid changes in pH or osmotic pressure in protozoan parasites. M-PPases couple pyrophosphate hydrolysis to the pumping of sodium ions and/or protons across the inner membrane of prokaryotes or the vacuole/acidocalcisome membranes of plants/parasites. These proteins are important in the lifecycle of several pathogenic species of parasites, including *Plasmodium falciparum*, which causes malaria, and in several species of pathogenic bacteria. There are no homologues in mammals, so M-PPases are an important potential drug target. Continuing from our initial M-PPase structure using X-ray crystallography, we are completing a model of the catalytic cycle using additional structural and biochemical data and are using this in drug design.

Results

We have solved the first structures of *Thermotoga maritima* M-PPase (TmPPase) in complex with an allosteric inhibitor, *N*-[(2-amino-6-benzothiazolyl)methyl]-1*H*-indole-2-carboxamide (ATC) at a resolution of 3.4 - 4.0 Å. The crystals contain a π-stacked head-to-tail dimer of ATC bound in a hydrophobic cleft near the exit channel of chain A. ATC stabilizes an asymmetric structure of TmPPase. Studies demonstrated that, as in the structure, *two* molecules of ATC are required for inhibition of the TmPPase *dimer*, and that inhibition is uncompetitive: ATC only binds in the presence of substrate. ATC is the first non-phosphorus and the first allosteric inhibitor identified for M-PPases.

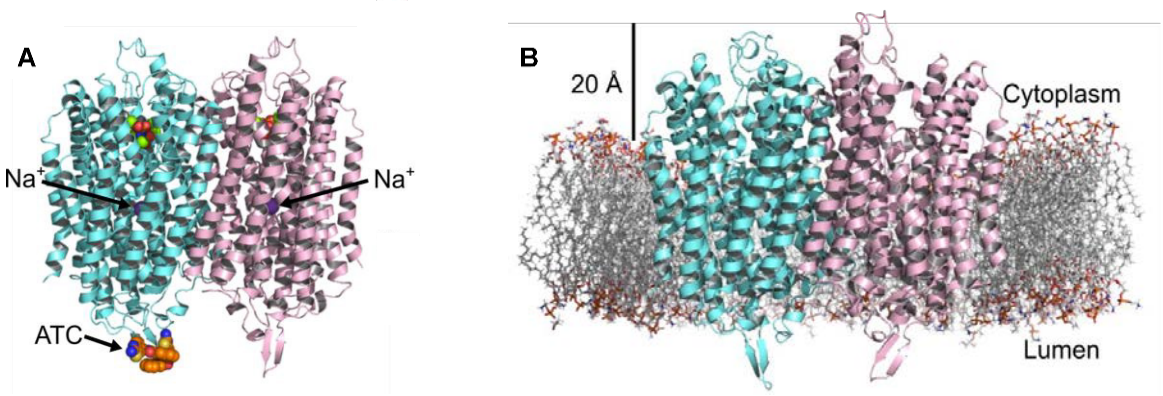

Figure 1: (A) TmPPase dimer of the ATC-bound structure showing ATC in orange, Na^+ in purple. The asymmetric structure around the exit channel near the ATC can be seen. (B) TmPPase dimer after molecular dynamics simulations (up to 500 ns) showing how it is inserted into the bilayer.

Our new model (Fig. 2) explains hows binding at the active site potentiates binding of the ATC dimer, and is consistent with other compounds (*unpublished*) that bind to conserved regions near the monomer-monomer interface in TmPPase and *do* kill malaria parasites at concentrations of 1-5 μM. They also bind in an allosteric manner.

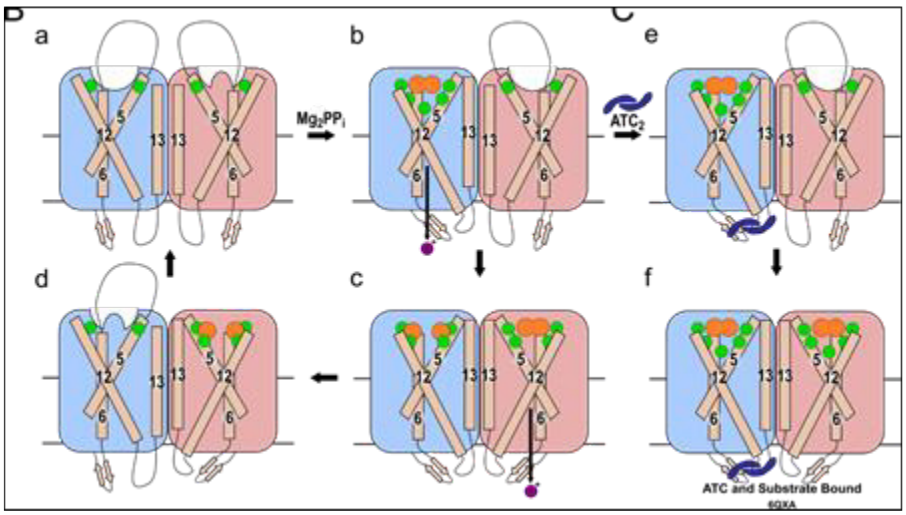

Figure 2: Revised mechanism of M-PPases, suggesting how binding of PP_i to one monomer potentiates binding at the other active site, but also enables ATC2 binding

Finally, we have developed a cysteine mutant pair that allows us to measure FRET and PELDOR changes as a function of binding of different ligands (Fig. 3). This demonstrates that, contrary to our expectations, PP_i binding to the enzyme is more similar to etidronate binding than it is to IDP binding, at least for the A546C:I584C FRET pair. This is now being further studied by PELDOR.

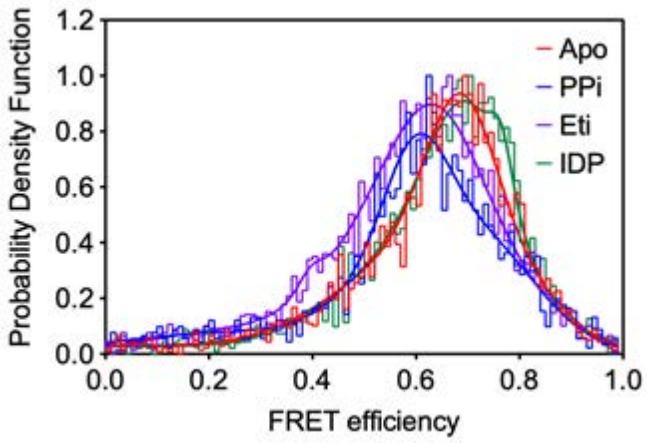

Figure 3: FRET efficiency for *apo*, pyrophosphate-, Etidronate- ($_3OPCHOHPO_3$) and imidodiphosphonate bound TmPPase

(1) We now have a novel understanding of how to inhibit M-PPases by binding by the exit channel. (2) We have a new working model that may explain how M-PPases, which have a single pumping channel, can pump both sodium and protons. (3) We are testing our new model both structurally (time-resolved X-ray crystallography; structures of other intermediates), computationally (steered molecular dynamics) and experimentally (FRET, PELDOR). The work will allow the development of drugs against significant human and animal parasites.

Publications

Holmes, A.O.M., Kalli, A.C. & Goldman, A. (2019) The Function of Membrane Integral Pyrophosphatases From Whole Organism to Single Molecule. *Front Mol Biosci* **6,** 132.

Vidilaseris, K., Kiriazis, A., Turku, A., Khattab, A., Johansson, N. G., Leino, T. O., Kiuru, P. S., Boije Af Gennäs, G., Meri, S., Yli-Kauhaluoma, J., Xhaard, H. & Goldman, A. (2019) Asymmetry in catalysis by Thermotoga maritima membrane-bound pyrophosphatase demonstrated by a nonphosphorus allosteric inhibitor. *Sci Adv* **5,** eaav7574.

Vidilaseris, K., Johansson, N. G., Turku, A., Kiriazis, A., Boije Af Gennäs, G., Yli-Kauhaluoma, J., Xhaard, H. & Goldman, A. (2019) Screening protocol for identification of *Thermotoga maritima* membrane-bound pyrophosphatase inhibitors. *J. Vis. Exp* DOI: 10.3791/60619.

Funding

This work was funded by the BBSRC, the University of Leeds, the European Union, the Academy of Finland and the Erkko Foundation and the EPSRC.

Collaborators

University of Leeds: Lars Jeuken, Sarah Harris, Colin Fishwick
External: University of Helsinki, University of South Bohemia, National Tsing Hua University

A newly identified Zika virus ion channel antiviral target

Emma Brown, Daniella Lefteri, Ravi Singh, Rebecca Thompson, Daniel Maskell, Gemma Swinscoe, Andrew Macdonald, Neil Ranson, Richard Foster, Clive McKimmie, Antreas Kalli and Stephen Griffin

Introduction

Ion channels are amongst the most successful drug targets in medicine. However, it remains under-appreciated that viruses also encode such proteins, termed “viroporins”, and these are increasingly recognised as excellent targets for antivirals targeting some of the clinically and economically important viral pathogens. However, only one class of agent has been licensed against viroporins since the 1960s, linked to the widely perceived failures of these drugs in terms of potency, specificity and low barriers to resistance.

The recent emergence of Zika Virus (ZIKV) across South America highlighted the lack of antiviral medications available to combat rapidly emerging epidemics caused by mosquito-borne *Flaviviruses*, which include dengue, Yellow Fever, Japanese Encephalitis, and West Nile in addition to ZIKV itself. This New World ZIKV displayed greatly increased virulence compared to older African strains, involving increased rates of neurological complications as well as the shocking incidence of foetal microcephaly following infection during pregnancy. In light of this, antivirals capable of limiting disease severity, particularly those able to limit the spread of infection, would have provided tremendous benefit to patients.

Flavivirus particles comprise a major envelope (E) glycoprotein, as well as a small membrane protein (M), forming highly ordered dimeric structures within the membrane elucidated by Cryo-EM. However, upon entry into cells via clathrin-mediated endocytosis, endosomal acidification promotes rearrangement of E into trimeric fusion complexes, whereas the structure of M during this scenario remains unknown.

We have discovered that when uncoupled from E dimers, M is also able to rearrange its stoichiometry within membranes, forming a pH-sensitive channel complex that functions during virus entry. M channels display sensitivity to the prototypic viroporin inhibitor, rimantadine, which in turn prevents ZIKV entry in cell culture and protects against infection using an *in vivo* model. Lastly, using molecular dynamics based channel models, we describe how the repurposing of previously licensed generic small molecules can specifically target two binding sites upon M channel complexes, leading to improved potency versus ZIKV entry and supporting that future development should lead to effective ZIKV antivirals.

Results

M protein is a small (9 kDa) hydrophobic protein comprising three helical domains towards the C terminus, with helices two and three traversing the membrane. Peptides corresponding to the C-terminal region displayed dose-dependent channel activity using a liposome-based dye release assay. Activity was increased by acidic pH, consistent with predictions that channels play a role during endocytosis. Moreover, both native PAGE and electron microscopy visualised the formation of oligomeric M complexes within the membrane-mimetic detergent, DHPC. Excitingly, M channels displayed sensitivity to the prototypic viroporin blocker, rimantadine, which we have previously used to identify druggable binding sites for viroporins due to its promiscuous binding capacity.

Importantly, rimantadine inhibited ZIKV replication in culture in a dose-dependent fashion. Time-of-addition assays supported that rimantadine was active during virus entry, supporting a role for M channels during the uncoating of the ZIKV capsid protein from the infectious genomic RNA. This is reminiscent of both the influenza A virus M2 viroporin, against which rimantadine was licensed, as well as the p7 protein of hepatitis C virus. Critically, rimantadine displayed protective antiviral activity in an immunocompetent preclinical model of ZIKV infection, suppressing viral titre to near undetectable levels post infection.

Molecular dynamics simulations supported that M was able to rearrange from dimers into hexamers when its structure was free to rearrange, mimicking the release from E dimers. Channels formed a compact hexameric structure (Figure 1) stabilised by helix one, and with the lumen lined by helix three. Consistent with *in vitro* pH response assays, protonation of

ionisable His residues maintained the open states of channel complexes relative to neutral simulations.

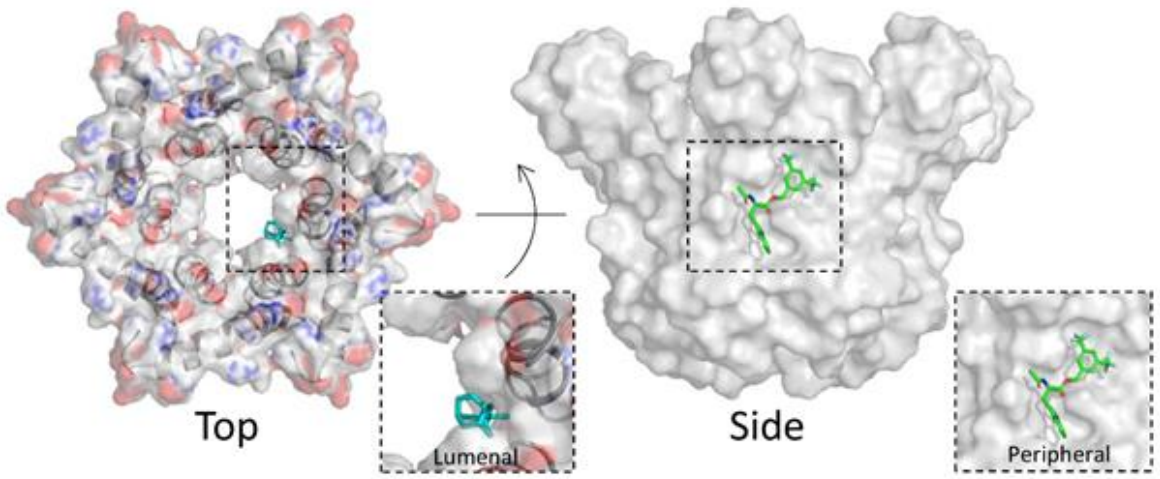

Figure 1: MD-derived models of the hexameric M protein complex showing the location of lumenal and peripheral compound binding sites used as templates for *in silico* high throughput screening.

Next, channel models were investigated for their suitability as potential templates for *in silico* drug screening, identifying two potential binding sites within the channel lumen and upon the membrane-exposed channel periphery. A chemical library comprising both generic and advanced trial compounds suited to drug repurposing was screened using eHITS versus the two binding sites. Short-listing of potential inhibitory compounds was determined by an attrition-based approach, intended to increase specificity to one or other site. Pleasingly, several compounds showed activity both *in vitro* as well as against ZIKV in culture, with top hits representing a ~1000-fold improvement upon rimantadine. Thus, we have established a firm platform upon which to base further structural, functional and medicinal chemistry development of M protein channel complexes, providing both insight into fundamental molecular and structural virology as well as an opportunity to develop novel therapeutics.

Funding
This work was funded by a studentship from the Leeds Institute of Medical Research

Collaborators
External: Alain Kohl (Glasgow CVR), Andres Merits (Tartu)

Developing high-speed atomic force microscopy (HS-AFM) to reveal dynamics of membrane proteins

George Heath

Introduction

Since the developments that have allowed a “revolution” in cryo-electron microscopy, solving membrane protein structures is becoming more and more common. While static structures provide vast amounts of information, they are often only half of a complex story concerning how a protein behaves in reality. How these structures change and react dynamically to, and with, their environment is now key to developing a full biological understanding. Therefore, focus must also turn to functional and mechanistic studies, specifically addressing conformational dynamics and state transitions. Recent advances in high-speed atomic force microscopy (HS-AFM) have made it possible to study the conformational dynamics of single unlabelled membrane proteins. Advancements in temporal resolution with the use of line scanning and height spectroscopy techniques show how HS-AFM can measure millisecond to microsecond dynamics, pushing this method beyond the spatial and temporal limits of other (less direct) techniques.

Results

Annexin-V has been shown, among other functions, to play an important role in membrane repair of eukaryotic cells. The influx of Ca^{2+} from the outside of the cell which occurs upon membrane lesion then leads to the rapid binding of Annexin-V-Ca^{2+} to the membrane and the self-assembly of Annexin-V into 2D-crystals, surrounding the membrane defect to prevent further pore expansion. Whilst binding and final assemblies have been well characterized, no techniques have been able to capture the full process to link between binding to the membrane, oligomerization and 2D self-assembly into a functional lattice structurally and quantitatively. Imaging the process with HS-AFM imaging mode we observe the appearance of 2-D crystals but the dynamics of individual proteins are simply too fast (as with many membrane proteins) to be resolved directly (Fig. 1a).

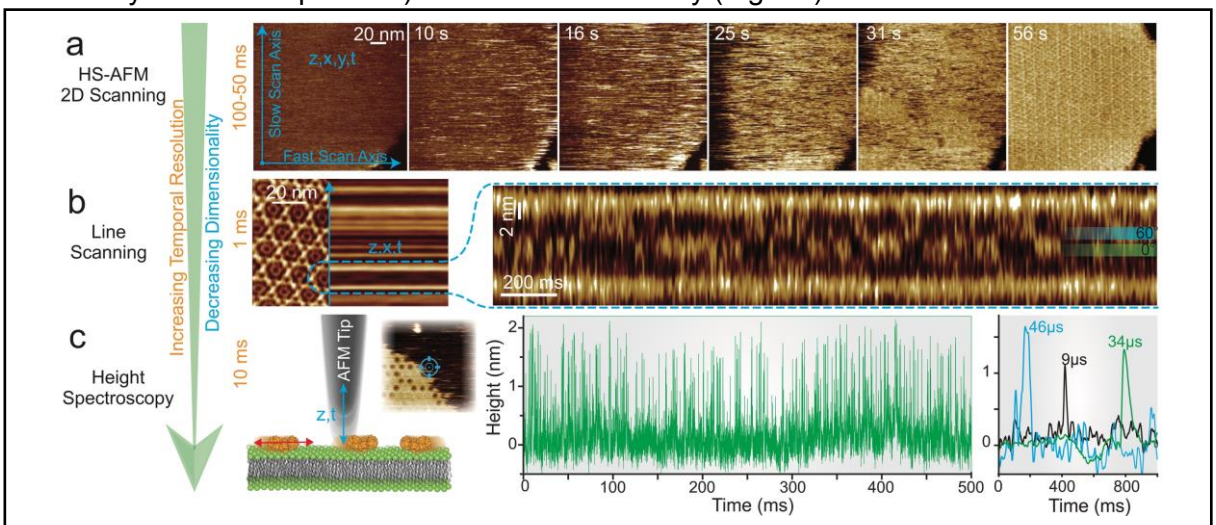

Figure 1: HS-AFM line scanning and HS-AFM height spectroscopy: increasing the temporal resolution by reducing the dimensionality of data acquisition. **(a)** HS-AFM 2D-scanning movie of A5 membrane-binding, self-assembly and formation of p6 2D-crystals upon UV-illumination-induced Ca^{2+}-release. Images can be captured at up to 10–20 frames per second. **(b)** Left: averaged HS-AFM image of an A5 p6-lattice overlaid with the subsequent line scanning kymograph, obtained by scanning repeatedly the central x-direction line as illustrated by the blue arrow with a maximum rate of 1ms per line. Right: line scanning kymograph across one protomer of the non-p6 trimer, outlined by the semicircular dashed line in the 2D image (left), at a rate of 417 lines per second (2.4ms/line). Overlaid on the kymography are the positions of the 0° and 60° states that the trimer alternately adopts. **(c)** Left: schematic showing the principle of HS-AFM height spectroscopy allowing 10 µs temporal resolution. The AFM tip is oscillated in z at a fixed x,y-position, detecting single molecule dynamics. Right: Height/time traces obtained by HS-AFM-HS allowing determination of the local A5 concentration and diffusion rates (the colored traces on the very right are a zoomed overlay of three traces displaying diffusion events under the tip in the low microsecond time range.

Therefore, to bypass current imaging speed limitations and gain orders of magnitude in temporal resolution one can reduce scanning to a single line (HS-AFM line scanning) or a single point (HS-AFM height spectroscopy), giving millisecond and microsecond temporal resolution, respectively, without losing z-accuracy. By halting the y-piezo, i.e., "HS-AFM line scanning", the movements of annexin trimers within a 2D-lattice were monitored at millisecond rates. The rotational displacement between two preferred orientations could be observed by the movement of the apex of the trimer which rotated in 60° intervals as it interacted with the surrounding six annexin trimers (Fig. 1b). Analysis of the line scanning kymographs showed the trimer spent an equal amount of time in each orientation with average dwell-times of 35ms consistent with symmetric interactions with the neighboring lattice. Additionally, the 2.4 ms time resolution allowed the rotational velocity in both clockwise and counterclockwise directions to be captured mid rotation. HS-AFM line scanning is currently being applied to measure fast conformational changes involved in transporters and ion channels.

Halting the x-piezo as well as the y-piezo allows a further 100-fold gain in time resolution while maintaining Ångstrom accuracy height data (z, t). With ~10 µs temporal resolution, this method termed "HS-AFM height spectroscopy" (HS-AFM-HS) was used in an approach inspired by fluorescence spectroscopy to measure the mobility of rapidly diffusing membrane-bound molecules as they diffused under the tip (Fig. 1c). As the size of the AFM tip is much smaller than the diffusing molecules of interest, not only could diffusion coefficients be measured but also the oligomeric state and surface concentrations of the molecules. Using HS-AFM-HS to measure mobile membrane-bound annexin trimers showed sharp peaks in the height signal as the trimers diffused under the AFM tip. Increasing the surface concentration of trimers by either increasing the calcium or annexin concentrations in solution resulted in more frequent and stepwise longer-lived dwell-times up until a complete lattice was formed. Analysis of the surface concentration-dependent dwell-times was consistent with two processes: oligomer formation and diffusion reduction due to crowding. This data gave access to biochemical and biophysical parameters including affinities and association/dissociation kinetics describing entirely and quantitatively the Annexin-V membrane-association process. Furthermore, height spectroscopy was used to also measure the movements of trimers free to rotate in the lattice, providing a direct comparison to line-scanning measurements and demonstrating the ability to use this technique to make microsecond measurements at specific positions on proteins. This demonstration indicates direct applicability of this technique for the analysis of fast membrane protein dynamics such as ligand binding and unbinding events in channels, transport cycles of mammalian transporters or ATPase-driven processes.

Publications

Heath, G.R. & Scheuring S. (2019) Advances in high-speed atomic force microscopy (HS-AFM) reveal dynamics of transmembrane channels and transporters. *Curr. Opin. Struct. Biol.* **57**: 93-102.

Collaborators

External: Simon Scheuring (*Weill Cornell Medicine, USA)*

Investigating novel redox partners for bacterial lytic polysaccharide monooxygenase activation

Jessie Branch, Badri S Rajagopal, Alan Berry and Glyn R Hemsworth

Introduction

Lytic Polysaccharide MonoOxygenases (LPMOs) are copper-dependant enzymes that require oxygen and an electron donor to catalyse the oxidative cleavage of glycosidic bonds in polysaccharides. These enzymes have been under intense study in recent years due to their potential application in improved enzymatic biomass processing. LPMOs active on cellulose work by introducing an oxygen atom at either the C1 or C4 position of cellulose thereby leading to breakage of the polysaccharide chain. LPMOs are known to be capable of turning over O_2 to H_2O_2 in the absence of the substrate cellulose (Figure 1A). Based on this and significant other data, LPMOs were thought to use molecular oxygen to perform the reaction on the cellulose substrate directly (Figure 1B). More recently however, studies have implicated hydrogen peroxide as a co-substrate to LPMOs (Figure 1C), with the reaction in the absence of cellulose implicated as generating H_2O_2 as the oxidative species in the original mechanism as well.

There is an ongoing debate in the field as to the true co-substrate for LPMOs which could have serious implications on the utilisation of these enzymes in the biomass processing industry. In either case, reactive oxygen species are utilised during the course of the reaction which can damage the LPMO, and potentially other enzymes present in industrial enzyme mixtures. A potential way to control the reaction is through the electron transfer mechanism to the LPMO which is necessary to reduce the active site copper, and hence activate the enzyme. Several enzymes from fungi, including cellobiose dehydrogenase (CDH), have been shown to activate LPMOs but there is no such equivalent enzyme identified to date in bacteria. We are, therefore, investigating a series of previously uncharacterised, putative, redox-capable proteins as potential LPMO activators which could find utility in bioprocessing.

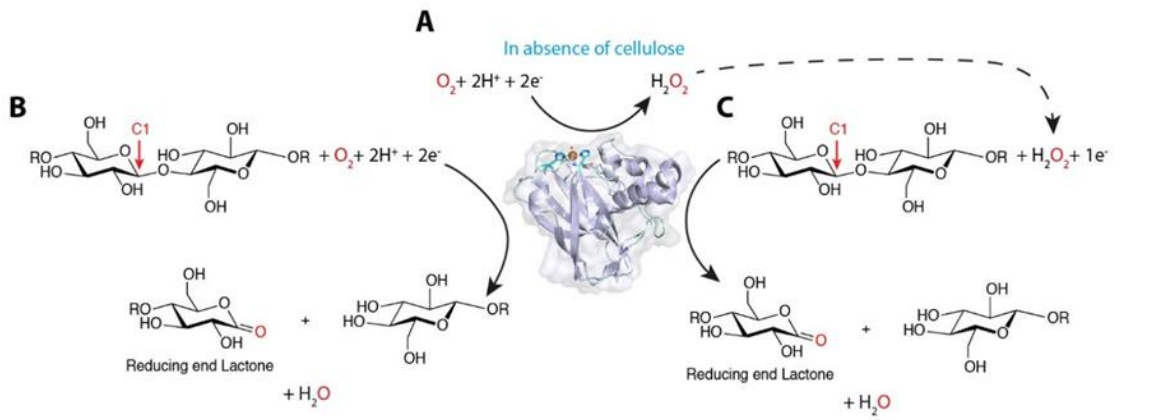

Figure 1: Reaction scheme for LPMOs. **(A)** In the absence of cellulose LPMOs turn over oxygen to generate hydrogen peroxide. **(B)** The traditionally accepted mechanism that LPMOs use electrons to activate molecular oxygen to introduce oxidative chain breaks into cellulose. **(C)** More recent proposals suggest that hydrogen peroxide acts as a co-substrate to facilitate LPMO action.

Results

Working with Prof Bernard Henrissat, founder of "CAZy" (a database of Carbohydrate-Active enZYmes, www.CAZy.org), we have identified a set of target proteins that contain X-domains, which have unknown functions but are often appended to Carbohydrate Binding Modules (CBMs) suggesting a role in polysaccharide processing. One such protein is Cbp2D from *Cellvibrio japonicus*. We have successfully expressed, purified, crystallised and determined the structure of a single domain (CjX183) from Cbp2D to 1.2Å resolution (Figure 2A). This structure reveals a *c*-type cytochrome in which an iron-containing haem molecule is covalently linked to the protein via thioether bonds. These types of domains are often

associated with an electron transfer function, further supporting the notion that Cbp2D could be an LPMO activator. Cytochromes have distinct UV-Vis spectra which allows easy monitoring of their redox state. Using this property, we have shown that CjX183 oxidises more rapidly as LPMO is added to the reduced *c*-type cytochrome in a concentration-dependent manner using the AA10 enzyme from *Cellulomonas fimi* (Figure 2B). This suggested that CjX183 was indeed donating electrons to the enzyme. We next used MALDI-ToF mass spectrometry to show that CjX183 was indeed capable of activating CfAA10 as oxidised cellulose oligosaccharide were detected when using CjX183 in place of a reducing agent in LPMO assays (Figure 2C and D). Interestingly, however, when using the Amplex red assay to detect H_2O_2 production in the absence of cellulose (Figure 2E), it appeared that when CjX183 was used instead of ascorbate significantly less H_2O_2 was produced. The ability of CfAA10 to boost cellulose breakdown by a GH7 exocellulase, however, was

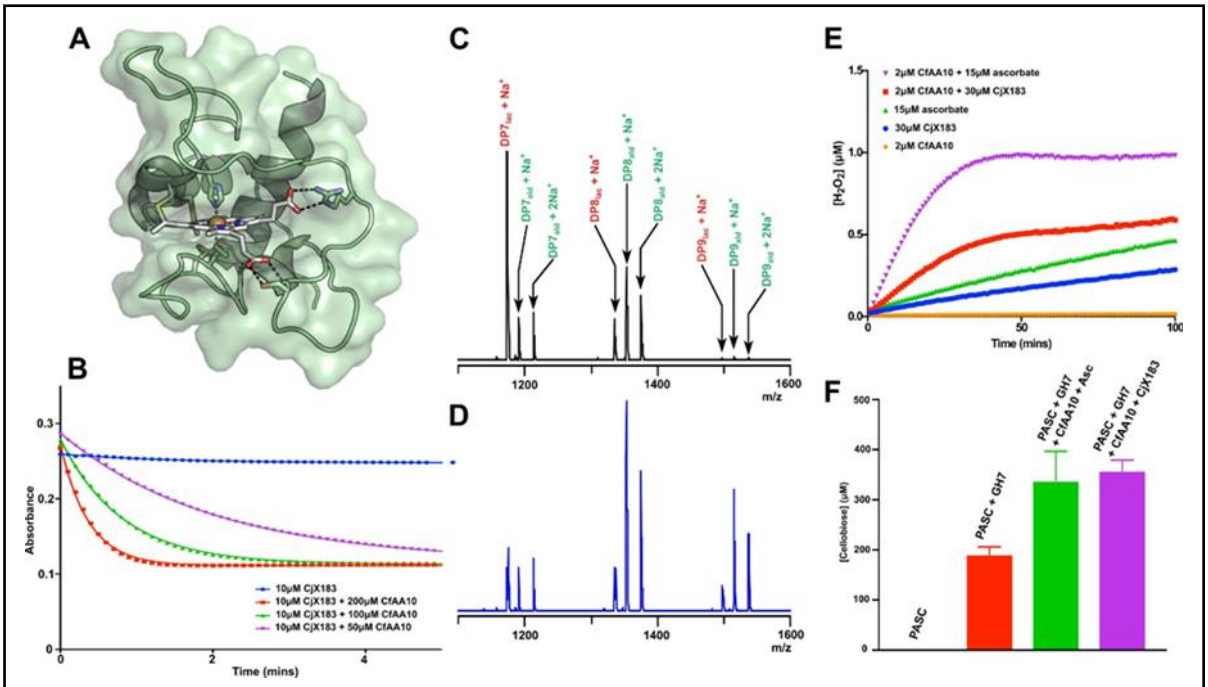

Figure 2: (A) The crystal structure of CjX183 shows a small α-helical protein with a covalently bound haem *c* molecule. **(B)** Decay of the 552nm peak corresponding to the reduced haem acts in a LPMO dependent manner. **(C)** MALDI-ToF data showing the production of oxidised cello-oligosaccharides from PASC using the CfLPMO and either ascorbate or **(D)** CjX183 as the electron source. **(E)** A coupled assay with Amplex Red reagent shows that CfAA10 produces less H_2O_2 when CjX183 is used as an electron source compared to ascorbate. **(F)** Boosting reactions shows that CfAA10 boosts cellulose degradation by a GH7 endocellulase equally with CjX183 or ascorbate.

uncompromised when using CjX183 in place of ascorbate (Figure 2F).
These results show that CjX183 is capable of activating a bacterial LPMO to drive oxidative cellulose cleavage in the same manner as small molecule electron donors. Use of CjX183 appears to generate less H_2O_2 when compared to reactions with ascorbate, despite this CjX183 and ascorbate appear to give equal boosting on cellulose breakdown by a processive exocellulase. These results suggest that use of a specific protein partner could be just as effective in enzyme cocktails whilst limiting the damaging effects of H_2O_2 on enzyme cocktails.

Funding
This work is funded by the BBSRC and the University of Leeds.

Collaborators
External: Prof Bernard Henrissat (AIX Marseille Université), Prof Paul Walton and Dr Alison Parkin (University of York)

Short chain diamines are the natural substrates of a PACE family multidrug efflux pump

Jacob Edgerton, Karl A. Hassan, Maria Nikolova, Leila Fahmy, Scott M. Jackson, David Sharples, Adrian Goldman and Peter J.F. Henderson

Introduction

Multidrug efflux pumps are highly promiscuous determinants of antimicrobial resistance in bacterial pathogens. Since efflux pumps evolved long before the widespread use of antimicrobials, drug transport is likely to be a side reaction in many efflux pumps, fortuitously beneficial to bacteria in hospitals. The AceI efflux protein from *Acinetobacter baumannii* is the prototype for the Proteobacterial Antimicrobial Compound Efflux (PACE) family of efflux pumps. AceI was only known to transport the synthetic biocide chlorhexidine, which was incongruous with its ancient origin. Here we demonstrate that the short chain diamines, cadaverine and spermidine, are the physiological substrates of AceI, and that transport is energised by an electrochemical gradient of protons.

Results

Both the wild-type AceI protein and an inactive AceI-E15Q mutant protein were purified and reconstituted into preformed liposomes composed of *E. coli* polar lipids. For comparison, empty liposomes were also generated using the same approach. An experimental system was established to generate an electrochemical gradient across the (proteo)liposome membranes, consisting of both a chemical proton gradient (ΔpH; inside acidic) and an electrical potential ($\Delta\Psi$; inside positive). The lumen of the proteoliposomes and empty liposomes contained Na^+ at pH 7.0. The (proteo)liposomes were diluted into a buffer containing isosmolar K^+ and a low concentration of the potassium ionophore valinomycin at pH 8.0 [publication]. The polarity of the pH and charge differential (inside positive and acidic) across the membrane could energise the uptake of externally applied substrates in exchange for a cation, such as a proton, by any active antiport system, in this case AceI.

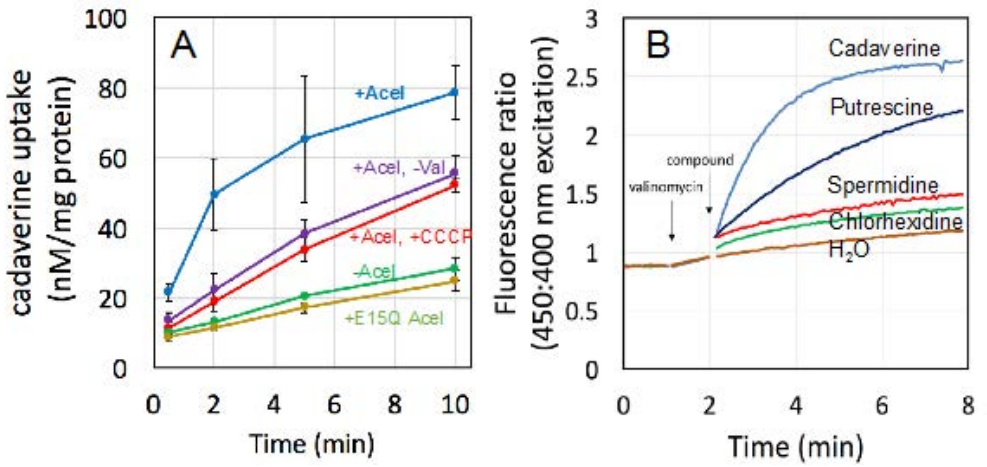

Figure 1: Cadaverine uptake (A) and pH changes (B) occurring in the lumen of AceI proteoliposomes upon addition of various polyamines. AceI proteoliposomes were formed in buffer containing Na^+ at pH 7.0, then diluted into buffer containing an isosmolar concentration of K^+ at pH 7. Valinomycin, 0.5 nM, was added, followed by 100 mM polyamine or water.

The proteoliposomes containing wild-type AceI and energised by an electrical and pH gradient positive and acidic inside rapidly accumulated [^{14}C]-cadaverine (Figure 1A). The initial rate of cadaverine uptake between the first and second assay time points (30 and 120 sec) was 17.0±5.9 nmol/mg protein/min compared to 0.04 ±0.70 nmol/mg protein into proteoliposomes containing the inactive AceI-E15Q mutant, was much slower and more linear across the course of the assay, indistinguishable from the rate into liposomes without any incorporated protein. AceI proteoliposomes treated with the protonophore CCCP, or without valinomycin, and so having ΔpH (inside acidic) but no $\Delta\Psi$, accumulated [^{14}C]-

cadaverine at an intermediate rate (Figure 1A). To determine whether the cation exchanged for cadaverine was a proton, we used a membrane-impermeable pH-sensitive fluorescent dye, 8-hydroxypyrene-1,3,6-trisulfonic acid (pyranine), to examine pH changes inside the lumen of AceI proteoliposomes during transport of diamine. Addition of 1 mM cadaverine to the energised AceI proteoliposomes resulted in alkalisation of the proteoliposome lumen, observed through a rapid increase in the 450:400 nm excitation fluorescence ratio of pyranine (Figure 1B). In contrast, there was no significant change in the internal pH in empty liposomes or proteoliposomes containing AceI-E15Q after cadaverine addition (Figure 1B). Taken all together, these results showed that AceI catalyses the exchange of protons for cadaverine.

Consistent with these observations on purified AceI, we demonstrated that expression of the *aceI* gene in the native host, *A. baumannii*, or after its cloning into *E. coli*, prevented accumulation of cadaverine into energised cells (Figure 2 and [publication]).

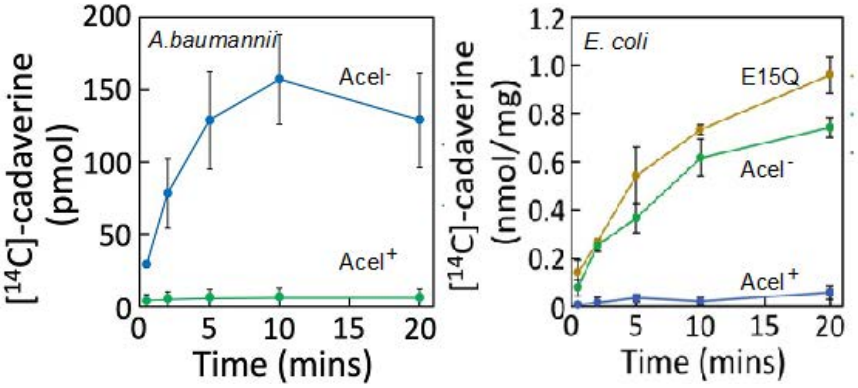

Figure 2: Uptake of [^{14}C]-cadaverine into *A. baumannii* or *E. coli* are prevented by activity of the *aceI* gene. Suspensions of each organism with the indicated phenotype were incubated with [^{14}C]-cadaverine and samples taken at intervals for determination of the content of radioactivity. Details are given in our publication.

In this study, we made several major advances in understanding the function of the prototypical PACE family multidrug efflux protein, AceI from *A. baumannii*. First, transport of cadaverine effected by the AceI protein reconstituted into liposomes was energised by the trans-membrane electrical gradient of protons. Secondly, cadaverine and putrescine are the natural substrates of AceI, whereas the longer polyamine, spermidine, is only a weak substrate. Thirdly, they show that resistance to multidrugs can be a fortuitous byproduct of the natural function of a transport system in driving natural toxins out of bacterial cells. These observations are important because diamines play vital roles in bacterial physiology and virulence and have significant commercial uses [publication]. Future work is directed towards determining the three-dimensional structure of AceI and of related PACE efflux proteins.

Publications

Hassan, K.A., Naidu, V., Liu, Q., Edgerton, J., Fahmy, L., Li, L., Mettrick, K.A., Jackson, S.M., Ahmad, I., Sharples, D., Henderson, P.J.F. & Paulsen, I.T. (2019) Short chain diamines are the physiological substrates of PACE family efflux pumps. *Proc. Natl. Acad. Sci. USA* **116**: 18015-18020.

Funding

EU Marie Curie Slodowska, Australian NHMRC, Lucite International, White Rose, BMS.

Collaborators

External: Ian Paulsen, Robert Poole, Mike Williamson, David Kelly, Graham Eastham, David Johnson, Mark Reynolds, Jonathan Runnacles.

The stability and infectivity of the norovirus virion is controlled by capsid protruding domains

Joseph Snowden, Daniel Hurdiss, Oluwapelumi Adeyemi, Neil Ranson, Nicola Stonehouse and Morgan Herod

Introduction

Norovirus infections are a leading cause of gastroenteritis in people of all ages worldwide. They impose a major economic burden, costing the global economy over $40-billion, and importantly over 200,000 lives, per annum. Disease outbreaks are typically associated with semi-enclosed communities, particularly healthcare facilities where they can result in closures and restrictions and the loss of thousands of bed days. There is no vaccine or therapy to prevent or treat norovirus gastroenteritis and control spread of the disease. A possible vaccination approach would be the use of virus-like particles (VLPs), i.e., viral capsids which lack the RNA genome and are therefore non-infectious. The norovirus capsid is composed of 180 copies of the major viral structural protein, VP1, and a small amount of minor structural protein, VP2. Each copy of VP1 is subdivided into two distinct domains: the S domain which forms the rigid base of the viral capsid and a P domain which projects radially into 80 “spikes” from the surface. The capsid is composed of two types of VP1 dimer: AB types which surround the 5-fold axis of symmetry and CC-types at the 2-fold axis. During the virus life-cycle this viral capsid is not only required to protect the viral genome from degradation but also deliver this into target cells to initiate infection. This is hypothesised to be through capsid conformational intermediates that coordinate virion disassembly upon specific cellular triggers. The conformational changes that the norovirus capsid is able to naturally undergo is undescribed. Using the murine norovirus (MNV) model system, we have investigated the alternative morphologies of the norovirus capsids.

Results

Firstly, we used cryo-electron microscopy to elucidate the high resolution “apo” structure of an infectious norovirus at 3.1 Å. Comparison to a recently published cryo-EM reconstruction

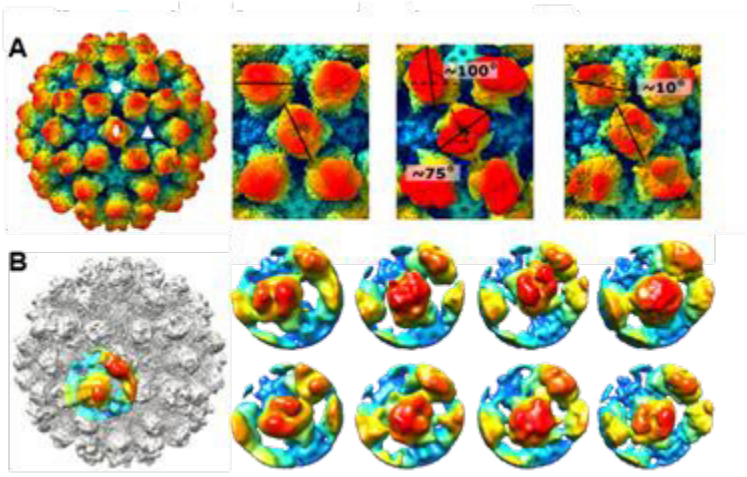

Figure 1: (A) Left: The 3.1 Å wtMNV density map with radial colouring and a five-fold ( ), three-fold (△) and two-fold ( ) icosahedral axes indicated. Right: Enlarged views centred on the icosahedral two-fold axes of our apo wtMNV reconstruction, a reconstruction of apo wtMNV and wtMNV complexes with GCDCA from Sherman et al. (2019). The angle of rotation for AB- or CC-type P domain dimers is shown. (B) Left: Our wtMNV map with mark for focussed classification highlighted. Right: Examples of different focussed 3D classes of AB-type dimers positioning.

of apo wildtype (wt) MNV revealed striking differences in the position and orientates P-domains relative to the S domains. In our reconstructions the P domains have undergone a large rotation and are compacted much closer to the S domains by ~10 Å (Figure 1A). Furthermore, we used focussed 3D classification of P domain dimers separately to investigate the mobility of these domains in isolation. The approach revealed a striking diversity in the orientation and location of AB-type P domain dimers (Figure 1B) but much

less variation in CC dimer positioning, suggesting that P domain dimers are highly mobile elements on the capsid surface. Given the dynamic nature of the virion, we next aimed to capture *in vitro* defined conformations of the norovirus virion that reflect the conformational changes capsids undergo during the viral life-cycle. Thermal stressing is an established approach to inducing alternative conformations of viral capsids that are informative of those that occur naturally. We applied this approach to study norovirus structural changes in combination with cryo-electron microscopy. Our novel reconstructions of heat-inactivated MNV demonstrated that there were no gross morphological differences in the positioning of the P domains with respect to the S domains. Furthermore, while the strength of the S domain density was not reduced upon heating, the P domain density was significantly weakened, suggesting greater P domain mobility. To further investigate the effect of heat treatment on the P domains, we performed focussed classification on heat inactivated MNV (hiMNV) CC-type P domain dimers. Interestingly, all of the classes showed the central CC-type dimer making contacts with adjacent AB-type dimers (Figure 2).

This is in comparison to infectious virus, where CC-type dimers populated a class with no interactions between CC- and AB-type dimers, which we termed a 'non-contacting' class. This suggested that heat treatment had increased P domain mobility, changing the conformational landscape explored by the P domains, resulting in a loss of infectivity. To investigate this suggestion further, we used *in vitro* evolution to select viruses with improved thermostability. We hypothesised that such stabilised viruses would have mutation specifically affecting VP1 P domain conformational mobility. In line with this hypothesis,

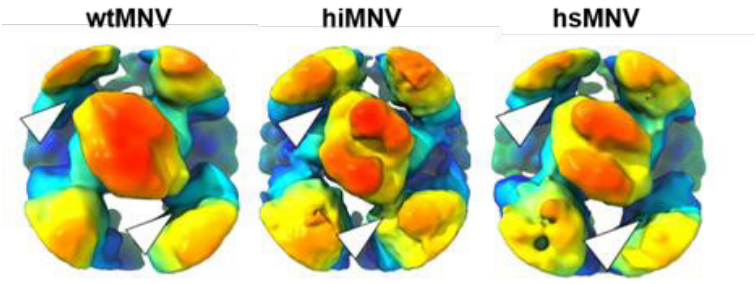

Figure 2: Example focussed classes of wtMNV, hiMNV and hsMNV CC-type P domain dimers, shown at 2 σ. The sites of contact between C-type and A-type P domains, used to determine 'non-contacting' status, are indicated by white arrowheads

stabilised MNV particles had a single mutation in the P domain of VP1. To understand the mechanism of stabilisation, we determined the structure of heat stable MNV (hsMNV). While CC-type P domain dimers appear virtually identical to infectious MNV, AB-type P domain dimers showed a subtle difference in their orientation. In the wtMNV map a potential interface is formed between A-type and C-type P domains, but for stabilised virus, the potential for this interface has been disrupted (Figure 2). Specifically, the AB-type P domain dimer has tilted upwards and rotated in an anti-clockwise direction angling away from the S domains and adjacent C-type P domain. When taken together our data suggests that the conformational landscape explored by the P domain dimers of the mutant virion has changed, allowing it to retain a balance between P domain mobility and flexibility at elevated temperatures. Our structural investigation on norovirus has described the dynamic nature of the norovirus virion. We showed that the infectious virion is a macromolecular complex with highly flexible P domains that are capable of sampling a range of conformational space, whilst maintaining functionality, and suggest the presence of large synchronous P domain movements.

Publications

Shawli G.T., Adeyemi O.O., Stonehouse N.J. & Herod M.R. (2019) The Oxysterol 25-Hydroxycholesterol Inhibits Replication of Murine Norovirus, *Viruses*. **11**: 97. *doi: 10.3390/v11020097*

Funding

This work was funded by the MRC and the Wellcome Trust

Cellular responses to amyloid fibrils and their assembly intermediates

Matthew Jackson, Chalmers Chau, Sheena Radford and Eric Hewitt

Introduction

The formation of insoluble amyloid fibrils is associated with a spectrum of human disorders: the amyloidoses. These disorders include Alzheimer's, Parkinson's, type 2 diabetes and dialysis-related amyloidosis (DRA). In each of these disorders the formation of amyloid fibrils is associated with cellular dysfunction and tissue destruction. Yet, despite decades of research the culprit species and mechanisms of amyloid toxicity remain poorly understood. Our goal is to determine how the structure and physical properties of amyloid fibrils and their assembly intermediates cellular function. This involves a multidisciplinary approach in which information obtained by NMR, atomic force microscopy, electron microscopy, photo-crosslinking, mass spectrometry and fluorescence based spectroscopic techniques is integrated with analyses of cellular function and viability.

Results

Many studies suggest that the principal culprits of toxicity are not amyloid fibrils, but the oligomers formed during amyloid assembly reactions. In recent work we have shown that a hexameric on-pathway assembly intermediate of β_2-microglobulin amyloid fibril assembly is non-toxic. This highlights that not all amyloid oligomers are toxic and that on-pathway intermediates may have very different biological properties compared to off-pathway oligomers.

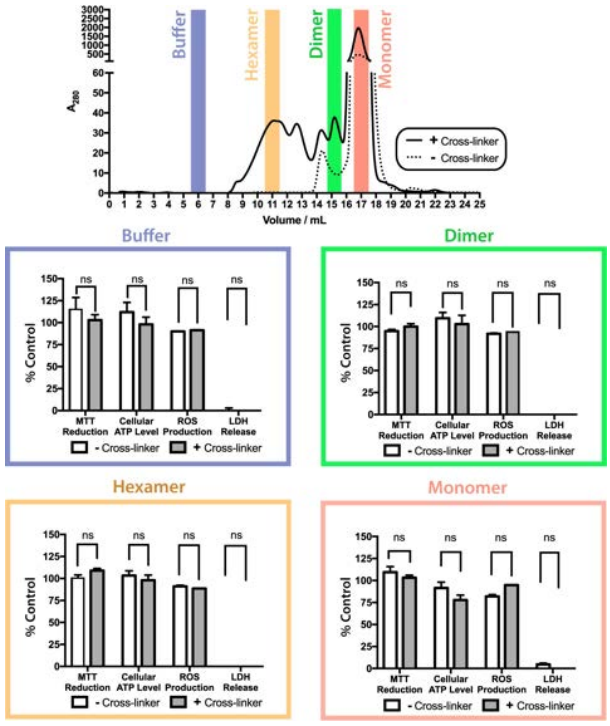

Figure 1: β_2-microglobulin ΔN6 oligomers are non-toxic.
Toxicity of cross-linked (solid line/gray bars) or uncross-linked (dotted line/white bars) ΔN6 species following purification by analytical SEC. Cell toxicity was assessed using MTT reduction, cellular ATP level, generation of reactive oxygen species (ROS), and LDH release assays. For assays of MTT reduction, ATP levels and ROS production, the data are normalized to PBS (100%) and NaN_3-treated controls (0%). LDH release is normalized to detergent lysed cells (100%) and PBS buffer treated controls (0%). The error bars represent mean S.E, * p 0.05.

Ongoing work is exploring how α-synuclein oligomers and amyloid fibrils cause cellular dysfunction in Parkinson's disease, studying this using a combination of approaches. We are

using pulldown proteomics to identify cellular proteins that bind to α-synuclein amyloid fibrils. Moreover, in collaboration with colleagues in Chemistry we are using photo-activatable cross-linkers to improve the detection of cellular proteins that interact with α-synuclein amyloid fibrils. In other work, we are collaborating with colleagues in Electrical and Electronic Engineering to study the cellular effects of α-synuclein oligomers in cells. Specifically, we are developing a nanopore sensing platform to perform quantitative delivery of α-synuclein oligomers into cells for functional analysis.

Publications

Karamanos, T.K., Jackson, M.P., Calabrese, A.N., Goodchild, S.C., Cawood, E.E., Thompson, G.S., Kalverda, A.P., Hewitt, E.W., & Radford, S.E. (2019) Structural mapping of oligomeric intermediates in an amyloid assembly pathway. *eLife*. **8**: e46574.

Walko M, Hewitt E, Radford SE and Wilson AJ (2019) Design and synthesis of cysteine-specific labels for photo-crosslinking studies. *RSC Advances.* **9**: 7610-7614.

Funding

This work was funded by the Wellcome Trust, the European Research Council and the EPSRC

Collaborators

University of Leeds: Paolo Actis and Andrew Wilson

Modular enzyme-inhibitor switch sensor for rapid wash-free diagnostic assays

Hope Adamson, Modupe Ajayi, Emma Campbell, Christian Tiede, Anna Tang,
Thomas Adams, Michael McPherson, Darren Tomlinson and Lars Jeuken

Introduction

A general assay platform for rapid detection of diverse analytes is needed to underpin development of new point-of-care and in-field diagnostics. Such tests are vital to accelerate and improve decision making relative to laboratory assays, across broad sectors including medicine, environmental monitoring and agricultural management. The enzyme-linked immunosorbent assay (ELISA) has long been the gold standard of immunoassays, as it is a highly sensitive and modular format. However, the use of separate molecular recognition "capture" reagents (e.g., antibodies) and signal generating "detection" reagents (e.g., antibody-enzyme conjugates), necessitates the use of multiple time-consuming immobilisation and wash steps, precluding use for point-of-care diagnostics. Engineered solutions include lateral flow and microfluidic systems with automated steps, but these are often semi-quantitative and can lack sensitivity. To overcome these limitations, the "capture" and "detection" elements can be combined at the molecular level to create an "active" enzyme-switch sensor, which directly transduces target binding into a signal.

Results

An enzyme-switch sensor was constructed by designing a target-driven disruption of a linked enzyme-inhibitor complex (Figure 1). Two recognition elements (Affimer A and B) are incorporated such that target binding by both leads to conformational disruption of the enzyme-inhibitor interaction and "switches on" the enzyme. The enzyme-inhibitor complex used was a β-lactamase (BLA) and a β-lactamase inhibitor protein (BLIP). For the recognition elements, Affimer affinity reagents were used, which are a class of non-immunoglobulin binding protein, based on a cystatin scaffold with two variable target binding regions.

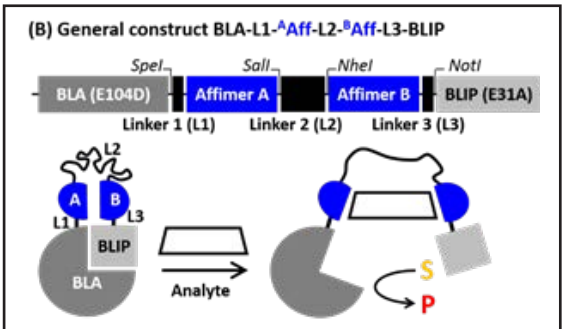

Figure 1: Construct design of enzyme switch. BLA = β-lactamase; Affimer A and B are recognition elements against the target; BLIP = β-lactamase inhibitor protein.

The applicability of our engineered enzyme-switch sensor is illustrated by detection of different targets, in three application areas including those of unmet need for rapid diagnostics: a therapeutic antibody (Herceptin), pentameric protein biomarker (human C-reactive protein, hCRP) and icosahedral plant virus (cow pea mosaic virus, CPMV). These three analytes were successfully targeted with pico-molar (pM) sensitivity, providing assays for therapeutic drug monitoring, health diagnostics and plant pathogen detection, respectively. Applicability to rapid diagnostics is confirmed by a rapid (minutes), simple (wash-free) and sensitive (pM) quantification of analytes in biological samples, along with consistency with validated ELISA analysis, robust batch-to-batch reproducibility and stability at fridge and room temperatures.

Sensors for three target classes, a protein biomarker hCRP (Figure 2), a plant virus CPMV and a therapeutic antibody Herceptin, were generated by exchanging only the Affimer proteins in the basic enzyme-switch structure. This confirms the modularity for the sensor, which is essential for simple and timely development of sensors. Batch-to-batch reproducibility of reagents is important in ensuring consistent manufacture of point-of-care tests. Three separate batches of sensors were produced and purified; each had a very similar dose response to hCRP, in terms of both absolute response and fold activity gain, with C50 = 0.3 – 0.5 nM.

The stability of sensor construct was assessed by comparing samples stored for 28 days at ca. 4 °C and ca. 20 °C (room temperature) with those from freezer storage at -80 °C. Room temperature storage for 28 days reduced the absolute response of the sensor by ca. 11 % with 10 nM hCRP. Importantly, the dose response in terms of fold activity gain was very similar regardless of whether samples were freshly thawed, or stored at 4 °C or 20 °C, with C50 = 0.3 – 0.5 nM. This confirms the robustness of sensor constuct to long term storage, even at room temperature, which is important for simple storage and handling requirements of point-of-care tests.

In summary, the enzyme-inhibitor switch offers simplicity, speed, stability and batch-to-batch reproducibility, with potential advantages for clinical point-of-care testing and in-field diagnostics, exemplified by relevant assays for therapeutic dose monitoring, health diagnostics and plant-pathogen detection. Integration into a portable diagnostic device may require development of an amperometric assay exploiting the electrochemical activity of hydrolyzed nitrocefin, to avoid optical detection and aid miniaturisation, or identification of an improved enzyme system affording a calibration-free ratiometric response and reduced serum interference. Auto-inhibited protein switches are used in Nature for sensing and regulation, and it is hoped that the general principles learned here can aid their translation into essential tools for synthetic biology, molecular imaging and high-throughput screening, in addition to their molecular diagnostic applications.

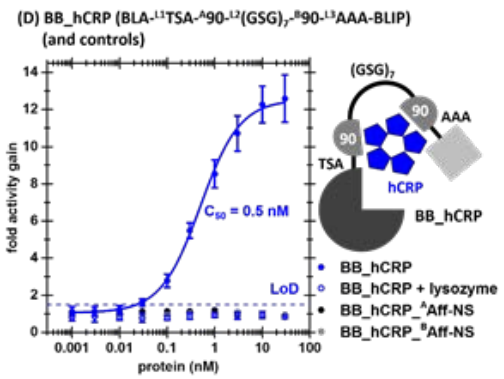

Figure 2: Dose response of optimised hCRP sensor and controls where Aff-hCRP90 at site A or B is replaced with a non-specific Affimer. 2 nM sensor incubated with hCRP (or lysozyme as a control, where indicated) for 10 min before 50 µM nitrocefin addition. Fold activity gain read after a further 5 min. Data are the mean of triplicates in six separate repeat experiments and error bars indicate standard deviation from the mean. The solid line is a 4PL regression fit and the dash line indicates the limit of detection (LoD).

Publications

Adamson, H., Ajayi, M.O. Campbell, E., Brachi, E., Tiede, C., Tang, A.A., Adams, T.L., Ford, R., Davidson, A., Johnson, M., McPherson, M.J., Tomlinson, D.C., Jeuken L.J.C. (2019) Affimer−Enzyme−Inhibitor Switch Sensor for Rapid Wash-free Assays of Multimeric Proteins, *ACS Sensors*, **4**: 3014-3022.

Funding

This work was funded by the Medical Research Council, MRC.

Collaborators

University of Leeds: Emma Hesketh, Neil Ranson and George Lomonossoff
External: Robert Ford (Avacta), Alex Davidson (Avacta), Matt Johnson (Avacta), Erika Brachi (Erasmus exchange student from the University of Torino, Italy)

Using molecular dynamics simulations to study the red blood cell anion exchanger 1

Dario De Vecchis and Antreas C. Kalli

Introduction

Anion exchanger 1 (AE1, Band 3, SLC4A1) is found in the red blood cell where it is responsible for the rapid exchange of bicarbonate and chloride across the red blood cell plasma membrane. Mutations found on AE1 have previously been shown to cause various diseases such as hereditary spherocytosis and Southeast Asian Ovalocytosis. Human AE1 consists of a N-terminal cytoplasmic domain (cdAE1) and a C-terminal membrane domain (mdAE1) that are connected by a poorly conserved linker region (Figure 1). The mdAE1 consists of 14 transmembrane (TM) helices, whilst cdAE1 functions primarily as an anchoring site for cytoskeletal proteins such as ankyrin and spectrin. Whilst crystal structures of the individual cdAE1 and mdAE1 domains have been obtained, a structure of the intact AE1 is not available. The long linker region that connects the two domains makes it very challenging to identify the relative orientation of the cdAE1 with respect to the mdAE1 using lab-based structural methodologies. Obtaining structural data about the intact AE1 would be a major step in understanding its function and interactions with partner proteins.

Recently, a cryo-electron microscopy (EM) reconstruction using the bovine homologue of AE1 suggested two possible orientations for the cdAE1: twisted and parallel. In contrast, a recent modeling approach supported by cross-linking experiments, proposed a more compact structure with the double-humped shape of cdAE1 facing the mdAE1. In this model, the linker region appears to be not symmetrical. Therefore, the two aforementioned studies suggest very different orientations of the cdAE1 relative to the mdAE1. In the light of these discrepancies, molecular dynamics simulations and modeling can be used to obtain structural/molecular data of the intact AE1. Constructing a complete model of the intact AE1 is critical as it will enable us to understand the complexities of its transport mechanism, the formation of AE1 tetramers and its interactions with partner proteins such as ankyrin, which

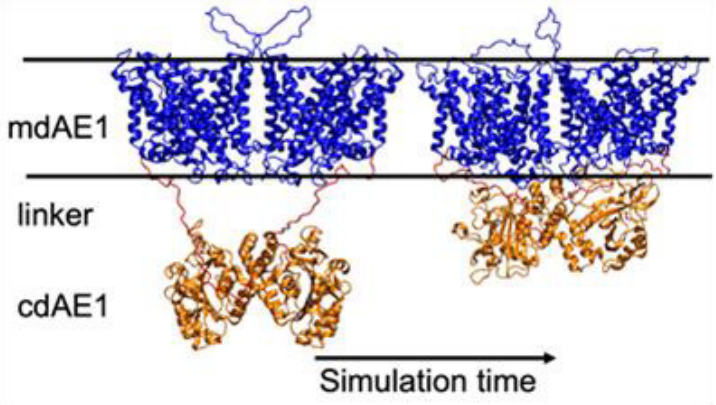

Figure 1: Structure of the AE1 model at the beginning and at the end of one of our simulations. The membrane domain of AE1 (mdAE1) is shown in blue, the linker region is shown in red, and the cytoplasmic domain of AE1 (cdAE1) is shown in orange. The black lines indicate the boundaries of the cell membrane.

binds to the tetrameric form.

In this study, we examined the interactions and dynamics of the cdAE1 and mdAE1 domains, proposing a near full-length model of the red cell anion exchanger AE1 in the outward-facing conformation. The N- and C-terminal regions of AE1 that are predicted to be disordered are omitted from the models. Our results demonstrate the critical role of the linker region and propose possible orientations of the cytoplasmic domain of AE1 with respect to the TM domain. Additionally, the models of the intact AE1 were simulated in a native-like model red blood cell plasma membrane. Our results show that the intact AE1 interacts preferentially with anionic phospholipids present in the inner leaflet and that cholesterol is

likely to stabilize the AE1 dimer interface. Residues that are involved in the interaction between the cdAE1 domain, the mdAE1 domain and the linker region were also identified.

Results

Firstly, we created a model of the intact AE1 using the available structures of the cdAE1 and the mdAE1. As mentioned above, the mdAE1 and the cdAE1 are connected with a long flexible linker (33 residues). The length of the linker allowed us to position the cdAE1 relative to the mdAE1 in four different orientations: the cdAE1 C-terminal dimerization arms (residues 314–347) facing the mdAE1, or facing the cytoplasm, (*rev-V* and *V* conformation, respectively), and in a *parallel* or a *twisted* orientation as suggested by a previous EM study in both the *rev-V* and *V* orientations. To determine whether there was a unique orientation of the cdAE1 and the mdAE1 we run coarse-grained molecular dynamics (CG-MD) simulations with all four AE1 models inserted in a model membrane consisting of a complex lipid mixture. Despite the differences in the initial orientation of the cdAE1 relative to the mdAE1, in all cases the cdAE1 forms a complex with the cytoplasmic side of the mdAE1 domain (Figure 1). Cluster analysis confirms that the structures increased their compactness with respect to the initial coordinates.

In order to identify which of our above models most likely represents the native cdAE1/mdAE1 complex, we have compared our models with available structural and biophysical data. In particular, residues that were previously suggested to interact with the cytoskeleton protein Ankyrin are only exposed to the cytoplasm in the *rev-V* conformers in our models. Additionally, residues 258–311 suggested as the possible site of interaction between AE1 and cardiac α-actin, are located in close proximity to the V-shape groove formed by the dimeric cdAE1. This groove in our models faces the cytoplasmic side in the *rev-V* conformers. Furthermore, Lys56, which is involved in the Memphis variant, is located at the interface between the cdAE1 and mdAE1 only in the *rev-V* conformers. Overall, our comparisons above suggest that the *rev-V* conformation is the most consistent with available biochemical and functional data, but because of the length of the linger region the *V* conformation may also be possible.

The complex bilayer in our simulations allowed us to also examine the interactions of AE1 with different lipids in the bilayer. Our simulations revealed that the cavity of the mdAE1 dimer interface is filled in with cholesterol, suggesting a possible role of cholesterol in AE1 stability and function. Interestingly, during the simulations the cavity between AE1 monomers is also occupied by other lipids (SM or POPC). Despite their relatively low concentration, PIP_2 molecules were also found to interact strongly with AE1 in our simulations, forming an anionic annulus around AE1. These data suggest that AE1 creates a unique footprint in the membrane by modifying its local lipid environment.

In summary, this study proposes possible models for the near full-length AE1. Our simulations suggest that when the cdAE1 is in complex with mdAE1 the V-shaped groove of cdAE1 is more likely to face the cytoplasm. However, this does not exclude a dynamic interaction that may change the orientation of cdAE1 relative to the mdAE1. Our results also show that some residues that are linked to diseases interact strongly with lipids suggesting that these mutations may change such interactions.

Publications

De Vecchis, D., Reithmeier, R. A. F. & Kalli, A. C. (2019) Molecular simulations of intact Anion Exchanger 1 reveal specific domain and lipid interactions. *Biophys. J.* **117**: 1364–1379.

Funding

This work was funded by the Academy of Medical Sciences and the Wellcome Trust.

Collaborators

External: Prof. Reinhart Reithmeier

Non-parametric determination of dominant eigenmodes of molecular dynamics

Sergei Krivov

Introduction

Recent advances in simulation and experiment have led to dramatic increases in the quantity and complexity of produced data, which makes the development of automated analysis tools very important. A powerful approach to analyze dynamics contained in such datasets is to describe or approximate it by diffusion on a free energy landscape, i.e., free energy as a function of reaction coordinates (RC). For the description to be quantitatively accurate RCs should be chosen in an optimal way. Committor functions represent one possible choice of such a coordinate. Another possibility are the dominant eigenvectors/eigenmodes of the transfer operator of the molecular dynamics. One advantage over the committor functions is that one does not need to provide the boundary states, whose accurate specification for complex systems, e.g., the protein folding, might be rather difficult. Another advantage is that a few dominant eigenmodes can be used as reaction coordinates, making the determination of multidimensional free energy landscapes possible. Determining such eigenmodes for practical systems is a very difficult unsolved problem.

Results

We have found a solution to this problem. We developed an adaptive nonparametric approach to accurately determine the dominant eigenvectors for an equilibrium trajectory of a realistic system. In contrast to alternative approaches, which require a functional form with many parameters to approximate eigenvectors and thus an extensive expertise with the system, the suggested approach is nonparametric and can approximate such eigenvectors with high accuracy without system specific information and minimal input from the user. To avoid overfitting for a realistically sampled system, the approach performs optimization in an adaptive manner. The power of the approach was illustrated on a paradigmatic system - a long equilibrium atomistic folding simulation of HP35 protein. We have determined the two slowest/dominant eigenvectors, which was confirmed by passing a stringent eigenvector validation test.

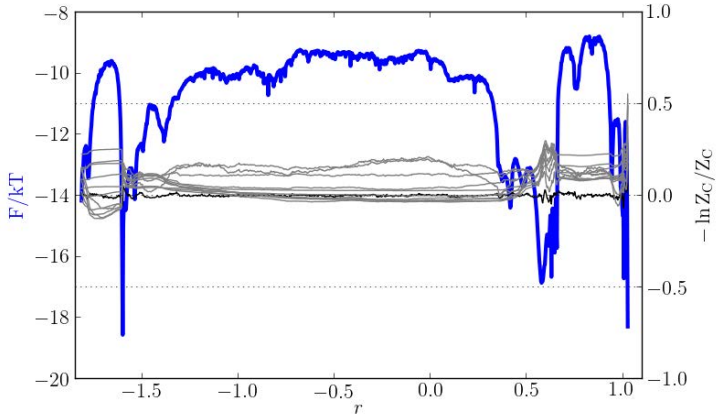

Figure 1: Blue line shows the free energy landscape of HP35 Nle/Nle mutant protein as a function of the first eigenvector. The eigenvector validation test shows that the determined coordinate is very close to an eigenvector: black lines show that $-\ln(Z_{C,1}/Z_0)$ profiles, are all close to 0 (up to a statistical error).

Receptor tyrosine kinase signalling in the absence of growth factor stimulation: response to cellular stress

Eleanor Cawthorne, Christopher Jones, Sabine Knapp, Chi-Chuan Lin, Dovile Milonaityte, Arndt Rohwedder, Caroline Seiler, Kin Man Suen and John Ladbury

Introduction

Receptor tyrosine kinases (RTKs) expressed on the plasma membrane of cells in normal tissue are rarely exposed to high concentrations of extracellular growth factors. Nonetheless, they express proteins associated with kinase-mediated signalling. We are interested in the signalling associated with these protein that occurs under basal conditions (which are close to the conditions experienced by normal tissue. In the absence of extracellular stimulation or genetic mutation, an oncogenic response can be driven by the competitive binding of SH3 domain-containing downstream effector proteins to proline-rich sequences on growth factor receptors. Of the approximately 50 plasma membrane receptor tyrosine kinases (RTKs) the majority have proline-rich sequences in their C-termini. These have a propensity to bind to the >300 proteins expressed in human cells which contain SH3 domains. These interactions occur in the absence of any extracellular stimulation (e.g. growth factors, cytokines). Proline-rich sequence binding to SH3 domains are promiscuous and the observed interactions with RTKs are dependent on the relative concentrations of the proteins involved.

We previously established that under non-stimulatory conditions the fibroblast growth factor receptor 2 (FGFR2) recruits the adaptor protein, growth factor receptor binding protein 2 (Grb2) through its C-terminal SH3 domain. In cells depleted of Grb2 other proteins can access the proline-rich motif on FGFR2. One of these proteins, phospholipase C(gamma)1 (Plcγ1) is activated on binding and through turnover of plasma membrane phospholipids to produce second messengers, raises cellular calcium levels which are responsible for increased cell motility and invasive behaviour. In ovarian and lung adenocarcinoma patients with low levels of Grb2 and increased expression of Plcγ1 higher incidence of metastasis leads to greatly reduced survival outcomes.

The dependence of signalling described above on respective concentrations of RTKs and SH3 domain containing proteins mean that there is no on-off switch for this form of signalling, the outcomes are dictated solely by fluctuations of protein concentrations. As a result, one key driver for this form of signalling is cellular stress. We are working to establish how stresses experienced by tissue (e.g. pH change associated with acid reflux in the oesophagus) can lead to cancer outcomes.

Results

We have extended our studies in this area to explore other RTK-SH3 domain-containing protein interactions to establish whether the up-regulation of signal transduction through these interactions is a general phenomenon. This leads to the hypothesis that two tiers of intracellular signalling can be derived from receptors with intrinsic protein kinase activity:
1) Ligand-induced elevation in kinase activity resulting in tyrosylphosphate-mediated effector protein recruitment and committal to a defined cellular outcome (e.g. proliferation).
2) Receptor phosphorylation-independent activation of downstream effectors through SH3 domain/proline-rich sequence interactions, which appear to be required for cell homeostasis/metabolic control.

Hyperactivity of the Tier 1 signalling is a feature of receptor tyrosine kinase-related cancers arising from genetic mutation. Although the tier 2 signalling mechanism occurs under basal conditions, and is thus likely to be associated with cellular maintenance, we have shown that fluctuations in expression levels of SH3-containing proteins can drive cells into pathological phenotypes including proliferation and metastasis.

We are testing this hypothesis with a range of methods extending from cell-based assays (including fluorescence lifetime imaging microscopy) through to structural and in vitro biophysical analysis.

We are optimising a screening protocol to establish the extent of Tier 2 signalling in a range of cells and conditions. We have identified novel interactions involving well studied proteins as well as less understood systems. These are being validated and the phenotypic outcomes of knocking down these interactions are being explored to establish the effects of signalling in normal tissue.

We have focused on gastro-intestinal (GI) cancers and have begun to explore the effects of stress on intracellular protein expression and the outcomes on Tier 2 signalling. We have shown that by mimicking conditions experienced in the GI tract we can affect expression of receptor tyrosine kinases.

In addition to identifying the signalling pathways which are initiated as a result of fluctuations in protein concentrations in cell-based assays, we are exploring the interactions associated with up-regulation of Tier 2 signalling using both biophysical and structural biological methods. High-resolution structural detail on the receptor-ligand interactions are providing invaluable detail on the mode of recruitment of signalling proteins as well as information towards potential inhibition of aberrant pathways that lead to pathogenic outcome.

Publications

Lin, C. –C., Suen, K. M., Stainthorp, A., Wieteska, L., Biggs, G. S., Leitão, A., Montanari, C. A., & Ladbury, J. E. (2019) Targeting the Shc-EGFR interaction with indomethacin inhibits MAP kinase pathway signalling. *Cancer Letters* **457**, 86-97.

Maori, E., Navarro, I. C., Boncristiani, H., Seilly, D. J., Rudolph, K. L. M., Sapetschnig, A., Lin, C. –C., Ladbury, J. E., Evans, J. D., Heeney, J. L. & Miska, E. A. (2019) A secreted RNA binding protein forms RNA-stabilizing granules in the honey bee royal jelly. *Molecular Cell* **74**, 598-608.

Fearnley, G. W. W., Odell, A.F., Abdul-Zani, I., Latham, A. M., Hollstein, M. C., Wheatcroft, S. B., Ladbury, J. E., & Ponnambalam, S. (2019) Tpl2 is required for VEGF-A-stimulated signal transduction and endothelial cell function. *Biology Open* **8**, bio034215.

Shahul Hameed, U. F., Liao, C., Radhakrishnan, A. K., Huser, F., Aljedani, S. S., Zhao, X., Momin, A. A., Melo, F. A., Guo, X., Brooks, C., Li, Y., Cui, X., Gao, X., Ladbury, J. E., Jaremko, L., Jaremko, M., Li, J., Arold, S. T. (2019) H-NS uses an autoinhibitory conformational switch for environment-controlled gene silencing. *Nucleic Acids Research* **47**, 2666-2680.

Funding

This work is funded by Cancer Research UK.

Collaborators

University of Leeds: Phillip Quirke, Susan Short, Alex Breeze, Darren Tomlinson
External: Prof. Zamal Ahmed, Mien-Chie Hung and Swathi Arur (University of Texas, MD Anderson Cancer Center, USA.), Mikhail Bogdanov (University of Texas, USA), Richard Grose (Barts Cancer Institute, London).

Understanding the mechanisms by which small DNA tumour viruses cause disease

Ethan Morgan, Gemma Swinscoe, Michelle Antoni, James Scarth, Molly Patterson, Corinna Brockhaus, Eleni-Anna Loundras, Yigen Li, Miao Wang, Diego Barba Moreno and Andrew Macdonald

Introduction

Small DNA tumour viruses are the causative agents of severe diseases in humans. Notable examples include cervical cancer, which is exclusively associated with infection with human papillomaviruses (HPV), and polyomavirus-associated nephropathy (PVAN) and Merkel cell carcinoma (MCC) caused by the BK and MCV polyomaviruses. We undertake a broad ranging analysis of these viruses to identify new targets for therapeutic intervention.

Infection with HPV causes ~6% of human cancers, including nearly all cervical carcinomas as well as head and neck squamous carcinomas (HNSCC). Despite FDA-approved prophylactic vaccines, the burden of HPV-associated malignancy will remain high for decades due to the limited availability of the vaccines in low income countries, poor coverage where access is possible, and the long latency period separating infection from carcinogenesis. Although HPV-specific antivirals are needed, their development is hindered by an incomplete understanding of the virus life cycle and essential interactions with host factors within the infected keratinocyte.

Results

Using an approach incorporating molecular and cellular biology with cutting edge cell culture and cancer models further informed by patient samples, we explore the roles of the HPV oncoproteins in the virus life cycle and in transformation. In particular, we demonstrated that the host transcription factor STAT3 is absolutely essential for the HPV18 life cycle in primary human keratinocytes. Ablation of STAT3 function using small molecule inhibitors, siRNA depletion or expression of dominant negative forms of STAT3 impaired HPV transcription and led to a loss of the characteristic proliferation observed in keratinocytes infected with HPV.

Using cytology samples from patients with cervical disease, we saw an increase in STAT3 activation that correlated with cervical disease progression. Further, we defined an oncogenic autocrine signalling loop in which HPV-coded oncoproteins drive the expression of the pro-inflammatory cytokine interleukin 6 (IL-6) to activate STAT3 (Figure 1). This circuit was active in cervical disease and ablation either by pharmacological intervention or siRNA mediated depletion of key components led to the death of HPV-transformed cells. Together, these studies show that STAT3 is an essential host factor for HPV, that STAT3 is deregulated in HPV cancers and as such is a target for anti-HPV therapeutics in cancer.

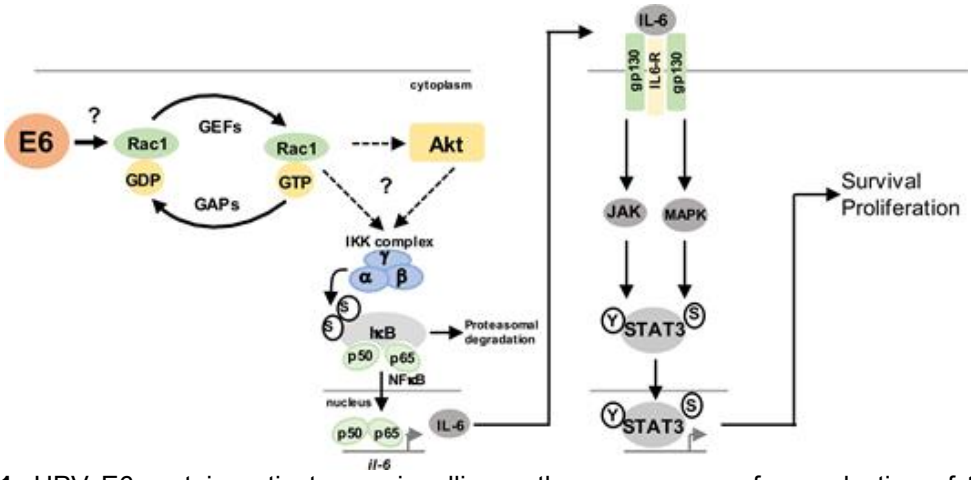

Figure 1: HPV E6 protein activates a signalling pathway necessary for production of the pro-inflammatory cytokine IL-6. Secreted IL-6 binds to the gp130-IL-6 receptor complex and drives signalling for phosphorylation and activation of STAT3 in an autocrine and paracrine manner.

Publications

Morgan, E.L., & Macdonald, A. (2019). Pharmacological targeting of JAK2 inhibits the tumourigenesis of HPV positive cervical cancer cells through inhibition of STAT3 and STAT5 activity. *Cancers.* **11**: E1934, *doi: 10.3390/cancers11121934*.

Moens, U. & Macdonald, A. (2019). Effect of the large and small t antigens of human polyomaviruses on signalling pathways. *International Journal of Molecular Sciences.* **20**: 3914, *doi: 10.3390/ijms20163914*.

Morgan, E.L. & Macdonald, A. (2019). Autocrine STAT3 activation in HPV positive cervical cancer through a virus-driven Rac1 - NFκB - IL-6 signalling axis. *PLoS Pathogens*. **15**: e1007835, *doi: 10.1371/journal.ppat.1007835*.

Chong, S., Antoni, M., Harber, M., Macdonald, A. & Magee, C. (2019). BK virus: Current understanding of pathogenicity and clinical disease in transplantation. *Rev. Med. Virol.* **8**: e2044, *doi: 10.1002/rmv.2044*

Funding

This work was funded by Wellcome Trust, the MRC, the BBSRC, Kidney Research UK and the Faculty of Biological Sciences, University of Leeds.

Collaborators

University of Leeds: Adrian Whitehouse, Neil Ranson, Richard Foster, Adel Samson and Stephen Griffin.
External: Sally Roberts and Joanna Parish (University of Birmingham) and Iain Morgan (University of Virginia, USA).

Cellular cholesterol abundance regulates potassium accumulation within endosomes and is an important determinant in Bunyavirus entry

Frank Charlton, Samantha Hover, Jack Fuller, Hayley Pearson, Ibrahim Al-Masoud, Adrian Whitehouse, Andrew Tuplin, Andrew Macdonald, Juan Fontana, John N. Barr and Jamel Mankouri

Introduction

The Bunyavirales order of segmented negative-sense RNA viruses includes >500 isolates that infect insects, animals, and plants and are often associated with severe and fatal disease in humans. To multiply and cause disease, bunyaviruses must translocate their genomes from outside the cell into the cytosol, achieved by transit through the endocytic network. We have previously shown that the model bunyaviruses Bunyamwera virus (BUNV) and Hazara virus (HAZV) exploit the changing potassium concentration ($[K^+]$) of maturing endosomes to release their genomes at the appropriate endosomal location. K^+ was identified as a biochemical cue to activate the viral fusion machinery, promoting fusion between viral and cellular membranes, consequently permitting genome release.

Results

We have further defined the biochemical prerequisites for BUNV and HAZV entry and their K^+ dependence. Using drug-mediated cholesterol extraction along with viral-entry and K^+ uptake assays, we report three major findings: (1) BUNV and HAZV require cellular cholesterol during endosomal escape; (2) cholesterol depletion from host cells impairs K^+ accumulation in maturing endosomes, revealing new insights into endosomal K^+ homeostasis; and (3) “priming” BUNV and HAZV virions with K^+ before infection alleviates their cholesterol requirement. Taken together, our findings suggest a model in which cholesterol abundance influences endosomal K^+ levels and consequently the efficiency of bunyavirus infection. The ability to inhibit bunyaviruses with existing cholesterol-lowering drugs may offer new options for future antiviral interventions for pathogenic bunyaviruses.

Publications

Charlton, F.W., Hover, S., Fuller, J., Hewson, R., Fontana, J., Barr, J.N., Mankouri, J. (2019) Cellular cholesterol abundance regulates potassium accumulation within endosomes and is an important determinant in Bunyavirus entry. *J Biol Chem*. **294**: 7335-7347.

Davies, K., Afrough, B., Mankouri, J., Hewson, R., Edwards, T.A., Barr, J.N. (2019) Tula orthohantavirus nucleocapsid protein is cleaved in infected cells and may sequester activated caspase-3 during persistent infection to suppress apoptosis. *J Gen Virol*. **100**: 1208-1221.

Fuller, J., Surtees, R.A., Slack, G.S., Mankouri, J., Hewson, R., Barr, J.N. (2019) Rescue of infectious recombinant Hazara nairovirus from cDNA reveals the nucleocapsid protein DQVD caspase cleavage motif performs an essential role other than cleavage. *J. Virol.* **93**: e00616-19.

Fuller, J., Surtees, R.A., Shaw, A.B., Álvarez-Rodríguez, B., Slack, G.S., Bell-Sakyi, L., Mankouri, J., Edwards, T.A., Hewson, R., Barr, J.N. (2019) Hazara nairovirus elicits differential induction of apoptosis and nucleocapsid protein cleavage in mammalian and tick cells. *J Gen Virol*. **100**: 392-402.

Funding

This work was funded by the Royal Society and the University of Leeds.

Collaborators

External: Alan Kohl (MRC-University of Glasgow Centre for Virus Research), Steve Goldstein (Loyola University Chicago)

Electron microscopy of membrane proteins to underpin structure guided inhibitor design

David Klebl, Rachel Johnson and Stephen Muench

Introduction

Structure based drug design has traditionally been underpinned by X-ray crystallography and nuclear magnetic resonance. However, recent developments in electron microscopy (EM) have led to a step change in our ability to solve the “high resolution” structure of previously intractable proteins. This has been reflected by the recent rapid expansion in membrane protein structures solved by cryoEM revealing new insights into structure, mechanism and regulation. My group are focused on methods development in two areas broad areas. The first is the development of a new grid making technology that can rapidly freeze grids and trap changes in structure in the low ms timeframe (>6ms). The second is in the use of new methodologies for stabilizing membrane proteins, for example, styrene maleic acid co-polymer lipoproteins (SMALPs).

Results

The group have been working on a range of membrane protein systems that are important for cellular homeostasis. These include the Niemann-Pick type C (NPC) protein which drives sterol integration into the membrane and is essential for sterol homeostasis. Through a collaboration with the Pedersen group in Aarhus we helped to present a framework for sterol membrane integration with the first cryoEM reconstruction of NPC1 (Figure 1A). A long-standing collaboration with the Hasnain group in Liverpool has revealed new insights into the quinol-dependent nitric oxide reductases (qNORs) with the publication of the first dimeric structure, revealed by single particle cryo-EM (Figure 1B). This has provided new insights into the activity of this family of proteins and shown a clear water channel which serves as a proton source.

The group in collaboration with Prof Howard White have also developed a unique apparatus that is capable of using voltage assisted spraying of a sample to trigger a reaction and trap different states after ~7ms time delay. This device relies on the mixing of two samples (substrate and reactant) as they are sprayed onto a fast-moving EM grid which is subsequently vitrified in liquid ethane. We have now used this setup to prepare EM grids capable of producing sub 4Å structures (Figure 1C). This allows us to trap intermediate states of a reaction where large conformational changes are present, such as ribosome cycling. This device can also be used to study oligomerization pathways and virus assembly. The speed at which grids can be made has also allowed us to investigate the role of the air-water-interface on the behavior of the sample within cryo-EM. Commonly, grid making takes >10 seconds which allows for multiple interactions of the protein sample with the air-water-interface which can result in preferred orientation and protein damage. By significantly increasing the speed of grid making we have seen that the interactions with the air-water-interface are still present but the degree of preferred orientation is reduced when grids are rapidly made <200ms. Moreover, studies with the ribosome have shown that damage can occur within the traditionally blotted sample which is reduced when making the grids rapidly that may be reflective of the reduced time at the air-water-interface.

The group is also working with industrial partners, (GlaxoSmithKline and UCB pharma) through a joint BBSRC grant to study a range of systems and develop new methodologies for EM. This includes the use of new ways to extract and isolate membrane proteins in more “native” environments through the use of styrene maleic acid (SMA) co-polymers and other related systems. This year we worked on a project to show that proteins could be extracted from cells while avoiding significant cell death that could be useful for cell biopsy. We have also developed a new strategy for SMA extraction and subsequent exchange into an amphipol polymer which allows for downstream analysis by mass spectrometry.

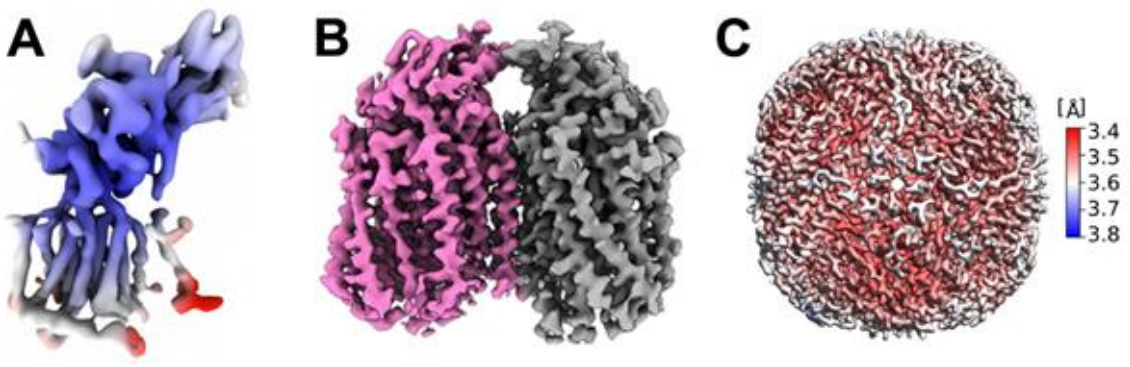

Figure 1: Single particle cryo-EM reconstruction of NPC1 (**A**) and the dimeric qNOR (**B**). (**C**) Single particle cryoEM structure of apoferritin generated from grids prepared on the new rapid mixing and freezing setup.

Publications

Kontziampasis, D., Klebl, D.P., Iadanza, M.G., Scarff, C.A., Kopf, F., Sobott, F., Monteiro, C.F., Trebbin, M., Muench S.P. & White H.D. (2019) A cryo-EM grid preparation device for time-resolved structural studies. *IUCrJ* **6**: 1024-1031.

Winkler, M.B.L., Kidmose, R.T., Szomek, M., Thaysen, K., Rawson, S., Muench, S.P., Wunster, D. & Pedersen B.P. (2019) Structural insight into eukaryotic sterol transport through Niemann Pick Type C proteins. *Cell* **179**: 485-497.

Gopalasingam, C.C., Johnson, R.M., Chiduza, G.N., Tosha, T., Yamamoto, M., Shiro, Y., Antonyuk, S.V., Muench, S.P. & Hasnain, S.S. (2019) Dimeric structures of quinol-dependant nitric oxide reductase (qNOR) revealed by cryo-Electron microscopy. *Sci. Advances* **5**: *doi 10.1126/sciadv.aax1803*.

Chiduza, G.N., Johnson, R., Wright, G.S., Antonyuk, S., Muench S.P. & Hasnain, S.S. (2019) LAT1 (SLC7A5) and CD98hc (SLC3A2) complex dynamics revealed by single particle cryo-EM. *Act cryst D*. **75**: 660-669.

Smith, A.J., Wright, K.E., Muench, S.P., Schumann, S., Whitehouse, A., Porter, K.E. & Colyer, J. (2019) Styrene maleic acid recovers proteins from mammalian cells and tissues while avoiding significant cell death. *Sci. rep*. **9**: *doi: 10.1038/s41598-019051896-1*.

Funding

This work was supported by the BBSRC and Wellcome Trust.

Collaborators

University of Leeds: Colin Fishwick, Robin Bon and Frank Sobott
*Externa*l: Howard White (Eastern Virgina Medical School), Martin Trebbin (State University of New York), Samar Hasnain & Dr Svetlana Antonyuk (University of Liverpool), Dr Chun-wa Chung (GlaxoSmithKline), Dr Tom Ceska (UCB Pharma), Bjorn Pedersen (Aarhus University).

Demonstration of the biological relevance of building blocks and fragments that are accessible via unified diversity-oriented synthetic approaches

Rong Zhang, Chris Arter, Richard Bayliss, Shiao Chow, Daniel Foley, Joan Mayol-Llinas, Scott Rice, Stuart Warriner and Adam Nelson

Introduction

The discovery of biologically-active small molecules is an enduring theme in chemical biology and medicinal chemistry. However, the historical exploration of chemical space has been highly uneven and unsystematic: a sixth of known cyclic organic compounds are based on just 30 (of 2.5 million) known molecular scaffolds! This uneven exploration stems, in large part, from the narrow toolkit of reliable reactions that currently underpins molecular discovery. We have an ongoing and vibrant research programme that has resulted in unified approaches to diverse building blocks for bioactive molecular discovery. Using a range of exemplar protein targets, we have now demonstrated that our unified approaches can provide distinctive starting points for the discovery of bioactive small molecules.

Results

Firstly, we studied the expansion of the structural diversity of BACE1 inhibitors. BACE1 is an aspartic protease that is responsible for the formation of amyloid β by sequential cleavage of amyloid precursor protein. To expand the structural diversity of a series of BACE1 inhibitors, we prepared a diverse range of analogues that incorporated novel and diverse ring systems (Figure 1). In each case, the requisite building blocks were accessed using a unified synthetic approach that we had previously developed. It was demonstrated that replacement of a lipophilic substituent was possible with maintenance of both potency and drug-likeness and that structural diversity of the inhibitors could be significantly expanded.

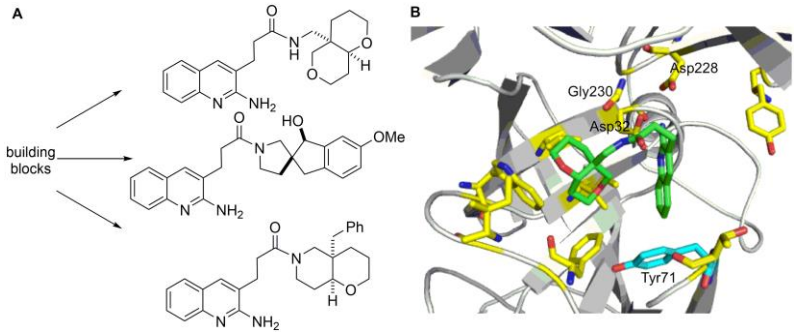

Figure 1: Discovery of novel BACE1 inhibitors by harnessing diverse building blocks prepared using a unified synthetic approach. Left: Synthesis of novel BACE1 inhibitors. Right: Docked pose of an exemplar BACE1 inhibitor.

Secondly, progress has been made with construction and evaluation of a shape-diverse fragment sets. The shape diversity of existing fragment sets does not generally reflect that of all theoretically possible fragments. We therefore designed a shape-diverse fragment set that was significantly more three-dimensional than existing fragment sets. The set was assembled using both commercially-available fragments, and by harnessing several unified synthetic approaches that we had previously developed. The fragment set was screened by high-throughput protein crystallography against Aurora-A kinase, and four fragment hits were discovered that targeted the binding site of allosteric regulators (Figure 2). In the longer term, it is envisaged that the fragment set could be screened against a range of functionally-diverse proteins, allowing the added value of more shape-diverse screening collections to be more fully assessed.

The development of unified strategies that are able to deliver skeletally diverse scaffolds is demanding. Nonetheless, such approaches can provide access to building blocks and fragments with controlled properties that can significantly expand opportunities in drug discovery. We have translated many of our unified diversity-oriented synthetic approaches such that they can be exploited within drug discovery programmes.

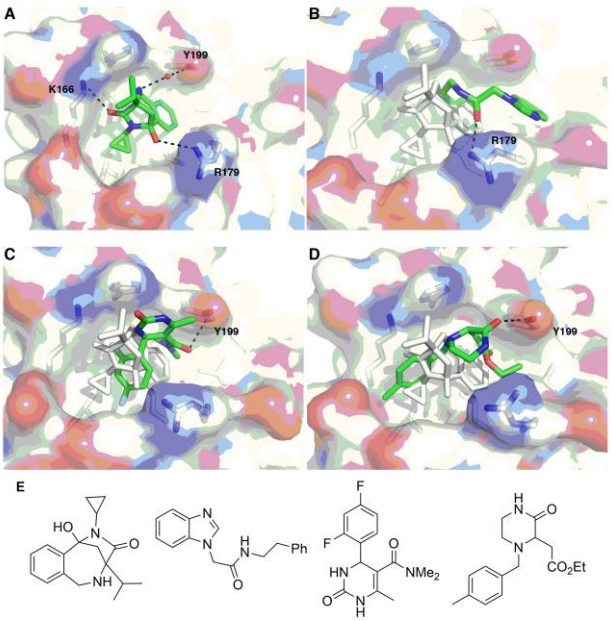

Figure 2: Hits from the screen of a shape-diverse fragment set against Aurora A kinase. Panels A-D: Interactions (black) between protein residues and the fragment hits. Panel E: Structures of the fragment hits.

Publications

Mayol-Llinas, J., Chow, S. & Nelson, A. (2019) Expansion of the structure–activity relationships of BACE1 inhibitors by harnessing diverse building blocks prepared using a unified synthetic approach. *ChemMedChem* **10**: 616-620.

Zhang, R., McIntyre, P. J., Collins, P. M., Foley, D. J., Arter, C. , von Delft, F., Bayliss, R., Warriner, S. & Nelson, A. (2019) Construction of a Shape-Diverse Fragment Set: Design, Synthesis and Screen against Aurora-A Kinase. *Chem. Eur. J.* **25**: 6831-6839.

Nelson, A. (2019) Catalytic machinery of enzymes expanded. *Nature* **570**: 172-173.

Rice, S., Cox, D. J., Marsden, S. P. & Nelson, A. (2019) Unified synthesis of diverse building blocks for application in the discovery of bioactive small molecules. *Tetrahedron* **38**, 130513-130520.

Ibarra, A. A., Bartlett, G. J., Hegedüs, Z., Dutt, S., Hobor, F., Horner, K. A., Hetherington, K., Spence, K., Nelson, A., Edwards, T. A., Woolfson, D. N., Sessions, R. B. & Wilson, A. J. (2019) Predicting and Experimentally Validating Hot-Spot Residues at Protein–Protein Interfaces. *ACS Chem. Biol.* **14**: 2252-2263.

Collaborators

University of Leeds: Professor Steve Marsden
External: Dr Patrick McIntyre (University of Leicester); Dr Patrick Collins and Professor Frank von Delft (Diamond Light Source); and Dr Daniel Cox (Redbrick Molecular).
We also acknowledge other scientific collaborators who have also contributed strongly to other aspects of our on-going research programme.

Funding

We thank EPSRC, the University of Leeds, AstraZeneca, Takeda, LifeArc and Redbrick Molecular for support.

Understanding the interaction mode between CCDC61 and microtubules

Yiheng Wang and Takashi Ochi

Introduction

Centrosomes are the main microtubule-organising centres in animal cells and, therefore, crucial for correct cell division. The organelles also play important roles in actin organisation, cellular signalling, cell polarity and immunosynapsis. The centriole, which is the core structure of the centrosome, is essential for generating cilia where centrioles are called basal bodies (Figure 1). Cilia are crucial for chemo-, mechano- and photo-sensing, and also are essential for generating fluid flow and locomotion to certain cell types. A group of diseases caused by defects of ciliary functions is called ciliopathies, which display abnormal development in many parts of the human body.

The centriole has a characteristic 9-fold rotational symmetry consisting of nine copies of microtubule blades (Figure 1). This symmetry is maintained throughout the axoneme of the cilium and is probably crucial for functions of centrosomes and cilia. Interestingly, the 9-fold rotational symmetry of the centriole is broken by its accessary structures such as basal feet, striated fibres and ciliary rootlets (Figure 1). This asymmetric feature of centrioles is important for cilia to keep their polarity and beat in the same direction on the surface of multiciliated cells. Structures of those accessories appear to be different in cell types and even between centrosomes and centrioles. What is the molecular basis of biogenesis of the accessary structures?

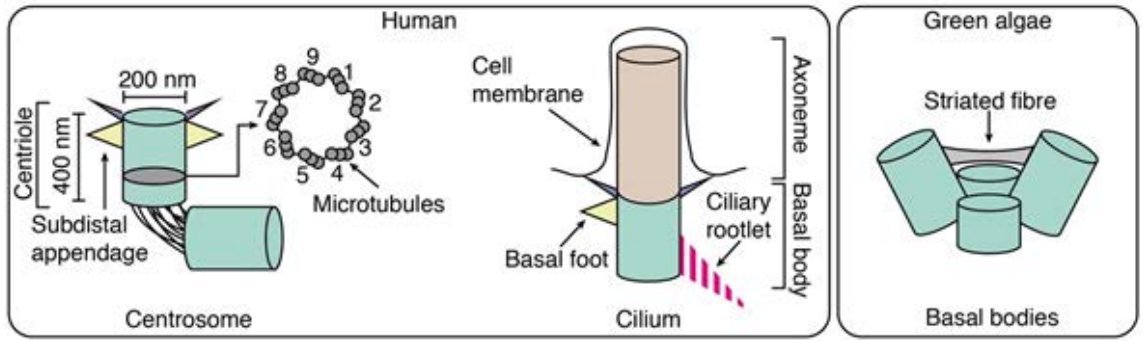

Figure 1. Centrioles and basal bodies in human and green algae. These are schematic representations of a centrosome and cilium in human and basal bodies of cilia of green algae.

CCDC61 is one of highly-conserved centrosomal proteins and is known to play a role in assembly of the accessary structures of centrioles. In a green algae species *Chlamydomonas reinhardtii*, a genetic defect of CCDC61 (known as VFL3 in *Chlamydomonas*) resulted in absence of striated fibres, which connect two basal bodies at the base of cilia of the organism (Figure 1). A similar observation was made in another unicellular organism *Paramecium tetraurelia* and also a multicellular organism *Schmitea mediterranea*. Recently, it has been shown that CCDC61 also associates with subdistal appendages, which are substructures of centrosomal centrioles and important for the microtubule organisation (Figure 1). These results imply that CCDC61 has an evolutionary conserved function in the biogenesis of centriolar accessary structures. However, how CCDC61 exactly facilitates the biogenesis is unclear.

Results

To resolve this problem, we studied the structure of CCDC61 (*to be published*). Surprisingly, we found that the protein has a similar protein fold to an essential centrosomal protein SAS6, which plays a key role in establishing the 9-fold rotational symmetry of the centriole. SAS6 is known to form self-assembled 9-fold ring structure *via* two dimerisation domains of the proteins, whereas, we found that CCDC61 forms a linear proto-filament having a 3-fold

screw axis along the filament using similar dimerisation interfaces to SAS6. In addition to the filament formation of CCDC61, we found that it binds to microtubules *via* its coiled-coil domain. This interaction was disrupted by mutating five conserved positively-charged residues to the opposite-charged resides. We also showed that the microtubule binding of CCDC61 is essential for its function in *Chlamydomonas*. We then wanted to observe how the coiled-coil domain of CCDC61 interacts with microtubules to further understand how the interaction contributes to assembly of the centriolar substructures.

Cryo-EM experiments of the coiled-coil domain of human CCDC61 in complex taxol-stabilised microtubules were carried out to understand how CCDC61 binds to microtubules. Cryo-EM micrographs of the complex showed that the domains decorate the microtubules (Figure 2A). However, 2D class images of microtubule 13 proto-filaments in complex with CCDC61 showed that the coiled-coil domain does not seem to bind to the microtubules in a regular manner (Figure 2B). These results imply that missing domains of CCDC61, particularly the head domain, might be important for making a regular array of the protein on microtubules.

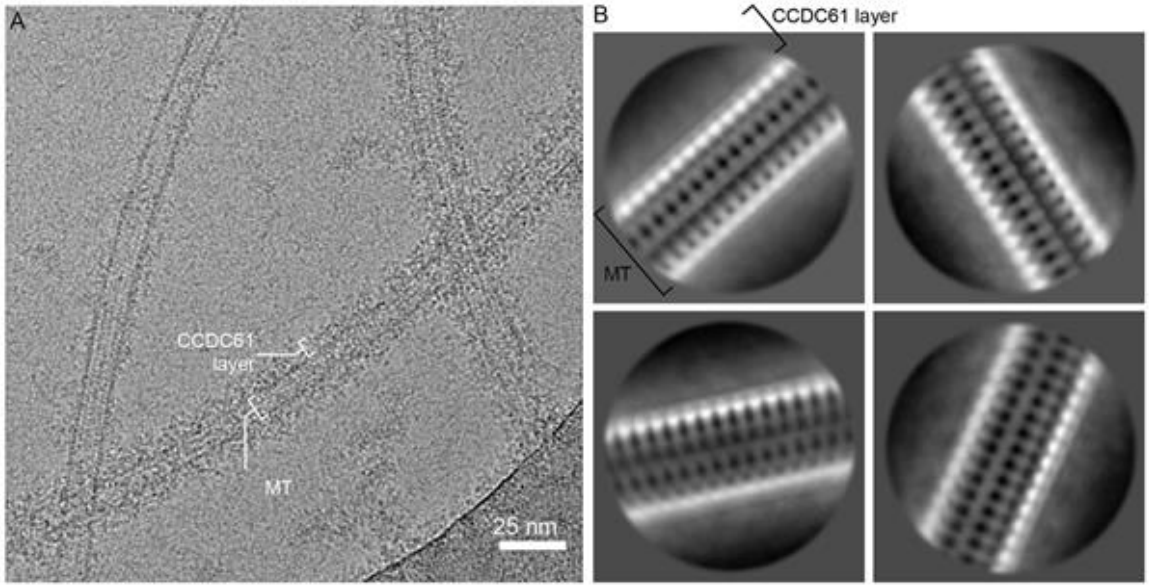

Figure 2. CCDC61 binds to microtubules. (A) Cryo-EM micrograph of the coiled-coil domain of CCDC61 in complex with microtubules. White brackets indicate microtubule (MT) and the layer of CCDC61 proteins. Scale bar, 25 nm. (B) 2D class images of the coiled-coil domain of CCDC61 in

Funding
This work is supported by the University of Leeds.

Transient silencing of antibiotic resistance by mutation

Louise Kime, Christopher Randall, Frank Banda, John Wright, Joseph Richardson and Alex O'Neill

Introduction

Antibiotic resistance negatively impacts the treatment of bacterial infection. To guide optimal treatment, clinical microbiology laboratories routinely perform susceptibility testing to determine the antibiotic sensitivity of an infecting pathogen. This approach relies on the assumption that it can reliably distinguish bacteria capable of expressing antibiotic resistance in patients. Unfortunately, this assumption may not always hold true.

Sporadic literature reports describe isolates of pathogenic bacteria that harbour an antibiotic resistance gene but remain susceptible to the corresponding antibiotic as a consequence of a genetic defect. Such strains represent a source from which antibiotic resistance could rapidly re-emerge to cause treatment failure in patients. Here, we report the first systematic investigation into the prevalence and nature of this phenomenon, which we term "silencing of antibiotic resistance by mutation" (SARM).

Results

We tested 1,470 multidrug resistant clinical isolates of *Staphylococcus aureus* for their susceptibility to a panel of clinically-deployed antistaphylococcal drugs. In parallel, all strains were subject to whole genome sequencing in collaboration with the Wellcome Trust Sanger Institute, and their genomes interrogated for antibiotic resistance determinants *in silico* using the Antimicrobial Resistance Identification By Assembly (ARIBA) tool.

Approximately 10% of the strain collection carried antibiotic resistance genes that had become inactivated by mutation, with ~3% of the isolates exhibiting SARM to clinically-deployed antistaphylococcal drugs (Figure 1). Mutational events responsible for resistance gene silencing included point mutations (insertions, deletions and substitutions) and insertion of transposable elements within the resistance gene that disrupted expression. The most common type of mutation detected in SARM strains was single nucleotide deletion within poly(A) tracts, a phenomenon thought to result from slippage of DNA polymerase during replication of these tracts. The genetic changes identified resulted in loss of resistance gene function in a variety of ways, but frequently as a result of frameshift.

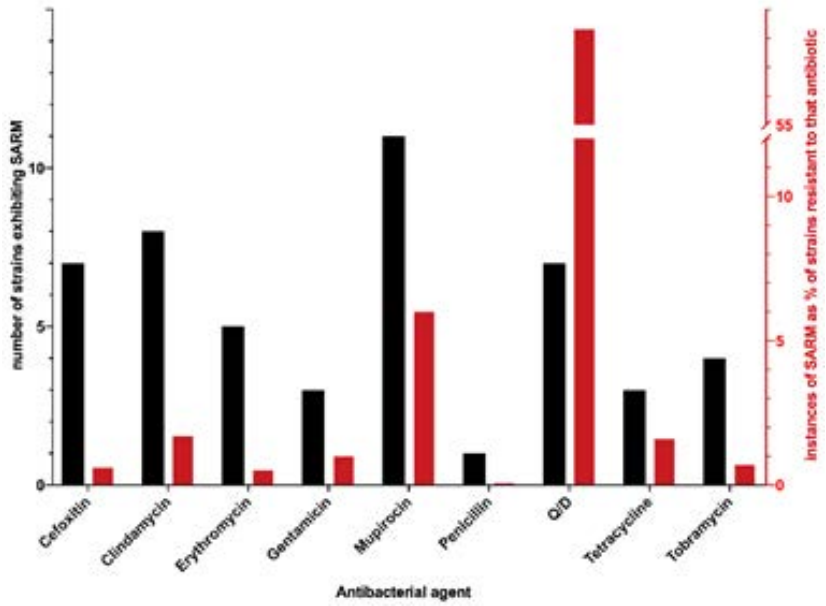

Figure 1: Prevalence of SARM to clinically deployed antibacterial drugs in *S. aureus*. The numbers of SARM strains identified for given agents are shown as black bars (left *y* axis), while the red bars (right *y* axis) show this value as a percentage of the total number of isolates exhibiting phenotypic resistance to that drug in this study. Q/D: quinupristin-dalfopristin.

Upon challenge with the cognate antibiotic, reversion to phenotypic resistance was detected in >90% of SARM strains. Loss of SARM was most often due to direct reversion of the original silencing mutation, though examples of indirect suppression were also observed. Reversion to resistance occurred at frequencies ($>10^{-9}$) readily achievable in infected patients, implying that reversion of SARM would likely occur during treatment and lead to therapeutic failure.

Our results establish that SARM is prevalent, effectively transient and evades routine detection, rendering it a significant potential threat to antibacterial chemotherapy. We recommend that, wherever practicable, SARM be investigated as a potential cause in cases of unanticipated therapeutic failure in the treatment of bacterial infection.

Publications

Kime, L., Randall, C. P., Banda, F. I., Coll, F., Wright, J., Richardson, J., Empel, J., Parkhill, J. & O'Neill, A. J. (2019) Transient silencing of antibiotic resistance by mutation represents a significant potential source of unanticipated therapeutic failure. *mBio* **10**: e01755-19.

Funding

This work was funded by the Antimicrobial Resistance Cross-Council Initiative.

Collaborators

External: Francesc Coll (London School of Hygiene and Tropical Medicine, UK), Joanna Empel (National Medicines Institute, Poland), Julian Parkhill (University of Cambridge, UK)

Experimental data, physical models and computers in protein science

Emanuele Paci

Introduction

Our research focuses on the development and application of novel computational tools to investigate structure and functional dynamics of biomolecules. One of our aims is fully exploit the wealth of experimental data that is increasingly available thanks to the development of advanced high throughput techniques. Most of our research involves experiments performed in collaboration with colleagues from the Astbury Centre and further afield. A central topic of our research is to develop and use data-driven approaches to determine the relation between sequence and physical properties of polypeptide chain, whether this is a stable structure or a heterogeneous ensemble of structures. Much of our work involves molecular simulation of the dynamics and interactions within and between protein systems. Data generated from simulation are used to interpret and direct experimental measurements such as hydrogen-deuterium exchange probed by mass spectroscopy, nuclear magnetic resonance and small-angle X-ray scattering (SAXS) .

Results

Among our current interests is the development of *ab initio* methods to determine the structure of proteins and protein complexes. All available structure predictors share the inconvenience of not being able to score the correct model higher than decoys. Atomistic simulation can be used to assess the stability of different models. For a specific class of antibody analogues (DARPins) we developed a procedure that provides with high-fidelity structures of DARPins in complex with any receptor based on the sequence of the former and the structure of the latter (Figure 1). In collaboration with Darren Tomlinson we aim to extend the approach to Affimers, a class of antibody analogues developed at Astbury.

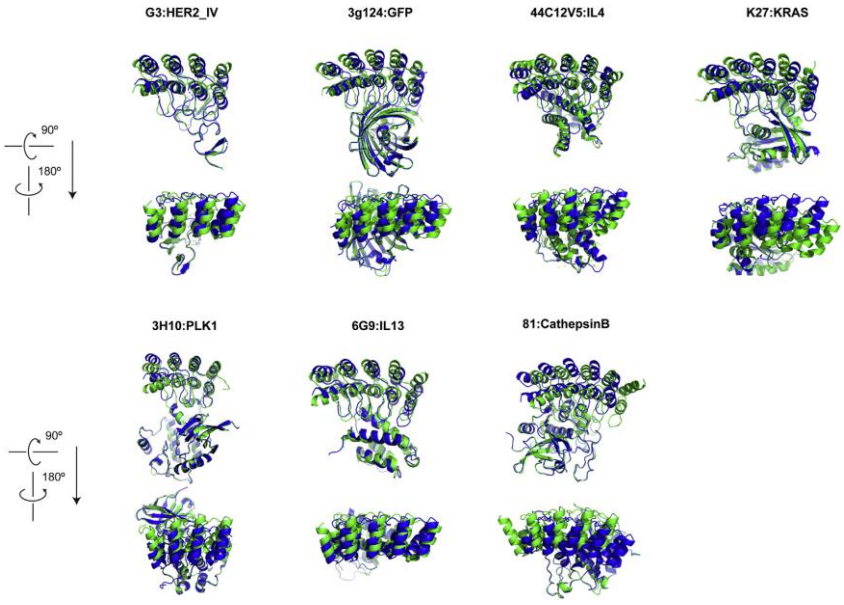

Figure 1: Final models of complexes involving DARPins: for all complexes for which structures are available the approach produces structures that are acceptable according to CAPRI criteria.

Another topic we have been working of for several years is why some polypeptide sequences form elongated structures, i.e., physical objects whole length scales with the number of aminoacids in the chain. In collaboration with Michelle Peckham we have characterised and rationalised why some polyampholytic sequences (i.e., full of positively and negatively charged aminoacids) perfectly elongated helices for any number of aminoacids. In collaboration with Jen Potts (York/Sydney) we are exploring the structural properties of a number of proteins that are expressed on the surface of bacteria and elicit immune response. These proteins are made of a large number of repeats, with virtually

identical sequences. While the linker between pairs of domains cannot explain the extension of the protein, it appears that they are effectively extended from experimental data (e.g. SAXS). Simulation of two-repeat constructs for which structure is available show that the mutual orientation of the two domains is restricted, and models for larger constructs (Figure 2) confirm that the length increases proportionally to the number of domains.

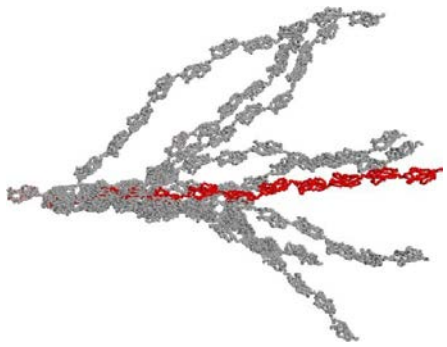

Figure 2: Ensemble of structures of a 12-domain Rib construct obtained by replicating domain 1 using translations and rotations observed during the MD simulation of Rib2R.

Publications

Whelan, F., A. Lafita, S. C. Griffiths, R. E. M. Cooper, J. L. Whittingham, J. P. Turkenburg, I. W. Manfield, A. N. St John, E. Paci, A. Bateman and J. R. Potts (2019). Defining the remarkable structural malleability of a bacterial surface protein Rib domain implicated in infection. *Proc. Natl. Acad. Sci. U. S. A*. **116**: 26540-26548.

Wodak, S. J., E. Paci, et al. (2019). Allostery in Its Many Disguises: From Theory to Applications. *Structure* **27**: 566-578.

Skinner, S. P., G. Radou, R. Tuma, J. J. Houwing-Duistermaat and E. Paci (2019). Estimating Constraints for Protection Factors from HDX-MS Data. *Biophys J* **116**: 1194-1203.

Ross, J. F., G. C. Wildsmith, M. Johnson, D. L. Hurdiss, K. Hollingsworth, R. F. Thompson, M. Mosayebi, C. H. Trinh, E. Paci, A. R. Pearson, M. E. Webb and W. B. Turnbull (2019). Directed Assembly of Homopentameric Cholera Toxin B-Subunit Proteins into Higher-Order Structures Using Coiled-Coil Appendages. *J. Am. Chem. Soc.* **141**: 5211-5219.

Radom, F., E. Paci and A. Pluckthun (2019). Computational Modeling of Designed Ankyrin Repeat Protein Complexes with Their Targets. *J. Mol. Biol.* **431**: 2852-2868.

Lepsik, M., R. Sommer, S. Kuhaudomlarp, M. Lelimousin, E. Paci, A. Varrot, A. Titz and A. Imberty (2019). Induction of rare conformation of oligosaccharide by binding to calcium-dependent bacterial lectin: X-ray crystallography and modelling study. *Eur. J. Med. Chem.* **177**: 212-220.

Hao, Y., J. P. England, L. Bellucci, E. Paci, H. C. Hodges, S. S. Taylor and R. A. Maillard (2019). Activation of PKA via asymmetric allosteric coupling of structurally conserved cyclic nucleotide binding domains. *Nat. Commun*. **10**: 3984.

Batchelor, M., M. Wolny, E. G. Baker, E. Paci, A. P. Kalverda and M. Peckham (2019). Dynamic ion pair behavior stabilizes single alpha-helices in proteins. *J. Biol. Chem.* **294**: 3219-3234.

Collaborators

University of Leeds: R. Tuma, J. Houwing-Duistermaat**,** B. Turnbull, R. Bayliss, D. Brockwell, R. Richter, D. Donnelly, M. Peckham, D. Tomlinson

External: J. Clarke (Cambridge), A. Plückthun (Zurich), C. Kleanthous (Oxford), J. Potts (York), R. Maillard (Georgetown), A. Imberty and M. Lepsik (Grenoble)

Stable Single Alpha Helices – stabilised by transient salt bridges

Matthew Batchelor, Marcin Wolny and Michelle Peckham

Introduction

Over the past 15 years, we have been investigating unique single alpha helical (SAH) domains. These are alpha helices that are stable in solution as an elongated structure and without forming part of a 3D protein fold. We discovered these novel domains when we first attempted to characterise the predicted coiled coil of various different myosin isoforms. We found that the predicted coiled-coil of these myosin isoforms (Myosin class 6, 7 and 10) contained a high number of oppositely charged residues (glutamate (Glu), arginine (Arg), lysine (Lys)) and lacked a hydrophobic seam. We showed that a purified short peptide from myosin 10 was monomeric, highly helical and thus formed a single alpha helical domain in isolation.

We have since shown that this motif is widespread and found in many proteins other than myosin. We have characterised this structure by atomic force microscopy to show that it has the behaviour of a constant force spring. We have also been able to generate artificial SAH sequences that have helped us understand how Glu-Arg and Glu-Lys pairs contribute to the formation and stability of SAH domains. However, an outstanding question was how are the ionic interactions (salt bridges) between oppositely charged residues stabilising the SAH domain. These types of interactions are commonly depicted as fixed, even though they only provide a marginal energetic benefit compared to individually solvated charged groups.

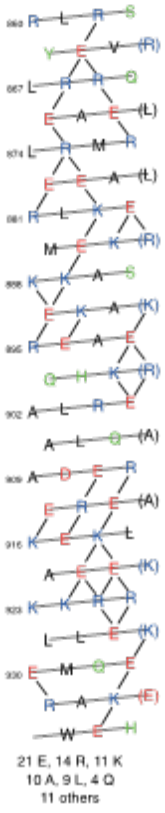

Figure 1: The M7a SAH domain plotted as a helical net. Lines between residues indicate potential ionic interactions.

To answer this question, we used a combination of Nuclear Magnetic Resonance (NMR) spectroscopy and molecular dynamics simulations to understand salt bridge behaviour in these novel domains, using the SAH domain of Myosin 7a (M7a) as a key example.

Results

First, we confirmed that the M7a SAH sequence (Figure 1) does indeed form a SAH domain by a combination of circular dichroism experiments under different conditions to demonstrate its helical nature and analytical ultracentrifugation to demonstrate that it is monomeric. Next, we obtained a 2D ^{1}H-^{15}N TROSY (transverse relaxation optimised spectroscopy) for M7a SAH. Of interest here is that spectrum shows a remarkable lack of dispersion, more typical of a disordered protein than of a globular protein with similar molecular mass. However, we were able to obtain a virtually complete backbone assignment, and could show that the peptide maintained a helical structure under these conditions despite variation in numbers of potential salt bridge interactions along the helix.

The main focus of the NMR experiments was to investigate side-chain behaviour and the potential ion pair formation between Glu and either Arg or Lys side chains. Our NMR experiments demonstrated that all the Glu residues were in the deprotonated (COO^-) form and not freely able to rotate, suggesting that they are interacting with other residues in the protein. Under low pH (5.5) and at a temperature of 10°C to slow proton exchange, we found evidence for interactions between Arg and other residues, suggesting they are involved in ion pair formation. However, we were unable to find evidence for persistent salt bridges (hydrogen-bonded ion pairs). We

concluded that salt bridge formation is transient and/or looser ion pairs are formed (e.g. bridged by an intervening water molecule). Simulations of the sequence showed a similar picture.

In summary, it is likely that SAH domain stability is not driven by strong, hydrogen-bonded, persistent salt bridges, but via a network of fluctuating ion pairs that continuously form and break. This additionally suggests that many other salt bridges are not stable, fixed interactions but likely to fluctuate, in many other structures.

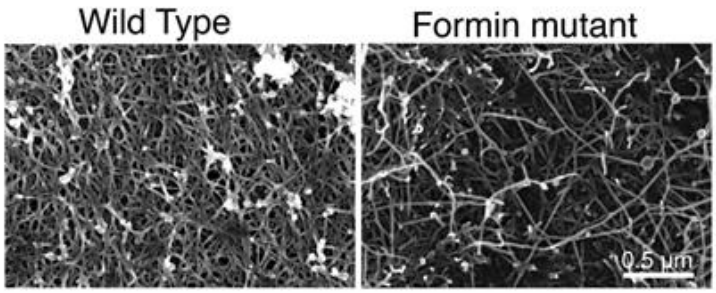

Figure 2: Scanning Electron Micrographs of part of the actin cytoskeleton in wild type and mutant (formin KO) cells

In other work, we are continuing to work on super-resolution imaging, and using Affimers as small non-antibody binding proteins that are excellent for this approach. We are also using a range of electron microscopy approaches to image the cytoskeleton in cells. In this example (Figure 2) we used Scanning Electron Microscopy to image the difference in actin organization between wild type and formin mutant (knockout) cells in the amoeba (*Dictyostelium*) to demonstrate how loss of formins has a strong effect on actin organization (with Hans Faix).

Publications

Batchelor, M., Wolny, M., Baker, E. G., Paci, E., Kalverda, A. P., & Peckham, M. (2019) Dynamic ion pair behavior stabilizes single alpha helices in proteins. *J. Biol. Chem.* **294:** 3219-3234.

Carrington, G., Tomlinson, D., and Peckham, M. (2019). Exploiting nanobodies and Affimers for superresolution imaging in light microscopy. *Mol. Biol. Cell.* **30**: 2737-2740.

Litschko, C., Bruhmann, S., Csiszar, A., Stephan, T., Dimchev, V., Damiano-Guercio, J., Junemann, A., Korber, S., Winterhoff, M., Nordholz, B., Ramalingam, N., Peckham, M., Rottner, K., Merkel, R., and Faix, J. (2019). Functional integrity of the contractile actin cortex is safeguarded by multiple Diaphanous-related formins. *Proc. Natl. Acad. Sci. U. S. A.* **116**: 3594-3603.

Funding

This work was funded by BBSRC.

Collaborators

University of Leeds: Mark Harris, Peter Knight, Emanuele Paci, Arnout Kalverda
External: Emily Baker (University of Bristol), Hans Faix (Hanover Medical School, Germany)

Conformation, oligomericity, folding and dynamics of membrane proteins revealed by PELDOR/DEER spectroscopy

Bolin Wang and Christos Pliotas

Introduction

Pulsed Electron DOuble Resonance (PELDOR, also known as DEER) spectroscopy can measure distances (2 – 16) nm between unpaired electrons introduced to selected sites of a protein complex, irrespective of its size. This approach combines the specificity and reversibility of cysteine modification, with the accuracy of PELDOR in reporting stoichiometry and conformation of membrane proteins, in a variety of environments including physiological conditions and/or lipid membranes. We have coupled PELDOR with cysteine modification (nitroxide spin labels) on the large conductance mechanosensitive (MS) channel MscL, the ion channel with the highest pressure activation threshold across life kingdoms: 1) on multiple sites of MscL interrogating changes in channel conformation and gating transitions (Figure 1a) and 2) on a separate single site to assess ion channel folding in bacterial strains engineered to control cytotoxicity.

Mechanosensation is the ability of ion channels to sense changes in membrane tension and respond by altering their structure and function. Previously, the degree of lipid chain availability within transmembrane nano-pockets (NPs) of ion channels has been linked with mechanosensitivity, but the effect of lipid chain disruption on mechanical activation has not been demonstrated. We have restricted lipid chain access within NPs by covalent cysteine modification on sites spanning all protein domains and monitored channel conformation by PELDOR. For a single site located at the entrance of the NPs we promoted allosteric channel opening in the absence of pressure. The modification restricted lipid chain access to the NPs and thus the final contact lipid chains make with the protein to mediate bilayer tension. We propose this method could be used to reversibly generate allosteric responses in mechanically gated channels. Membrane proteins execute a wide variety of critical functions in all organisms but bacterial recombinant membrane protein production is hampered by poor cellular accumulation and severe toxicity for the host, which leads to low biomass and yields. Here, we systematically looked for gene overexpression and culturing conditions that maximize the accumulation of membrane-integrated and well-folded recombinant MPs in these strains. We have found that, under optimal conditions, SuptoxD and SuptoxR strains achieve greatly enhanced recombinant production for a variety of MP, irrespective of their archaeal, eubacterial, or eukaryotic origin.

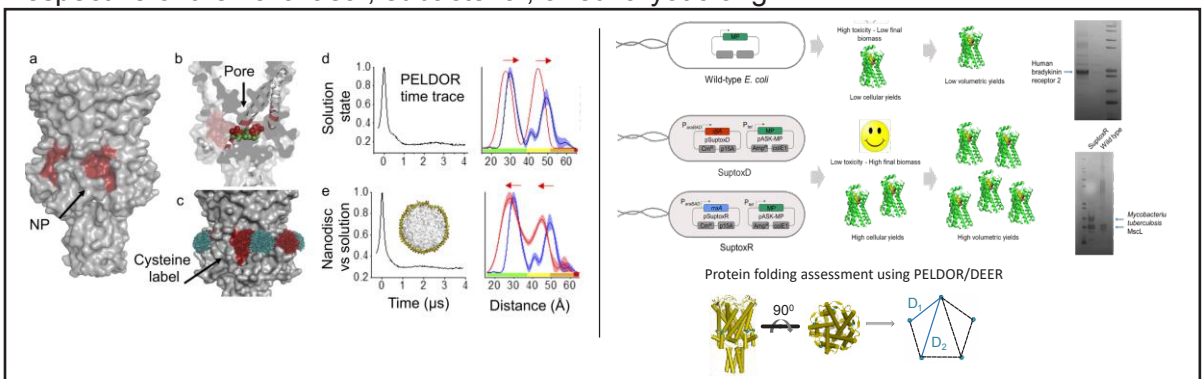

Figure 1: a. NP-forming region residues (red surface view) **b.** NP-bottom (red spheres) and pore constriction site (green spheres) forming residues. **c.** modification (red sticks) disrupting access to NPs. **d.** Raw PELDOR traces (left columns) and resulting distance distributions (right columns). Red lines correspond to closed state modelled distances. Blue shade areas correspond to measured distances. Modified channel distance distribution shift (highlighted by red arrows) between the "closed structure MscL model" and "PELDOR distances in solution. **e.** Distance shift between modified MscL solution and nanodiscs suggesting a reversible change in the presence of membrane tension. Right panel: Engineered bacterial strains concept for controlled cell cytotoxicity. PELDOR distance measurements were used to assess ion channel folding expressed in these strains by further assigning their oligomeric (pentamer) and conformational (closed) state in solution.

Furthermore, using PELDOR and biochemical assays we show that the use of these strains enables the production of well-folded bacterial MscL and human Bradykinin 2 (BR2) GPCR receptor suitable for functional and structural studies.

Results

If the essential feature of MS channel activation is lipid removal from the NPs, then opening should occur by sterically excluding lipid chain contacts to NP-forming residues (Figure 1a, 1b and 1c). 20 TbMscL mutants were generated with respect to the NPs and for thirteen positions we obtained PELDOR time traces. For a single site located at the NP entrance we observed a significant structural response, consistent with a helical movement of ~6 Å and pore expansion (Figure 1d). A reversed distance shift was observed after reconstitution into nanodiscs (Figure 1e). The distances shorten, in agreement with the closed modelled distances, suggesting a reversible induced change, from the open to closed state. In summary, we have demonstrated that disruption of lipid chain penetration within NPs generates a mechanosensitive ion channel structural and functional response. Importantly, we offer insights into how lateral tension is transmitted from the membrane through the lipid chains to the NP and gates ion channels. We demonstrate that allosteric mechanical gating of ion channels can be achieved by disulfide cysteine modification on sites located at the entrance of the NP and distal to the channel pore.

PELDOR distance measurements were used to assess ion channel folding expressed in these strains by further assigning their oligomeric and conformational state in solution. In particular MscL was found to be well-folded in a pentameric form and in its closed state. Further human Bradykinin receptor 2 was produced in the same bacterial strains in high yields, purified in homogeneity and found to be monodisperse and well-folded. We anticipate that SuptoxD and SuptoxR will become expression hosts for recombinant membrane protein production in bacteria.

Publications

Kapsalis, C., Wang, B., El Mkami, H., Pitt, S. J., Schnell, J., Smith, T. K., Lippiat J. D., Bode, B. E., Pliotas C., (2019) Allosteric activation of an ion channel triggered by modification of mechanosensitive nano-pockets. *Nat Commun* **10**: 4619, *doi:10.1038_s41467-019-12591-x.ris*.

Michou, M., Kapsalis, C., Pliotas, C., (2019) Skretas, G., Optimization of Recombinant Membrane Protein Production in the Engineered Escherichia coli Strains SuptoxD and SuptoxR. *ACS Synth Biol* **8**: 1631-1641, *doi:10.1021/acssynbio.9b00120*.

Funding

This work was funded by Royal Society of Edinburgh, Tenovus Scotland, Carnegie Trust and the Universities of Leeds and St Andrews.

Collaborators

University of Leeds: JD Lippiat
External: J Schnell (University of Oxford) C Kapsalis, H El Mkammi, SJ Pitt, TK Smith, BE Bode (University of St Andrews) M Michou, G Skretas (National Hellenic Research Foundation)

Molecular details of β_2m amyloid assembly pathways

Nicolas Guthertz, Theodoros Karamanos, Núria Benseny-Cases, Roberto Maya, Emma Cawood, Hugh Smith, Eric Hewitt and Sheena Radford

Introduction

β_2-Microgobulin (β_2m) is the light chain of the major histocompatibility complex class I, which functions by presenting antigens to T-cells. After dissociation from this complex, β_2m is found in the serum and degraded and excreted by the kidneys. β_2m is implicated in two different diseases in which amyloid deposition is observed. In patients with renal failure undergoing long-term haemodialysis, β_2m concentrations in their serum can increase > 60-fold. In addition, a truncated version of the protein that lacks the N-terminal 6 residues (ΔN6) is formed by proteolytic digestion. ΔN6 aggregates more rapidly than the wild-type (WT) protein and has been shown to catalyse aggregation of WT β_2m. The resulting proteins co-assemble into amyloid fibrils that accumulate in the joints, leading to pathological bone destruction and the disease called dialysis-related amyloidosis (DRA). The second disease is a rare systemic amyloidosis in which a hereditary single point mutation (D76N) causes amyloid deposition of the variant protein in the spleen, liver, heart, salivary glands and nerves. These patients have normal renal function and normal serum β_2m concentration, suggesting that D76N and ΔN6 aggregate via different mechanisms. Here, we used NMR experiments, combined with kinetic analyses of amyloid formation to map the early stages of aggregation of WT, ΔN6 and D76N β_2m. We describe the role of extracellular matrix in facilitating aggregation of the WT protein in DRA, the structures of oligomeric intermediates in the amyloid assembly pathway of ΔN6, and initial studies of the aggregation of D76N.

Results

(i) The role of extracellular matrix materials in catalysing WT β_2m aggregation into amyloid:

Collagen I is found in the joints and low molecular weight (LMW)-heparin (a glycosaminoglycan) is commonly administrated as an anticoagulant during dialysis. Given that WT β_2m does not aggregate into amyloid *in vitro*, we posited that cellular components in the joint region may stimulate WT β_2m aggregation by enhancing partial unfolding into amyloidogenic species. Using detailed kinetic analysis, we were able to demonstrate that LMW-heparin accelerates the aggregation of WT β_2m into amyloid, while collagen I inhibits assembly by preventing secondary nucleation of aggregation on the fibril surface. These results provide new insights into the specificity of β_2m aggregation in DRA and may pave the way to new routes to abrogating aggregation in dialysis patients.

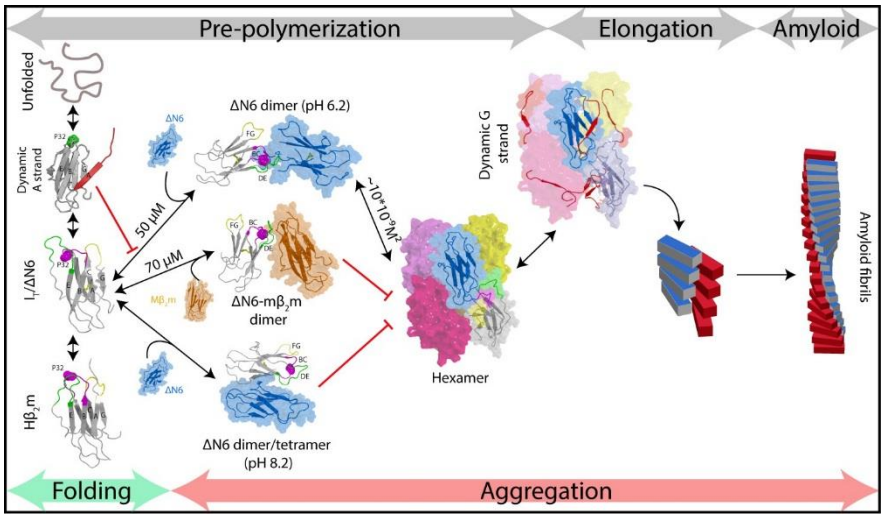

Figure 1: Schematic representation of the mechanism of amyloid formation for ΔN6. ΔN6 forms an elongated head-to-head dimer which can then trimerise to create a hexamer, both of which are kinetically defined as on-pathway to amyloid fibrils. ΔN6 can also form off-pathway dimers, either as a homodimer interacting side-by-side, or by forming a heterodimer with murine β_2m (mβ_2m).

(ii) The structures of oligomers that initiate ΔN6 aggregation into amyloid:

The early stages of amyloid assembly involve the formation of oligomers, many of which are cytotoxic. Defining the structures of these ephemeral species is crucial to developing deeper

understanding of amyloid formation at a structural level and to defining new route towards therapeutic intervention. We have used a suite of NMR methods, combined with kinetic analyses and other biophysical methods to map, for the first time, the structures of dimers and hexamers that form in the early stages of ΔN6 aggregation (Figure 1). These oligomers were proven kinetically to be obligate for amyloid formation and, interestingly, are not cytotoxic. These exciting results suggest that it may be possible to inhibit aggregation by targeting these early protein-protein interactions. Developing small molecule inhibitors that fulfil this task is the focus of our on-going work.

(iii) How does D76N β_2m aggregate into amyloid?

Current work in our laboratory is also focussing on how the identity of residue 76 affects β_2m aggregation and gives rise to amyloid disease of the visceral organs. While the crystal structures of WT and D76N β_2m are similar, the aggregation kinetics and protein stability are drastically different (Figure 2). Interestingly, these differences are not predicted using a wide range of algorithms, showing that residue 76 must play a unique role in defining the aggregation pathway of this 99 residues protein. How, and why, residue 76 dictates aggregation of β_2m is actively under investigation using NMR, mutation and kinetic analyses.

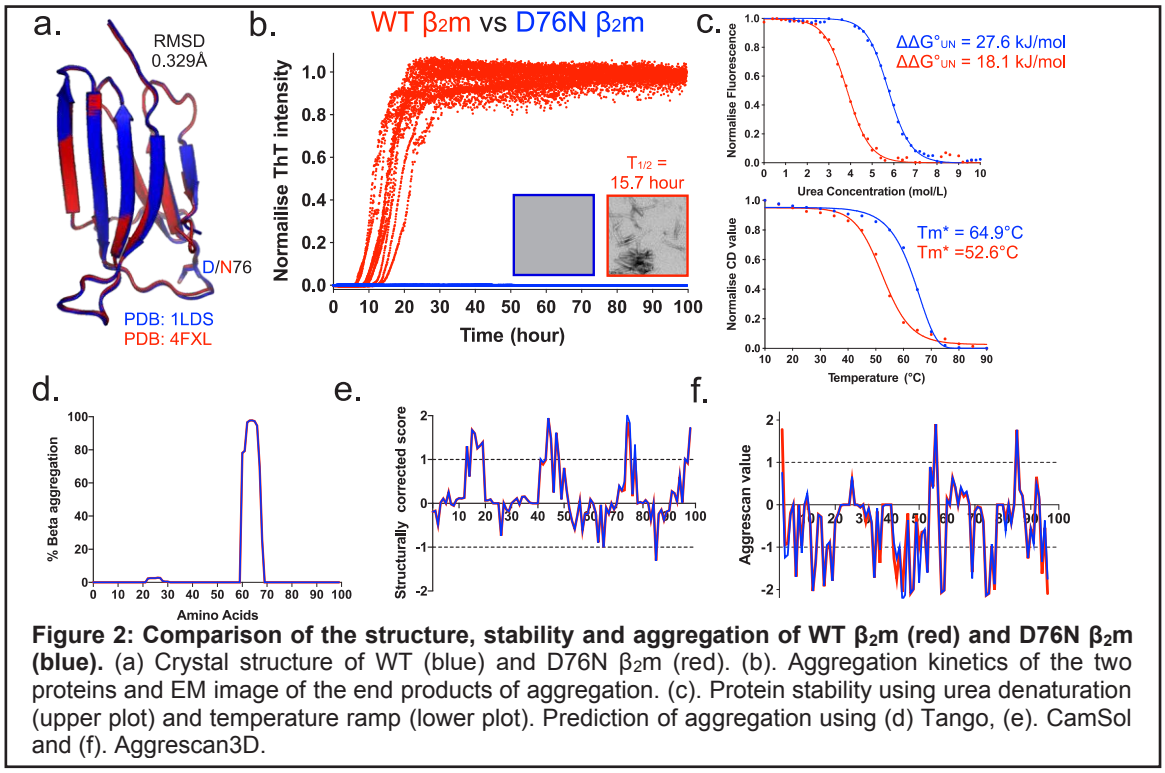

Figure 2: Comparison of the structure, stability and aggregation of WT β_2m (red) and D76N β_2m (blue). (a) Crystal structure of WT (blue) and D76N β_2m (red). (b). Aggregation kinetics of the two proteins and EM image of the end products of aggregation. (c). Protein stability using urea denaturation (upper plot) and temperature ramp (lower plot). Prediction of aggregation using (d) Tango, (e). CamSol and (f). Aggrescan3D.

Publications

Karamanos, T.K., Jackson, M. P., Calabrese, A.N., Goodchild, S.C., Cawood, E.E., Thompson, G.S., Kalverda, A.P., Hewitt, E.W., and Radford, S.E. (2019) Structural mapping of oligomeric intermediates in an amyloid assembly pathway. *eLife*, **8**, e46574.

Benseny-Cases, N., Karamanos, T.K., Hoop, C.L., Baum, J., and Radford, S.E. (2019) Extracellular matrix components modulate different stages in β_2-microglobulin amyloid formation. *J. Biol. Chem.*, **294**, 9392-9401.

Funding

This work was funded by the Wellcome Trust, the European Research Council and a Marie Curie International Exchange Fellowship.

Collaborators

University of Leeds: Arnout Kalverda, Alex Breeze
External: Jean Baum (Rutgers University, New Jersey)

The role of SurA PPIase domains in preventing outer membrane protein aggregation

Bob Schiffrin, Julia Humes, Antonio Calabrese, Anna Higgins, David Brockwell and Sheena Radford

Introduction

The outer membranes (OMs) of Gram-negative bacteria perform numerous essential and diverse functions. These functions are mediated by β-barrel outer membrane proteins (OMPs) which are found exclusively in the OMs of bacteria, mitochondria and chloroplasts. In bacteria, OMP biogenesis begins with their synthesis on cytosolic ribosomes. These hydrophobic, aggregation-prone OMPs must then be translocated across the inner membrane and chaperoned across the periplasm, before their final folding and insertion into the OM. This final step is catalysed by the ~200 kDa hetero-oligomeric β-barrel Assembly Machinery (BAM). Remarkably, OMPs are assembled in an environment without an external energy source as the periplasm is devoid of ATP. SurA is the major, conserved OMP chaperone in the periplasm with key roles in homeostasis and virulence. In *E. coli*, SurA (~45 kDa) has a core domain and two peptidylprolyl isomerase (PPIase) domains, the role(s) of which remain unresolved (Fig. 1a,b). While recent genetic, structural and biochemical investigations have increased our understanding of the OMP assembly pathway, it remains unclear how unfolded OMP substrates interact with periplasmic chaperones, how OMPs are delivered to the BAM complex and how they are assembled by BAM. Our work aims to gain insight into all of these aspects of the OMP assembly pathway using purified components and a range of biochemical and biophysical techniques. Here, we have investigated the role of the three domains of SurA in chaperoning OMP substrates using bioinformatics analysis together with binding and aggregation assays.

Results

We began our investigation into the role of PPIase domains in SurA function by quantifying the distribution of SurA homologues with zero, one or two PPIase domains in different proteobacterial classes. SurA homologues in later proteobacteria predominantly contain two PPIase domains, with this architecture present in 92% and 88% of sequences from the β- and γ-classes, respectively (Fig. 1c). The results indicate that two PPIase domains within SurA have been acquired and conserved during evolution, suggesting that they confer an evolutionary advantage.

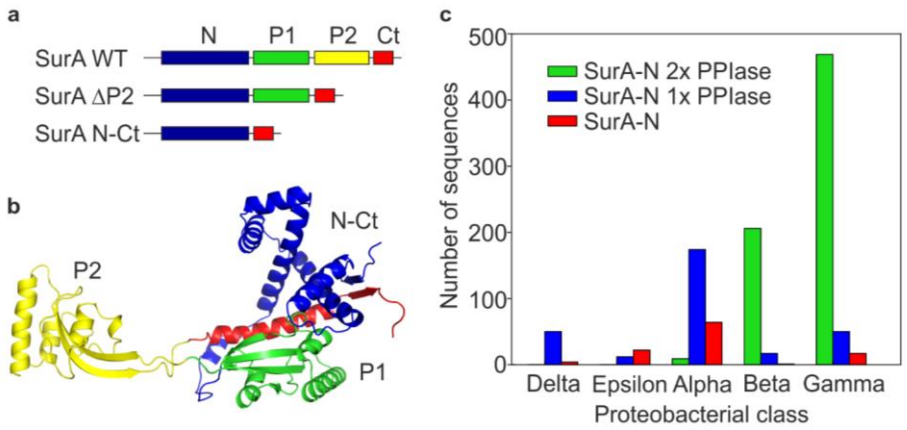

Figure 1: Domain architecture and conservation of the SurA chaperone. (a) Domains in *E. coli* SurA and deletion variants. (b) Crystal structure of wild-type SurA. (c) Multiple PPIase domains in SurA homologues are conserved in later proteobacteria.

To assess whether any single characteristic of OMP sequences correlates with the predominance of SurA homologues containing two PPIase domains in β- and γ-proteobacteria, the properties of 350,000 predicted OMP sequences from different proteobacterial classes were analysed. Interestingly, we found no clear correlation between

the sequence length, number of β-strands, hydrophobicity, amino acid content or aggregation propensity, and the addition and conservation of multiple PPIase domains in SurA homologues in β- and γ-proteobacterial species. We next investigated the role of the PPIase domains in SurA function by deleting one or both PPIase domains from *E. coli* SurA (Fig. 1a) and assessed the ability of the resulting SurA variants to bind and prevent the aggregation of two model OMPs, tOmpA (8-stranded,19 kDa) and OmpT (10-stranded, 33 kDa) (Fig. 2). The results show that tOmpA aggregation is effectively prevented by SurA WT, and SurA variants with one (SurA ΔP2) or both (SurA NCt) PPIase domains removed. By contrast, only SurA WT prevented the aggregation of OmpT. Surprisingly, an *increase* in OmpT aggregation was observed upon addition of increasing amounts of the SurA domain deletion variant. Binding experiments using microscale thermophoresis (MST) correlated with the aggregation data. A low μM K_d was measured for tOmpA binding to all SurA variants, as well as OmpT binding to SurA WT. However, no binding curve was observed for OmpT binding to either of the SurA domain deletion variants, suggesting that SurA PPIase domains are required to recognise the larger OmpT client.

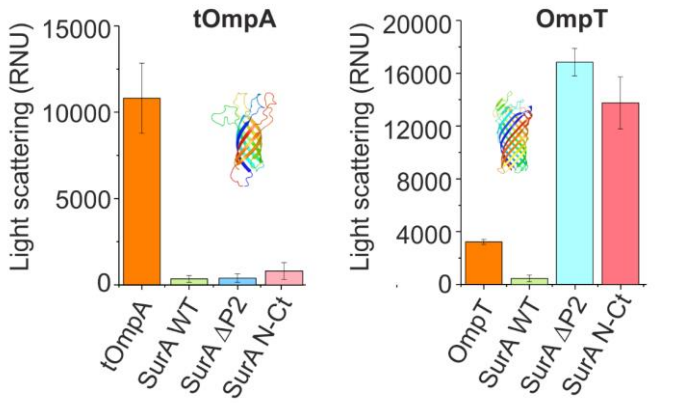

Figure 2: Extent of tOmpA (left) and OmpT (right) aggregation in the presence of SurA WT and domain deletion variants. Data for a 100-fold excess of chaperone is shown. Aggregation was measured by nephelometry at a 30 minute time point.

Overall, the results demonstrate that the core domain of SurA endows its generic chaperone ability, while the presence of PPIase domains enhances its chaperone activity for specific OMPs, suggesting one reason for the conservation of multiple PPIase domains in SurA in proteobacteria. Future work will now focus on two areas: (1) the molecular details of SurA-OMP interactions, in particular the location of binding sites and how coordination between domains enables chaperone behaviour, and (2) the role of the SurA domains in delivery of the OMP substrates to the BAM complex. This information may inform new strategies to control bacterial infections as the OMP assembly pathway is essential, extracytoplasmsic, and widely conserved across Gram-negative pathogens, and therefore an excellent potential antibiotic target.

Publications

Humes, J.R., Schiffrin, B., Calabrese, A.N., Higgins, A.J., Westhead, D.R., Brockwell, D.J., Radford, S.E. (2019) The role of SurA PPIase domains in preventing aggregation of the outer membrane proteins tOmpA and OmpT. *J. Mol. Biol.*, 2019. **431**, 1267-83.

Funding

This work was funded by the BBSRC, the Wellcome Trust, and the NIH.

Collaborators

University of Leeds: David R. Westhead

Combining transient expression and cryo-EM to obtain high-resolution structures of Luteovirid particles

Matthew Byrne, Emma Hesketh, Rebecca Thompson, Miriam Walden and Neil Ranson

Introduction

Plant viruses are responsible for global economic losses estimated in excess of 30 billion dollars each year. Ranking amongst the most destructive of these viruses is a family known as the Luteoviridae. The Luteovirids infect a wide range of food crops, including cereals, legumes, cucurbits, sugar beet, sugarcane, and potato and, as such, are a major threat to global food security. A molecular-level understanding of how Luteovirids are carried by their aphid vectors could allow the design of new agrochemicals that stop the spread of these viruses. To this end, we set out to characterise the capsids of the type-species in each of the three Luteoviridae genera by cryo-EM.

Results

To allow structural characterization of the Luteovirid type-species capsids by cryo-EM, we expressed Barley yellow dwarf virus (BYDV), Potato leafroll virus (PLRV), Pea enation mosaic virus (PEMV) virus like particles (VLPs) in plants using the pEAQ-HT vector system. This system allows the placement of the sequence to be expressed between a modified 5' untranslated region (UTR) and the 3' UTR from cowpea mosaic virus RNA-2, ensuring high levels of expression of the resulting mRNA. Following expression, plant material was harvested and VLPs were purified to homogeneity, before being analysed by electron microscopy.

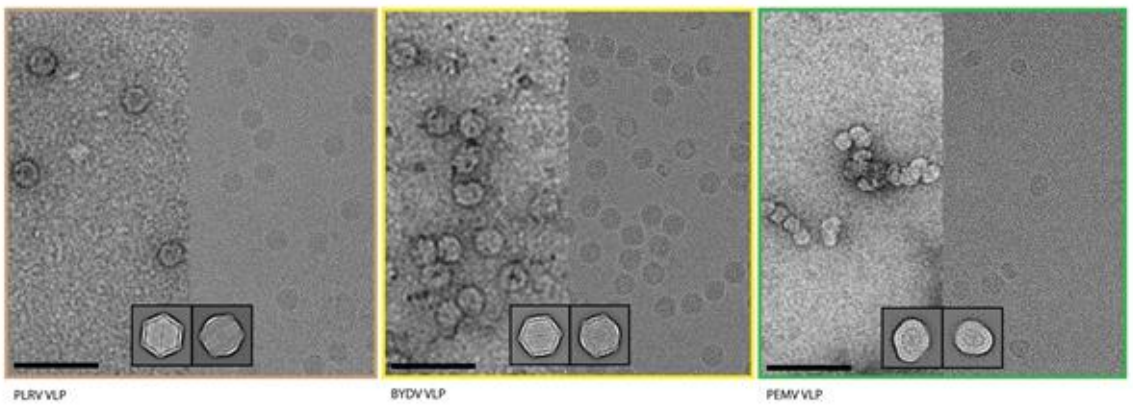

Figure 1: BYDV and PLRV VLPs form stable capsids.
Representative cryo-EM and negative-stain micrographs for each of the Luteovirid VLPs. Inset: representative 2d classes from cryo-EM data collection. (Left) Potato leafroll virus VLPs. (Middle) Barley yellow dwarf virus VLPs. (Right) Pea enation mosaic virus 1 VLPs. Scale bar represents 100 nm at magnifications shown.

BYDV and PLRV coat proteins (CPs) assembled into monodisperse, homogeneous particles of the anticipated diameter (Figure 1). However, PEMV1 CP assembled into amorphous, aggregation-prone particles, a phenomenon that persisted when imaged using cryo-EM (Figure 1).

When analysed by cryo-EM, both BYDV and PLRV VLPs were mono-disperse (Figure 1), so datasets were collected for each. Image processing yielded density maps at a resolution of 3.0 Å for BYDV and 3.4 Å for PLRV. Density maps for each structure were of sufficient quality and resolution to allow unambiguous building of the shell (S) domain of the CP. In both cases the N-terminal R (RNA-binding) domain is not resolved in the cryo-EM density, except in the 'C' conformer of BYDV, where an additional six residues of the R domain (residues 55–60) are visible. The structures for BYDV and PLRV each reveal a Luteovirid capsid composed of 180 CP monomers. The CP monomers each contain a single canonical

jellyroll fold, and are arranged with T= 3 icosahedral quasi-symmetry to give a particle with a diameter of 30 nm.

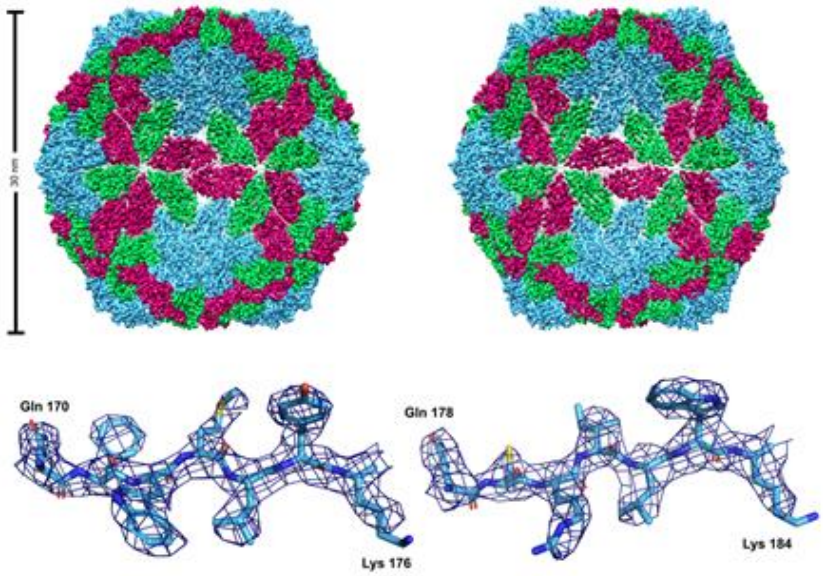

Figure 2: Cryo-EM Structures of Luteovirid Capsids BYDV (left) and PLRV (right). Top: cryo-EM maps of whole virus capsid, coloured according to CP quasi-conformers, where subunit A is blue, subunit B is green, and subunit C is red. Bottom: section of representative density and molecular model for each virus.

The capsids described in our paper answer long-standing questions about the luteovirids. In the past, insights into their architecture have been limited to those from homology modelling or biophysical analyses, such as chemical crosslinking and mass spectrometry. Although we were unable to produce monodisperse PEMV VLPs amenable to structural characterisation by cryo-EM, we were able to utilise our experimental BYDV and PLRV structures as templates in the generation of a PEMV homology model – providing atomic models for the capsids of the type-species in each of the three Luteoviridae genera. We therefore provide a platform from which Luteovirid interactions with their insect vectors can be rationally interrogated at the molecular level, towards the prevention of Luteovirid infection of important food crops.

Funding
This work was supported by the UK Biotechnological and Biological Sciences Research Council BB/R00160X/1.

Publications
Byrne, M.J., Steele, J.C., Hesketh, E.L, Walden, M., Thompson, R.F, Lomonossoff, G.P. & Ranson, N.A. (2019). Harnessing the power of biotechnology and cryo-EM for new discovery in plant structural virology. *Structure,* **27**, 1-10.

Collaborators:
External: John Steele, George Lomonossoff (John Innes Centre, Norwich, UK).

Multivalent recognition at fluid surfaces

Ralf Richter

Introduction

The interaction between a biological membrane and its environment is a complex process: it involves multivalent binding between ligand/receptor pairs, which can self-organize in patches. Any description of the specific binding of biomolecules to membranes must account for the key characteristics of multivalent binding, namely, its unique ability to discriminate sharply between high and low receptor densities (a property also termed 'superselectivity'), but also for the effect of the lateral mobility of membrane-bound receptors to cluster upon binding. A systematic quantitative analysis of the interplay of these two aspects had previously been challenging owing to the lack of well-defined experimental systems for study.

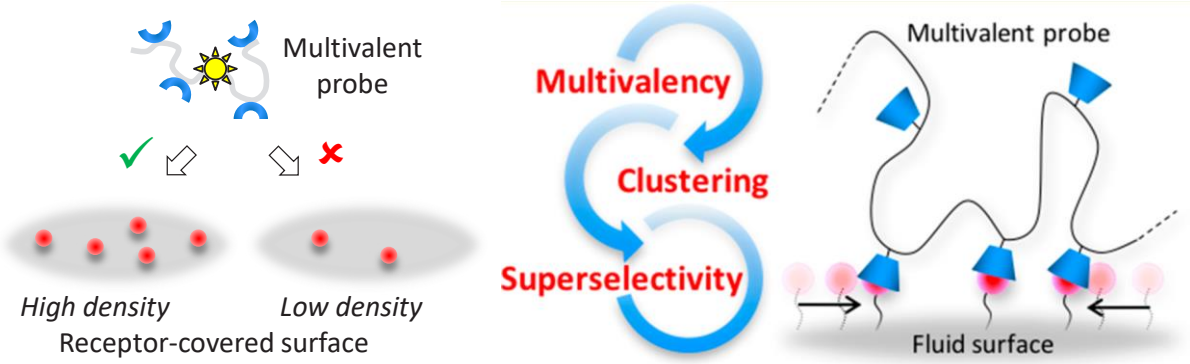

Figure 1: Illustration of key characteristics of multivalent binding to surfaces: superselective recognition (left) and probe-induced receptor clustering (right). Our work defines the interplay between these two aspects, using probes made from linear polymers with multiple ligands.

Results

We have developed an experimental model system – based on host-guest chemistry and probes made with the extracellular matrix polysaccharide hyaluronan – that allows us to compare systematically the effects of multivalent interactions on fluid and immobile surfaces. A crucial feature of our model system is that it allows to independently control the membrane surface chemistry, the properties of the multivalent binder, and the binding affinity. We find that multivalent probes retain their superselective binding behaviour at fluid interfaces. Supported by numerical simulations, we demonstrate that, as a consequence of receptor clustering, superselective binding is enhanced and shifted to lower receptor densities at fluid interfaces.

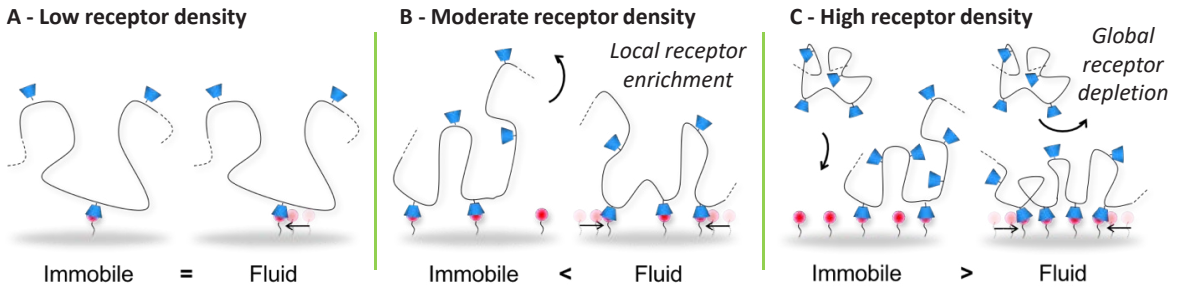

Figure 2: Illustration of the main binding regimes. (**A**) At low receptor densities, binding is monovalent and probes bind immobile and fluid surface equally well. (**B**) At moderate receptor coverage, binding becomes multivalent and recruitment of additional receptors occurs in the fluid case, which increases overall binding (local enrichment of guests). (**C**) At high receptor coverage, the initially adsorbed polymers recruit most of the laterally mobile receptors, which limits further multivalent interactions and thus decreases overall binding (global depletion of guests). A fourth regime of very high guest surface densities is not shown here, where steric exclusion limits binding and binding is again the same for immobile and fluid surfaces.

To translate our findings into a simple, predictive tool, we develop an analytical model that enables rapid predictions of how the superselective binding behaviour is affected by the lateral receptor mobility as a function of the physico-chemical characteristics of the multivalent probe.

The obtained knowledge should facilitate rationalizing multivalent binding to biological membranes, and thereby contribute to understanding the mechanisms of cellular communication. Our model, which captures the key physical mechanisms underpinning multivalent binding to biological membranes, will also greatly facilitate the rational design of nanoprobes for the superselective targeting of cells and tissues. We have particular interest in exploiting our findings to develop probes for the superselective targeting of cancer cells for biomedical applications.

Publications

Dubacheva, G. V., Curk, T., Frenkel, D. & Richter, R. P. (2019) Multivalent Recognition at Fluid Surfaces: The Interplay of Receptor Clustering and Superselectivity. *J Am Chem Soc* **141**: 2577-2588.

Funding

This work was funded by the European Union (Marie Curie Actions and European Research Council), the Chinese Academy of Sciences, the Slovenian Research Agency, and the EPSRC.

Collaborators

External: Galina V. Dubacheva (CIC biomaGUNE, San Sebastian, Spain & École Nationale Supérieure, Cachan, France; now University Grenoble Alpes, France), Tine Curk (Chinese Academy of Sciences, Beijing, China & University of Maribor, Slovenia, now Northwestern University, Illinois, United States), Daan Frenkel (University of Cambridge, UK)

A *trans*-acting cyclase off-loading strategy for non-ribosomal peptide synthetases

Asif Fazal, Divya Thankachan, Daniel Francis, Michael Webb and Ryan Seipke

Introduction

Non-ribosomal peptides are a large family of structurally complex and diverse natural products, some of which are important antibiotics (*e.g.*, penicillin, vancomycin, daptomycin, tyrocidine). They are biosynthesised by large modular multidomain enzymes called non-ribosomal peptide synthetases (NRPSs), which are organised into relatively independently functioning modules composed of single enzymatic domains that work in an assembly line-like manner until the final polypeptide structure is generated. During biosynthesis, the growing peptide chain remains covalently linked to the 4´-phosphopantetheinyl cofactor of the peptidyl carrier protein (PCP) domains. The terminal module usually possesses a C-terminal thioesterase (TE) domain, which off-loads the terminal peptide intermediate from the PCP onto a conserved serine residue whereby either a hydrolytic or macrocylisation reaction occurs to produce the mature peptide. Surugamides are produced by an unusual NRPS biosynthetic pathway composed of four NRPS enzymes (Fig. 1); two of these (SurAD) make cyclic octapeptide antibiotics named surugamide A-E and acylsurugamide A, which harbours an unusual butylated L-Lys residue; the remaining two (SurBC) make a cyclic decapeptide named cyclosurugamide F. An intriguing feature of the surugamide biosynthetic pathway is that the terminal biosynthetic modules of SurC and SurD lack a traditional C-terminal TE domain, which begs the question: how do the final peptides get off-loaded and cyclised?

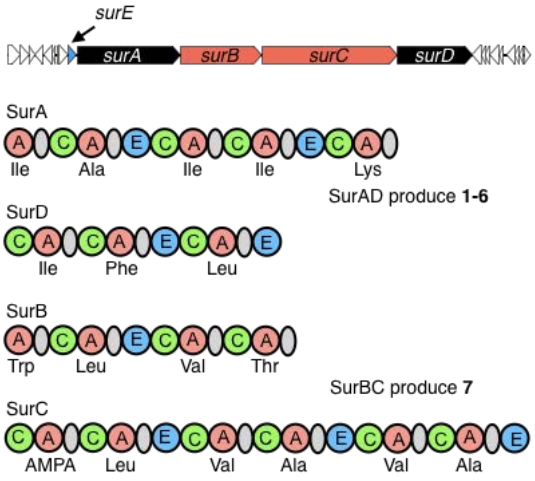

Figure 1: The surugamide biosynthetic gene cluster and its products. A, adenylation domain; C, condensation domain; E, epimerase domain; AMPA, 3-amino-2-methylpropionic acid. Grey ovals indicate peptidyl carrier proteins. Blue shading indicates the bond formed during SurE cyclisation.

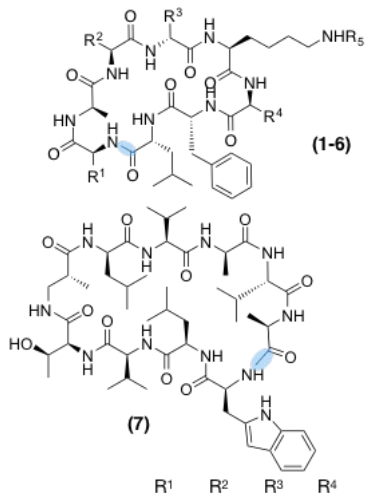

	R^1	R^2	R^3	R^4	R^5
surugamide A (**1**)	L-Ile	D-Ile	L-Ile	L-Ile	H
surugamide B (**2**)	L-Ile	D-Val	L-Ile	L-Ile	H
surugamide C (**3**)	L-Val	D-Ile	L-Ile	L-Ile	H
surugamide D (**4**)	L-Ile	D-Ile	L-Val	L-Ile	H
surugamide E (**5**)	L-Ile	D-Ile	L-Ile	L-Val	H
acyl-surugamide A (**6**)	L-Ile	D-Ile	L-Ile	L-Ile	butryl

Results

The absence of an obvious *cis*-acting mechanism for off-loading the final peptide from the terminal PCP domains of SurC and SurD led us to hypothesise that one or more *trans*-acting (or standalone) release factors may be encoded by genes within the surugamide biosynthetic gene cluster (BGC). Inspection of other genes within the BGC revealed the presence of a gene (*surE*) which encodes a protein belonging to InterPro Family IPR012338, indicating it is a member of the β-lactamase superfamily, which includes transpeptidases and esterases. Analysis of SurE indicates that it possesses the Ser-Lys-Tyr-His tetrad active site motif characteristic of Class C β-lactamases and that it is phylogenetically distinct from

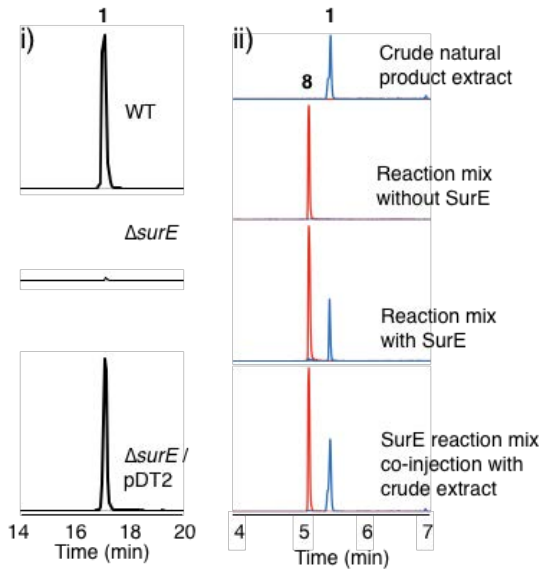

Figure 2: *surE* is essential for the production of surugamide A *in vivo* F. i) LC-HRMS analysis of chemical extracts prepared from the indicated strains. The *m/z* corresponding to the $[M+H]^+$ ion derived from **1.** ii) LC-HRMS analysis of *in vitro* SurE reaction with SNAC-surugamide A. The *m/z* corresponding to the $[M+H]^{2+}$ ions derived from **1** (blue, $C_{48}H_{81}N_9O_8$) and the SNAC substrate (red, $C_{52}H_{90}N_{10}O_9S$) are shown. The intensity scale for all EICs depicted in A and B is $1x10^6$.

type I and type II thioesterases. In order to test whether *surE* encodes a *trans*-acting off-loading factor, we deleted *surE* in *S. albus* and tested, by LC-HRMS, the resulting mutant strain for its ability to produce **1**. This revealed that only a trace amount of **1** was detectable in the extract prepared from the Δ*surE* strain (Fig. 2i) Complementation of the Δ*surE* mutant with pDT2, which contained the *surE* gene under the control of the constitutive *ermE** promoter, restored production of **1** to near wild-type levels and verified that loss of its production was not due to another mutational event (Fig. 2i). We conclude that SurE is required for the production of **1** presumably because it off-loads the linear aminoacyl-S-thioester intermediate and performs a head-to-tail cyclisation reaction to result in **1.** Next, we synthesized an *N*-acetylcysteamine (SNAC) thioester mimic of **1** and purified the SurE protein and assessed its ability to utilise this substrate. When SurE is incubated with SNAC-surugamide A it catalyzes the formation of **1** as judged by LC-HRMS/MS (Fig. 2ii). Our data unambiguously demonstrate that SurE is a *trans*-acting cyclase that off-loads the terminal linear aminoacyl-S-thioester intermediate of surugamide A and performs head-to-tail cyclisation reactions to result in **1.**

In summary, we have identified and characterised *in vivo* and *in vitro* a trans-acting release factor, SurE, that off-loads surugamide A via macrolactamization from its assembly line. This work improves the paradigmatic understanding of how non-ribosomal peptides are off-loaded from terminal PCP domains in NRPS assembly lines and in the process has identified a stand-alone (thereby more amenable to augmentation) release factor that could aid in reengineering of non-ribosomal peptide biosynthesis.

Publications

Thankachan D., Fazal A., Francis, D., Song L., Webb, M.E., & Seipke R.F. (2019) A *trans*-acting cyclase offloading strategy for nonribosomal peptide synthetases. *ACS Chem Biol* **14 (5)**, 845-849.

Funding

This work was funded the University of Leeds.

Collaborators

External: Lijiang Song (University of Warwick)

Structural mechanism of synergistic activation of Aurora kinase B/C by phosphorylated INCENP

Sneha Chatterjee and Frank Sobott

Introduction

Aurora kinases are essential for cell proliferation; Aurora kinase C (AURKC) is activated by binding to the C-terminal domain of the inner centromere protein (INCENP). Full activation requires phosphorylation of two serine residues of INCENP that are conserved throughout evolution. Here we study the structure of the fully active complex of phosphorylated AURKC bound to INCENP, which is phosphorylated on its TSS motif. Crystal structures obtained in collaboration with Jon Elkins (SGC Oxford), in conjunction with structural MS data, show that TSS motif phosphorylation stabilises the kinase activation loop of AURKC. The TSS motif phosphorylations alter the substrate-binding surface consistent with a mechanism of altered kinase substrate selectivity and stabilisation of the protein complex against unfolding. Our data reveal the structural and biochemical mechanism of synergistic activation of AURKC:INCENP.

Results

The crystal structure shows how phosphorylated INCENP makes extensive hydrogen-bonding interactions with the activation loop and αC-helix of AURKC, and contributes significantly to arranging the active conformation and substrate binding region of the kinase (Fig. 1).

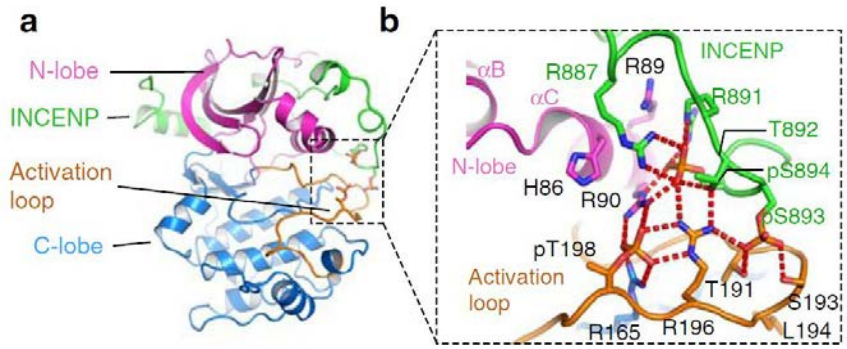

Figure 1: The phosphorylated INCENP "IN-box" binds the activation loop of Aurora kinase C tightly

Seeing that the TSS motif phosphorylations were involved both in stabilising the conformation of the activation loop and in stabilising helix αC, we speculated that a lack of TSS motif phosphorylation would alter the substrate affinity/selectivity of the Aurora:INCENP complex. To test this hypothesis, we overexpressed and purified AURKC:INCENP complexes containing TSS motif mutations S893A or S894A, which prevent phosphorylation. We also tested W897A; Trp897 is adjacent to the TSS motif and forms substantial binding interactions with AURKC. All three mutations resulted in a reduced rate of reaction with peptide substrate, as well as a reduced rate of auto-phosphorylation in the absence of a peptide substrate. This leads to the conclusion that INCENP TSS motif phosphorylation changes the substrate selectivity of the AURKC complexes, as expected for a mechanism in which phosphorylated INCENP stabilises the activation loop and these two motifs together provide the binding site for the substrate.

We prepared complexes of AURKC:INCENP, AURKC:INCENP-S894A and AURKC:INCENP-S893A/S894A/W897A. S894A would be expected to disrupt the majority of the hydrogen bonding around the phosphorylated TSS motif, while the triple-mutant complex was prepared to give the maximum chance of distinguishing the effect of the TSS motif. We hypothesised that the mutant complexes would have greater structural flexibility in the region of the TSS motif, which would be less strongly bound to AURKC. We utilised native electrospray ionisation (ESI) with ion mobility-mass spectrometry (IM-MS) to measure the

degree of complex formation (% bound, at a concentration of 10 µM), collision cross sections (rotationally averaged sizes, CCS) and intrinsic stabilities (gas-phase collision-induced

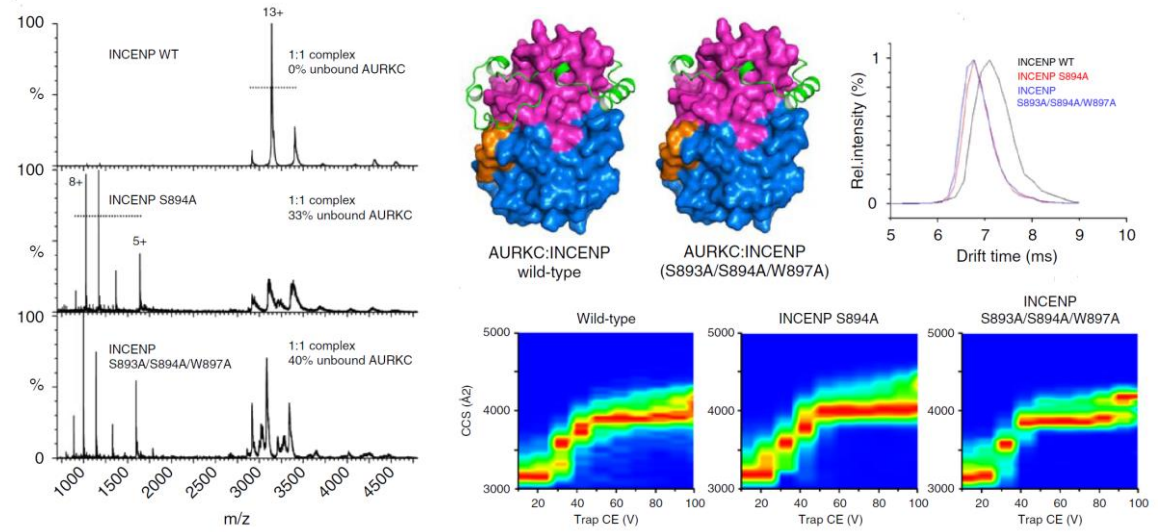

Figure 2: TSS motif binding affects AURKC:INCENP binding and the overall compactness of the complex.
Left: Native mass spectra of AURKC:INCENP complexes show that, under the same gentle ionisation conditions, the wild-type complex remains intact while the non-phosphorylated INCENP mutants are only partially bound (free INCENP at m/z 1000-2000).
Top right: Models derived from the crystal structures show the effect of loss of TSS motif binding from a phosphorylated and ordered INCENP TSS motif (wild type) to an unphosphorylated TSS motif and dis-ordered C-terminal part of INCENP (triple mutant). Drift time profiles derived from ion mobility experiments show that wild-type AURKC:INCENP complexes are overall less compact (longer drift times; black curve) than those with the single or triple mutant INCENP, as expected from the models.
Bottom right: Collision-induced unfolding plots, i.e. T_m-shift like experiments inside the mass spectrometer, show that the AURKC:INCENP mutant complexes reach the greatest extension already at lower activation energies as well as additional unfolding steps, consistent with greater structural flexibility.

unfolding profiles) of these AURKC:INCENP complexes (Fig. 2).

Single and triple mutants of INCENP, which reduce or abolish TSS motif phosphorylation, show a weakening of the interaction with AURKC and greater structural flexibility, as evidenced by native MS and ion mobility data. Interfering with INCENP TSS motif binding to AURKC may be an interesting anti-mitotic strategy; but it remains an open question to what extent differing effects of Aurora kinase inhibitors may be due to weakening of INCENP binding and/or alteration of substrate binding.

Publications

Abdul Azeez KR, Chatterjee S, Yu C, Golub TR, Sobott F, Elkins JM. (2019), Structural mechanism of synergistic activation of Aurora kinase B/C by phosphorylated INCENP, *Nat Commun*. **18**;10(1):3166

Funding

This work was funded by a PhD research grant from the Agency for Innovation by Science and Technology (IWT-Flanders, Belgium) to Sneha Chatterjee.

Collaborators

External: Kamal R. Abdul Azeez, Jonathan M. Elkins (Structural Genomics Consortium, University of Oxford) Channing Yu, Todd R. Golub (Broad Institute, Boston, USA).

Clinical pharmacokinetics of a lipid-based formulation of risperidone

Paul Taylor

Introduction

Our preclinical studies showed that a formulation, VAL401, of risperidone with the naturally occurring conjugated linoleic acid known as rumenic acid (9-*cis*,11-*trans*-linoleic acid) provides potential anticancer activity, while preclinical testing of unformulated risperidone did not. Herein, we start to explore how rumenic acid affects the pharmacokinetic distribution of risperidone in humans.

Results

We conducted a phase 2 clinical trial in late-stage non-small cell lung cancer patients to assess the safety, tolerability, pharmacokinetics and efficacy of VAL401 in the treatment of patients with locally advanced or metastatic non-small cell lung adenocarcinoma. By measuring the blood concentrations of both risperidone and its primary metabolite, 9-hydroxyrisperidone, after a single oral dose, the combined efect of the new formulation in the specifed population was compared with historic data on the absorption, metabolism and clearance of risperidone. The mean concentration–time data collected for all eight patients are presented in Fig. 1.

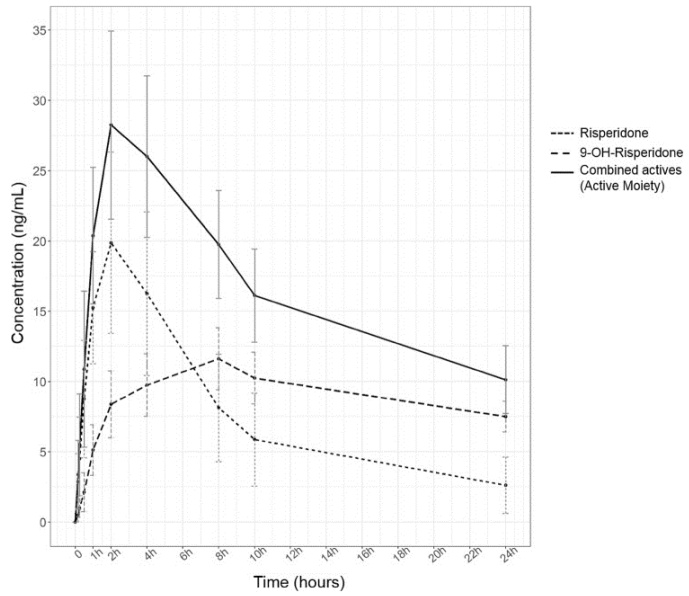

Figure 1: Mean concentrations in plasma plotted as time courses for risperidone (dotted line), its active metabolite 9-hydroxyrisperidone (dashed line) and the total active moiety risperidone (solid line).

While our values for AUC, C_{max} and clearance of risperidone alone and in combination with 9-hydroxy-risperidone are very similar to the manufacturer's data, the half-life values from the present work are shorter. The plasma protein binding levels for risperidone and 9-hydroxyrisperidone are 89% and 74%, respectively. Hence, a possible explanation for the difference in the pharmacokinetic profiles is that more of the active moiety is present as risperidone rather than 9-hydroxyrisperidone, leading to increased binding of the active moiety by plasma proteins when using VAL401. This would be consistent with increased lymphatic uptake and decreased "first pass" hepatic metabolism.

Publications

Dilly S.J., Morris G.S., Taylor, P.C., Parmentier, F., Williams, C., Afshar, M. (2019) Clinical Pharmacokinetics of a Lipid‐Based Formulation of Risperidone, VAL401: Analysis of a Single Dose in an Open‐Label Trial of Late‐Stage Cancer Patients. *Eur. J. Drug Metab. Pharmacokinet.*, **44**, 557-565.

Funding

This work was funded by ValiSeek Ltd.

Collaborators

External: S.J. Dilly, G.S. Morris (ValiSeek Ltd), F. Parmentier, C. Williams, M. Afshar (Ariana Pharmaceuticals).

Structural studies of avian reovirus RNA chaperone σNS

Jack Bravo, Alexander Borodavka, Rebecca Thompson, Neil Ranson, Joseph Cockburn and Roman Tuma

Introduction

Reoviruses are human, animal and plant pathogens exhibiting a multi-layered icosahedral shell that encloses a segmented dsRNA genome, encompassing up to twelve unique RNA molecules. Each viral particle harbours an exact number of segments, which are all essential for replication in the host cell. The genomic segments are packaged as single-stranded precursors and replicated into dsRNA inside nascent viral particles by a virion-associated RNA-dependent RNA polymerase. However, the specific mechanism of packaging the exact number of segments remains elusive. We use avian reovirus (AVR) as a model system to study the packaging mechanism. AVR, as many other reoviruses, replicates within cytoplasmic viral inclusion bodies (VIB), the viroplasms, which are also known as viral factories. VIBs are membrane-less organelles formed with the help of abundant viral non-structural proteins. In the case of AVR these are μNS and σNS, the former serving as a 'scaffold' for VIB formation while the latter being an RNA chaperone. It is thought that the RNA chaperone resolves non-specific RNA-RNA interactions in favour of specific pairing between segment precursors, leading to a hypothetical 'assortment complex' which contains the complete set of segments. Further progress in the delineation of the packaging mechanism and the role of the σNS chaperon is hindered by the lack of high-resolution structural information. Using small angle X-ray scattering we have established that σNS apoprotein is a predominantly elongated hexamer while, upon addition of RNA, it further oligomerized into octamers. Such heterogeneity precluded obtaining diffracting crystals and hence we turned to electron cryo-microscopy followed by image analysis and classification to deal with the structural heterogeneity, with the hope to obtain high resolution structural information by single particle reconstruction.

Results

Protein concentration was optimized to about 1 mg/ml in order to obtain micrographs populated with high numbers of oligomers without overlap. Images were recorded from

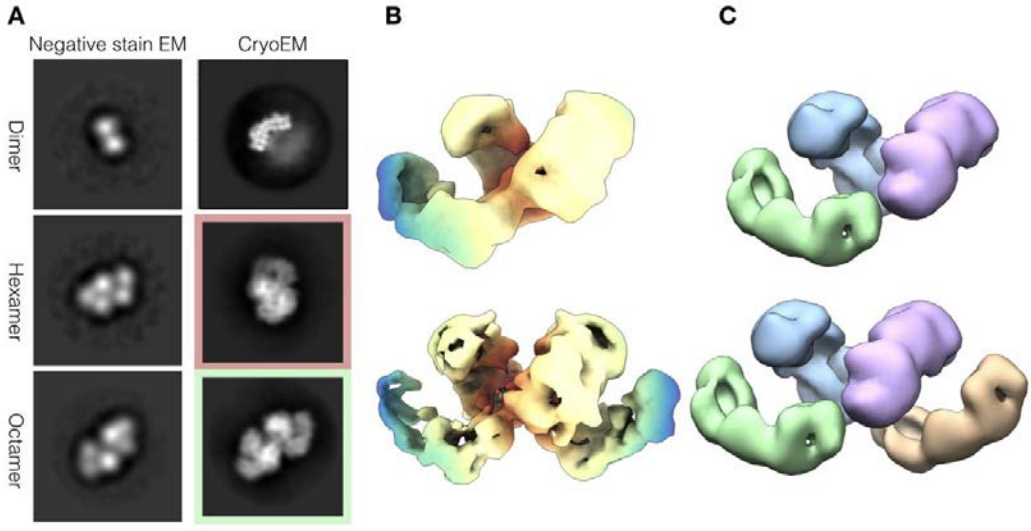

Figure 1: (A) 2D class averages from negative stain EM (left) and cryoEM (right) of dimeric, hexameric and octameric species. (B) Initial 3D classes corresponding to hexamers (A, pink box) and octamers (A, green box). (C) initial 3D models of the dimer fitted into 3D class averages of hexamer and octamer, respectively, revealing plausible quaternary organisation.

vitrified grids using a Titan Krios equipped with a K2 detector. Corrected images (motion, contrast transfer) yielded over a million extracted particles (1,011,851) which were subsequently classified into three major species: dimers, hexamers and octamers. These

species were confirmed by negative stain (Figure 1A). The initial class averages of the hexamer and octamer (Figure 1B) indicated a dimer as a plausible building block (Figure 1C).

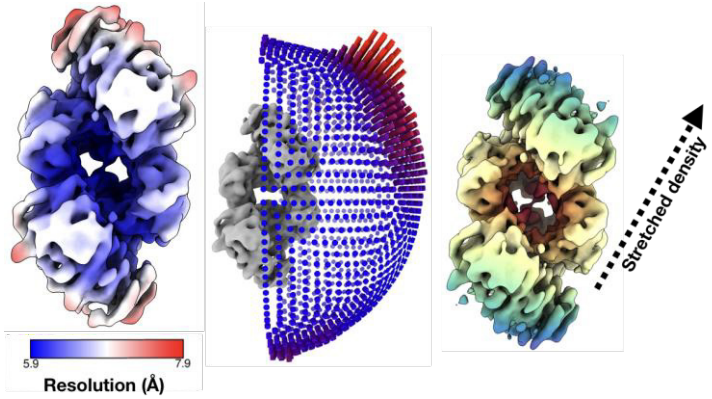

Figure 2: (Left) Local resolution of σNS octamer. Resolution ranges from 5.9Å in the centre of the particle to 7.9Å at the periphery. (Middle) Angular distribution plot of octamer reconstruction (C2 symmetry). Strong preferred orientation is present, resulting in stretched density in the final reconstruction (right) in the plane of the preferred orientation.

Particle images were subjected to further rounds of 2D and 3D classifications and images belonging to octameric species were selected (154,617) and subjected to reconstruction using C2 symmetry, yielding density with an overall resolution of 6.7Å (local resolution ranging from 5.9 to 7.9Å, Figure 2). However, the uneven sampling of particle orientations led to an apparent directional stretch of the density. The final map confirms pseudo-helical quaternary structure built from dimers that create a deep groove spiralling around the oligomer, which may serve as the RNA binding site.

Funding
This work was funded by BBSRC and the Wellcome Trust.

Arbovirus replication and host–cell interactions

Andrew Tuplin

Introduction

Chikungunya virus (CHIKV) is a re-emerging, pathogenic *Alphavirus* transmitted to humans by *Aedes spp.* mosquitoes. We have mapped the RNA structure of the 5' region of the CHIKV genome using selective 2'-hydroxyl acylation analysed by primer extension (SHAPE) to investigate intramolecular base-pairing at single-nucleotide resolution. Taking a structure-led reverse genetic approach, in both infectious virus and sub-genomic replicon systems, we identified six RNA replication elements essential to efficient CHIKV genome replication—including novel elements, either not previously analysed in other alphaviruses or specific to CHIKV. Importantly, through a reverse genetic approach we demonstrate that the replication elements function within the positive-strand genomic copy of the virus genome, in predominantly structure-dependent mechanisms during efficient replication of the CHIKV genome. Comparative analysis in human and mosquito-derived cell lines reveal that a novel element within the 5'UTR is essential for efficient replication in both host systems, while those in the adjacent nsP1 encoding region are specific to either vertebrate or invertebrate host cells. In addition to furthering our knowledge of fundamental aspects of the molecular virology of this important human pathogen, we foresee that results from this study will be important for rational design of a genetically stable attenuated vaccine.

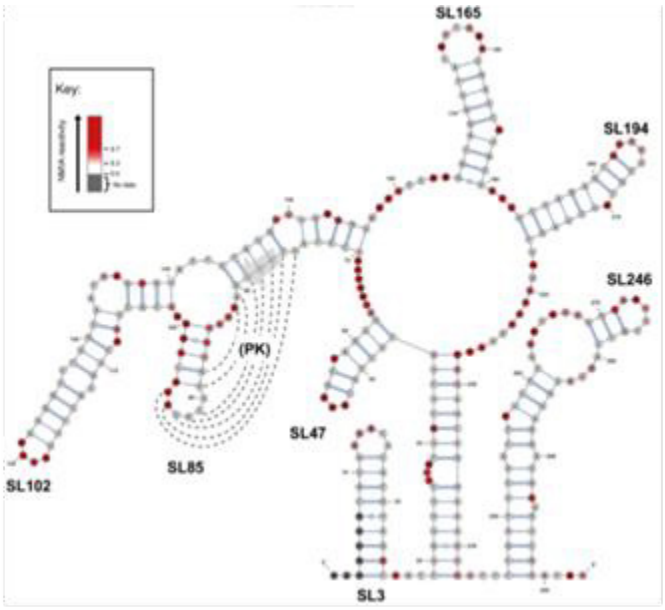

Figure 1: SHAPE reactivity thermodynamically derived model of Chikungunya virus RNA folding, generated using SHAPE-directed constraints. The AUG start codon of nsP1 is denoted by a grey arrow. SHAPE reactivities are shown as a heat map: grey indicates no data, white SHAPE reactivities between 0-0.3 and increasing intensities from light pink to dark red indicate increasing SHAPE reactivities, as denoted by the key. High reactivity (red) denotes unpaired nucleotides whereas low reactivity (white) denotes base-paired nucleotides. RNA replication elements are labelled SL3, SL47, SL85, SL102, SL165, SL194 and SL246. PK denotes a putative pseudoknot structure, where dotted lines represent potential base-pairing.

Publications

Lattimer, J., Stewart, H., Locker, N., Tuplin, A., Stonehouse, N.J., Harris, M. (2019). Structural and functional analysis of the equine hepacivirus 5′ untranslated region highlights the conservation of translational mechanisms across the hepaciviruses. *Journal of General Virology*.

Müller, M., Slivinski, N., Todd, E.J.A.A., Khalid, H., Li, R., Karwatka, M., Merits, A., Mankouri, J., Tuplin, A. (2019). Chikungunya virus requires cellular chloride channels for efficient genome replication. *PLoS Neglected Tropical Diseases*.

Gao, Y., Goonawardane, N., Ward, J., Tuplin, A., and Harris, M. (2019). Multiple roles of the non-structural protein 3 (nsP3) alphavirus unique domain (AUD) during Chikungunya virus genome replication and transcription. *PLoS Pathogens*.

Kendall, C., Khalid, H., Müller, M., Banda, D.H., Kohl, A., Merits, A., Stonehouse, N.J. and Tuplin, A. (2019) Structural and phenotypic analysis of Chikungunya virus RNA replication elements. *Nucleic Acids Research*. **47**, pp. 9296-9312

Collaborators:

University of Leeds: M. Harris, A. Zhuravleva, N. Stonehouse and J. Mankouri
External: Alain Kohl (MRC Centre for Virus Research, UK), Andrew Davidson (University of Bristol, UK) and Andres Merits (University of Tartu, Estonia).

Directed assembly of protein tubes

James Ross, Gemma Wildsmith, Michael Johnson, Daniel Hurdiss, Kristian Hollingsworth, Rebecca Thompson, Chi Trinh, Emanuele Paci, Mike Webb and Bruce Turnbull

Introduction

Protein self-assembly is ubiquitous in nature giving rise to diverse biological structures from microtubules to virus capsids. There is a growing interest in mimicking the programmed self-assembly of proteins for applications in synthetic biology and bionanoscience. Coiled-coil protein motifs lend themselves to rational design of supramolecular structures as their assembly properties can be predicted directly from the peptide sequence. In this project we have investigated a strategy for assembly of pentameric subunits for the cholera toxin into more complex architectures that is loosely inspired by the way that polyomaviruses use C-terminal peptide extensions to arrange their pentameric capsomeres into virus particles.

Results

Coiled-coil sequences were introduced at the C-terminus of the gene for the non-toxic sub-unit of cholera toxin. Following expression and purification of the resulting protein, a small number of spherical particles could be observed by negative stain electron microscopy. Upon incubation in ammonium sulfate solution, long extended protein assemblies were produced. However, the high salt concentration precluded structural analysis by cryo-EM. Nevertheless, crystallisation of the fusion protein led to the formation of protein tubes in which the unit cell comprised four pentamers connected by three observable trimeric coiled-coils located inside the tubes (Figure 1). Three of these short ribbons assemble to form protein rings with no additional coiled-coil interactions observable between the short ribbons. The rings then assemble into tubes that run throughout the crystal lattice. Fusion of coiled-coils to globular proteins has potential to become a generalised strategy for the directed assembly of proteins to create systems with more complex architectures.

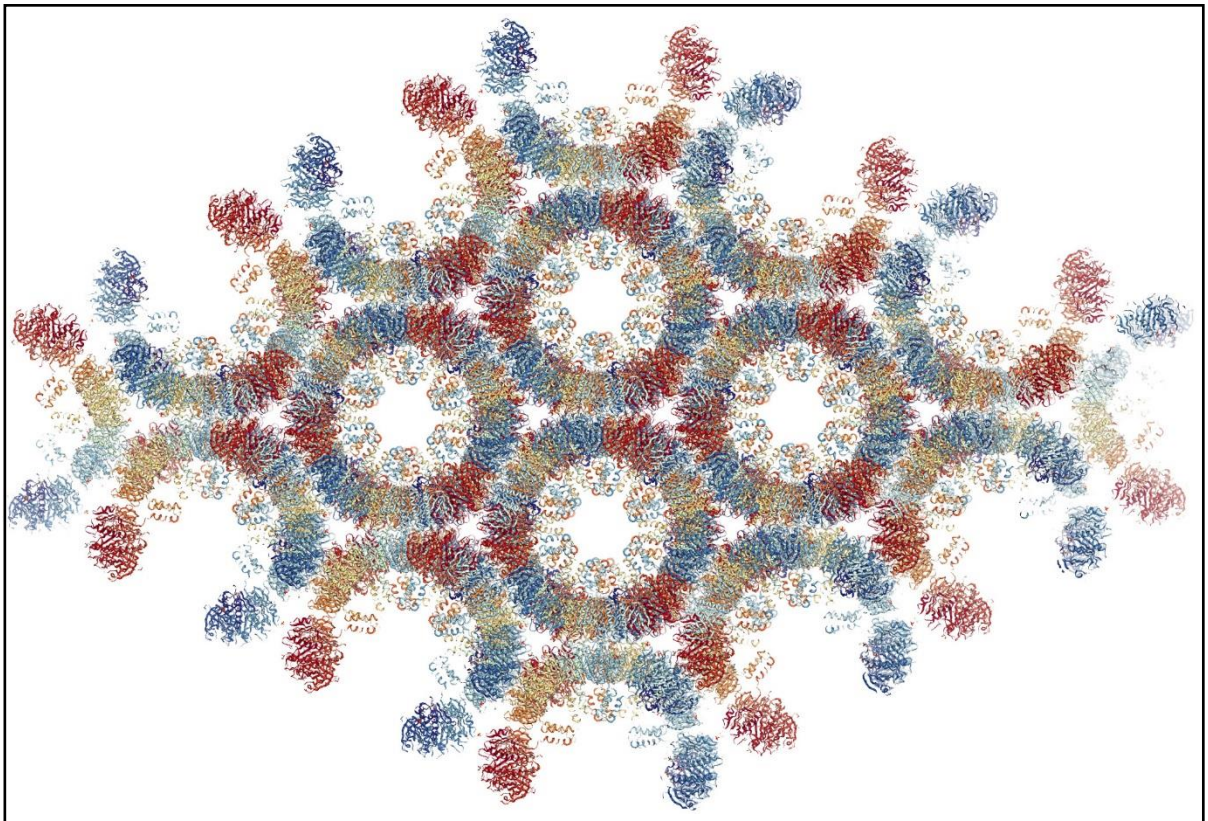

Figure 1: Protein tubes self-assembled from the non-toxic B-subunit of cholera toxin fused to a C-terminal coiled-coil sequence. The unit cell of the structure comprises four pentamers connected by three trimeric coiled-coils as seen to the left and right of the image. Image created from 6hsv.pdb.

Publications

Ross, J. F., Wildsmith, G. C., Johnson, M., Hurdiss, D., Hollingsworth, K., Thompson, R. F., Mosayebi, M., Trinh, C. H., Paci, E., Pearson, A. R., Webb, M, E., Turnbull, W. B. (2019) Directed Assembly of Homopentameric Cholera Toxin B-Subunit Proteins into Higher-Order Structures Using Coiled-Coil Appendages. *J. Am. Chem. Soc.* **141**: 5211-5219.

Turnbull, W. B., Imberty, A., Blixt, O. (2019) Synthetic glycobiology. *Interface Focus* **9**: 20190004

Huang, K., Parmeggiani, F., Ledru, H., Hollingsworth, K., Mas Pons, J., Marchesi, A., Both, P., Mattey, A. P., Pallister, E., Bulmer, G. S., van Munster, J. M., Turnbull, W. B., Galan, M. C., Flitsch, S. L. (2019) Enzymatic synthesis of N-acetyllactosamine from lactose enabled by recombinant β1,4-galactosyltransferases. *Org. Biomol. Chem.* **17**: 5920-5924.

Mahon, C. S., Wildsmith, G. C., Haksar, D., de Poel, E., Beekman, J. M., Pieters, R. J., Webb, M. E., Turnbull, W. B. (2019) A 'catch-and-release' receptor for the cholera toxin. *Faraday Disc.* **219**: 112-127.

Funding

This work was funded by the Wellcome Trust and BBSRC.

Collaborators

External: Arwen Pearson (University of Hamburg), Majid Mosayebi (University of Bristol)

Expanding the use of depsipeptides for protein modication by use of sortase

Zoe Arnott, Holly Morgan, Kristian Hollingsworth, Yixin Li, Jonathan Dolan, Darren Machin, Bruce Turnbull and Michael Webb

Introduction

Protein labelling is a key technique for biophysical and cellular studies of proteins. Quantitative and chemoselective labelling of proteins underpins many different techniques including fluorescence imaging, single molecule fluorescence and surface plasmon resonance. The principle focus of the research group is to develop new selective and quantitative approaches to such labelling. We have recently focussed on the use of the housekeeping protein sortase for this purpose.

Results

We have previously reported the use of depsipeptide substrates in tandem with sortase to quantitatively label proteins. These can effectively be used to label proteins containing an N-terminal glycine. Alternatively, proteins in which a recognition sequence is engineered into the protein can be labelled using a large excess of a peptide. We will shortly report our attempts to broaden work on the N-terminal labelling of proteins. We have investigated two principle areas – the optimisation of labelling using faster calcium-independent forms of the enzyme, and the use of enzymes with differential selectivity.

While sortase-labelling using the wild-type enzyme is effective, the timescale of labelling (~4 h) is not convenient for use in the laboratory. Additionally, the requirement for calcium means that some buffers must be avoided (e.g., phosphate buffers), and proteins that are sensitive to calcium cannot be labelled. We investigated the use of Srt7M, a heptamutant of sortase, which is both faster and calcium-independent. In tandem with our depsipeptide substrates we were able to quantitatively label a wide variety of proteins in under 30 minutes including the model protein MBP, fluorescent labelling cholera toxin for cellular tracing and biotinylation of PanD for study of its interaction with PanZ by SPR.

.

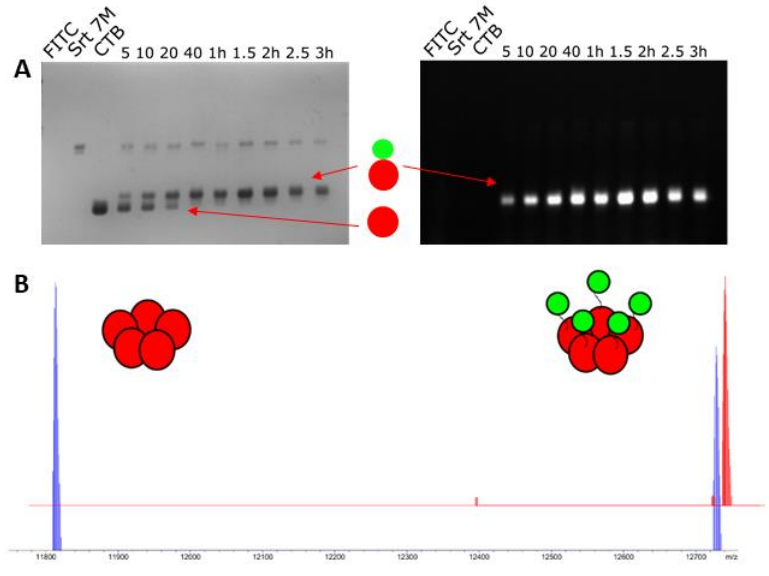

Figure 1: Quantitative labelling of Cholera toxin B subunit (CTB) using a fluorescein-containing substrate depsipeptide and sortase 7M **A** Time course of labelling of CTB using 5 mol% Srt 7M and 3 equivalents of a fluorescein peptide substrate at room temperature. Left: coomassie-stained, Right fluorescence image. Complete labelling can be observed after 40 minutes. **B** Electrospray mass spectrometry analysis of CTB labelling reaction during reaction (blue) and after 2 hours (red). After 2 hours, the unlabelled CTB cannot be detected.

A second challenge is labelling of proteins two or more times. In this case, we need to use sortases with different substrate specificities – many such enzymes have been reported but the effectiveness of combining depsipeptide substrates with these has not been assessed. We have now developed and assessed depsipeptide substrates for reported enzymes with many different substrate specificities including LPXTG, APXTG, LAXTG. FPXTG and LPXSG and have compared the cross-reactivity between the enzymes and other possible

substrates to identify sets which are mutually orthogonal. We are now applying these sets to the labelling of protein complexes with multiple N- and C-termini.

In summary, we have developed a number of effective methods for N-terminal labelling of proteins. Current work is now focussed on developing equivalent methods for C-terminal labelling.

Funding
This work was funded by BBSRC

Collaborators
University of Leeds: Stuart Warriner
External: Daniel Ungar (University of York)

Virus-host cell interactions: manipulation of a RNA modification pathway

Belinda Baquero-Perez, Oliver Manners, James Murphy, Sophie Schumann, Tim Mottram, Becky Foster, Zoe Jackson, Holli Carden, Katie Harper, Euan McDonnell, Freddy Weaver, Ellie Harrington and Ade Whitehouse

Introduction

Infection is a major cause of cancer worldwide. Viruses are associated with ~15% of human cancers, which approximates to about 2 million new cases every year in the world. We have utilised a range of cutting-edge transcriptomic and quantitative proteomic approaches to globally identify how the human tumour virus, Kaposi's sarcoma-associated herpesvirus (KSHV), affects the cellular environment to enhance its own replication and drive tumourigenesis. We have recently identified a novel cellular pathway that KSHV manipulates to enhance its own replication. This pathway, known as the m^{6}A methylation pathway, chemically adds a methyl group to adenosines in messenger RNA (mRNA). Once modified these mRNAs are then recognised by so-called 'm^{6}A reader' proteins which bind the m^{6}A chemically modified mRNA and then determine what happens to that modified mRNA.

Results

1. Mapping the KSHV m^{6}A methylome. We have developed dedicated software (m^{6}aViewer) which implements a novel m^{6}A peak-calling algorithm to identify high-confidence m^{6}A methylated residues in mRNAs. Utilising this software, we mapped m^{6}A modifications in the KSHV transcriptome by performing m^{6}A-seq. Results show that the KSHV transcriptome is heavily m^{6}A methylated, with 75 m^{6}A peaks being mapped in 42 KSHV ORFs.

2. Identification of a new family of m^{6}A readers. To determine whether any m^{6}A readers uniquely interact with m^{6}A methylated viral mRNAs, RNA affinity coupled to mass spectrometry analysis was performed. Intriguingly, eight members from the Tudor domain 'Royal family', including SND1 (Staphylococcal nuclease domain-containing protein 1), were specifically enriched using m^{6}A-modified KSHV sequences. This suggested that SND1 and perhaps other Royal family proteins were novel m^{6}A reader proteins. Electromobility shift assays demonstrated the ability of specific Royal domains to selectively bind m^{6}A-modified viral RNA, and a modified RIP-seq technique characterised for the first time the transcriptome-wide binding profile of SND1 to cellular and KSHV mRNAs. This revealed SND1 as a bona fide RNA-binding protein that targets m^{6}A-modified RNAs in KSHV-infected cells.

3. m^{6}A methylation is essential for KSHV lytic replication. Importantly, depletion of SND1 in KSHV-infected cells significantly reduced the stability of viral m^{6}A methylated RNAs, leading to a global impairment of KSHV lytic replication. These data identify SND1 as an essential m^{6}A reader for KSHV lytic replication and implicate the 'Royal family' as a new family of m^{6}A readers.

Publications

Baquero-Pérez, B., Antanaviciute, A., Yonchev, I.D., Carr, I.M., Wilson, S.A. & Whitehouse, A. (2019). The Tudor SND1 protein is an m^{6}A RNA reader essential for KSHV replication. *eLife*, **8**:e47261.

Manners, O., Baquero-Perez, B. & Whitehouse, A. (2019). Epitranscriptomics: widespread regulatory control in virus replication. *BBA Gene Regulatory Mechanisms, BA - Gene Regulatory Mechanisms* 1862, 370–381.

Harper, K.L., McDonnell, E. & Whitehouse, A. (2019). CircRNAs: from anonymity to novel regulators of gene expression in cancer. *International Journal of Oncology*, **55**, 183-193.

Smith, A.J., Wright, K.E., Muench, S.P., Schumann, S., Whitehouse, A., Porter, K.E. & Colyer, J. (2019). Styrene maleic acid recovers proteins from mammalian cells and tissues while avoiding significant cell death. *Scientific Reports* **9**(1):16408.

Funding
This work was funded by the BBSRC, MRC, Rosetrees Trust and Wellcome Trust.

Collaborators
University of Leeds: Andrew Macdonald, Jamel Mankouri, Andrew Smith
External: James Boyne (University of Bradford) and Stuart Wilson (University of Sheffield)

Inhibition of protein-protein interactions using designed molecules

Emma Cawood, Som Dutt, Zsofia Hegedus, Claire Grison, Kristina Hetherington, Fruzsina Hobor, Katherine Horner, Jennifer Miles, Thomas Edwards, Adam Nelson, Stuart Warriner, Michael Webb and Andrew Wilson

Introduction

This report summarises our ongoing efforts to develop methods to understand and modulate protein-protein interactions (PPIs). This represents a major challenge both in terms of providing tools to understand biomacromolecule structure/ function and tools to elaborate chemical probes. This report highlights two approaches to understand and modulate PPIs.

Results

A significant proportion of PPIs involve the docking of a helical epitope from one protein into a cleft on its partner. Using a generic scaffold to mimic the spatial and angular projection of "hot-spot" side chains of a peptide found at the PPI interface offers the potential to elaborate a rule-based approach for PPI inhibition, and to access more "drug-like" small molecules. We previously developed such topographical mimics of the α-helix and have now adapted this approach to develop a novel replacement strategy whereby a segment of protein structure (the S-peptide from RNase S) is replaced by a helix mimetic (Fig. 1). The resultant prosthetic replacement forms a non-covalent complex with the S protein leading to restoration of catalytic function, despite the absence of a key catalytic residue. The most effective ligand was shown to display pseudo-first order kinetics with enzymatic efficiency dependent on both concentration of proteomimetic, and RNA, and, to bind directly to S-protein with low μM affinity. As further evidence of the potential to generate new capabilities using this approach, we demonstrated that the S-protein/proteomimetic enzyme function can be readily regulated using an additional protein – hDM2 – which competitively binds to the proteomimetics, a property not observed for the S-protein/S-peptide complex. Non-covalent MS analyses suggested the mimetic bound to the S-peptide binding site on the S-protein, a conclusion supported by molecular modelling.

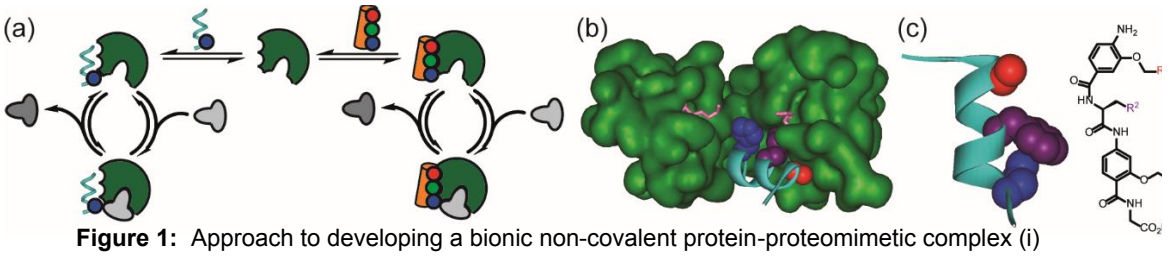

Figure 1: Approach to developing a bionic non-covalent protein-proteomimetic complex (i) Schematic depicting strategy to replace a segment of protein structure with a proteomimetic; (ii) X-ray crystal structure of Bovine Ribonuclease *S*-protein (green)/*S*-peptide (cyan) complex (PDB ID: 1CJQ), highlighting key catalytic residues and an *i*, *i* + 3 and *i* +7 constellation of side chains (iii) *S*-peptide sequence (expansion) upon which to design a helix mimetic and chemical structure of an oligoamide foldamer designed to mimic α-helices.

Our second contribution was a collaborative study with the University of Bristol. We developed a novel predictive approach that provides an informed choice of hot-spot residues. We considered multiple methods for *in silico* alanine scanning applied to different PPIs, and have developed a new fast method, BUDE alanine scanning, which is able to take multiple models for a particular target (e.g., from NMR ensembles or MD simulations), and provides statistical information for ΔΔG values. The method can be accessed via a web-app: http://balas.app. We demonstrated ΔΔG of single-alanine variants changes over structural ensembles and the use of multiple methods in tandem is more powerful. Averaging five different *in silico* tools to predict ΔΔG at PPI interfaces facilitates accurate prediction of hot-residues. To evaluate the utility of the approach, we have performed detailed experimental analyses on three target systems: GKAP/Shank-PDZ (1Q3P), NOXA-B/MCL-1 (2JM6) and SIMS/SUMO (2LAS). In each case, the majority of methods correctly identified the majority of hot-residues and non-hot residues but each method was incorrect for different residues, whereas taking the average of all methods, all but one residue was correctly predicted.

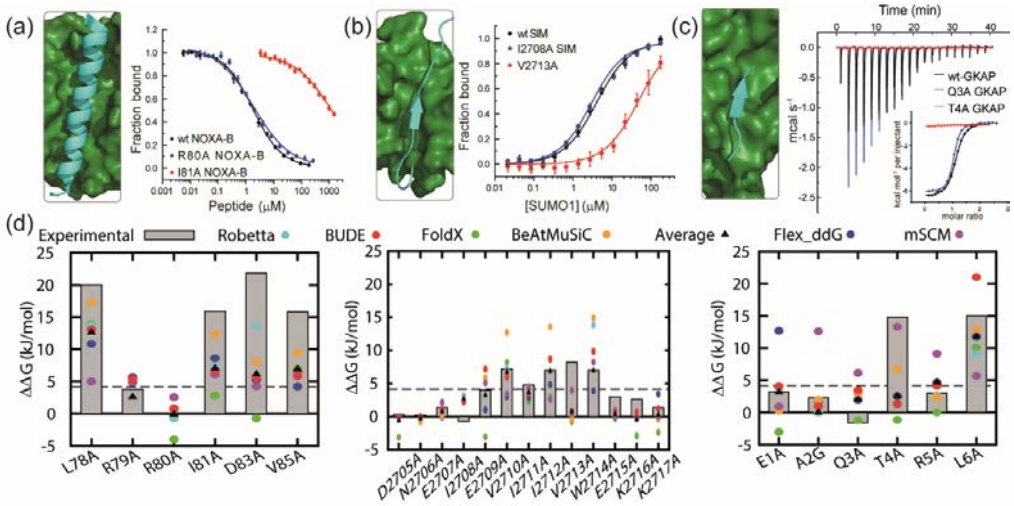

Figure 2: Experimental and predicted alanine scanning results for PPIs (a) crystal structure for NOXA-B/MCL-1 (PDB ID: 2JM6) and representative competition fluorescence anisotropy inhibition curves for inhibition of the FITC-NOXA-B/MCL-1 interaction using variant NOXA-B peptides, (b) NMR structure for SIMS/SUMO (PDB ID: 2LAS) and representative fluorescence anisotropy titration curves for interaction of FITC labelled variant SIMS peptides with SUMO, (c) crystal structure for GKAP/SHANK-PDZ (PDB ID: 1Q3P) and representative isothermal titration calorimetry curves for interaction of acetylated GKAP variant peptides with SHANK-PDZ; (d) comparison of predictive and experimental ΔΔG values (bars represent experimental data for each targets) for NOXA-B/MCL-1, SIMS/SUMO and GKAP/SHANK-PDZ.

In summary, we have expanded understanding of PPIs and the toolkit available for their modulation. This will in future be applied to discovery of inhibitors of clinically relevant PPIs.

Publications

Ibarra A.A., Bartlett G.J., Hegedüs Z., Dutt S., Hobor F., Horner K. A., Hetherington K., Spence K., Nelson A., Edwards T. A., Woolfson, D. N. Sessions R. B., Wilson A. J. (2019) Predicting and Experimentally Validating Hot-spot Residues at Protein-Protein Interfaces, *ACS Chem. Biol.*, **14**, 2252-2263.

Wang Y., Peng Y., Zhang B., Zhang X., Li H., Wilson A.J., Mineev K.S., Wang X. (2019) Targeting trimeric transmembrane domain 5 of oncogenic latent membrane protein 1 using a computationally designed peptide, *Chem. Sci.*, **10**, 7584-7590

Arrata I., Grison C.M., Coubrough H.M., Prabhakaran P., Little M. A., Tomlinson D.C., Webb M.E., Wilson A.J. (2019) Control of Conformation in α-Helix Mimicking Aromatic Oligoamide Foldamers Through Interactions Between Adjacent Side-Chains, *Org. Biomol. Chem.*, **17**, 3861-3867

Hegedus, Z. Grison, C.M. Miles J.A., Rodriguez-Marin S., Warriner S.L., Webb M.E., Wilson A.J. (2019) A Catalytic Protein–Proteomimetic Complex: Using Aromatic Oligoamide Foldamers as Activators of RNase S, *Chem. Sci.*, **10**, 3956-3962.

Funding

We acknowledge The University of Leeds, EPSRC, MRC, ERC, EU-H2020, The Royal Society Newton Programme and The Leverhulme Trust for financial support of this research.

Collaborators

University of Leeds: Darren Tomlinson
External: Dek Woolfson, Richard Sessions and Gail Bartlett (University of Bristol), Christian Ottmann (Eindhoven), Xiaohui Wang (Changchun Institute of Applied Chemistry, China), and AstraZeneca, Domainex, Northern Institute of Cancer Research

Understanding peptide assembly mechanisms

Sam Bunce, Martin Walko, Emma Cawood, Alison Ashcroft, Eric Hewitt, Sheena Radford and Andrew Wilson

Introduction

Understanding the structural mechanism by which proteins and peptides aggregate is crucial, given the role of fibrillar aggregates in debilitating amyloid diseases and bioinspired materials. Yet, this is a major challenge as the assembly involves multiple heterogeneous and transient intermediates. Our team is engaged in a multidisciplinary programme of research that aims to harness the distinct capabilities of chemical biology methods (e.g., photocrosslinking, chemical probes) together with state-of-the-art biophysical, structural and computational methods to understand peptide and protein assembly in greater detail.

Results

We analyzed the co-aggregation of $A\beta_{40}$ and $A\beta_{16-22}$, two widely studied peptide fragments of $A\beta_{42}$ implicated in Alzheimer's disease. Using fluorescence assays, electrospray ionization (ESI)-IMS-MS, and PIC experiments to study the structural mechanism of co-assembly, we demonstrated that $A\beta_{16-22}$ increases the aggregation rate of $A\beta_{40}$ through a surface-catalyzed secondary nucleation mechanism. Discontinuous molecular dynamics simulations allowed aggregation to be tracked from the initial random coil monomer to the catalysis of nucleation on the fibril surface.

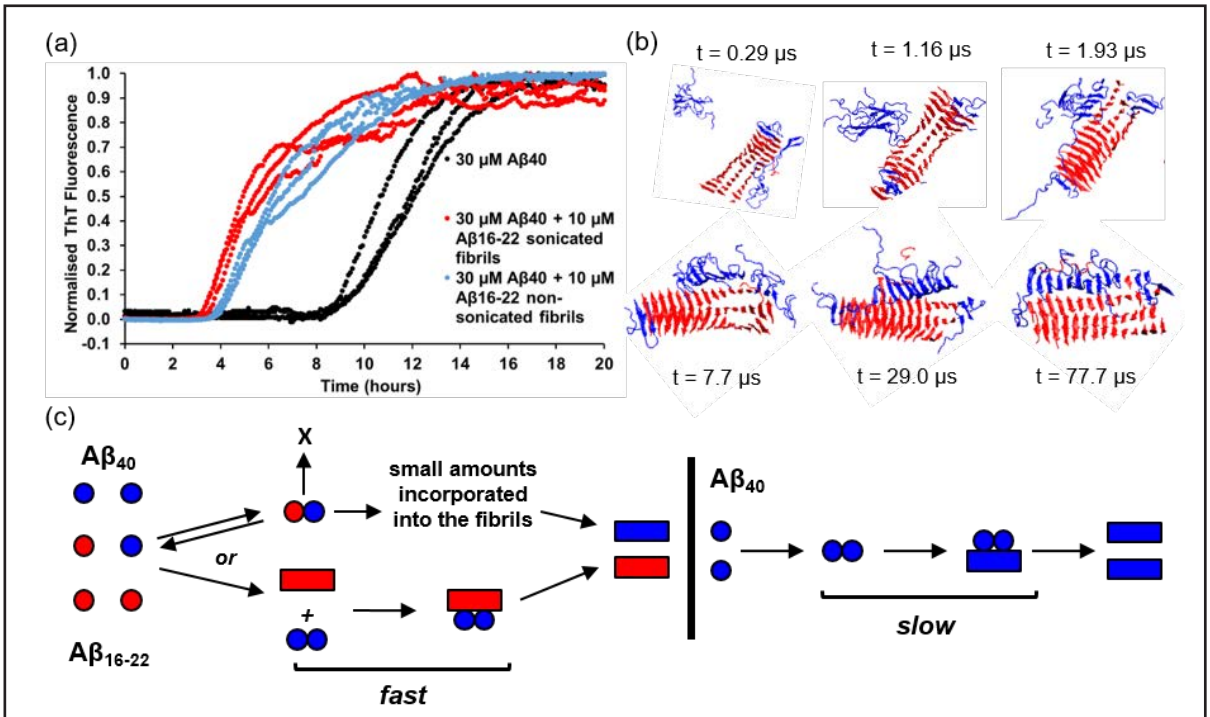

Figure 1: $A\beta_{16-22}$ fibrils increase the aggregation rate of $A\beta_{40}$ by surface-catalyzed secondary nucleation (a) $A\beta_{16-22}$ fibrils or sonicated $A\beta_{16-22\ fibrils}$ were added to $A\beta_{40}$ monomers, and the aggregation rate was measured by ThT fluorescence indicating secondary nucleation and that elongation is not dominant, (b) Simulation snapshots of the process by which $A\beta_{16-22}$ fibrils (red) increase the aggregation rate of $A\beta_{40}$ (blue) through a surface-catalyzed secondary nucleation, (c) A schematic description of the mechanism is also included, with $A\beta_{40}$ in blue and $A\beta_{16-22}$ in red.

Simulations performed on monomers of $A\beta_{40}$ showed that the initially unstructured peptides could assemble and adopt a metastable oligomer structure comprising antiparallel intramolecular β strands linked by disordered regions assembled into antiparallel intermolecular sheets, with β strands stacked perpendicular to the long axis. As the simulation proceeded, this oligomer lost some β-sheet content and then by the end of the simulation, peptides in the oligomer underwent structural rearrangement from antiparallel β-

strand conformations to the parallel β-sheet conformation observed for published $A\beta_{40}$ fibrils/ structures. Preformed $A\beta_{16-22}$ fibrils were observed to increase the early-stage aggregation rate of $A\beta_{40}$ whilst monomeric $A\beta_{16-22}$ peptides did not, supporting secondary nucleation as the mechanism of enhanced $A\beta_{40}$ aggregation by $A\beta_{16-22}$. At the early stage of the co-assembly simulations, $A\beta_{40}$ peptides were present in an oligomer: either associated at the end of the $A\beta_{16-22}$ fibril, or elongated across it. At this stage, the $A\beta_{40}$ peptides in the oligomer and on the surface were observed to adopt a predominantly random coil conformation with small amounts of β-strand structure. The β-sheets were observed to act as templates for peptides present in the random coil conformation and to pull them more fully to the $A\beta_{16-22}$ fibril surface. Thus, as the simulation progressed, the $A\beta_{40}$ peptides remaining in solution were recruited by those on the fibril surface. Once the oligomer became fully associated with the fibril surface, the amount of β-sheet structure in the surface-associated oligomer increased; antiparallel β strands formed via inter- and intramolecular hydrogen bonding, leading to sheet formation consistent with the early stages observed in the simulations performed for $A\beta_{40}$ alone. Thus these experimentally validated simulations portray the structural mechanism of surface-catalyzed nucleation.

In summary, this new understanding may pave the way to the generation of surfaces able to enhance or suppress assembly and may inform effective design of ligands that modulate therapeutically important amyloid assembly.

Publications

Bunce S. J., Wang Y., Stewart K. L., Ashcroft A. E., Radford S. E., Hall C. K., Wilson A. J. (2019) Molecular Insights into the surface catalyzed secondary nucleation of Amyloid-β_{40} ($A\beta_{40}$) by the peptide fragment $A\beta_{16-22}$, *Sci. Adv.,* **5**, eaav8216

Wang, Y. Bunce S. J., Radford S. E., Wilson A. J., Auer S., Hall C. K. (2019) Thermodynamic Phase Diagram of Amyloid-β (16-22) Peptide, *Proc. Natl. Acad. Sci. USA,* **116**, 2091-2096

Funding

We acknowledge The University of Leeds, EPSRC, BBSRC ERC and The Wellcome Trust for financial support of this research.

Collaborators

External: Carol Hall (North Carolina State University)

Chemical crosslinking mass spectrometry of the cancer super-controller N-Myc and Aurora A Kinase

Jaime Pitts, Eoin Leen, Frank Sobott, Richard Bayliss and Megan Wright

Introduction

The pleiotropic oncogenic transcription factor Myc is deregulated or amplified in many cancers. Myc regulates ~15% of human genes, and notably controls cell division and apoptosis. Here we use crosslinking mass spectrometry (XL-MS) to explore how Aurora Kinase A (AURKA), which is critical for mitosis, interacts with N-Myc. AURKA is known to stabilise N-Myc by blocking its proteasomal degradation, shown by a previously obtained structure with N-Myc 61-89. However, it has proven difficult to obtain crystal structures of the full N-Myc transactivation domain (TAD, residues 1-137), which is disordered, in complex with AURKA and other potential drug target kinases. Myc is a family of genes with conserved motifs called Myc boxes. Previous peptide-array data shows that Myc boxes 0, 1 and 2 are involved with interaction between N-Myc and AURKA and not just N-Myc 61-89.

XL-MS gives insights into the structure and dynamics of proteins and complexes. We used the nucleophile-reactive chemical crosslinker disuccinimidyl dibutyric urea (DSBU) with analysis tool MeroX to build a model of the interactions of N-Myc TAD with AURKA. This approach also serves as a testbed for XL-MS of small, intrinsically disordered proteins with larger globular proteins. XL-MS should give 'medium' resolution structural understanding of the interaction by giving distance restraints between pairs of residues within and between proteins. Here, we discuss optimisation of the crosslinking reaction and MS data collection.

Results

The XL-MS workflow consists of validating formation of a crosslinked complex, optimising the reaction conditions by SDS-PAGE and then optimising the mass spectrometric analysis of the crosslinked complex following peptidic digest. We used N-terminal 6×His or 3×FLAG tagged N-Myc 1-137 with AURKA. A titration of DSBU was performed to maximise the yield of the biologically relevant complex whilst minimising over-crosslinked, artefact complexes. Our results showed that 0.025 mM DSBU gives a single band of AURKA in complex with N-Myc (1:1) (Fig. 1).

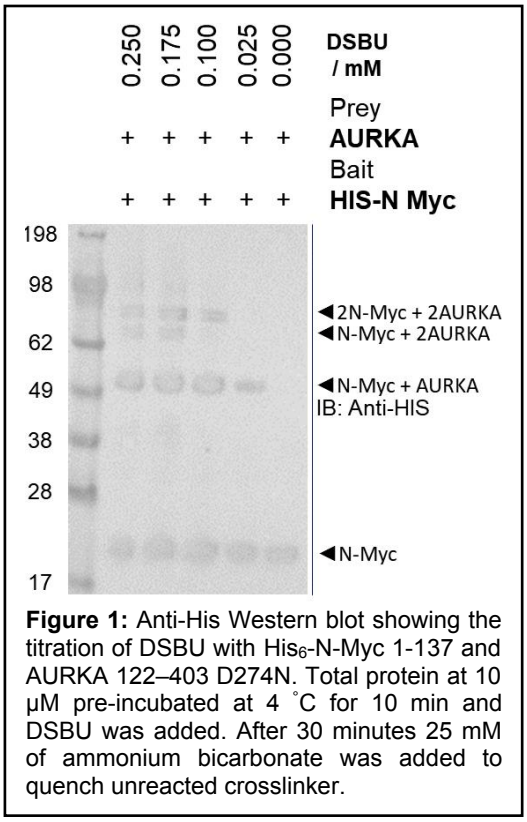

Figure 1: Anti-His Western blot showing the titration of DSBU with His_6-N-Myc 1-137 and AURKA 122–403 D274N. Total protein at 10 μM pre-incubated at 4 ˚C for 10 min and DSBU was added. After 30 minutes 25 mM of ammonium bicarbonate was added to quench unreacted crosslinker.

Following crosslinking, complexes were digested and analysed by nano-HPLC/nano-ESI-MS/MS using a Thermo Scientific Orbitrap Fusion mass spectrometer. The best coverage of crosslinked peptides was obtained by an in-gel stepped digestion with trypsin followed by chymotrypsin. The use of 'inclusion' lists generated in-silico using the sequences of N-Myc and AURKA before LC-MS/MS analysis also improved coverage. XL-MS is typically performed with 1 mM DSBU for 1 hour at room temperature. However, we used 40 times less crosslinker at 4 ˚C for 30 minutes. This underlines that N-Myc is behaving as a reactive disordered region rather than a globular protein; indeed, most of the residues able to crosslink (such as lysine, serine, tyrosine and threonines) do crosslink to AURKA. (Fig. 2).

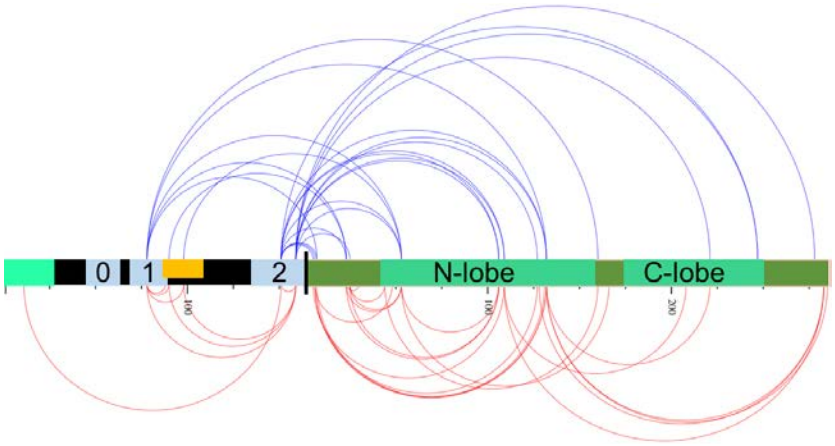

Figure 2: xVis diagram showing the crosslinks between N-Myc (left) and AURKA (right) (blue), and intra-protein crosslinks (red). Myc box 1 reacts mainly with the N-lobe of AURKA and Myc box 2 reacts with the N- and C-lobes of the kinase. The yellow section of N-Myc represents 61-89 found in structure 5G1X.

The cross-links were identified with MeroX and mapped onto the previously obtained crystal structure (Fig. 3). They show that both the front and back face of the N-lobe of AURKA are crosslinked to N-Myc, which cannot be explained with a singular interaction with N-Myc 61-89 and suggests that N-Myc wraps fully around the N-lobe of AURKA.

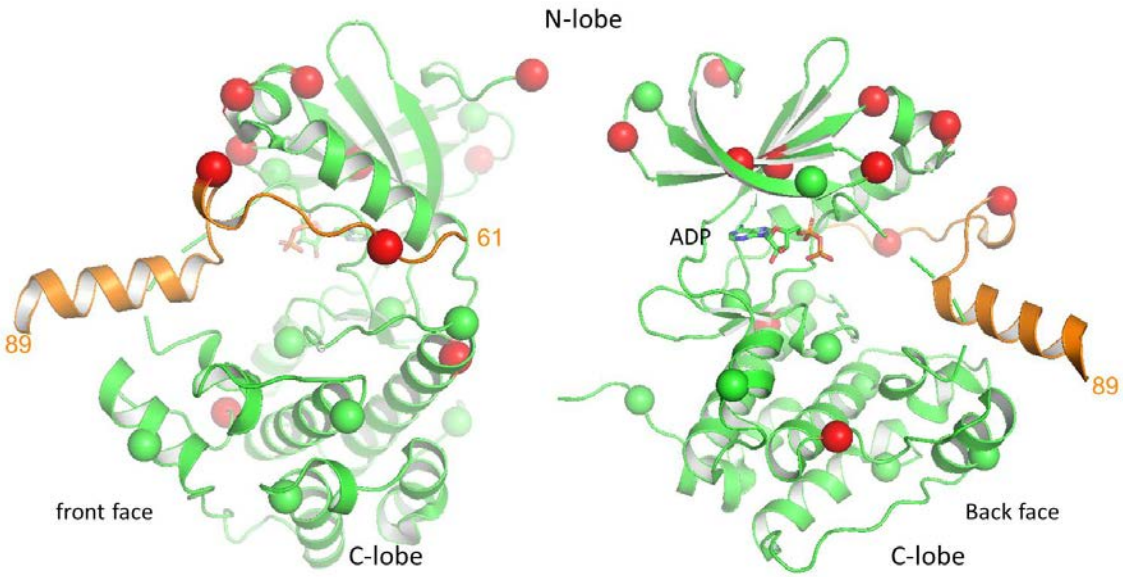

Figure 3: Crosslinks between 3×FLAG N-Myc 1-137 and AURKA 122-403 mapped onto the AURKA (green)/N-Myc 61-89 (orange) crystal structure (PDB: 5G1X). Red spheres show crosslinked residues.

In summary, we optimised XL-MS and used it to show that the previously obtained crystal structure of AURKA with N-Myc does not tell the whole picture of the interaction, consistent with data from peptide arrays. Thus XL-MS is a useful platform to characterise this interaction in more detail and to explore how N-Myc interacts with other less well characterised proteins.

Funding
This work was funded by the Howard Morris scholarship, the University of Leeds and the ERC (AUROMYC).

Collaborators
University of Leeds: James Ault, Rachel George
External: Claudio Iacobucci and Andrea Sinz (Department of Pharmaceutical Chemistry & Bioanalytics, Institute of Pharmacy, Charles Tanford Protein Center, Martin Luther University Halle-Wittenberg)

Defining the structural mechanisms of – and developing tools for – human DNA damage response and repair in cancer cells

William Wilson and Qian Wu

Introduction

DNA damage response (DDR) and repair play critical roles in influencing the efficiency and sensitivity of many cancer treatments. The large amount of DNA damage, especially DNA double-strand breaks (DSBs), generated during chemo/radiotherapy can kill cancer cells, which are under high replication stress. Hence, further inhibition of DDR and repair can enhance treatment outcome. DNA double-strand breaks (DSBs) are repaired by two major repair pathways: Non-Homologous End Joining (NHEJ) and Homologous Recombination (HR) (Figure 1A). These two pathways repair DSBs with different speed, accuracy and cell cycle preference. The degree of DNA end resection is one of the key regulation factors for the pathway choice between NHEJ and HR. Compared with normal cells, cancer cells often contain mutations that cause disfunction in DNA repair pathways. For example, breast cancer cells with mutations in *BRCA1* or *BRCA2* genes have a deficient HR pathway, therefore DSBs are mainly repaired through the NHEJ pathway, which is more error prone. These cancer cells were recently exploited in cancer chemotherapy by poly (ADP-ribose) polymerase (PARP) inhibitors using a principle called synthetic lethality. However, intrinsic or acquired resistance to these drugs occurs in many patients, causing a lack of response or tumour regrowth. It is important to understand the structural mechanisms of DDR and repair in order to classify various functions that influence cancer treatments.

Results

We study Shieldin-CST complex that binds DNA ends through the 53BP1 signalling cascade. Shieldin complex (SHLD1, SHLD2, SHLD3 and Rev7) were recently identified through whole-genome CRISPR-Cas9 screening in BRCA1-deficient breast cancer cells treated with PARP inhibitors. It binds to DSB sites with 3' overhang ssDNA, preventing further DNA end resection and therefore promotes DNA repair through NHEJ. The structural mechanism of how Shieldin-CST complex functions at the DNA ends is largely unknown. We are in the process of purifying, characterizing and determining the structures of individual domains and large Shieldin-CST complex on DNA using both cryo-EM and X-ray crystallography methods (Figure 1B). This project involves collaborations with Prof. Sung, Prof. Jackson and Prof. Sobott's groups.

Through our structural study, we are also developing a group of small protein molecules (Affimers, which function like antibodies but are much smaller) that can inhibit particular domains of DDR complexes through collaboration with Dr Tomlinson's group to provide a molecular understanding of how these complexes influence the sensitivity of cancer cells to each type of cancer treatment (Figure 1A). These Affimer protein tools will also provide the opportunities for modulating the function of DNA repair protein and super-resolution imaging in cancer cells.

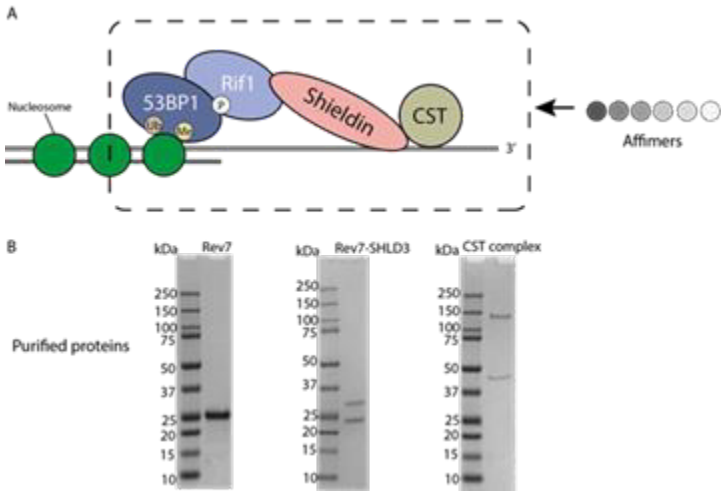

Figure 1: Structural study and tool development of Shieldin-CST complex. A) Shieldin-CST complex at DNA ends. Affimers are generated for targeting this Shieldin-CST complex at DNA ends with 53BP1 and Rif1. B) Purified recombinant proteins for Rev7, SHLD3 in Shieldin complex and CST complex.

Publications

Wu, Q. Structural mechanism of DNA-end synapsis in non-homologous end joining pathway for repairing double-strand breaks: bridge over troubled ends. (2019) *Biochem. Soc. Trans.* **47** (6), 1609-1619.

Wu, Q., Liang, S., Ochi, T., Chirgadze, D.Y., Huiskonen, J.T., Blundell, T.L. (2019) Understanding the structure and role of DNA-PK in NHEJ: How X-ray diffraction and cryo-EM contribute in complementary ways, *Progress in Biophysics and Molecular Biology* **147** 26-32.

Funding

Qian Wu's lab is currently funded by University Academic Fellowship, University of Leeds.

Collaborators:

University of Leeds: Dr Darren Tomlinson, Prof Frank Sobott
External: Stephen Jackson (University of Cambridge), Patrick Sung (University of Texas Health Science Centre at San Antonio)

Metabolic control of BRISC-SHMT2 assembly regulates immune signalling

Miriam Walden, Upasana Sykora, Safi Masandi, Francesca Chandler, Martina Foglizzo, Laura Marr, Lisa Campbell and Elton Zeqiraj

Introduction

Serine hydroxymethyltransferase 2 (SHMT2) is localised to the mitochondria where it functions in one-carbon folate metabolism, which supports nucleotide synthesis and cell growth, using pyridoxal-5'-phosphate (PLP) as a cofactor. Apo SHMT2 is a dimer with no metabolic function, whereas PLP binding induces the active, tetrameric conformation. An N-terminally truncated isoform (SHMT2α) is localised to the cytoplasm where it controls inflammatory cytokine signalling through its interaction with the deubiquitylase (DUB) complex BRISC. BRISC is required for the deubiquitylation of ligand-activated interferon receptors 1 and 2 (IFANR1/2). Direct interaction between BRISC and SHMT2 enhances the delivery of BRISC to ubiquitylated IFNAR1/2, allowing deubiquitylation of lysine-63-linked ubiquitin chains, and limiting the endocytosis and lysosomal degradation of these receptors. The association between BRISC and SHMT2 therefore provides a potential link between metabolism and inflammation. High-resolution structural information for human BRISC is currently unavailable and the molecular basis for SHMT2 binding and regulation is unknown.

Results

We present the cryo-electron microscopy (cryo-EM) structure of the BRISC complex bound to dimeric SHMT2α at a resolution of 3.8 Å, which reveals the BRISC architecture and the molecular basis of the inhibition of DUB activity by SHMT2 (Figure 1).

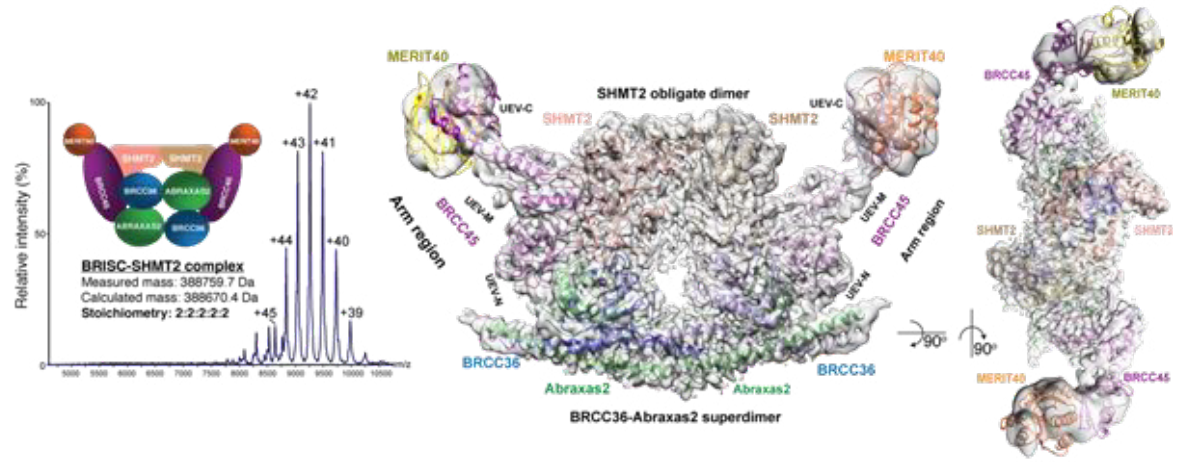

Figure 1: Structure of the BRISC-SHMT2 complex at 3.8 Å resolution. Native mass spectrometry shows a 2:2:2:2:2 stoichiometry of the individual protein subunits within the complex.

BRISC is a U-shaped dimer of four subunits comprising a central core region and two extending arms. SHMT2 bridges the arm regions and sterically blocks the active site thereby inhibiting deubiquitylase activity. This inhibition is dependent on the enzymatically inactive, dimeric form of SHMT2, with the active tetramer unable to bind to BRISC. This suggests a previously unknown role for dimeric (PLP-free) SHMT2 in regulating the DUB activity of BRISC.

Structure-guided mutations were used to probe the relevance of the BRISC-SHMT2 interaction in cells. An E144R mutation in Abraxas 2 completely abolished BRISC-SHMT2 association and greatly reduced downstream IFN-induced inflammatory signalling (Figure 2). A double L211R/L215R mutation in SHMT2 also abolished association and inflammatory signalling and, moreover, both mutants resulted in increased levels of ubiquitylated IFNAR1/2. Collectively, these findings reveal the specific Abraxas 2 and SHMT2 surfaces that are required for BRISC-SHMT2 complex assembly and immune signalling in cells.

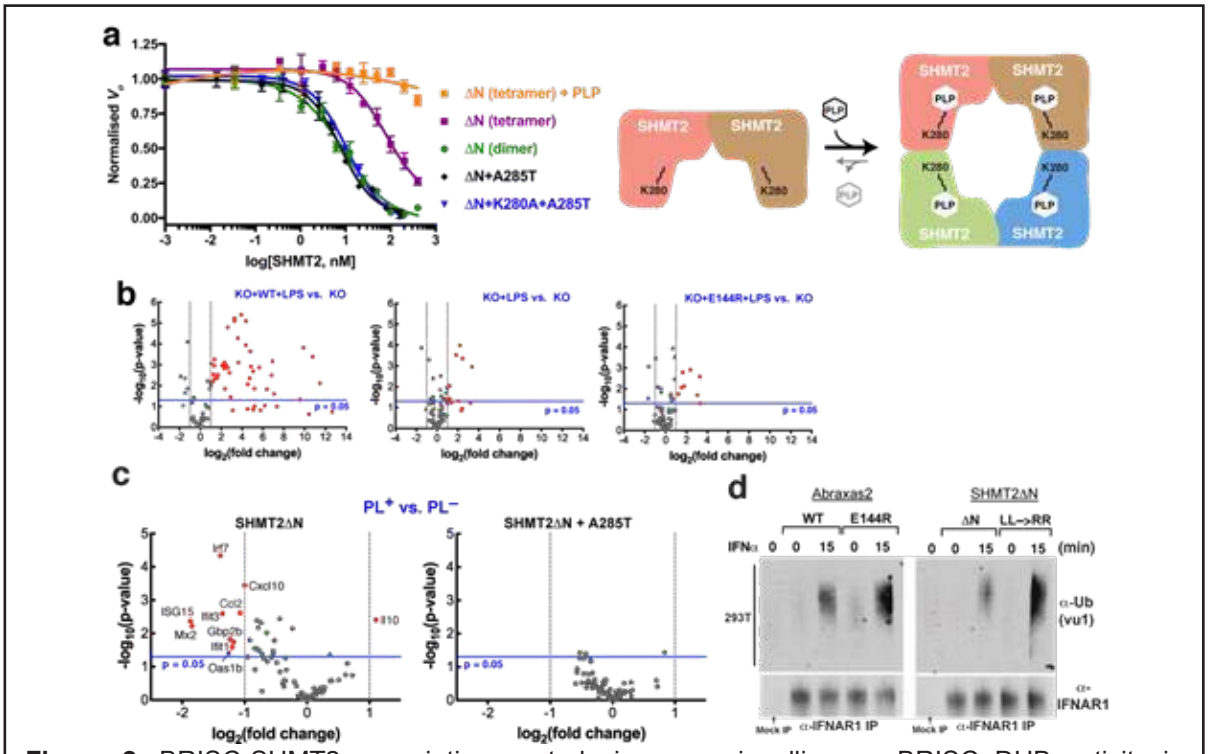

Figure 2: BRISC-SHMT2 association controls immune signalling. **a**. BRISC DUB activity is inhibited by dimeric, but not tetrameric SHMT2. SHMT2 oligomerisation is regulated by PLP binding. **b**. Volcano plots illustrating the fold change in gene expression of IFN-stimulated genes. Abraxas 2 E144R mutation reduces expression of most genes as compared to wild-type. **c**. Volcano plots comparing IFN-induced gene expression in the absence or presence of pyridoxal (PL). PLP-resistant SHMT2 mutants show no change in expression. **d**. Ubiquitylation levels of IFNAR1 after IFN stimulation. Mutations in SHMT2 and Abraxas 2 result in increased levels.

The structure of BRISC-SHMT2 explains why the dimeric SHMT2 – but not the PLP-bound tetramer – inhibits DUB activity. The SHMT2 interface used for BRISC binding overlaps with that used for tetramerisation, and therefore the SHMT2 tetramer and the BRISC-SHMT2 complexes are mutually exclusive. This suggests that PLP-induced tetramerisation could regulate BRISC-SHMT2 complex formation in cells. Increasing intracellular levels of PLP markedly reduced the interaction between BRISC and SHMT2 and led to a pyridoxal-dependent reduction of nine IFN-induced genes (Figure 2). This reduction was not observed when PLP-resistant SHMT2 mutants were expressed (A285T).

We propose that SHMT2 acts as a reversible endogenous BRISC inhibitor that prevents non-specific DUB activity. Furthermore, association of these proteins is regulated by the oligomerisation state of SHMT2, which in turn is controlled by availability of intracellular PLP. This reveals a direct link between vitamin metabolism and control of immune responses.

Publications

Walden M, Tian L, Ross RL, Sykora UM, Byrne DP, Hesketh EL, Masandi SK, Cassel J, George R, Ault JR, El Oualid F, Powłowski K, Salvino JM, Eyers PA, Ranson NA, Del Galdo F, Greenberg RA & Zeqiraj E. (2019) Metabolic control of BRISC-SHMT2 assembly regulates immune signalling. *Nature*. 570 (7760):194-199.

Funding

This work was funded by the Wellcome Trust, the Royal Society, the BBSRC and the MRC.

Collaborators

University of Leeds: Rebecca Ross, Emma Hesketh, Rachel George, James Ault, Neil Ranson, Francesco Del Galdo

External: Lei Tian, Dominic Byrne, Joel Cassel, Farid El Oualid, Krzysztof Pawłowski, Joseph Salvino, Patrick Eyers, Roger Greenberg

The molecular chaperone BiP controls activation of the ER stress sensor Ire1 through several independent mechanisms

Nicholas Hurst, Sam Dawes and Anastasia Zhuravleva

Introduction

Folding and maturation of the majority of secreted and membrane proteins occur in the endoplasmic reticulum (ER) with the assistance of the ER protein quality control (PQC) networks. The protein folding capacity in the ER must be efficiently adjusted to physiological and pathological changes in the ER protein load. The balance between the protein load and the ER folding capacity relies on a regulatory mechanism called the unfolded protein response (UPR). Ire1, the most conserved of ER stress sensors, is activated when its luminal domain (LD) senses ER stress: upon accumulation of unfolded proteins in the ER, Ire1 LD oligomerizes. LD oligomerization results in consequent clustering of the cytoplasmic domain (CD) and its autotransphosphorylation and activation. The active Ire1 non-conversionally slices mRNA of a transcription factor X-box binding protein 1 (XBP1), resulting in its stable form that upregulates ER chaperones and PQC enzyme, aiming to resolve ER stress. Despite a significant progress in structural characterization of the Ire1 activation cascade, our knowledge about the initial step of Ire1 activation, oligomerization of Ire1-LD, remains controversial and incomplete. Particularly, a gap in the current understanding of the Ire1 activation process has come from ongoing debates about a role of the ER molecular chaperone BiP in Ire1 activation. In this study, to examine different mechanisms by which BiP interacts with human Ire1-LD, we have performed detailed biophysical characterization of how the molecular chaperone BiP and model Ire1 substrates control the Ire1-LD activation cascade. We believe that our results open up new perspectives in the understanding of mechanisms that control and fine-tune Ire1 activation.

Results

To understand the activation process in molecular details, we performed detailed biophysical characterization of the luminal domain of human Ire1α (called Ire1-LD in this study) and elucidated how the presence and the absence of its model substrates affect the Ire1-LD oligomeric state and how the molecular chaperone BiP controls this process. In agreement with previous observations, our MST, SEC and MS data consistently report on formation of dimer and low-weight oligomers in the absence of substrate. The apparent oligomerization constant of this process is 0.2 ± 0.03 μM (Figure 1A). In turn, model peptide substrates favour the formation of large Ire1-LD oligomers (Figure 1B) that become insoluble at higher substrate concentrations (Figure 1C and D). Negative-stain TEM of insoluble Ire1-LD demonstrates the formation of fibril-like oligomers (Figure 1D). Solid state NMR of these fibrils revealed that Ire1-LD oligomers form from the folded form of the protein.

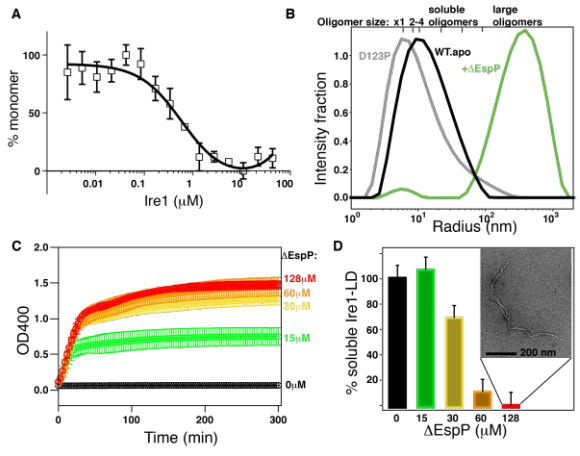

Figure 1. Substrate-induced Ire1-LD oligomerization: (A) Dimerization of Ire1-LD in the absence of ΔEspP monitored by MST. (B) Oligomerization of Ire1-LD in the presence of ΔEspP monitored by DLS. (C and D) Formation of insoluble oligomers of Ire1-LD in the presence of the different concentrations of ΔEspP monitored by turbidity (OD 400, C) and the solubility essay (D). TEM image (D right corner) of insoluble Ire1-LD fibrils.

Altogether these data suggest that, in the presence of model substrates, Ire1-LD adopts an elongated (fibril-like) oligomeric structure. This dynamic oligomerization process and the size of oligomers depend on substrate affinity and substrate concentrations.
Intriquinguly, we observed no formation of insoluble oligomers in the presence of BiP and ATP. Moreover, if insoluble substrate-bound Ire1-LD oligomers are incubated with BiP in the presence of ATP, the turbid Ire1-LD solution becomes clear within a minute, suggesting that BiP enables fast and efficient solubilisation of large Ire1-LD oligomers. Moreover, submolar concentrations of BiP are sufficient to observed solubilisation of Ire1-LD fibrils. These effects are significantly smaller (if noticeable) in the absence of ATP and/or when chaperone activity of BiP is compromised. In the absence of ATP, BiP co-precipitates with insoluble Ire1-LD oligomers as reported by SDS-PAGE (Figure 2A). However, no interactions were observed between BiP and low oligomeric Ire1-LD species by methyl NMR (Figure 2B). These observations suggest that BiP specifically interacts with higher-order oligomeric species of Ire1-LD under tight control of ATP binding and hydrolysis, reminiscent of 'canonical' chaperone-like interactions between BiP and its protein substrates: In the absence of ATP, BiP binds to Ire1-LD oligomers; the addition of ATP results in fast BiP release. This dynamic,

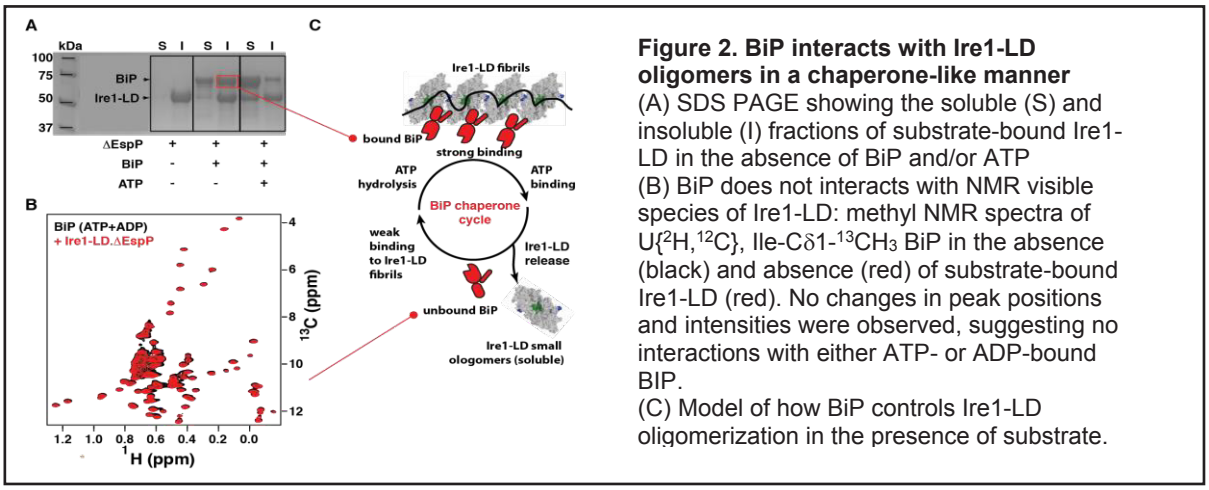

Figure 2. BiP interacts with Ire1-LD oligomers in a chaperone-like manner
(A) SDS PAGE showing the soluble (S) and insoluble (I) fractions of substrate-bound Ire1-LD in the absence of BiP and/or ATP
(B) BiP does not interacts with NMR visible species of Ire1-LD: methyl NMR spectra of U{^{2}H,^{12}C}, Ile-Cδ1-^{13}CH$_3$ BiP in the absence (black) and absence (red) of substrate-bound Ire1-LD (red). No changes in peak positions and intensities were observed, suggesting no interactions with either ATP- or ADP-bound BIP.
(C) Model of how BiP controls Ire1-LD oligomerization in the presence of substrate.

ATP-dependent cycling between the Ire1-bound and -unbound BiP results in destabilization of Ire1-LD oligomers.
Another level of complexity in regulation of Ire1 activation by BiP comes from transient non-conversional (ATP-independent) interactions between Ire1-LD and BiP nucleotide-binding domain (NBD). We demonstrated that these non-conversional interactions significantly reduce formation of intermolecular S-S bonds and covalent oligomerization of Ire1-LD. Whilst the formation of S-S bonds in Ire1-LD has been previously shown to play a regulatory role in the PDIA6-dependent pathway and linked to downstream responses of Ire1, we speculate that the amount and accessibility of BiP in the ER might play an important role in fine-tuning of the PDIA6-dependent pathway of Ire1 activation. Altogether, our results suggest BiP regulates the Ire1 activation process through multiple mechanisms. The fact that BiP affects different steps of the Ire1-LD activation cascades through highly specific interactions with different Ire1-LD oligomeric species indicates that BiP enables precise and stress-specific fine-tuning of the Ire1 conformational ensemble, including the amount and size of oligomeric (active) Ire1 species, their reversibility and interconversion rates. The accessibility of different interaction patterns between Ire1 and BiP, interaction with Ire1 unfolded protein substrates, and evolutional features of Ire1 homologues and orthologous are the main factors that orchestrate the complex, multistep process that senses and triggers Ire1 activation through reshaping the Ire1-LD conformational landscape.

Funding
BBSRC, BBSRC DTP, White Rose University Consortium

Collaborators
University of Leeds: Richard Bayliss, Frank Sobott
External: Beining Chen (University of Sheffield)

ASTBURY SEMINARS 2019

10 January 2019
Elucidating mechanisms of cell shape formation and cytoskeleton remodeling using cryo-EM
Naoko Mizuno (Max Planck Institute of Biochemistry)

7 February 2019
Molecular mechanisms of influenza virus replication
Ervin Fodor (University of Oxford)

7 March 2019
New drugs for multidrug-resistant bacteria
Stephan Sieber (University of Munich)

2 May 2019
Self-assembly of membrane hole punchers of the immune system
Bart Hoogenboom (University College London and London Centre for Nanotechnology)

13 June 2019
Weighing the evidence for molecular chaperone function
Justin Benesch (University of Oxford)

3 October 2019
Order, disorder: allosteric control of Aurora-A kinase in space and time
Richard Bayliss (University of Leeds)

7 November 2019
Order within disorder: complementary NMR insight
Steve Matthews (Imperial College London)

5 December 2019
Structures and signalling mechanisms of human neurotransmitter receptors
Radu Aricescu (MRC Laboratory of Molecular Biology)

PUBLICATIONS

Abou-Saleh R.H., McLaughlan J.R., Bushby R.J., Johnson B.R., Freear S., Evans S.D. and Thomson N.H. (2019) Molecular effects of glycerol on lipid monolayers at the gas liquid interface: Impact on microbubble physical and mechanical properties. *Langmuir* **35**:10097-10105.

Adamson H., Ajayi M.O., Campbell E., Brachi E., Tiede C., Tang A.A., Adams T.L., Ford R., Davidson A., Johnson M.*, et al.* (2019) Affimer-enzyme-inhibitor switch sensor for rapid wash-free assays of multimeric proteins. *ACS Sens* **4**:3014-3022.

Adamson H., Nicholl A., Tiede C., Tang A.A., Davidson A., Curd H., Wignall A., Ford R., Nuttall J., McPherson M.J.*, et al.* (2019) Affimers as anti-idiotypic affinity reagents for pharmacokinetic analysis of biotherapeutics. *Biotechniques* **67**:261-269.

Adeyemi O.O., Sherry L., Ward J.C., Pierce D.M., Herod M.R., Rowlands D.J. and Stonehouse N.J. (2019) Involvement of a nonstructural protein in poliovirus capsid assembly. *J Virol* **93**:e01447-18.

Adib R., Montgomery J.M., Atherton J., O'Regan L., Richards M.W., Straatman K.R., Roth D., Straube A., Bayliss R., Moores C.A.*, et al.* (2019) Mitotic phosphorylation by NEK6 and NEK7 reduces the microtubule affinity of eml4 to promote chromosome congression. *Sci Signal* **12**: eaaw2939.

Alfaro-Chavez A.L., Liu J.W., Porter J.L., Goldman A. and Ollis D.L. (2019) Improving on nature's shortcomings: Evolving a lipase for increased lipolytic activity, expression and thermostability. *Protein Eng Des Sel* **32**:13-24.

Amos S., Kalli A.C., Shi J.Y. and Sansom M.S.P. (2019) Membrane recognition and binding by the phosphatidylinositol phosphate kinase PIP5K1A: A multiscale simulation study. *Structure* **27**:1336-1346.

Amsbury S. and Benitez-Alfonso Y. (2019) Phloem unloading tightening the pores to unload the phloem. *Nat Plants* **5**:561-562.

Armistead F.J., De Pablo J.G., Gadelha H., Peyman S.A. and Evans S.D. (2019) Cells under stress: An inertial-shear microfluidic determination of cell behavior. *Biophys J* **116**:1127-1135.

Arrata I., Grison C.M., Coubrough H.M., Prabhakaran P., Little M.A., Tomlinson D.C., Webb M.E. and Wilson A.J. (2019) Control of conformation in alpha-helix mimicking aromatic oligoamide foldamers through interactions between adjacent side-chains. *Org Biomol Chem* **17**:3861-3867.

Azeez K.R.A., Chatterjee S., Yu C.N., Golub T.R., Sobott F. and Elkins J.M. (2019) Structural mechanism of synergistic activation of Aurora kinase B/C by phosphorylated INCENP. *Nat Commun* **10**:3166.

Bakail M., Rodriguez-Marin S., Hegedus Z., Perrin M.E., Ochsenbein F. and Wilson A.J. (2019) Recognition of ASF1 by using hydrocarbon-constrained peptides. *ChemBioChem* **20**:891-895.

Bao P., Paterson D.A., Harrison P.L., Miller K., Peyman S., Jones J.C., Sandoe J., Evans S.D., Bushby R.J. and Gleeson H.F. (2019) Lipid coated liquid crystal droplets for the on-chip detection of antimicrobial peptides. *Lab Chip* **19**:1082-1089.

Baquero-Perez B., Antanaviciute A., Yonchev I.D., Carr I.M., Wilson S.A. and Whitehouse A.

(2019) The Tudor SND1 protein is an m(6)a RNA reader essential for replication of Kaposi's sarcoma-associated herpesvirus. *eLife* **8**:e47261.

Batchelor M., Wolny M., Baker E.G., Paci E., Kalverda A.P. and Peckham M. (2019) Dynamic ion pair behavior stabilizes single -helices in proteins. *J Biol Chem* **294**:3219-3234.

Bayfield O.W., Klimuk E., Winkler D.C., Hesketh E.L., Chechik M., Cheng N.Q., Dykeman E.C., Minakhin L., Ranson N.A., Severinov K.*, et al.* (2019) Cryo-EM structure and *in vitro* DNA packaging of a thermophilic virus with supersized t=7 capsids. *Proc Natl Acad Sci USA* **116**:3556-3561.

Beard H.A., Hauser J.R., Walko M., George R.M., Wilson A.J. and Bon R.S. (2019) Photocatalytic proximity labelling of MCL-1 by a BH3 ligand. *Comm Chem* **2**:133.

Beech D.J. and Kalli A.C. (2019) Force sensing by piezo channels in cardiovascular health and disease. *Arterioscler Thromb Vasc Biol* **39**:2228-2239.

Benitez-Alfonso Y. (2019) The role of abscisic acid in the regulation of plasmodesmata and symplastic intercellular transport. *Plant Cell Physiol* **60**:713-714.

Benseny-Cases N., Karamanos T.K., Hoop C.L., Baum J. and Radford S.E. (2019) Extracellular matrix components modulate different stages in β_2-microglobulin amyloid formation. *J Biol Chem* **294**:9392-9401.

Berdiell I.C., Hochdorffer T., Desplanches C., Kulmaczewski R., Shahid N., Wolny J.A., Warriner S.L., Cespedes O., Schunemann V., Chastanet G.*, et al.* (2019) Supramolecular iron metallocubanes exhibiting site-selective thermal and light-induced spin-crossover. *J Am Chem Soc* **141**:18759-18770.

Blythe N.M., Muraki K., Ludlow M.J., Stylianidis V., Gilbert H.T.J., Evans E.L., Cuthbertson K., Foster R., Swift J., Li J.*, et al.* (2019) Mechanically activated piezo1 channels of cardiac fibroblasts stimulate p38 mitogen-activated protein kinase activity and interleukin-6 secretion. *J Biol Chem* **294**:17395-17408.

Booth A., Marklew C.J., Ciani B. and Beales P.A. (2019) In vitro membrane remodeling by ESCRT is regulated by negative feedback from membrane tension. *iScience* **15**:173-184.

Brown P., Tan A.C., El-Esawi M.A., Liehr T., Blanck O., Gladue D.P., Almeida G.M.F., Cernava T., Sorzano C.O., Yeung A.W.K.*, et al.* (2019) Large expert-curated database for benchmarking document similarity detection in biomedical literature search. *Database* **2019**:baz085.

Bunce S.J., Wang Y.M., Stewart K.L., Ashcroft A.E., Radford S.E., Hall C.K. and Wilson A.J. (2019) Molecular insights into the surface-catalyzed secondary nucleation of amyloid-β_{40} ($A\beta_{40}$) by the peptide fragment $A\beta_{16-22}$ *Sci Adv* **5:**eaav8216.

Byrne M.J., Steele J.F.C., Hesketh E.L., Walden M., Thompson R.F., Lomonossoff G.P. and Ranson N.A. (2019) Combining transient expression and cryo-EM to obtain high-resolution structures of luteovirid particles. *Structure* **27**:1761-1770.

Cahill S.T., Tyrrell J.M., Navratilova I.H., Calvopina K., Robinson S.W., Lohans C.T., McDonough M.A., Cain R., Fishwick C.W.G., Avison M.B.*, et al.* (2019) Studies on the inhibition of AmpC and other beta-lactamases by cyclic boronates. *Biochim Biophys Acta-Gen Subj* **1863**:742-748.

Cain R., Salimraj R., Punekar A.S., Bellini D., Fishwick C.W.G., Czaplewski L., Scott D.J., Harris G., Dowson C.G., Lloyd A.J.*, et al.* (2019) Structure-guided enhancement of

selectivity of chemical probe inhibitors targeting bacterial seryl-tRNA synthetase. *J Med Chem* **62**:9703-9717.

Carrier D.J., van Roermund C.W.T., Schaedler T.A., Rong H.L., Ijlst L., Wanders R.J.A., Baldwin S.A., Waterham H.R., Theodoulou F.L. and Baker A. (2019) Mutagenesis separates ATPase and thioesterase activities of the peroxisomal ABC transporter, comatose. *Sci Rep* **9**:10502.

Carrington G., Tomlinson D. and Peckham M. (2019) Exploiting nanobodies and affimers for superresolution imaging in light microscopy. *Mol Biol Cell* **30**:2737-2740.

Chand S., Beales P.A., Claeyssens F. and Ciani B. (2019) Topography design in model membranes: Where biology meets physics. *Exp Biol Med* **244**:294-303.

Charlton F.W., Hover S., Fuller J., Hewson R., Fontana J., Barr J.N. and Mankouri J. (2019) Cellular cholesterol abundance regulates potassium accumulation within endosomes and is an important determinant in Bunyavirus entry. *J Biol Chem* **294**:7335-7347.

Chen X.Y. and Richter R.P. (2019) Effect of calcium ions and pH on the morphology and mechanical properties of hyaluronan brushes. *Interface Focus* **9:**20180061.

Chiduza G.N., Johnson R.M., Wright G.S.A., Antonyuk S.V., Muench S.P. and Hasnain S.S. (2019) LAT1 (SLC7A5) and CD98hc (SLC3A2) complex dynamics revealed by single-particle cryo-EM. *Acta Crystallogr Sect D-Struct Biol* **75**:660-669.

Chong S., Antoni M., Macdonald A., Reeves M., Harber M. and Magee C.N. (2019) Bk virus: Current understanding of pathogenicity and clinical disease in transplantation. *Rev Med Virol* **29**:e2044.

Colombano G., Caldwell J.J., Matthews T.P., Bhatia C., Joshi A., McHardy T., Mok N.Y., Newbatt Y., Pickard L., Strover J.*, et al.* (2019) Binding to an unusual inactive kinase conformation by highly selective inhibitors of inositol-requiring enzyme 1α kinase-endoribonuclease. *J Med Chem* **62**:2447-2465.

Cornwell O., Bond N.J., Radford S.E. and Ashcroft A.E. (2019) Long-range conformational changes in monoclonal antibodies revealed using FPOP-LC-MS/MS. *Anal Chem* **91**:15163-15170.

Davies H.S., Baranova N.S., El Amri N., Coche-Guerente L., Verdier C., Bureau L., Richter R.P. and Debarre D. (2019) An integrated assay to probe endothelial glycocalyx-blood cell interactions under flow in mechanically and biochemically well-defined environments. *Matrix Biol* **78-79**:47-59.

Davies K., Afrough B., Mankouri J., Hewson R., Edwards T.A. and Barr J.N. (2019) Tula orthohantavirus nucleocapsid protein is cleaved in infected cells and may sequester activated caspase-3 during persistent infection to suppress apoptosis. *J Gen Virol* **100**:1208-1221.

De Bruyn P., Hadzi S., Vandervelde A., Konijnenberg A., Prolic-Kalinsek M., Sterckx Y.G.J., Sobott F., Lah J., Van Melderen L. and Loris R. (2019) Thermodynamic stability of the transcription regulator PaaR2 from Escherichia coli O157:H7. *Biophys J* **116**:1420-1431.

De Vecchis D., Reithmeier R.A.F. and Kalli A.C. (2019) Molecular simulations of intact anion exchanger 1 reveal specific domain and lipid interactions. *Biophys J* **117**:1364-1379.

Deinum, E.E., Mulder, B.M., Benitez-Alfonso, Y. (2019) From plasmodesma geometry to effective symplasmic permeability through biophysical modelling. *Elife*. **8**. pii: e49000.

Deivasikamani V., Dhayalan S., Abudushalamu Y., Mughal R., Visnagri A., Cuthbertson K., Scragg J.L., Munsey T.S., Viswambharan H., Muraki K.*, et al.* (2019) Piezo1 channel activation mimics high glucose as a stimulator of insulin release. *Sci Rep* **9**:16876.

Dilly S.J., Morris G.S., Taylor P.C., Parmentier F., Williams C. and Afshar M. (2019) Clinical pharmacokinetics of a lipid-based formulation of risperidone, val401: Analysis of a single dose in an open-label trial of late-stage cancer patients. *Eur J Drug Metabol Pharmacokinet* **44**:557-565.

Dos Santos Rodriguez, F., Firczuk, H., Breeze, A.L., Cameron, A.D., Walko, M., Wilson, A.J., Zanchin, N.I.T. & McCarthy, J.E.G. (2019) The *Leishmania* PABP1–eIF4E4 interface: A novel 5′–3′ interaction architecture for trans-spliced mRNA. *Nucleic Acids Res*. **47**, 1493-1504.

Drulyte I., Obajdin J., Trinh C.H., Kalverda A.P., van der Kamp M.W., Hemsworth G.R. and Berry A. (2019) Crystal structure of the putative cyclase IdmH from the indanomycin nonribosomal peptide synthase/polyketide synthase. *IUCrJ* **6**:1120-1133.

Dubacheva G.V., Curk T., Frenkel D. and Richter R.P. (2019) Multivalent recognition at fluid surfaces: The interplay of receptor clustering and superselectivity. *J Am Chem Soc* **141**:2577-2588.

Duncan J.A., Foster R. and Kwok J.C.F. (2019) The potential of memory enhancement through modulation of perineuronal nets. *Br J Pharmacol* **176**:3611-3621.

Dutoit R., Van Gompel T., Brandt N., Van Elder D., Van Dyck J., Sobott F. and Droogmans L. (2019) How metal cofactors drive dimer-dodecamer transition of the M42 aminopeptidase Tmpep1050 of *Thermotoga maritima*. *J Biol Chem* **294**:17777-17789.

Edwards, T.A. and Barr, J.N. (2019). Reply to Rameix-Welti, “No incongruity in respiratory syncytial virus M2-1 protein remaining bound to viral mRNAs during their entire life time.” *mBio* **10**:e00629-19.

Fearnley G.W., Abdul-Zani I., Latham A.M., Hollstein M.C., Ladbury J.E., Wheatcroft S.B., Odell A.F. and Ponnambalam S. (2019) Tpl2 is required for VEGF-A-stimulated signal transduction and endothelial cell function. *Biol Open* **8**:bio034215.

Fowler C.A., Sabbadin F., Ciano L., Hemsworth G.R., Elias L., Bruce N., McQueen-Mason S., Davies G.J. and Walton P.H. (2019) Discovery, activity and characterisation of an AA10 lytic polysaccharide oxygenase from the shipworm symbiont *Teredinibacter turnerae*. *Biotechnol Biofuels* **12**:232.

Frandsen K.E.H., Tovborg M., Jorgensen C.I., Spodsberg N., Rosso M.N., Hemsworth G.R., Garman E.F., Grime G.W., Poulsen J.C.N., Batth T.S.*, et al.* (2019) Insights into an unusual auxiliary activity 9 family member lacking the histidine brace motif of lytic polysaccharide monooxygenases. *J Biol Chem* **294**:17117-17130.

Fuller J., Surtees R.A., Shaw A.B., Alvarez-Rodriguez B., Slack G.S., Bell-Sakyi L., Mankouri J., Edwards T.A., Hewson R. and Barr J.N. (2019) Hazara nairovirus elicits differential induction of apoptosis and nucleocapsid protein cleavage in mammalian and tick cells. *J Gen Virol* **100**:392-402.

Fuller J., Surtees R.A., Slack G.S., Mankouri J., Hewson R. and Barr J.N. (2019) Rescue of infectious recombinant hazara nairovirus from cDNA reveals the nucleocapsid protein DQVD caspase cleavage motif performs an essential role other than cleavage. *J Virol* **93**:e00616-19.

Gabelica V., Shvartsburg A.A., Afonso C., Barran P., Benesch J.L.P., Bleiholder C., Bowers M.T., Bilbao A., Bush M.F., Campbell J.L.*, et al.* (2019) Recommendations for reporting ion mobility mass spectrometry measurements. *Mass Spectrom Rev* **38**:291-320.

Gao Y.N., Goonawardane N., Ward J., Tuplin A. and Harris M. (2019) Multiple roles of the non-structural protein 3 (nsP3) alphavirus unique domain (AUD) during chikungunya virus genome replication and transcription. *PLoS Pathog* **15**:e1007239.

Goodchild J.A., Walsh D.L. and Connell S.D. (2019) Nanoscale substrate roughness hinders domain formation in supported lipid bilayers. *Langmuir* **35**:15352-15363.

Gopalasingam C.C., Johnson R.M., Chiduza G.N., Tosha T., Yamamoto M., Shiro Y., Antonyuk S.V., Muench S.P. and Hasnain S.S. (2019) Dimeric structures of quinol-dependent nitric oxide reductases (qNORs) revealed by cryo-electron microscopy. *Sci Adv* **5**:eaax1803.

Grison M.S., Kirk P., Brault M.L., Wu X.N., Schulze W.X., Benitez-Alfonso Y., Immel F. and Bayer E.M. (2019) Plasma membrane-associated receptor-like kinases relocalize to plasmodesmata in response to osmotic stress. *Plant Physiol* **181**:142-160.

Hallac F.S., Fragkopoulos I.S., Connell S.D. and Muller F.L. (2019) Micro-mechanical properties of single high aspect ratio crystals. *Crystengcomm* **21**:5738-5748.

Hameed U.F.S., Liao C.Y., Radhakrishnan A.K., Huser F., Aljedani S.S., Zhao X.C., Momin A.A., Melo F.A., Guo X.R., Brooks C.*, et al.* (2019) H-NS uses an autoinhibitory conformational switch for environment-controlled gene silencing. *Nucleic Acids Res* **47**:2666-2680.

Hancock A.M., Meredith S.A., Connell S.D., Jeuken L.J.C. and Adams P.G. (2019) Proteoliposomes as energy transferring nanomaterials: Enhancing the spectral range of light-harvesting proteins using lipid-linked chromophores. *Nanoscale* **11**:16284-16292.

Hanson B.S., Head D. and Dougan L. (2019) The hierarchical emergence of worm-like chain behaviour from globular domain polymer chains. *Soft Matter* **15**:8778-8789.

Hao Y.X., England J.P., Bellucci L., Paci E., Hodges H.C., Taylor S.S. and Maillard R.A. (2019) Activation of PKA via asymmetric allosteric coupling of structurally conserved cyclic nucleotide binding domains. *Nat Commun* **10**:3984.

Harper K.L., McDonnell E. and Whitehouse A. (2019) CircRNAs: From anonymity to novel regulators of gene expression in cancer (review). *Int J Oncol* **55**:1183-1193.

Hassan K.A., Naidu V., Edgerton J.R., Mettrick K.A., Liu Q., Fahmy L., Li L.P., Jackson S.M., Ahmad I., Sharples D.*, et al.* (2019) Short-chain diamines are the physiological substrates of PACE family efflux pumps. *Proc Natl Acad Sci USA* **116**:18015-18020.

Heath, G.R. & Scheuring S. (2019) Advances in high-speed atomic force microscopy (HS-AFM) reveal dynamics of transmembrane channels and transporters. Curr. Opin. Struct. Biol. 57: 93-102.

Hegedus Z., Grison C.M., Miles J.A., Rodriguez-Marin S., Warriner S.L., Webb M.E. and Wilson A.J. (2019) A catalytic protein-proteomimetic complex: Using aromatic oligoamide foldamers as activators of RNAse S. *Chem Sci* **10**:3956-3962.

Herod M.R., Adeyemi O.O., Ward J., Bentley K., Harris M., Stonehouse N.J. and Polyak S.J. (2019) The broad-spectrum antiviral drug arbidol inhibits foot-and-mouth disease virus genome replication. *J Gen Virol* **100**:1293-1302.

Hesketh E.L., Tiede C., Adamson H., Adams T.L., Byrne M.J., Meshcheriakova Y., Kruse I., McPherson M.J., Lomonossoff G.P., Tomlinson D.C*., et al.* (2019) Affimer reagents as tools in diagnosing plant virus diseases. *Sci Rep* **9**:7524.
Holmes, A.O.M., Kalli, A.C. & Goldman, A. (2019) The Function of Membrane Integral Pyrophosphatases From Whole Organism to Single Molecule. *Front Mol Biosci* **6,** 132.

Huang K., Parmeggiani F., Ledru H., Hollingsworth K., Pons J.M., Marchesi A., Both P., Mattey A.P., Pallister E., Bulmer G.S*., et al.* (2019) Enzymatic synthesis of n-acetyllactosamine from lactose enabled by recombinant beta 1,4-galactosyltransferases. *Org Biomol Chem* **17**:5920-5924.

Huggins D.J., Biggin P.C., Damgen M.A., Essex J.W., Harris S.A., Henchman R.H., Khalid S., Kuzmanic A., Laughton C.A., Michel J*., et al.* (2019) Biomolecular simulations: From dynamics and mechanisms to computational assays of biological activity. *Wiley Interdiscip Rev-Comput Mol Sci* **9**:e1393.

Humes J.R., Schiffrin B., Calabrese A.N., Higgins A.J., Westhead D.R., Brockwell D.J. and Radford S.E. (2019) The role of SurA PPIase domains in preventing aggregation of the outer-membrane proteins tompa and ompt. *J Mol Biol* **431**:1267-1283.

Iacobucci C., Piotrowski C., Aebersold R., Amaral B.C., Andrews P., Bernfur K., Borchers C., Brodie N.I., Bruce J.E., Cao Y*., et al.* (2019) First community-wide, comparative cross-linking mass spectrometry study. *Anal Chem* **91**:6953-6961.

Ibarra A.A., Bartlett G.J., Hegedus Z., Dutt S., Hobor F., Horner K.A., Hetherington K., Spence K., Nelson A., Edwards T.A*., et al.* (2019) Predicting and experimentally validating hot-spot residues at protein-protein interfaces. *ACS Chem Biol* **14**:2252-2263.

Johnson R.M., Higgins A.J. and Muench S.P. (2019) Emerging role of electron microscopy in drug discovery. *Trends BiochemSci* **44**:897-898.

Jones S.J., Taylor A.F. and Beales P.A. (2019) Towards feedback-controlled nanomedicines for smart, adaptive delivery. *Exp Biol Med* **244**:283-293.

Kapsalis C., Wang B.L., El Mkami H., Pitt S.J., Schnell J.R., Smith T.K., Lippiat J.D., Bode B.E. and Pliotas C. (2019) Allosteric activation of an ion channel triggered by modification of mechanosensitive nano-pockets. *Nat Commun* **10**:4619.

Karamanos T.K., Jackson M.P., Calabrese A.N., Goodchild S.C., Cawood E.E., Section G.S.T., Kalverda A.P., Hewitt E.W. and Radford S.E. (2019) Structural mapping of oligomeric intermediates in an amyloid assembly pathway. *eLife* **8**:e46574.

Kearney K.J., Pechlivani N., King R., Tiede C., Phoenix F., Cheah R., Macrae F.L., Simmons K.J., Manfield I.W., Smith K.A*., et al.* (2019) Affimer proteins as a tool to modulate fibrinolysis, stabilize the blood clot, and reduce bleeding complications. *Blood* **133**:1233-1244.

Kendall C., Khalid H., Muller M., Banda D.H., Kohl A., Merits A., Stonehouse N.J. and Tuplin A. (2019) Structural and phenotypic analysis of chikungunya virus RNA replication elements. *Nucleic Acids Res* **47**:9296-9312.

Kime L., Randall C.P., Banda F.I., Coll F., Wright J., Richardson J., Empel J., Parkhill J. and O'Neill A.J. (2019) Transient silencing of antibiotic resistance by mutation represents a significant potential source of unanticipated therapeutic failure. *mBio* **10**:e01755-19.

Kirkham C.M., Scott J.N.F., Wang X.L., Smith A.L., Kupinski A.P., Ford A.M., Westhead

D.R., Stockley P.G., Tuma R. and Boyes J. (2019) Cut-and-run: A distinct mechanism by which V(D)J recombination causes genome instability. *Mol Cell* **74**:584-597.

Kontziampasis D., Klebl D.P., Iadanza M.G., Scarff C.A., Kopf F., Sobott F., Monteiro D.C.F., Trebbin M., Muench S.P. and White H.D. (2019) A cryo-EM grid preparation device for time-resolved structural studies. *IUCrJ* **6**:1024-1031.

Lapitan L.D.S., Xu Y.H., Guo Y. and Zhou D.J. (2019) Combining magnetic nanoparticle capture and poly- enzyme nanobead amplification for ultrasensitive detection and discrimination of DNA single nucleotide polymorphisms. *Nanoscale* **11**:1195-1204.

Lattimer J., Stewart H., Locker N., Tuplin A., Stonehouse N.J. and Harris M. (2019) Structure-function analysis of the equine hepacivirus 5 ' untranslated region highlights the conservation of translational mechanisms across the hepaciviruses. *J Gen Virol* **100**:1501-1514.

Laurent H., Soper A. and Dougan L. (2019) Biomolecular self-assembly under extreme Martian mimetic conditions. *Mol Phys* **117**:3398-3407.

Lee S.C., Collins R., Lin Y.P., Jamshad M., Broughton C., Harris S.A., Hanson B.S., Tognoloni C., Parslow R.A., Terry A.E.*, et al.* (2019) Nano-encapsulated *Escherichia coli* divisome anchor ZipA, and in complex with FtsZ. *Sci Rep* **9:**18712.

Lee V.E. and O'Neill A.J. (2019) Potential for repurposing the personal care product preservatives bronopol and bronidox as broad-spectrum antibiofilm agents for topical application. *J Antimicrob Chemother* **74**:907-911.

Leng J., Shoura M., McLeish T.C.B., Real A.N., Hardey M., McCafferty J., Ranson N.A. and Harris S.A. (2019) Securing the future of research computing in the biosciences. *PLoS Comput Biol* **15:**e1006958.

Lennyte F., Dittwald P., Claesen J., Baggerman G., Sobott F., O'Connor P.B., Laukens K., Hooyberghs J., Gambin A. and Valkenborg D. (2019) Mind: A double-linear model to accurately determine monoisotopic precursor mass in high-resolution top-down proteomics. *Anal Chem* **91**:10310-10319.

Lepsik M., Sommer R., Kuhaudomlarp S., Lelimousin M., Paci E., Varrot A., Titz A. and Imberty A. (2019) Induction of rare conformation of oligosaccharide by binding to calcium-dependent bacterial lectin: X-ray crystallography and modelling study. *Eur J Med Chem* **177**:212-220.

Lin C.C., Suen K.M., Stainthorp A., Wieteska L., Biggs G.S., Leitao A., Montanari C.A. and Ladbury J.E. (2019) Targeting the Shc-EGFR interaction with indomethacin inhibits map kinase pathway signalling. *Cancer Lett* **457**:86-97.

Litschko C., Bruhmann S., Csiszar A., Stephan T., Dimchev V., Damiano-Guercio J., Junemann A., Korber S., Winterhoff M., Nordholz B.*, et al.* (2019) Functional integrity of the contractile actin cortex is safeguarded by multiple diaphanous-related formins. *Proc Natl Acad Sci USA* **116**:3594-3603.

Lulla V., Dinan A.M., Hosmillo M., Chaudhry Y., Sherry L., Irigoyen N., Nayak K.M., Stonehouse N.J., Zilbauer M., Goodfellow I.*, et al.* (2019) An upstream protein-coding region in enteroviruses modulates virus infection in gut epithelial cells. *Nat Microbiol* **4**:280-292.

Macleod T., Ward J., Alase A.A., Bridgewood C., Wittmann M. and Stonehouse N.J. (2019) Antimicrobial peptide ll-37 facilitates intracellular uptake of rna aptamer apt 21-2 without inducing an inflammatory or interferon response. *Front Immunol* **10**:857.

Mahon C.S., Wildsmith G.C., Haksar D., de Poel E., Beekman J.M., Pieters R.J., Webb M.E. and Turnbull W.B. (2019) A 'catch-and-release' receptor for the cholera toxin. *Faraday Discuss* **219**:112-127.

Majiya H., Chowdhury K.F., Stonehouse N.J. and Millner P. (2019) TMPyP functionalised chitosan membrane for efficient sunlight driven water disinfection. *J Water Process Eng* **30**:100475.

Malone L.A., Qian P., Mayneord G.E., Hitchcock A., Farmer D.A., Thompson R.F., Swainsbury D.J.K., Ranson N.A., Hunter C.N. and Johnson M.P. (2019) Cryo-EM structure of the spinach cytochrome b(6) f complex at 3.6 angstrom resolution. *Nature* **575**:535-539.

Mancuso E., Tonda-Turo C., Ceresa C., Pensabene V., Connell S.D., Fracchia L. and Gentile P. (2019) Potential of manuka honey as a natural polyelectrolyte to develop biomimetic nanostructured meshes with antimicrobial properties. *Front Bioeng Biotechnol* **7**:344.

Manners O., Baquero-Perez B. and Whitehouse A. (2019) M(6)a: Widespread regulatory control in virus replication. *Biochim Biophys Acta-Gene Regul Mech* **1862**:370-381.

Maori E., Navarro I.C., Boncristiani H., Seilly D.J., Rudolph K.L.M., Sapetschnig A., Lin C.C., Ladbury J.E., Evans J.D., Heeney J.L.*, et al.* (2019) A secreted RNA binding protein forms RNA-stabilizing granules in the honeybee royal jelly. *Mol Cell* **74**:598-608.

Marsian J., Hurdiss D.L., Ranson N.A., Ritala A., Paley R., Cano I. and Lomonossoff G.P. (2019) Plant-made nervous necrosis virus-like particles protect fish against disease. *Front Plant Sci* **10**:880.

Mayol-Llinas J., Chow S. and Nelson A. (2019) Expansion of the structure-activity relationships of BACE1 inhibitors by harnessing diverse building blocks prepared using a unified synthetic approach. *MedChemComm* **10**:616-620.

Mazurenko I., Hatzakis N.S. and Jeuken L.J.C. (2019) Single liposome measurements for the study of proton-pumping membrane enzymes using electrochemistry and fluorescent microscopy. *J Vis Exp*. **144**:e58896.

Michou M., Kapsalis C., Pliotas C. and Skretas G. (2019) Optimization of recombinant membrane protein production in the engineered *Escherichia coli* strains SuptoxD and SuptoxR. *ACS Synth Biol* **8**:1631-1641.

Mikula K.M., Kolodziejczyk R. and Goldman A. (2019) Structure of the UspA1 protein fragment from moraxella catarrhalis responsible for C3d binding. *J Struct Biol* **208**:77-85.

Miles J., Scherz-Shouval R. and van Oosten-Hawle P. (2019) Expanding the organismal proteostasis network: Linking systemic stress signaling with the innate immune response. *Trends BiochemSci* **44**:927-942.

Miles J.A., Machattou P., Nevin-Jones D., Webb M.E., Millard A., Scanlan D.J. and Taylor P.C. (2019) Identification of a cyanobacterial aldehyde dehydrogenase that produces retinoic acid *in vitro*. *Biochem Biophys Res Commun* **510**:27-34.

Minard A., Bauer C.C., Chuntharpursat-Bon E., Pickles I.B., Wright D.J., Ludlow M.J., Burnham M.P., Warriner S.L., Beech D.J., Muraki K.*, et al.* (2019) Potent, selective, and subunit-dependent activation of TRPC5 channels by a xanthine derivative. *Br J Pharmacol* **176**:3924-3938.

Moens U. and Macdonald A. (2019) Effect of the large and small t-antigens of human polyomaviruses on signaling pathways. *Int J Mol Sci* **20**:E3914.

Morgan E.L. and Macdonald A. (2019) Autocrine STAT3 activation in HPV positive cervical cancer through a virus-driven Rac1-NF κB-IL-6 signalling axis. *PLoS Pathog* **15:**e1007835.

Morgan E.L. and Macdonald A. (2019) JAK2 inhibition impairs proliferation and sensitises cervical cancer cells to cisplatin-induced cell death. *Cancers* **11**:E1934.

Muench S.P., Antonyuk S.V. and Hasnain S.S. (2019) The expanding toolkit for structural biology: Synchrotrons, x-ray lasers and cryoEM. *IUCrJ* **6**:167-177.

Muller M., Slivinski N., Todd E., Khalid H., Li R., Karwatka M., Merits A., Mankouri J. and Tuplin A. (2019) Chikungunya virus requires cellular chloride channels for efficient genome replication. *Plos Neglect Trop Dis* **13:**e0007703.

Narramore S., Stevenson C.E.M., Maxwell A., Lawson D.M. and Fishwick C.W.G. (2019) New insights into the binding mode of pyridine-3-carboxamide inhibitors of *E. coli* DNA gyrase. *Bioorg Med Chem* **27**:3546-3550.

Nelson A. (2019) Protein engineering catalytic machinery of enzymes expanded. *Nature* **570**:172-173.

Ohmann A., Gopfrich K., Joshi H., Thompson R.F., Sobota D., Ranson N.A., Aksimentiev A. and Keyser U.F. (2019) Controlling aggregation of cholesterol-modified DNA nanostructures. *Nucleic Acids Res* **47**:11441-11451.

Oram J. and Jeuken L.J.C. (2019) Tactic response of *Shewanella oneidensis* mr-1 toward insoluble electron acceptors. *mBio* **10:**e02490-18.

Osterlund N., Moons R., Ilag L.L., Sobott F. and Graslund A. (2019) Native ion mobility-mass spectrometry reveals the formation of beta-barrel shaped amyloid-beta hexamers in a membrane-mimicking environment. *J Am Chem Soc* **141**:10440-10450.

Parsons E.S., Stanley G.J., Pyne A.L.B., Hodel A.W., Nievergelt A.P., Menny A., Yon A.R., Rowley A., Richter R.P., Fantner G.E.*, et al.* (2019) Single-molecule kinetics of pore assembly by the membrane attack complex. *Nat Commun* **10**:2066.

Pavic A., Holmes A.O.M., Postis V.L.G. and Goldman A. (2019) Glutamate transporters: A broad review of the most recent archaeal and human structures. *Biochem Soc Trans* **47**:1197-1207.

Perez M.A., Moriones O.H., Bastus N.G., Puntes V., Nelson A. and Beales P.A. (2019) Mechanomodulation of lipid membranes by weakly aggregating silver nanoparticles. *Biochemistry* **58**:4761-4773.

Pollock N.L., Rai M., Simon K.S., Hesketh S.J., Teo A.C.K., Parmar M., Sridhar P., Collins R., Lee S.C., Stroud Z.N.*, et al.* (2019) SMA-PAGE: A new method to examine complexes of membrane proteins using SMALP nano-encapsulation and native gel electrophoresis. *Biochim Biophys Acta-Biomembr* **1861**:1437-1445.

Radom F., Paci E. and Pluckthun A. (2019) Computational modeling of designed ankyrin repeat protein complexes with their targets. *J Mol Biol* **431**:2852-2868.

Remenyi R., Li R. and Harris M. (2019) On-demand labeling of snap-tagged viral protein for pulse-chase imaging, quench-pulse-chase imaging, and nanoscopy-based inspection of cell lysates. *Bio-protocol* **9**:e3177.

Ribeiro A.J.M., Das S., Dawson N., Zaru R., Orchard S., Thornton J.M., Orengo C., Zeqiraj E., Murphy J.M. and Eyers P.A. (2019) Emerging concepts in pseudoenzyme classification, evolution, and signaling. *Sci Signal* **12:**eaat9797.

Rice S., Cox D.J., Marsden S.P. and Nelson A. (2019) Unified synthesis of diverse building blocks for application in the discovery of bioactive small molecules. *Tetrahedron* **75**:130513.

Rodrigues F.H.D., Firczuk H., Breeze A.L., Cameron A.D., Walko M., Wilson A.J., Zanchin N.I.T. and McCarthy J.E.G. (2019) The Leishmania PABP1-eIF4E4 interface: A novel 5-3 interaction architecture for trans-spliced mRNAs. *Nucleic Acids Res* **47**:1493-1504.

Rongkaumpan G., Amsbury S., Andablo-Reyes E., Linford H., Connell S., Knox J.P., Sarkar A., Benitez-Alfonso Y. and Orfila C. (2019) Cell wall polymer composition and spatial distribution in ripe banana and mango fruit: Implications for cell adhesion and texture perception. *Front Plant Sci* **10**:858.

Ross J.F., Wildsmith G.C., Johnson M., Hurdiss D.L., Hollingsworth K., Thompson R.F., Mosayebi M., Trinh C.H., Paci E., Pearson A.R.*, et al.* (2019) Directed assembly of homopentameric cholera toxin b-subunit proteins into higher-order structures using coiled-coil appendages. *J Am Chem Soc* **141**:5211-5219.

Rowlands D.J. (2019) Career thoughts and recollections: 50 years of publishing in the journal of general virology. *J Gen Virol* **100**:1390-1392.

Shawli G.T., Adeyemi O.O., Stonehouse N.J. and Herod M.R. (2019) The oxysterol 25-hydroxycholesterol inhibits replication of murine norovirus. *Viruses-Basel* **11**:e97.

Shen K.N., Gamerdinger M., Chan R., Gense K., Martin E.M., Sachs N., Knight P.D., Schlomer R., Calabrese A.N., Stewart K.L.*, et al.* (2019) Dual role of ribosome-binding domain of NAC as a potent suppressor of protein aggregation and aging-related proteinopathies. *Mol Cell* **74**:729-741.

Silva S., Shimizu J.F., de Oliveira D.M., de Assis L.R., Bittar C., Mottin M., Sousa B.K.D., Mesquita N., Regasini L.O., Rahal P.*, et al.* (2019) A diarylamine derived from anthranilic acid inhibits ZIKV replication. *Sci Rep* **9**:17703.

Skinner S.P., Radou G., Tuma R., Houwing-Duistermaat J.J. and Paci E. (2019) Estimating constraints for protection factors from HDX-MS data. *Biophys J* **116**:1194-1203.

Smith A.J., Wright K.E., Muench S.P., Schumann S., Whitehouse A., Porter K.E. and Colyer J. (2019) Styrene maleic acid recovers proteins from mammalian cells and tissues while avoiding significant cell death. *Sci Rep* **9**:16408.

Sobrinos-Sanguino M., Velez M., Richter R.P. and Rivas G. (2019) Reversible membrane tethering by ZipA determines FtsZ polymerization in two and three dimensions. *Biochemistry* **58**:4003-4015.

Stikane A., Hwang E.T., Ainsworth E.V., Piper S.E.H., Critchley K., Butt J.N., Reisner E. and Jeuken L.J.C. (2019) Towards compartmentalized photocatalysis: Multihaem proteins as transmembrane molecular electron conduits. *Faraday Discuss* **215**:26-38.

Tanaka M., Takahashi Y., Roach L., Critchley K., Evans S.D. and Okochi M. (2019) Rational screening of biomineralisation peptides for colour-selected one-pot gold nanoparticle syntheses. *Nanoscale Adv* **1**:71-75.

Thankachan D., Fazal A., Francis D., Song L.J., Webb M.E. and Seipke R.F. (2019) A trans-

acting cyclase offloading strategy for nonribosomal peptide synthetases. *ACS Chem Biol* **14**:845-849.

Thompson R.F., Iadanza M.G., Hesketh E.L., Rawson S. and Ranson N.A. (2019) Collection, pre-processing and on-the-fly analysis of data for high-resolution, single-particle cryo-electron microscopy. *Nat Protoc* **14**:100-118.

Tsai J.Y., Tang K.Z., Li K.M., Hsu B.L., Chiang Y.W., Goldman A. and Sun Y.J. (2019) Roles of the hydrophobic gate and exit channel in *Vigna radiata* pyrophosphatase ion translocation. *J Mol Biol* **431**:1619-1632.

Turnbull W.B., Imberty A. and Blixt O. (2019) Synthetic glycobiology. *Interface Focus* **9**: 20190004.

Twarock R. and Stockley P.G. (2019). RNA-mediated virus assembly: Mechanisms and consequences for viral evolution and therapy. *Ann Rev Biophys* **48**:495-514.

Vidilaseris K., Johansson N.G., Turku A., Kiriazis A., af Gennas G.B., Yli-Kauhaluoma J., Xhaard H. and Goldman A. (2019) Screening for *Thermotoga maritima* membrane-bound pyrophosphatase inhibitors. *J Vis Exp* **153:**e60619.

Vidilaseris, K., Johansson, N. G., Turku, A., Kiriazis, A., Boije Af Gennäs, G., Yli-Kauhaluoma, J., Xhaard, H. & Goldman, A. (2019) Screening protocol for identification of *Thermotoga maritima* membrane-bound pyrophosphatase inhibitors. *J. Vis. Exp* DOI: 10.3791/60619.

Vidilaseris K., Kiriazis A., Turku A., Khattab A., Johansson N.G., Leino T.O., Kiuru P.S., af Gennas G.B., Meri S., Yli-Kauhaluoma J.*, et al.* (2019) Asymmetry in catalysis by *Thermotoga maritima* membrane-bound pyrophosphatase demonstrated by a nonphosphorus allosteric inhibitor. *Sci Adv* **5**:eaav7574.

Walden M., Tian L., Ross R.L., Sykora U.M., Byrne D.P., Hesketh E.L., Masandi S.K., Cassel J., George R., Ault J.R.*, et al.* (2019) Metabolic control of brisc-shmt2 assembly regulates immune signalling. *Nature* **570**:194-199.

Walko M., Hewitt E., Radford S.E. and Wilson A.J. (2019) Design and synthesis of cysteine-specific labels for photo-crosslinking studies. *RSC Adv* **9**:7610-7614.

Wang Y.B., Peng Y.H., Zhang B., Zhang X.Z., Li H.Y., Wilson A.J., Mineev K.S. and Wang X.H. (2019) Targeting trimeric transmembrane domain 5 of oncogenic latent membrane protein 1 using a computationally designed peptide. *Chem Sci* **10**:7584-7590.

Wang Y.M., Bunce S.J., Radford S.E., Wilson A.J., Auer S. and Hall C.K. (2019) Thermodynamic phase diagram of amyloid-beta (16-22) peptide. *Proc Natl Acad Sci USA* **116**:2091-2096.

Whelan F., Lafita A., Griffiths S.C., Cooper R.E.M., Whittingham J.L., Turkenburg J.P., Manfield I.W., John A.N.S., Paci E., Bateman A.*, et al.* (2019) Defining the remarkable structural malleability of a bacterial surface protein rib domain implicated in infection. *Proc Natl Acad Sci USA* **116**:26540-26548.

Winkler M.B.L., Kidmose R.T., Szomek M., Thaysen K., Rawson S., Muench S.P., Wustner D. and Pedersen B.P. (2019) Structural insight into eukaryotic sterol transport through Niemann-Pick type C proteins. *Cell* **179**:485-497.

Wodak S.J., Paci E., Dokholyan N.V., Berezovsky I.N., Horovitz A., Li J., Hilser V.J., Behar I., Karanicolas J., Stock G.*, et al.* (2019) Allostery in its many disguises: From theory to

applications. *Structure* **27**:566-578.

Wu Q. Structural mechanism of DNA-end synapsis in non-homologous end joining pathway for repairing double-strand breaks: bridge over troubled ends. (2019) *Biochem. Soc. Trans.* **47** (6), 1609-1619.

Wu Q., Liang S.K., Ochi T., Chirgadze D.Y., Huiskonen J.T. and Blundell T.L. (2019) Understanding the structure and role of DNA-pk in nhej: How X-ray diffraction and cryo-EM contribute in complementary ways. *Prog Biophys Mol Biol* **147**:26-32.

Xanthis I., Souilhol C., Serbanovic-Canic J., Roddie H., Kalli A.C., Fragiadaki M., Wong R., Shah D.R., Askari J.A., Canham L.*, et al.* (2019) β1 integrin is a sensor of blood flow direction. *J Cell Sci* **132:**jcs229542.

Ye S.J., Brown A.P., Stammers A.C., Thomson N.H., Wen J., Roach L., Bushby R.J., Coletta P.L., Critchley K., Connell S.D.*, et al.* (2019) Sub-nanometer thick gold nanosheets as highly efficient catalysts. *Adv Sci* **6**:1900911.

Zhang R., McIntyre P.J., Collins P.M., Foley D.J., Arter C., von Delft F., Bayliss R., Warriner S. and Nelson A. (2019) Construction of a shape-diverse fragment set: Design, synthesis and screen against Aurora-A kinase. *Chem-Eur J* **25**:6831-6839.

Zhou D.M., Zhao Y.G., Kotecha A., Fry E.E., Kelly J.T., Wang X.X., Rao Z.H., Rowlands D.J., Ren J.S. and Stuart D.I. (2019) Unexpected mode of engagement between enterovirus 71 and its receptor scarb2. *Nat Microbiol* **4**:414-419.

The Astbury Centre for
Structural Molecular Biology
University of Leeds
Leeds
LS2 9JT
Tel: 0113 343 3086
astbury@leeds.ac.uk
www.astbury.leeds.ac.uk

UNIVERSITY OF LEEDS
University of Leeds
Leeds, United Kingdom
LS2 9JT
Tel: 0113 243 1751
www.leeds.ac.uk